MATERIALS PHYSICS AND MECHANICS

MATERIALS PHYSICS AND MECHANICS

International scientific journal "**Materials Physics and Mechanics**" is published by Peter the Great St.Petersburg Polytechnic University in collaboration with Institute of Problems of Mechanical Engineering of the Russian Academy of Sciences in both hard copy and electronic versions.

The journal provides an international medium for the publication of reviews and original research papers written in English and focused on the following topics:

- Mechanics of composite and nanostructured materials.
- Physics of strength and plasticity of composite and nanostructured materials.
- Mechanics of deformation and fracture processes in conventional materials (solids).
- Physics of strength and plasticity of conventional materials (solids).
- Physics and mechanics of defects in composite, nanostructured, and conventional materials.
- Mechanics and physics of materials in coupled fields.

Owner organizations: Peter the Great St. Petersburg Polytechnic University; Institute of Problems of Mechanical Engineering RAS.

Materials Physics and Mechanics is indexed in Chemical Abstracts, Cambridge Scientific Abstracts,
Web of Science Emerging Sources Citation Index (ESCI) and Elsevier Bibliographic Databases (in particular, SCOPUS).

МЕХАНИКА И ФИЗИКА МАТЕРИАЛОВ

Materials Physics and Mechanics

Том 50, номер 2, 2022 год

Тематика журнала

Международный научный журнал "Materials Physics and Mechanics" издается Санкт-Петербургским политехническим университетом Петра Великого в сотрудничестве с Институтом проблем машиноведения Российской Академии Наук в печатном виде и электронной форме. Журнал публикует обзорные и оригинальные научные статьи на английском языке по следующим тематикам:
- Механика композиционных и наноструктурированных материалов.
- Физика прочности и пластичности композиционных и наноструктурированных материалов.
- Механика процессов деформации и разрушения в традиционных материалах (твердых телах).
- Физика прочности и пластичности традиционных материалов (твердых тел).
- Физика и механика дефектов в композиционных, наноструктурированных и традиционных материалах.
- Механика и физика материалов в связанных полях.

Редколлегия принимает статьи, которые нигде ранее не опубликованы и не направлены для опубликования в другие научные издания. Все представляемые в редакцию журнала "Механика и физика материалов" статьи рецензируются. Статьи могут отправляться авторам на доработку. Не принятые к опубликованию статьи авторам не возвращаются.

Журнал "Механика и физика материалов" ("Materials Physics and Mechanics") включен в систему цитирования Web of Science Emerging Sources Citation Index (ESCI), SCOPUS и РИНЦ.

Contents

Strengthening of nanocrystalline alloys by grain boundary segregations

A.G. Sheinerman[✉]

Institute for Problems of Mechanical Engineering RAS, 61, Bolshoi Pr. V.O., St. Petersburg, Russia, 199178

[✉] asheinerman@gmail.com

Abstract. We suggest a model that describes the strengthening of nanocrystalline metallic alloys due to inhomogeneous grain boundary (GB) segregations. Within the model, inhomogeneous GB segregations are modeled by spherical dilatational inclusions whose elastic fields interact with lattice or GB dislocations. We consider two modes of plastic deformation of nanocrystalline alloys: GB sliding realized via the motion of GB dislocations over GBs and slip of lattice dislocations across grains. The calculations demonstrate that in the case of GB sliding, which occurs in nanocrystalline alloys with the finest grains, inhomogeneous segregations induce only moderate strengthening. In contrast, high strengthening due to GB segregations is achieved in nanocrystalline alloys with larger grain sizes, deformed through lattice dislocation slip. This implies that the preferred kind of segregations for maximum strengthening of nanocrystalline alloys can depend on their grain size.
Keywords: nanocrystalline alloys; grain boundaries; segregations; strengthening

Citation: Sheinerman AG. Strengthening of nanocrystalline alloys by grain boundary segregations. *Materials Physics and Mechanics*. 2022;50(2): 193-199. DOI: 10.18149/MPM.5022022_1.

1. Introduction
Due to their ultrahigh strength and thermal stability, nanocrystalline metal alloys draw much attention last years [1-4]. In contrast to coarse-grained materials, where plastic deformation processes are carried out mainly due to the motion of dislocations within grains, in nanocrystalline alloys, the structure and composition of grain boundaries (GBs) have a primary effect on plastic deformation processes and strength. In particular, GB segregations of alloying elements have a great effect on the mechanical properties of nanocrystalline alloys. Although such segregations, under certain conditions, can lead to the embrittlement of nanocrystalline alloys, they can stabilize such alloys, inhibiting grain growth, and also lead to an increase in the ultimate strength or an increase in ductility. Examples of this are nanocrystalline steels [2], nanocrystalline silver-based alloys with ensembles of growth twins [3], and nanocrystalline Ni-Mo alloys [4] with record values of ultimate strength and hardness.

The strengthening effect of GB segregations has been attributed to various factors. For example, in [5,6] it was assumed that the increase in strength due to GB segregations is

associated with a decrease in the activation volume for the nucleation of dislocations, experimentally recorded [6] for the Zr-Nb alloy with GB segregations of sulfur. Computer simulations [7] of nanocrystalline Ag with Cu segregations demonstrated that strengthening can result from the inactivation of GB dislocation sources by GB segregations. At the same time, the results of computer simulations [8] show that strengthening can also stem from the hindering effect of GB segregations on dislocation motion across grains.

In [9], a moderate increase in the yield strength of nanocrystalline Al was demonstrated in the presence of Co segregations and the absence of a strengthening effect was documented for Mg segregations. An earlier work [10] showed the reverse (softening) effect of Pb segregations on the strength of nanocrystalline Al. In both cases, the simulation showed that the deformation of nanocrystalline Al (with Mg or Pb segregations) is carried out by GB sliding or GB sliding combined with GB migration. Therefore, it can be concluded that even if Pb segregations suppress intragranular dislocation slip, they can facilitate GB sliding, which leads to a decrease in yield strength.

At the same time, recent experiments with nanocrystalline Ni-Mo alloys [4] have shown that, in such alloys, low-temperature annealing, presumably leading to the appearance of Mo GB segregations [4], can, in contrast, suppress GB sliding and, thereby, significantly increase the hardness of such alloys. Computer simulations [11] of the deformation of Ag-Ni and Ag-Cu nanocrystalline alloys showed that the possibility of GB sliding in nanocrystalline alloys with segregations depends on the type of segregations. In particular, in this work, segregations in Ag-Cu alloys, distributed along the entire length of GBs, did not prevent GB sliding, which led to softening. In contrast, segregations in nanocrystalline Ag-Ni alloys, which formed clusters in certain areas of GBs, created obstacles for GB sliding, leading to high flow stresses in such alloys.

Thus, the results of experiments and computer simulations demonstrate that GB segregations can strengthen nanocrystalline alloys but the mechanism of strengthening is not clear enough yet. To fill this gap, here we suggest a model that describes the effect of clustered GB segregations on the yield strength of nanocrystalline metallic alloys deformed via GB sliding or through intragranular dislocation slip.

2. Strengthening of nanocrystalline alloys deformed via GB sliding

Consider a solid containing grain boundary (GB) segregations. Within the model, we treat the segregations as dilatational spherical inclusions of radius R_0 (Fig. 1a). We focus on the case of small GBs, whose size does not exceed several diameters of the inclusions and therefore assume that each GB contains not more than one inclusion. To examine the effect of the spherical inclusions on GB sliding, we assume that GB sliding occurs via the slip of edge GB dislocations over GBs. Each spherical inclusion creates an elastic stress field that creates forces acting on dislocations in its vicinity. Since the stress field of the inclusion is a short-range one and drops as R^{-3} outside the inclusion [12] (where R is the distance from the inclusion center), we assume that each inclusion at a GB can affect GB sliding only over this and adjacent GBs.

Now consider the geometry of an individual spherical inclusion at a GB (Fig. 1b). We introduce a Cartesian coordinate system (x, y, z) and a spherical coordinate system (R, θ, φ) with the origin at the center of the spherical inclusion (Fig. 1b). Here θ is the angle between the radius vector of a point and the z-axis, while φ is the angle between the projection of the radius vector onto the xy-plane and the x-axis. The y- and z-axes of the Cartesian coordinate system lie in the GB plane, while the x-axis is normal to the GB.

(a)   (b)

(c)
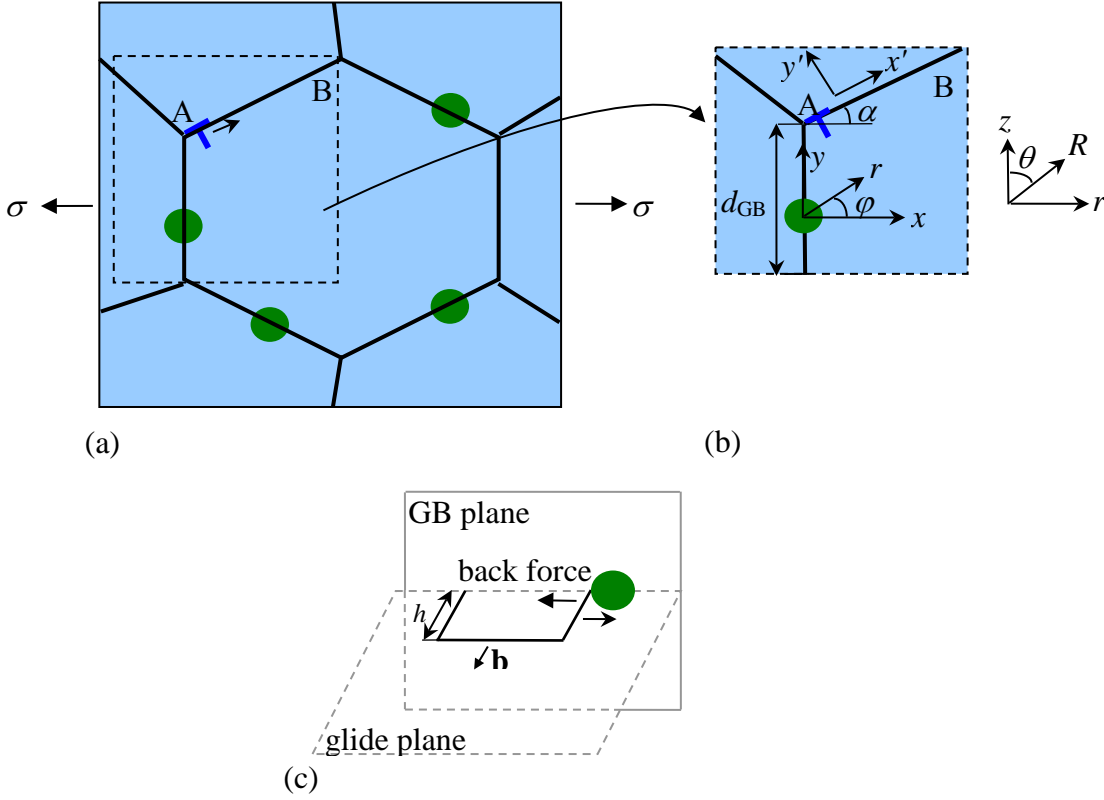
Fig. 1. Nanocrystalline solid with GB segregations. (a) A fragment of a nanocrystalline solid with GB segregations. GB sliding along GB AB occurs via the slip of a GB dislocation from triple junction A toward triple junction B. (b) Geometry of the coordinate systems used to calculate the stress field of a GB segregation. (c) Intragranular dislocation slip occurs via the generation of a glide dislocation loop at a GB and its expansion inside the grain interior. GB segregation exerts a back force on the segment of the expanding dislocation loop

In the examined case of the dilatational eigenstrain of inclusion, the eigenstrain tensor ε_{ij}^{*} can be written as

$$\varepsilon_{ij}^{*} = \varepsilon^{*}\delta_{ij} , \tag{1}$$

where $i, j = x, y, z$, ε^{*} is the lattice mismatch between the inclusion and the matrix, defined as (e.g., ([13])

$$\varepsilon^{*} = \frac{a_{i} - a_{m}}{a_{m}} , \tag{2}$$

a_{i} and a_{m} are the lattice parameters of the inclusion and matrix, respectively, and δ_{ij} is the Kronecker delta equal to unity if $i = j$ and to zero otherwise. In the linear approximation, we have:

$$a_{s} \approx a_{m} + 100(c_{s} - c_{m})\Delta a , \tag{3}$$

where Δa is the change of the lattice parameter of the alloy associated with an increase of the solute concentration by 0.01 (that is, by 1 at.%), and c_{s} and c_{m} is the average solute concentration in the segregations and matrix, respectively.

In the approximation of an elastically homogeneous isotropic solid with the shear modulus G and Poison's ratio ν , the stress field of the inclusion can be written as [12]

$$\sigma_{RR} = 2A \begin{cases} 1, R < R_0 \\ (R_0 / R)^3, R > R_0 \end{cases}, \tag{4}$$

$$\sigma_{\theta\theta} = \sigma_{\varphi\varphi} = A \begin{cases} -2, R < R_0 \\ (R_0 / R)^3, R > R_0 \end{cases}, \tag{5}$$

$$\sigma_{R\theta} = \sigma_{R\varphi} = \sigma_{\theta\varphi} = 0, \tag{6}$$

where $A = 2(1+\nu)G\varepsilon * /[3(1-\nu)]$.

From formulae (4) to (6) it is easy to see that the stress σ_{xy} created by the spherical inclusion at the GB plane $x = 0$ is equal to zero. This implies that the inclusion does not create any forces on the dislocations moving over this GB. At the same time, it can affect the motion of dislocations over adjacent GBs. For definiteness, we calculate the effect of the inclusion stress field on the dislocation motion over GB AB (Fig. 1a,b). To do so, it is sufficient to calculate the maximum shear stress $\sigma_{x'y'}$ exerted by the inclusion at GB AB. (Here the x'- and y'-axes are directed as shown in Fig. 1b and make the angle α with the x- and y-axis, respectively.) Evidently, the maximum stress acts at triple junction A, which is closest to the inclusion.

In the cylindrical coordinate system (r, φ, z) with the origin in the inclusion center (Fig. 1b), the stress σ_{rr} can be written as

$$\sigma_{rr} = \sigma_{RR} \sin^2 \theta + \sigma_{\theta\theta} \cos^2 \theta. \tag{7}$$

In turn, at triple junction A characterized by $x = 0$, the stress $\sigma_{x'y'}$ follows as

$$\sigma_{x'y'} = (\sigma_{rr} - \sigma_{\varphi\varphi}) \cos \alpha \sin \alpha = A \sin^2 \theta \cos \alpha \sin \alpha (R_0 / R)^3. \tag{8}$$

For definiteness, we assume that triple junction A lies symmetrically with respect to the inclusion center, that is, occupies the region $-d_{GB} / 2 < z < d_{GB} / 2$, where d_{GB} is the GB length. Then, with an account for the relations $\sin^2 \theta = r^2 / (z^2 + r^2)$ and $R = (z^2 + r^2)^{1/2}$, the average stress $\bar{\sigma}_{x'y'}$ acting on the dislocation segment at triple junction A can be presented as

$$\bar{\sigma}_{x'y'} = (1 / d_{GB}) \int_{-d_{GB}/2}^{d_{GB}/2} \sigma_{x'y'} dz = \frac{2AR_0^3 \sin(2\alpha)(6r^2 + d_{GB}^2)}{3r^2 (4r^2 + d_{GB}^2)^{3/2}}. \tag{9}$$

Assuming that the distance from the inclusion center to the center of triple junction A is a random quantity in the interval $R_0 < r < d_{GB} - R_0$, the average value of $\bar{\sigma}_{x'y'}$ (averaged for various distances from the inclusion center to triple junction A) can be written as

$$<\bar{\sigma}_{x'y'}> = (1 / d_{GB}) \int_{R_0}^{d_{GB}-R_0} \bar{\sigma}_{x'y'} dr. \tag{10}$$

The stress $<\bar{\sigma}_{x'y'}>$ exerts a back force on the dislocation at triple junction A and thereby hinders GB dislocation slip over GB AB. To provide such slip, the applied load should increase (compared to the case where segregations are absent) in such a way as to increase the resolved shear stress in GB AB by $<\bar{\sigma}_{x'y'}>$. As a result, the contribution σ_{seg} of GB segregations to the yield strength can be estimated as $\sigma_{seg} = M <\bar{\sigma}_{x'y'}>$, where M is the Taylor factor approximately equal to 3.06 for metals and alloys with fcc crystal lattices [14].
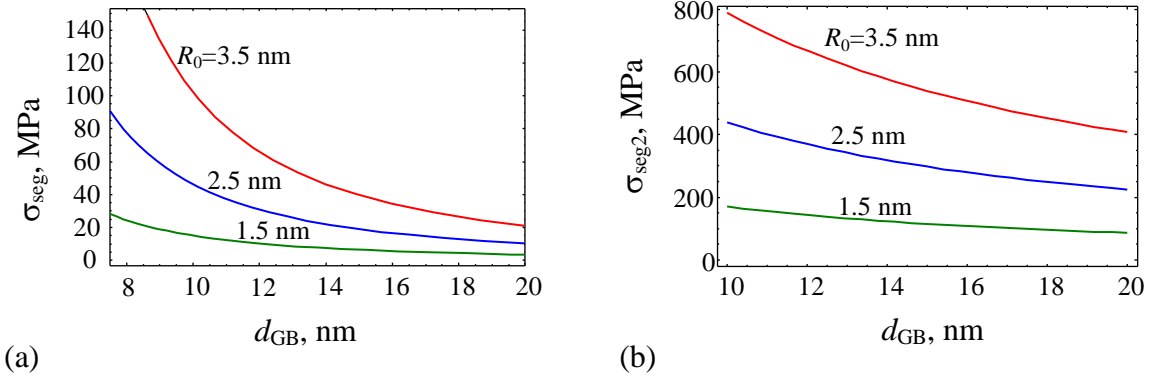
Fig. 2. Dependences of the stresses σ_{seg} (a) and σ_{seg2} (b) that characterize the GB segregation-induced strengthening in the 1570 Al alloy with GB Mg segregations in the case of plastic deformation via GB sliding and lattice dislocation slip, respectively, on the GB length d_{GB}

Now let us calculate σ_{seg} for the exemplary case of the 1570 Al alloy containing Mg segregations at GBs and characterized by the following parameter values [15]: $G = 27$ GPa, $\nu = 0.34$, $\varepsilon^* = 0.01$. We also put $\alpha = \pi / 3$. The dependences of σ_{seg} on d_{GB} are shown in Fig. 2a, for various values of the segregation radius R_0. It is seen in Fig. 2a that σ_{seg} increases with an increase in the segregation radius and/or decrease in grain size. The grain size dependence of σ_{seg} is related to the reduction of the distance between segregations and the nearest triple junction with a decrease in grain size.

3. Strengthening of nanocrystalline alloys deformed via lattice dislocation slip

Figure 2a demonstrates that clustered GB segregations can increase the yield strength of nanocrystalline metallic alloys in the case where plastic deformation is realized via GB sliding. Now compare the effect of such segregations on GB sliding with their effect on intragranular dislocation slip. To do so, we adopt model [15], where the stress field of each GB segregation exerts a force on the straight segment of an expanding rectangular glide dislocation loop (Fig. 1c). Following [15], we assume that dislocation loops grow in the directions parallel to the GB planes without increasing their height (denoted as h in Fig. 1c). At the same time, in contrast to ref. [15], which considered ultrafine-grained alloys where each GB incorporates various segregations, here we focus on the case of nanocrystalline alloys, which contain no more than one segregation in each GB.

The hampering forces exerted by spherical segregations on the moving segments of the dislocation loops increase the yield strength. Using the calculation procedure suggested in ref. [15], we have calculated the contribution σ_{seg2} of GB segregations to the yield strength in the situation where plastic deformation is realized via the motion of lattice dislocations across grains from one GB to another. The dependences of σ_{seg2} on d_{GB} for the 1570 Al alloy containing Mg segregations at GBs are shown in Fig. 2b for $h = 3.7$ nm and the values of other parameters specified above. It is seen in Fig. 2b that the stress σ_{seg2} increases with a decrease in grain size and/or increase in the segregation radius, similarly to the behavior of the stress σ_{seg}. Also, the comparison of Figs. 2a and 2b clearly demonstrates that for the same grain size and segregation radius, σ_{seg2} is much larger than σ_{seg}. This implies that clustered segregations are more effective in hampering intragranular lattice slip than in preventing

GB sliding. Thus, it is logical to assume that clustered segregations are not very effective for strengthening nanocrystalline metallic alloys with finest grains, where the presence of the inverse Hall-Petch dependence associated with GB sliding leads to softening. At the same time, clustered segregations should be very effective for strengthening nanocrystalline metallic alloys with larger grain sizes, which deform through lattice dislocation slip across grains.

4. Conclusions

In summary, GB segregations can exert a high strengthening effect in nanocrystalline metallic alloys. For clustered GB segregations, the highest strengthening is achieved in the case of not very small grains, when nanocrystalline alloys deform via lattice dislocation slip. For nanocrystalline alloys with the finest grains, clustered segregations can provide only moderate strengthening. Therefore, one can assume that the ultrahigh strengthening of nanocrystalline alloys, deformed via GB sliding, due to GB segregations [4] is associated with the choice of the alloying elements that promote GB sliding and their homogeneous segregations along entire GBs. Thus, one can assume that the most effective kind of GB segregations in nanocrystalline alloys can depend on their grain size. For nanocrystalline alloys with the finest grains, the highest strengthening can be achieved in the case of homogeneous GB segregations, while for nanocrystalline alloys with higher grain sizes inhomogeneous clustered segregations can provide the highest strengthening.

References

1. Chookajorn, T, Murdoch HA, Schuh CA. Design of stable nanocrystalline alloys. *Science*. 2012;337(6097): 951-954.
2. Kim JG, Enikeev NA, Seol JB, Abramova MM, Karavaeva MV, Valiev RZ, Park CG, Kim HS. Superior strength and multiple strengthening mechanisms in nanocrystalline TWIP steel. *Scientific Reports*. 2018;8: 11200.
3. Ke X, Ye J, Pan Z, Geng J, Besser MF, Qu D, Caro A, Marian J, Ott RT, Wang YM, Sansoz F. Exceptional strength and electrical coonductivity in nanocrystalline-nanotwinned metals and defect-induced softening. *Nature Materials*. 2019;18: 1207-1214.
4. Hu J, Shi YN, Sauvage X, Sha G, Lu K. Grain boundary stability governs hardening and softening in extremely fine nanograined metals. *Science*. 2017;355(6331): 1292-1296.
5. Valiev RZ, Enikeev NA, Murashkin MY, Kazykhanov YU, Sauvage X. On the origin of the extremely high strength of ultrafine-grained Al alloys produced by severe plastic deformation. *Scripta Materialia*. 2010;63(9): 949-952.
6. Chang KI, Hong SI. Effect of sulphur on the strengthening of a Zr-Nb alloy. *Journal of Nuclear Materials*. 2008;373(1-3): 16-21.
7. Borovikov V, Mendelev MI, King AH. Solute effects on interfacial dislocation emission in nanomaterials: Nucleation site competition and neutralization. *Scripta Materialia*. 2018;154: 12-15.
8. Turlo V, Rupert TJ. Grain boundary complexions and the strength of nanocrystalline metals: Dislocation emission and propagation. *Acta Materialia*. 2018;151: 100-111.
9. Babicheva RI, Dmitriev SV, Bai L, Zhang Y, Kok SV, Kang G, Zhou K. Effect of grain boundary segregation on the deformation mechanisms and mechanical properties of nanocrystalline binary aluminum alloys. *Computational Materials Science*. 2016;117: 445-454.
10. Jang S, Purohit Y, Irving DL, Padgett C, Brenner D, Scattergood RO. Influence of Pb segregation on the deformation of nanocrystalline Al: Insights from molecular simulations. *Acta Materialia*. 2008;56(17): 4750-4761.

11. Pan Z, Sansoz F. Heterogeneous solute segregation suppresses strain localization in nanocrystalline Ag-Ni alloys. *Acta Materialia*. 2020;200: 91-100.

12. Mura T. *Micromechanics of Defects in Solids*. Dordrecht: Martinus Nijhoff Publishers; 1987.

13. Glas F. Elastic relaxation of a truncated circular cylinder with uniform dilatational eigenstrain in a half space. *Physica Status Solidi B*. 2003;237(2): 599-610.

14. Taylor GI. Plastic strain in metals. *Journal of the Institute of Metals*. 1938;62: 307-324.

15. Bobylev SV, Enikeev NA, Sheinerman AG, Valiev RZ. Strength enhancement induced by grain boundary solute segregations in ultrafine-grained alloys. *International Journal of Plasticity.* 2019;123: 133-144.

THE AUTHOR

Sheinerman A.G.
e-mail: asheinerman@gmail.com
ORCID: 0000-0001-9909-2950

Hybrid optimization approach on electrical discharge machining process for hybrid Al-Al$_2$O$_3$/B$_4$C composites

P.K. Gupta, M.K. Gupta$^{\boxtimes}$

Department of Mechanical Engineering, Motilal Nehru National Institute of Technology Allahabad, Prayagraj-211004, Uttar Pradesh, India

$\boxtimes$ mnnit.manoj@gmail.com, mkgupta@mnnit.ac.in

Abstract. In the present investigation, influences of process parameters such as pulse current, pulse on time, gap voltage, and sample compositions on the machining of hybrid Al-Al$_2$O$_3$/B$_4$C composites through wire electrical discharge machining (WEDM) are carried out. The parameters were optimized to minimize both material removal rate (MRR) and surface roughness (SR) through Taguchi and Grey relational analysis. The hybrid Al-Al$_2$O$_3$/ B$_4$C MMCs containing the micro-particles of Al$_2$O$_3$ (purity 99 % and 100-325 mesh size) and B$_4$C (purity 99% and 400 mesh size) were prepared by stir casting with varying proportions (i.e. 100/0, 75/25, 50/50, 25/75 and 0/100) of Al$_2$O$_3$ and B$_4$C as a reinforcements. The morphology of the machined samples was also examined through SEM and found the presence of micro-ridges, micro craters, micro-cracks, black patches, debris, and micro-voids. The experimental results revealed the optimal grouping of process parameters as sample composition of B75A25 (75% B$_4$C +25% Al$_2$O$_3$), pulse on time of 32 µs, pulse current of 2 A, and gap voltage of 40 V.
Keywords: hybrid composites, metal matrix composites, optimization, wire electrical discharge machining, scanning electron microscopy

1. Introduction
Apart from many advantages (i.e. high strength to weight ratio, higher transverse stiffness and strength, no water absorption, and good elevated temperature resistance) and many applications (i.e. automotive, aerospace, and structural) of single reinforced metal matrix composites (MMCs), they have some limitations also [1,2]. These limitations may be overcome using hybrid metal matrix composites (HMMCs). HMMCs can be prepared by reinforcing two or more types of ceramic particles or synthesis fibres in the metal matrix [3]. HMMCs are being considered in various fields due to their enhanced properties over single reinforced composites. These can be proffered for numerous engineering applications like

automobile, marine, aerospace, structural, and mineral processing because of the improved specific strength, wear resistance, and thermal properties [4].

For utilization of synthesized MMCs, they are subjected to various cutting actions with conventional and non-conventional machining processes. During machining of MMCs by conventional processes, high temperatures are generated which leads to deformation of the cutting tools and worsen the product quality, also increasing the fabrication cost. Therefore non-conventional machining comes into the picture for the machining of these typical materials. The employ of non-conventional machining methods can enhance product quality and lessen the production costs for such materials. Among the existing non-conventional machining processes, WEDM is commonly accepted to fabricate complex profiles in composite materials [5].

WEDM is an electro thermal machining process that uses a moving conductive wire as an electrode to obtain the desired shape. In WEDM process, the selection of proper cutting parameters is an important task to avoid less MRR and poor surface finish due to wire breakage and short-circuiting [6]. Several researchers have reported their studies on MRR and SR of MMCs and HMMCS using WEDM. Kumar et al. [7] worked on optimization of WEDM for aluminium-based composites through GRA and reported optimum conditions as: peak current = 12A, pulse on time = 100 microseconds, wire feed rate = 6 m/min and wt.% of B_4C = 5. Goyal et al. [8] observed that the pulse on time and peak current are found to be the most significant factors towards MRR for Ni49Ti51 shape memory alloy. Kumar et al. [9] reported the optimum machining conditions for Al-SiC-B_4C composites as current = 20 A, pulse on time = 108.6 microseconds, wire feed rate = 10 mm/min, and 5.65% of the B4C content in the composites. Prasad et al. [10] also investigated the machining behaviour of Ti alloy through WEDM process. Karabulut et al. [11] found that the surface finish of AA6061-B_4C composite was predominantly affected by the peak current and voltage. Shayan et al. [12] also analyzed the influence of parameters on the performance of dry wire EDM for cemented tungsten carbide. Finally, EDM and WEDM machining processes are found to have better dimensional stability for high-strength temperature-resistant materials like MMCs and HMMCs [13-15]. Kanlayasiri and Boonmug [16] studied the machining of die steel through WEDM and observed that pulse on time and pulse peak current are the most influential factors for surface roughness. In another work, pulse on time and discharge current are found to be the most significant factors of surface roughness for Al- SiC MMCs [17]. Some other researchers' works based on the machining of MMCs and HMMCs are tabulated in Table1.

From the review of various literature, it was observed that very less works are carried out on the effect of reinforcement on the machinability of WEDM process. Further, no work is reported so far on the optimization of machining parameters for Al (6061)-Al_2O_3/B_4C through the hybrid GRA and Taguchi method. Therefore, the effect of variation in the proportion of Al_2O_3 and B_4C on MRR and SR of Al (6061)-Al_2O_3/B_4C and their optimization through the hybrid GRA and Taguchi method is performed.

2. Material and Manufacturing Process

Materials. The Al alloy (6061) is one of the most commonly used matrix materials for MMCs with chemical composition as provided in Table 2 [26]. To prepare the hybrid MMCs, Al alloy (6061) as matrix material and boron carbide (purity 99% and 400 mesh size (37μm)) and alumina (purity 99% and 100-325 mesh size (44-149μm)) as reinforcements were usedin the present work. All of the reinforcing and matrix materials were purchased from the local resources in Prayagraj, Uttar Pradesh, India.

Table 1. Review of hybrid metal matrix composite machined by electrical discharge machining

S.No.	Hybrid Composites	Electro-Discharge Machining				Ref.
		Parameters	Optimization Techniques	Optimized Values	Conclusions	
1.	Al7075/Al$_2$O$_3$/SiC	Pulse on time, Pulse off time, Pulse Current, Wire drum speed	Taguchi based GRA	Pulse on time = 4 μ s, Pulse off time = 6 μ s, Pulse current = 2A, Wire drum speed = 4m/min	• The surface roughness was increased with high discharge energy in spark and drum speed • Kerf width was improved with increasing drum speed due to the creation of large size cavities, voids and particles pull out	[18]
2.	Al6061/SiC/Graphite	Current, Pulse on time, Voltage, Flushing pressure	Least square techniques and ANOVA	-	Tool wear rate was increased with an increasing current and voltage but it decreased with increasing pulse on time and flushing pressure	[15]
3.	Al6063/SiC/Graphite	Voltage, Pulse current, Pulse off time, Pulse on time	Taguchi based GRA	Voltage = 60V, Pulse current = 32A, pulse on time = 4 μ s	The material removal rate and surface roughness were increased due to more energetic pulses because of the higher cavity formation	[19]
4.	Al6351/SiC/B$_4$C	Current, Pulse on time, Pulse duty factor, Gap voltage	ANOVA	The responses were influenced by pulse current with a contribution of 33.08% to electrode wear ratio, 76.65% to surface roughness, 48.08% to the power consumed	The machined surfaces contained craters, recast layers, surface waviness, and also the formation of bubbles	[20]

5.	AlSi10Mg/Graphite/Al$_2$O$_3$	Peak current, Flushing pressure, Pulse on time	ANOVA	Peak current with a contribution of 69.18% to surface roughness, Flushing pressure 43.26% contribution on MRR, Pulse on time 34.38% contribution on TWR	The surface roughness was increased with an increase in the flushing pressure due to the accumulation of alumina particles	[21]
6.	Al/B$_4$C/Graphite	Wire speed, Pulse on time, Pulse off time	Taguchi, RSM, ANOVA	Wire speed = 50m/min, Pulse on time= 5 μ s, Pulse off time =7 μ s	The MRR and SR were increased with the increase of wire speed and pulse-on time	[22]
7.	Al413/Fly ash/B$_4$C	Gap voltage, Pulse on time, Pulse off time, wire feed, reinforcement %	Taguchi, ANOVA	Gap voltage = 50V, Pulse on time =1 μ s, Pulse off time =10 μ s, Wire feed = 8m/min, Reinforcement = 6 %	The optimal predicted values were found for surface roughness and material removal rate 3.37 μ m and 13.0 mm^3/min respectively	[23]
8.	Al/SiC/B$_4$C	Peak current, Pulse on time, wire feed rate, B$_4$C content %, Pulse off time	Response surface methodology	Peak current = 20A, Pulse on time = 108.6 μ s, Wire feed rate = 10mm/min, B$_4$C content % = 5.65	The lower material removal rate was obtained in case of a lower wire feed rate due to lower heat energy strikes on the composite surfaces	[9]
9.	AZ31/Graphene/SiC	Reinforcement %, Doping %, Pulse on time, Pulse off time, Wire feed rate	Taguchi coupled GRA	Reinforcement = 0.2%, Doping = 10%, Pulse on time = 40 μ s, Pulse off time = 23 μ s, Wire feed rate = 2m/min	The variation in the thermal behaviour of reinforcements and matrix material affected the material removal rate	[24]
10.	Al6061/SiC/Graphite/Iron Oxide	Pulse peak current, Pulse on time, Pulse off time, Wire feed rate, Wire tension, Spark gap set voltage	ANOVA, Regression analysis	The improvement in MRR and Spark gap width by 33.72% and -27.28%	The size of craters formed on the machined surfaces affected by peak current and pulse on time	[25]

Table 2. Chemical composition of 6061Al alloy (wt.%)

Mg	Si	Cu	Cr	Fe	Al
0.92	0.57	0.21	0.12	0.09	Balance

Fabrication of composites. The flow chart diagram for fabrication of hybrid Al-Al$_2$O$_3$/B$_4$C composite is shown in Fig. 1. In Figure 1, firstly, an ingot of Al alloy (6061) was converted into small pieces and then poured into a graphite crucible for smooth melting through an electric coil furnace at a temperature of 750°C. Subsequently, the crucible and Al$_2$O$_3$ and B$_4$C particles were preheated at a temperature of 400°C. Thereafter, preheated powders of reinforcements were mixed at a rotation of 600 *rpm* by employing a stirrer in two consecutive steps of 3 wt. % of reinforcement each for half of 10 min. A drop in temperature of around 15-20°C was seen during the mixing process. The degasser (flux material) was used to throw away the trapped gases and maintain the temperature of the mixture constant. After all, the mixture of Al$_2$O$_3$ and B$_4$C particles into molten Al alloy was poured into a die of cast iron for the production of specimens.

Methodology. The developed composite materials were machined through wire electrode discharge machining with the help of the high-power servo stabilizer. A wire of molybdenum with a 0.25 mm diameter was used as a tool material to perform the experiments. The cutting length of 30 mm was kept constant for all the composites. The experimental details are provided in Table 3. The experiments were conducted with various input parameters such as sample compositions, gap voltage (V), pulse on time (μs), and pulse current (A) with an objective to minimize both MRR and SR. The following input parameters for the WEDM are given in Table 4.
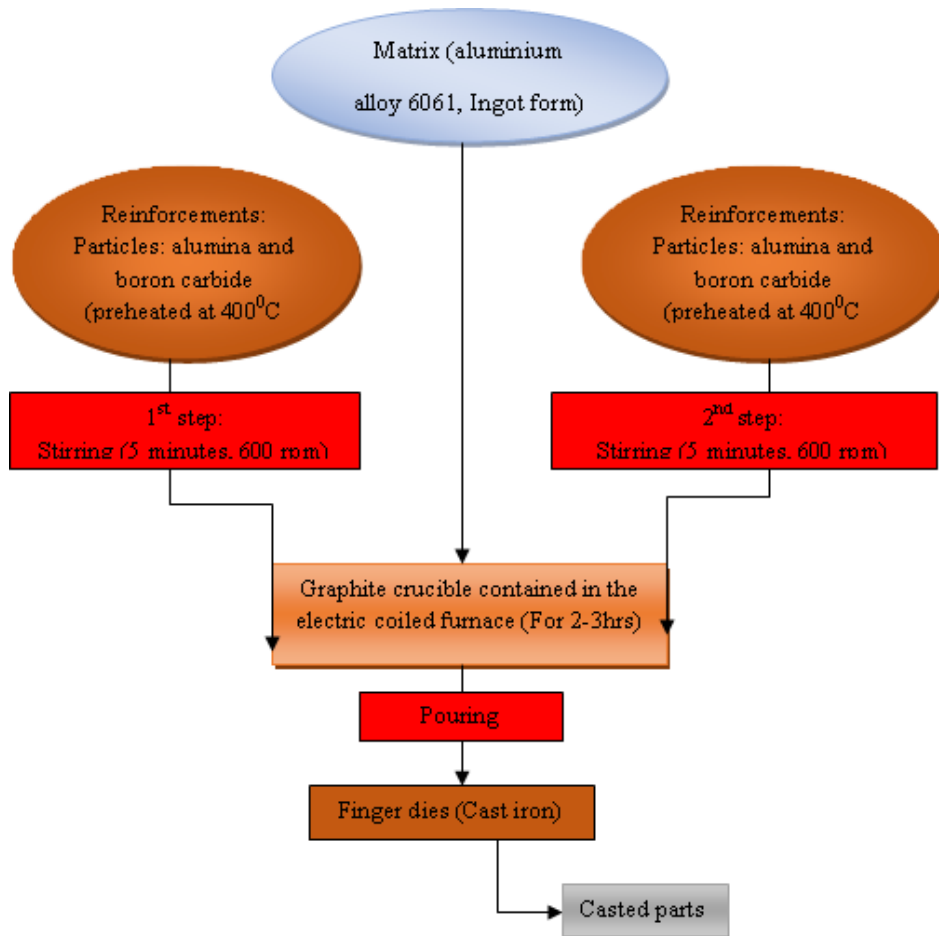
Fig. 1. Flow chart diagram for fabrication of hybrid metal matrix composites

Table 3. Experimental details for wire electrical discharge machining of hybrid metal matrix composites

Experimental facility	Specifications
Workpiece	Hybrid Al-MMCs (A0B0, B100A0, A100B0, A75 B25, B75A25, and B50A50
Machine	Wire electrical discharge machine (Ex 4032, Medha enterprises Kanpur)
Electrode	Molybdenum wire (0.25mm diameter)
Machining parameters	Sample composition (0/0, 100/0, 0/100, 25/75, 75/25, and 50/50),Gap voltage (40V, 44V, and 48 V), Pulse on time (32 μs, 64 μs, 128 μs), and Pulse current (2A, 3A , 4A)
Surface roughness measuring device	Surface roughness tester, and Make: Mitutoyo, Model: SJ-410

Table 4. The input process parameters for wire electrical discharge machining of hybrid metal matrix composites

Input process parameters	Level					
	1	2	3	4	5	6
Sample compositions	M1 (A0B0)	M2 (B100A0)	M3 (A100B0)	M4 (A75B25)	M5 (B75A25)	M6 (B50A50)
Gap voltage (V)	40	44	48	-	-	-
Pulse on time (μs)	32	64	128	-	-	-
Pulse current (A)	2	3	4	-	-	-

Table 5. Experimental results of material removal rate and surface roughness hybrid metal matrix composites

S. No	Sample Composition	Gap voltage (V)	Pulse on time (μs)	Pulse current (A)	MRR (cm^3/min)	SR (μm)
1	1	1	1	1	0.0252	3.0290
2	1	2	2	2	0.0222	3.2770
3	1	3	3	3	0.0190	3.6830
4	2	1	1	2	0.0102	1.3230
5	2	2	2	3	0.0141	1.7740
6	2	3	3	1	0.0174	1.9390
7	3	1	2	1	0.0208	2.7580
8	3	2	3	2	0.0207	2.7890
9	3	3	1	3	0.0247	2.6770
10	4	1	3	3	0.0186	2.4850
11	4	2	1	3	0.0248	2.5780
12	4	3	2	1	0.0209	2.7840
13	5	1	2	2	0.0244	2.0260
14	5	2	3	3	0.0206	2.2390
15	5	3	1	1	0.0186	2.2170
16	6	1	3	2	0.0185	2.6200
17	6	2	1	2	0.0245	2.4600
18	6	3	2	3	0.0207	2.3110

The experiments were designed by Taguchi method and L18 array was used for conducting the experiments. The experimental results are shown in Table 5. The MRR was computed by taking weight differences of before and after workpiece machining per minute. It was computed by the following formula.

$$MRR = \frac{W_i - W_f}{\rho\, t}, \qquad (1)$$

where W_i and W_f are weigh of the specimens before and after machining, ρ – density of the specimens and t – period of machining (minute).

The surface roughness of the machined area or section was measured through a profile meter (Mitutoyo-Model SJ-410) with a traverse length and speed of 5 mm and 0.25 mm/s respectively.

3. Results and discussion

Design of experiment (DOE). The design of the experiment is utilized for minimizing the number of experiments that can be done by Taguchi method. Minitab 17 software was used for designing the experiments as per requirements. Four input parameters with one of them having six levels and others having three levels were used as tabulated in Table 4. $L18$ array was used in this work and resultes are tabulated in Table 5.

Analysis of output/response parameters. The signal-to-noise ratio (S/N) was taken into account for analyzing the input parameter over the output response. The outputs/responses such as MRR and SR, both are the minimizing criteria of characteristics. So, smaller values of MRR and SR are set as better characteristics. The S/N can be found by the below equation (2).

$$\frac{S}{N} = -10\log_{10}[\frac{1}{n}\sum(y_{ij}2)], \qquad (2)$$

where, n – no of observations, y_{ij} – observed response, $i=1,2\ldots n$, $j=1,2\ldots k$.

Table 6. Signal to noise ratio (S/N) and normalized values for hybrid metal matrix composites

S. No	S/N ratio (MRR)	S/N ratio (SR)	Normalized value (MRR)	Normalized value (SR)
1	31.9720	-9.6260	1	0.2771
2	33.0729	-10.3095	0.7987	0.1720
3	34.4249	-11.3240	0.5874	0.0000
4	39.8280	-2.4312	0	1.0000
5	37.0156	-4.9791	0.2575	0.8089
6	35.1890	-5.7516	0.4758	0.7390
7	33.6387	-8.8119	0.70481	0.3919
8	33.6806	-8.9090	0.6964	0.3788
9	32.1461	-8.5530	0.9644	0.4263
10	34.6097	-7.9065	0.5558	0.5076
11	32.1110	-8.8934	0.9689	0.4682
12	33.5971	-6.1328	0.7111	0.3809
13	32.2522	-7.0011	0.9466	0.7021
14	33.7227	-6.9153	0.6943	0.6119
15	34.6097	-8.3660	0.5603	0.6212
16	34.6566	-7.8187	0.5541	0.4504
17	32.2167	-7.2760	0.9519	0.5182
18	33.6806	-8.2760	0.6981	0.5814

Multi-response optimization using Grey Relational Analysis. Nowadays, multi-criteria decision-making (MCDM) techniques have received attention among researchers due to their absolute capacity to judge unique choices on various criteria for possible determination of the best. In this work, MCDM combined with grey relational analysis (GRA) and Taguchi method has been proposed to study the optimization problem for the wire electrode discharge process of Al alloy (6061) hybrid composites. The GRA is the multi-

response optimization process contributing toward finding out the optimum combination of process parameters and the effect of each input parameter on the responses. The methodology consists of a number of steps as follows.

Step 1. Normalization. It is required to normalize the output responses before analyzing them with the grey relation theory and rated between 0 and 1. The normalization for output response such as MRR and SR can be done with the help of equation (3).

$$Z_{ij} = \frac{\max(y_{ij}, i = 1,2,3............n) - y_{ij}}{\max(y_{ij}, i = 1,2,3.........n) - \min(y_{ij}, i = 1,2,3........n)},$$ (3)

where y_{ij} is the Jth performance characteristics and $\min y_{ij}$ and $\max y_{ij}$ values of the Jth performance characteristics for the ith experiments respectively.

The calculated SN ratio for individual response/output and its normalized value are given in Table 6.

Step 2. Calculation of Grey relational coefficient. The grey relational coefficients can be calculated from the generalized formula as shown in equation (4) and also, the characteristics coefficient is assumed to be $\xi = 0.5$.

$$(y_0(k), y_i(k)) = \frac{\Delta_{min} + \xi\Delta_{max}}{\Delta_{0j}(k) + \xi\Delta_{max}},$$ (4)

where $i = 1,2...n$, $k = 1,2...m$, n is the number of experimental data items and m is the number of responses, $y_0(k)$ is the reference sequence ($y_0(k) = 1$, $k = 1,2...m$), $y_i(k)$ is the specific comparison sequence, $\Delta_{0j} = \|y_0(k) - y_j(k)\|$ – the absolute value of the difference between $y_0(k)$ and $y_i(k)$, $\Delta_{min} = \|y_0(k) - y_j(k)\|$ – the smallest value of $y_i(k)$, $\Delta_{max} = \|y_0(k) - y_j(k)\|$ – the largest value of $y_i(k)$, ξ is the coefficient constant, which is defined in the range $0 \le \xi \le 1$.

Table 7. Deviation sequence and corresponding grey relational coefficient and grey relational grade for hybrid metal matrix composites

S. No	Deviation sequence (MRR)	Deviation sequence (SR)	GRC (MR)	GRC (SR)	GRG	RANKS
1	0	0.7229	1	0.40887	0.7044	6
2	0.2013	0.8280	0.7129	0.376516	0.5447	12
3	0.4126	1.0000	0.5479	0.333333	0.4406	18
4	1	0.0000	0.3333	1	0.6667	8
5	0.7425	0.1911	0.4024	0.7235	0.5629	11
6	0.5242	0.2610	0.4882	0.6570	0.5726	10
7	0.2952	0.6081	0.6288	0.4512	0.5400	14
8	0.3036	0.6212	0.6222	0.4459	0.5341	15
9	0.0356	0.5737	0.9335	0.4657	0.6996	7
10	0.4442	0.4924	0.5295	0.5038	0.5167	16
11	0.0311	0.5318	0.9415	0.4846	0.7131	4
12	0.2889	0.6191	0.6338	0.4468	0.5403	13
13	0.0534	0.2979	0.9035	0.6267	0.7651	1
14	0.3057	0.3881	0.6206	0.5629	0.5918	3
15	0.4397	0.3788	0.5321	0.5689	0.5505	2
16	0.4459	0.5496	0.5286	0.4764	0.5025	17
17	0.0480	0.4818	0.9124	0.5093	0.7108	5
18	0.3019	0.4186	0.6236	0.5443	0.5839	9

Calculation of Grey relational grade. The grey relation grade (GRG) for multi-objective responses can be found with the help of the grey relational coefficient of different responses for the MRR and SR. The evaluations of performance characteristics depend on the GRG values.

The following sequencing order of all the experiments is tabulated in Table 7. The grade which decided the rank of performance characteristics was obtained by using the equation (4).

$$\delta j = \frac{1}{k} \sum_{i=1}^{m} y_{ij},$$ (4)

where δ_j – GRG for j-th experiment and k – number of performance characteristics.

Optimization techniques – Taguchi method. Based on GRG values, Taguchi optimization techniques are employed. The outcomes of this optimization were obtained as shown in Table 7. It is necessary to find out the effect of each parameter at different levels on the GRG. The obtained grey relational grade value for each level and corresponding average grade was presented in Table 7. Generally, the higher GRG value offers better output responses. The optimum condition can be found from response Table 8 (sample composition = B75A25 (75%B$_4$C +25% Al$_2$O$_3$), pulse on time (µs) = 32, pulse current (A) = 2, gap voltage (V) = 40). The sequence of input parameters that affect the multi-objective of minimum MRR and SR were sample composition followed by pulse on time, pulse current, and gap voltage.

Table 8. Response Table of grey relational grade for hybrid metal matrix composites

Level	Sample composition	Gap voltage (V)	Pulse on time (µs)	Pulse current (A)
1	0.5632	0.6159	0.6742	0.6176
2	0.6007	0.6096	0.5895	0.5565
3	0.5912	0.5646	0.5264	0.6160
4	0.5900			
5	0.6358			
6	0.5991			
Delta	0.0725	0.0513	0.1478	0.0612
Rank	2	4	1	3

Table 9. ANOVA results for hybrid metal matrix composites

Source	Degree of freedom	Sum of square	Mean square	Percentage Contribution
Sample code	5	0.008231	0.001646	3.08
Pulse on time (µs)	2	0.009391	0.004695	8.80
Pulse current(A)	2	0.066012	0.033006	61.83
Gap voltage (V)	2	0.014568	0.007284	13.65
Residual Error	6	0.040506	0.006751	12.65
Total	17			

Analysis of variance (ANOVA). It is the statistical method applied for finding the interaction between control factors utilized in the present experimental investigation. ANOVA was performed using Minitab version 17 software to find the contribution of each parameter for multi-objective responses. It is utilized to observe the interaction between the experimental parameters (sample code, pulse on time, pulse current, and gap voltage), and the results are presented in Table 9. The percentage contribution of process parameters for

minimum MMR and SR was found using ANOVA as such: sample code (3.08%), pulse on time (8.80%), pulse current (61.83%), and gap voltage (13.65%). The main effect plot for grey relational grade value is shown in Fig. 2. From the main effects plot of the mean, it was found that the combination of optimal parameters and their levels was SC5GV1POT1PC1.
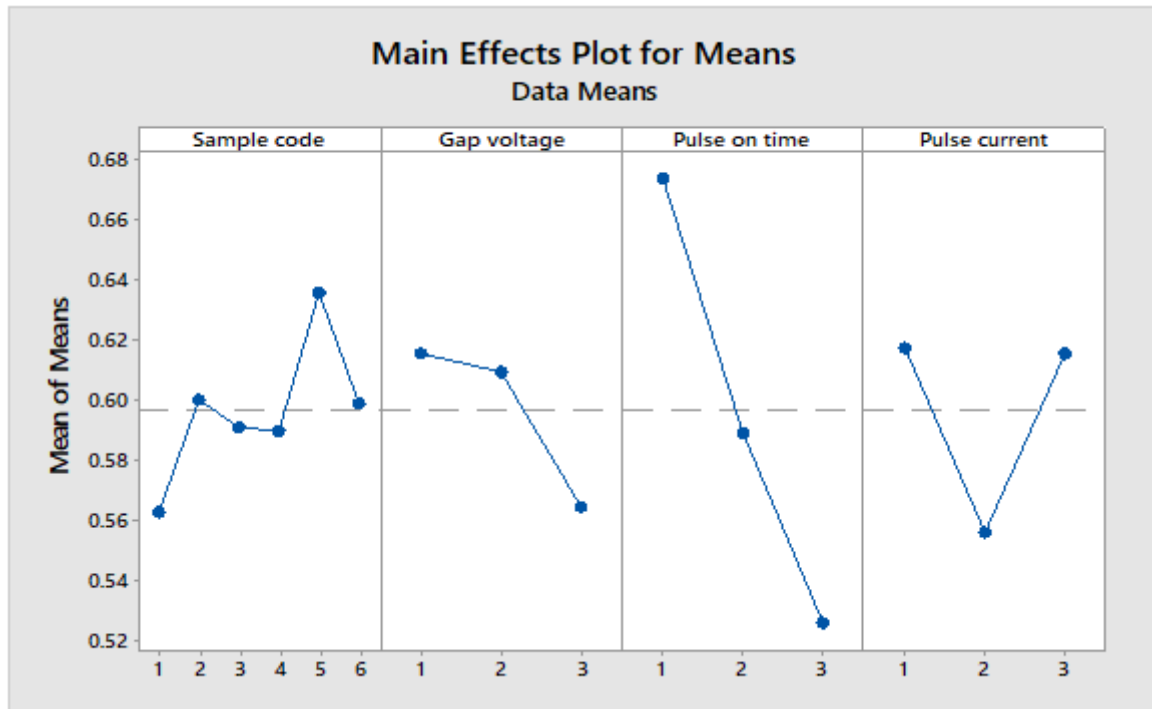
Fig. 2. Main effect plot of means for hybrid metal matrix composites (higher is better)

Confirmation tests. A confirmation experiment is performed to validate the hybrid approach of GRA and Taguchi implementation for optimization. The grouping of process parameters (Trial13) for which the quality characteristics yielded the peak value of grey relational grade (0.7651) was selected as the initial setting of the process parameter.

The responses received for the initial parameter setting were compared with the optimal parameter setting. It was observed that the hybrid approach of the GRA-Taguchi method had marginally improved the performance characteristics. From Table 10, an improvement in the performance is identified using the optimal condition in the WEDM process. The GRG is increased to 0.9886 from the initial parameter with a significant increase of 0.2235. Table 10 shows the confirmation test for the value of GRG for hybrid Al-Al$_2$O$_3$/B$_4$C composites.

Table 10. Confirmation test for hybrid metal matrix composites

Sources	Initial parameters	Optimum parameters	
		Prediction	Experimental
Combination of testing parameters	SC5GV1POT2PC2	SC5GV1POT1PC1	SC5GV1POT1PC1
Grey relational grade	0.7651	0.8283	0.9886
Improvement in grade		0.0632	0.2235

Parametric effect on the outputs/ responses

Material removal rate. The variations of MRR with a pulse on time at different pulse currents and voltage for hybrid metal matrix composites are shown in Fig. 3. It can be seen that the MRR of machined area for sample (A0B0) was higher in comparison to other composites such as B100A0, A100B0, A75B25, B75A25, and B50A50 due to its higher value of thermal

conductivity (175W/m-K) that quickly conducts the discharge energy on its surface. Also, there were lower values of MRR for all the developed composites (B100A0, A100B0, A75B25, B75A25, and B50A50) than Al alloy matrix because of the non-conductive nature of reinforcing materials such as alumina and boron carbide that protect the surface of composite from discharge energy [9]. As the discharge energy is responsible for the machining of the Al alloy (6061) sample and composites.
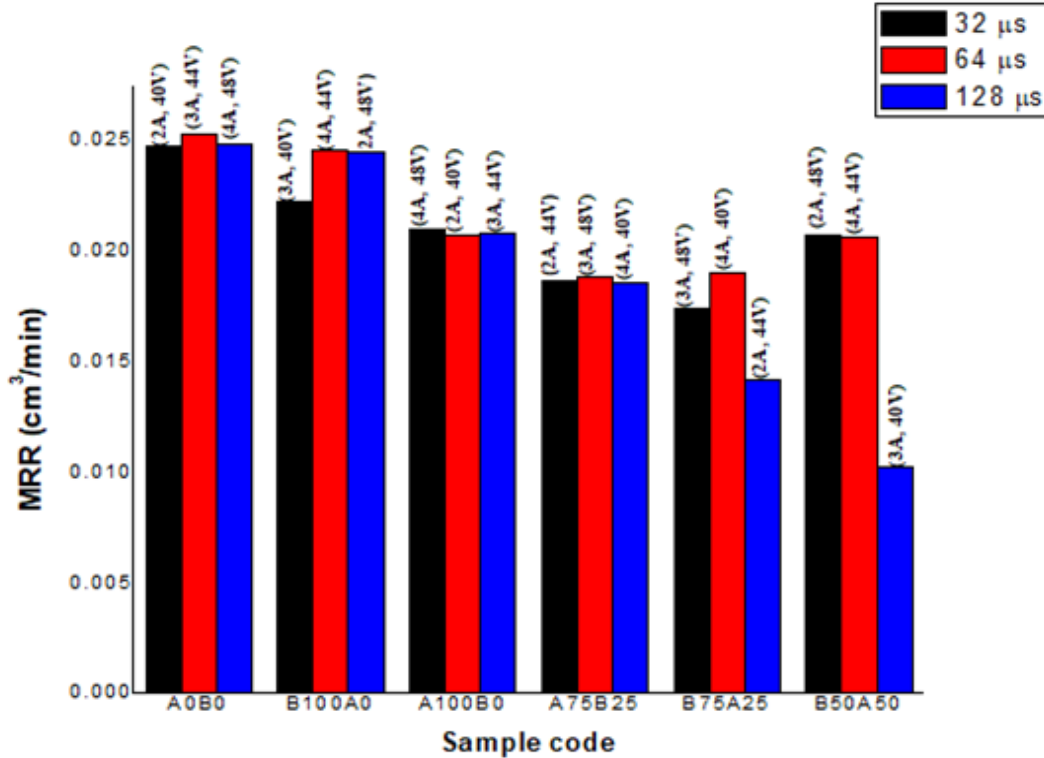
Fig. 3. Variations of material removal rate with a pulse on time at different pulse current and voltage for hybrid metal matrix composites

For sample A0B0, the MRR was increased with an increase in pulse on time from 32μs to 64μs due to the higher discharge energy available at the high value of gap voltage (44V) and pulse current (3A). The value of MRR was observed the lowest at the highest level of pulse on time (128μs) due to the welding phenomenon found in the molten pool of the Al alloy sample [8]. The composite sample B100A0 offered the higher MRR at a level of 64 μs pulse on time in comparison to pulse on time of 32μs due to more discharge strikes on the machined surface. The maximum MMR was seen at 64 μs of pulse on time for composite B100A0, whereas its lower value was seen at 128 μs pulse on time because of the rewelding phenomenon of molten metal. For sample A100B0, the lowest value of MRR was found at the level of pulse duration (64μs), pulse current (2A), and voltage gap (40V). A similar trend was found for the Al alloy sample.

For sample (A75B25), the MRR value was found to be increased with increasing the pulse duration from 32 μs to 64μs at a higher level of pulse current and gap voltage. Similar trends were found for the samples A0B0 and B100A0 as well. It was also found that the value of MRR was higher for sample B75A25 at a high value of pulse current (4A) and pulse duration (64 μs) for a given voltage due to discharge energy available for a prolonged time [7-9]. The lowest value of MRR for sample B75A25 was obtained at pulse on time 128 due to arcing of spark happened for machining conditions (2A, 44V). For the composite (B50A50), the MRR was decreased by decreasing the gap voltage for the prolonged pulse on time (64 μs). It happened due to the low spark energy on the machined surface. The lowest MRR

was observed for sample B50A50 at a pulse duration of 128µs credited to the welding and arcing phenomenon. The lowest value of MRR for all the composites including Al alloy was found at machining conditions (128µs, 3A, and 40V). Radhika et al. (21) worked on the optimization of electrical discharge machining parameters of aluminium hybrid composites using the Taguchi method and they observed that peak current is a highly influential parameter on surface roughness followed by a pulse of time and flushing pressure. Arunkumar and Raghunath [27] found that the peak current and pulse on time influenced considerably the material removal rate for Mg/SiC composites.

Surface roughness. The variations of surface roughness at different machining conditions with a pulse on time for different composites are shown in Fig. 4. In comparison with Al alloy, the entire composite samples (B100A0, A100B0, A75B25, B75A25, and B50A50) have the lowest average surface roughness due to the addition of nonconductive reinforcing materials such as alumina and boron carbide that reduces the extent of spark or discharge energy on the surface[7,8]. Shayan et al. [12] found similar results during the machining of cemented tungsten carbide with the help of dry wire electro-discharge machining.
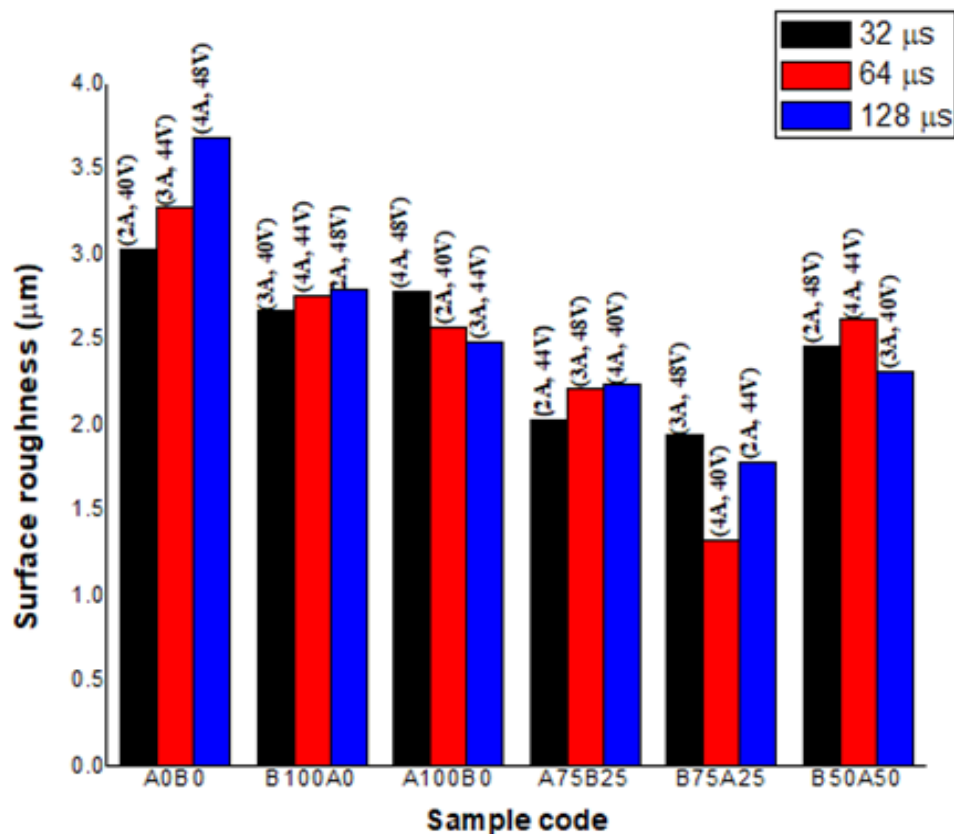
Fig. 4. Variations of surface roughness with a pulse on time at different pulse current and voltage for hybrid metal matrix composites

Generally, it is found that the extent of discharge or spark energy affects the surface characteristics. For sample A0B0, the SR was increased with an increasing pulse on time (32 µs to 128µs) due to the increased spark or discharge energy at all the machining conditions [16]. A similar trend was followed by the samples (B100A0) and A75B25. The sample A100B0 has a decreasing SR trend with increasing pulse on time (32 µs to 64µs) due to the decrease in gap voltage or intensity of pulse current. It was found that sample A100B0

had the lowest SR at machining conditions of 3A, 44V, and 128 µs due to the striations effect on the reinforcing particles [8].

Surface topography of the machined surface. Figure 5 shows the micrograph images of the WEDMed surface containing micro ridges, micro craters, micro-cracks, black patches, debris, and microvoids [13]. In Figure 5(a), more craters on the machined surface of monolithic aluminium alloy (A0B0) were observed. This happened due to matrix material removal because of the higher thermal conductivity of aluminium alloy 6061. The microvoids were observed due to the release of gases entrapped during machining and the electrochemical dissolution of the workpiece. In Figure 5(b), the micro-cracks were present near the particle-matrix interface because of debonding [28]. Similarly, micro craters were observed in the composite B100A0.
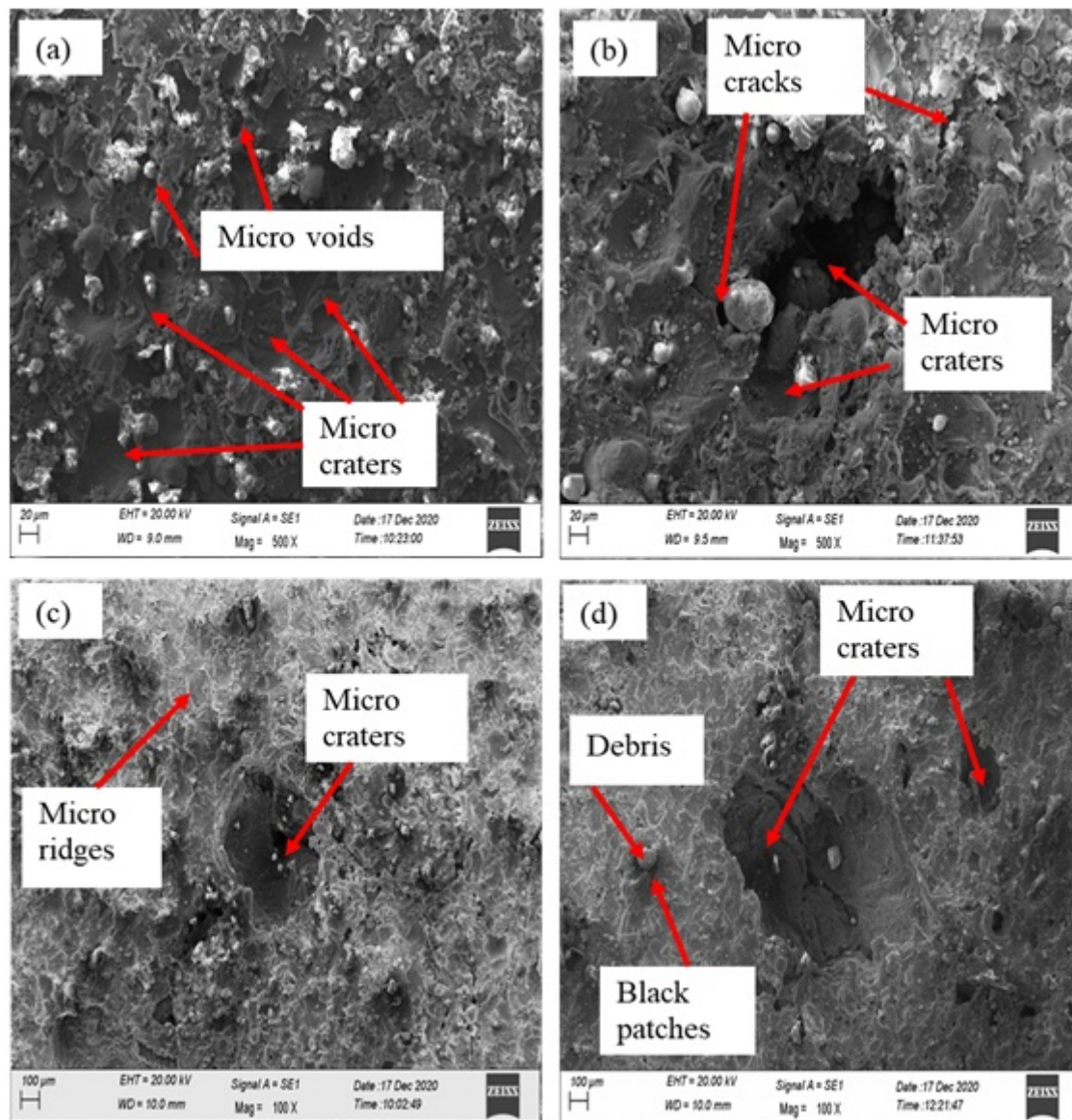
Fig. 5. Micrographs of machined surface for hybrid metal matrix composites: (a) B0A0, (b) B100A0, (C) B0A100, and (d) B75A25

Figure 5(c) shows the generation of micro ridges and micro craters. The pattern of micro ridges was uniform in one direction due to the generation of sparks in a particular direction. Plasma pressure is also responsible for creating a specified flow pattern of molten metal [7,8,28]. The micro craters were also observed indicating the removal of reinforcement

at that place due to loosened bonding between the reinforcement and matrix by heating. In Figure 5(d) there were black patches, debris, and tiny and shallow micro craters on the machined surface. The black patches were cast due to the arcing that occurred during the machining of the composites B75A25. Soni et al. [13] found that the formation of surface defects such as micro cracks and microvoids occurred at a higher pulse on time in their investigation.

4 Conclusions

The machining of the prepared hybrid MMCs was carried out using wire electrical discharge machining (WEDM). The process parameters such as pulse current, pulse on time, gap voltage, and sample compositions that influence the output responses including material removal rate (MRR) and surface roughness (SR) were optimized through Taguchi and Gray relational analysis (GRA). The following conclusions may be drawn:

- The average values of MRR and SR for hybrid Al-Al$_2$O$_3$/B$_4$C composites were found to be decreased with the decrease in pulse on time and gap voltage. Also, it was found that the MRR and SR were increased with an increase up to a certain value of pulse current, and beyond that decreased.

- The optimum machining conditions were obtained through an integrated GRA-Taguchi analysis: sample composition of B$_4$C= 75 % and Al$_2$O$_3$ = 25 %, pulse on time of 32μs, pulse current of 2A, and gap voltage of 40 V.

- The results of ANOVA clearly showed the percentage contribution of sample composition of 3.08 %, pulse on time of 8.80 %, pulse current of 61.83%, and gap voltage of 13.65%.

- From SEM images, there was an occurrence of micro ridges, micro craters, micro-cracks, black patches, debris, and microvoids on the WEDMed surfaces.

References

1. Rajesh S, Rajakarunakaran S, Pandian S. Modeling And Optimization Of Sliding Specific Wear And Coefficient Of Friction Of Aluminum Based Red Mud Metal Matrix Composite Using Taguchi Method And Response Surface Methodology. *Materials Physics and Mechanics.* 2012;15(2): 150-166.

2. Kumar NM, Kumaran SS, Kumaraswamidhas LA. An investigation of mechanical properties and material removal rate, tool wear rate in EDM machining process of Al2618 alloy reinforced with Si3N4, AlN and ZrB2 composites. *Journal of Alloys and Compounds.* 2015;650: 1-28.

3. Gupta PK, Gupta MK. Mechanical and microstructural analysis of Al-Al2O3/B4C hybrid composites. *Proceedings of the Institution of Mechanical Engineers, Part L: Journal of Materials: Design and Applications.* 2020;234(12): 1503-1514.

4. Singh L, Singh B, Saxena KK. Manufacturing techniques for metal matrix composites (MMC): an overview. *Advances in Materials and Processing Technologies.* 2020;6(2): 441-457.

5. Amini H, Soleymani Yazdi MR, Dehghan GH. Optimization of process parameters in wire electrical discharge machining of TiB2 nanocomposite ceramic. *Proceedings of the Institution of Mechanical Engineers, Part B: Journal of Engineering Manufacture.* 2011;225(12): 2220-2227.

6. Kuriakose S, Mohan K, Shunmugam MS. Data mining applied to wire-EDM process. *Journal of Materials Processing Technology.* 2003;142(1): 182-189.

7. Kumar SS, Uthayakumar M, Kumaran ST, Parameswaran P, Mohandas E, Kempulraj G, Babu BR, Natarajan SA. Parametric optimization of wire electrical discharge machining on

aluminium based composites through grey relational analysis. *Journal of Manufacturing Processes*. 2015;20: 33-39.

8. Goyal A, Rahman HU, Ghani SA. Experimental investigation & optimisation of wire electrical discharge machining process parameters for Ni49Ti51 shape memory alloy. *Journal of King Saud University-Engineering Sciences*. 2021;33(2): 129-135.

9. Kumar SS, Erdemir F, Varol T, Kumaran ST, Uthayakumar M, Canakci A. Investigation of WEDM process parameters of Al–SiC–B4C composites using response surface methodology. *International Journal of Lightweight Materials and Manufacture*. 2020;3(2): 127-135.

10. Prasad AR, Ramji K, Datta GL. An experimental study of wire EDM on Ti-6Al-4V Alloy. *Procedia Materials Science*. 2014;5: 2567-2576.

11. Karabulut Ş, Karakoç H, Çitak R. Effect of the B4C reinforcement ratio on surface roughness of A16061 based metal matrix composite in wire-EDM machining. In: *8th International Conference on Mechanical and Aerospace Engineering (ICMAE) 2017*. 2017. p.812-815.

12. Shayan AV, Afza RA, Teimouri R. Parametric study along with selection of optimal solutions in dry wire cut machining of cemented tungsten carbide (WC-Co). *Journal of Manufacturing Processes*. 2013;15(4): 644-658.

13. Soni H, Sannayellappa N, Rangarasaiah RM. An experimental study of influence of wire electro discharge machining parameters on surface integrity of TiNiCo shape memory alloy. *Journal of Material Research*. 2017;32(16): 3100-3108.

14. Garg MP, Kumar A, Sahu CK. Mathematical modeling and analysis of WEDM machining parameters of nickel-based super alloy using response surface methodology. *Sādhanā*. 2017;42(6): 981-1005.

15. Velmurugan C, Subramanian R, Thirugnanam S, Ananadavel B. Experimental investigations on machining characteristics of Al 6061 hybrid metal matrix composites processed by electrical discharge machining. *International Journal of Engineering, Science and Technology*. 2011;3(8): 87-101.

16. Kanlayasiri K, Boonmung S. Effects of wire-EDM machining variables on surface roughness of newly developed DC 53 die steel: Design of experiments and regression model. *Journal of Materials Processing Technology*. 2007;192: 459-464.

17. Fard RK, Afza RA, Teimouri R. Experimental investigation, intelligent modeling and multi-characteristics optimization of dry WEDM process of Al–SiC metal matrix composite. *Journal of Manufacturing Processes*. 2013;15(4): 483-494.

18. Lal S, Kumar S, Khan ZA, Siddiquee AN. Multi-response optimization of wire electrical discharge machining process parameters for Al7075/Al2O3/SiC hybrid composite using Taguchi-based grey relational analysis. *Proceedings of the Institution of Mechanical Engineers, Part B: Journal of Engineering Manufacture*. 2015;229(2): 229-237.

19. Gopalakannan S, Senthilvelan T, Ranganathan S. Statistical optimization of EDM parameters on machining of aluminium hybrid metal matrix composite by applying taguchi based grey analysis. *Journal of Scientific & Industrial Research*. 2013;72: 358-365.

20. Kumar SS, Uthayakumar M, Kumaran ST, Parameswaran P. Electrical discharge machining of Al (6351)–SiC–B4C hybrid composite. *Materials and Manufacturing Processes*. 2014;29(11-12): 1395-1400.

21. Radhika N, Sudhamshu AR, Chandran GK. Optimization of electrical discharge machining parameters of aluminium hybrid composites using Taguchi method. *Journal of Engineering Science and Technology*. 2014;9(4): 502-512.

22. Motorcu AR, Ekici E, Kuş A. Investigation of the WEDM of Al/B4C/Gr reinforced hybrid composites using the Taguchi method and response surface methodology. *Science and Engineering of Composite Materials*. 2016;23(4): 435-445.

23. Prakash JU, Moorthy TV, Peter JM. Experimental investigations on machinability of aluminium alloy (A413)/Flyash/B4C hybrid composites using wire EDM. *Procedia Engineering*. 2013;64: 1344-1353.

24. Kavimani V, Prakash KS, Thankachan T. Multi-objective optimization in WEDM process of graphene–SiC-magnesium composite through hybrid techniques. *Measurement*. 2019;145: 335-349.

25. Kumar A, Grover N, Manna A, Chohan JS, Kumar R, Singh S, Prakash C, Pruncu CI. Investigating the influence of WEDM process parameters in machining of hybrid aluminum composites. *Advanced Composites Letters*. 2020;29: 1-14.

26. Pang X, Xian Y, Wang W, Zhang P. Tensile properties and strengthening effects of 6061Al/12 wt% B4C composites reinforced with nano-Al2O3 particles. *Journal of Alloys and Compounds*. 2018;768: 476-484.

27. Arunkumar L, Raghunath BK. Electro discharge machining characteristics of Mg/SiCp metal matrix composites by powder metallurgy (P/M) techniques. *International Journal of Engineering and Technology.* 2013;5(5): 4332-4338.

28. Mythili T, Thanigaivelan R. Optimization of wire EDM process parameters on Al6061/Al2O3 composite and its surface integrity studies. *Bulletin of the Polish Academy of Sciences: Technical Sciences*. 2020;68(6): 1403-1412.

THE AUTHORS

Gupta M.K.
e-mail: mnnit.manoj@gmail.com
ORCID: 0000-0001-6174-364X

Gupta P.K.
e-mail: guptammmecpankaj@gmail.com
ORCID: -

Adaptive multiple synchronization and rotors phase shift tracking for two-rotor vibration machine

I.S. Zaitceva✉, B.R. Andrievsky

Institute for Problems in Mechanical Engineering RAS, 61, Bolshoi Pr. V.O., St. Petersburg, Russia

St. Petersburg State University, 7/9, Universitetskaya nab., St. Petersburg, Russia

✉ juliazaytsev@gmail.com

Abstract. The paper presents the results of simulation and experiments of the adaptive control algorithm for various values of the multiplicity of the rotor's rotational frequencies and a given phase shift between them for the twin-rotor vibratory unit SV-2M. The simulation and experimental results demonstrate the rotational speeds and phase shifts between the rotors. Also, the process of adaptive controller adjustment is shown. The performance of the vibration machine demonstrates the effectiveness of the proposed algorithm in wide operating modes. Further on, the development of automated control algorithms in vibration machines promises the transition toward intelligent vibration technologies. It allows regulating the type of vibration fields of the table in real-time, including improving the process of vibration mixing by chaotizing its movement.

Keywords: nonlinear oscillations, PI controller, asynchronous drive, unbalanced rotor, self-synchronization, vibration technologies, intelligent control

1. Introduction

Vibration technologies are a crucial automation component in various industries that allows for expanding the technical and economic effects. The development and improvement of vibration technologies and equipment do not stop and are closely related to the study of nonlinear oscillations and the possibility of their practical application [1]. The oscillatory effects of vibration machines are widely used in manufacturing and agriculture for bulk solid separation, vibrational transportation, vibration grinding, pile driving, mixing, etc. Despite all the advantages, vibration machines have a drawback associated with the lack of control over vibration oscillations during operation. In this connection, the issues of automation and the use of an adjustable drive in this direction are highly relevant.

For more than a hundred years, work has been underway to create new vibration technologies and designs of vibration machines in various scientific schools. It includes the well-known St. Petersburg Mekhanobr-Tekhnika Corp., based on the design and scientific departments of the Institute for the Ore Dressing. Differ areas of research work in Mekhanobr

are carried out in cooperation with several scientific and educational institutions [2]. Recently, on the initiative of Prof. Alexander Fradkov, based on laboratory equipment of the Institute for Problems in Mechanical Engineering of the Russian Academy of Sciences, the direction of feedback control of vibration machines with an unbalance vibration exciter began to develop. Modern automatic control methods can allow the controlling of all vibration parameters in real-time by changing the frequencies and phases of rotation of drive motors. The solution to such problems is attractive from scientific and engineering points of view. This is especially in demand in the case of using vibration equipment in cyber-physical systems [3]. It may be promising for smart vibration technologies since it will allow changing the type of platform vibration fields during operation and chiefly will open the way to chaotization of vibration mixing.

The synchronization phenomenon is widely used in vibration technology to obtain various forms of body vibrations, ensuring the stability of the vibration machine and maximum productivity. Based on the self-synchronization property, such classes of vibration machines as grain cleaners, conveyors, feeders, screens, crushers, and mills have been created. The single synchronization mode can occur naturally and is called self-synchronization [4]. The self-synchronization phenomenon of mechanical exciters leads to the fact that unrelated rotors of vibration exciters rotate with the same absolute value or multiples of the average angular velocities, and certain phase ratios are established between the rotors. Coordinated synchronous rotation of vibration exciters with a given phase shift between them is provided due to the internal properties of the oscillatory system itself. In the study of vibrations, it is assumed that the shafts of vibration exciters rotate uniformly on average throughout oscillations. There is also a connection between the vibrational and rotational coordinates of the system. This connection manifests itself in the mutual influence of the unbalanced shaft support vibration on the rotors and the reactive moments of the forces of inertia emanating from the uneven rotation of the rotors on the supports. The effect of self-synchronization is not always stable, for example, in the case of providing specified shifts in the phases of the rotors or multiple synchronizations. Under the varying mass conditions of the processed material, the synchronization can be ensured by control algorithms. Thus, the engineers are faced with the task of controlled synchronization of vibration machines. Multiple frequency synchronization is meant the proportionality of the speed of unbalanced rotors ω_i to the synchronous frequency ω^* for integers n_i [4]:

$$\omega_i = n_i \cdot \omega^*, i = 1, \dots, n. \tag{1}$$

Multiple coordinate synchronizations assume that the phases of vibration exciters ϕ_i satisfy the equality [3]:

$$\frac{\phi_i}{n_i} - \frac{\phi_k}{n_k} = L_{ik}, k = 1, \dots, n, i \neq k. \tag{2}$$

Formalized issues of controlled synchronization were considered in [4-6], where the presented general definition of controlled synchronization allows us to formulate the problem of synthesizing the controller of a dynamical system. There are several studies on the control of the synchronization of vibration machines [7-9]. In [7], the synchronization problem is solved using the speed gradient method [10], where the goal of control is to reach a given level of the system's total energy, which is determined by the steady-state average speeds of the rotors. The results of the proposed control law have been tested on a three-rotor vibrating machine with a varying mass of the processed load. In [8,9], it was found that the multiple synchronization region is limited for high speeds due to the tendency for rotors to self-synchronize when controlling the phase shift between two unbalanced rotors using a proportional-integral (PI) controller in the speed and phase control loops. Thus, shaped and non-uniform fields of trajectories of points of vibration exciter cannot be obtained due to the action of self-synchronization. The purpose of this paper is to ensure multiple speed synchronizations with a given phase shift.

2. Description of two-rotor vibration machine SV-2M

To conduct experiments on the reproduction of complex dynamic phenomena, study vibrational processes, and test algorithms for controlling rotational and oscillatory motion, several vibration stands were created [2,11,12]. The source of oscillations of the vibration machine is the actuator, in which an inertial element (vibration exciter) is installed in bearings, connected to the housing, and unbalanced relative to the entire axis of rotation. In this paper, we study the control of a two-rotor vibrating machine, shown in Fig. 1, and consisting of the following components. Three-phase asynchronous motors *1* are installed on the supporting frame *2*, connected through a shaft with unbalanced rotors *3*. The nominal motor output is 0.09 kV·A, and the rotor speed is 288 rad/s. The pre-resonant operating frequency range of the engines lies in the interval [30, 120] rad/s. The axes of the exciter rotors are perpendicular to the plane parallel to which the platform moves. The unit is equipped with lower springs for vibration isolation of platform *5* from the carrier frame and upper springs for securing the load.

Electric motors *1* are controlled in real-time through power frequency converters connected to the computer and current sensors in the motor power supply circuit. The rotor's rotation angles are measured by encoders. The oscillatory movements of the platform are measured by inductive displacement sensors. All components are used to create a complex mechatronic system in which all processes are inextricably linked.

The vibration machine can operate in the self-synchronization and controlled synchronization mode of vibration exciters. The rotation of the vibration exciters creates vibrations of platform *5*, the oscillation frequency of which is controlled.
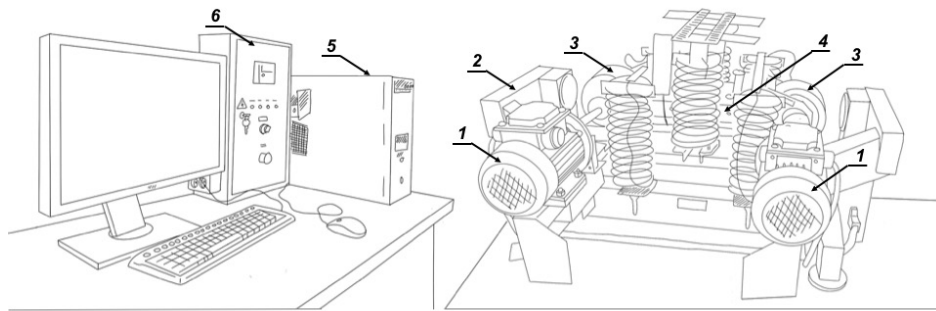
Fig. 1. System of two-rotor vibration unit

Before carrying out experiments on a vibration machine, it is advisable to conduct a computer simulation of the system to test a new control algorithm and select its unknown parameters. Although the accurate model of a vibration machine is very complex, it can be replaced by the following simplified model. As shown in [7,9], due to the principle of averaging for operating frequencies and also due to the presence of local controllers of asynchronous motors, their dynamics can be approximately described by the transfer function from the control signal $u(t)$ to the angular frequency of rotation of the rotor $\omega(t)$:

$$W_u^\omega(s) = \frac{K_d}{(T_1 s + 1)(T_2 s + 1)}, \tag{3}$$

where K_d is the drive gear ratios, T_1 and T_2 are the time constants.

Model (3) parameters were identified by the standard method of nonrecursive least squares estimation [6,8]. The results of the identification procedure showed that the variations of model parameters (3) for different operating frequency ranges are low, and their average values for both drives are: $K_d = 0.041$ rad/s, $T_1 = 1.75$ s, $T_2 = 0.246$ s.

3. Adaptive control of multiple synchronizations

The choice of the adaptive control law is associated not only with a complex mathematical description and change in time of its internal parameters but also with the possibility of changing the given input parameters the rotational speed of the rotors and the magnitude of the phase shift between them, without additional adjustment of the controller. In this paper, an adaptive PI controller with an implicit reference model (IRM) is used [13-15]. To describe it, consider the following equation for a minimum-phase single-input single-output (SISO) system:

$$A(p)\omega(t) = B(p)r(t), \tag{4}$$

where $\omega(t)$ and $r(t)$ are the actual and reference rotor speeds, $A(p)$ and $B(p)$ are polynomials in the time differentiation operator $p = d/dt$, which coefficients are unknown.

The desired dynamics of the stabilization process of the object (4) can be specified by an implicit differential equation. To do this, we introduce the stabilization error $e(t) = \omega(t) - r(t)$, its integral $\dot{\xi}(t) = e(t)$ and the adaptation error $\sigma(t)$ as follows [15]:

$$\sigma(t) = \tau\xi(t) + e(t), \tag{5}$$

where τ is the coefficient of the reference model, which is set according to the desired stabilization dynamics.

The PI speed control law for each rotor is written in the standard form [9]:

$$u(t) = -(K_i(t)\xi(t) + K_p(t)e(t)), \tag{6}$$

where $K_i(t)$ and $K_p(t)$ are integral and proportional coefficients. Then the structure of the adaptation algorithm is written as [15-17]:

$$\dot{K}_i(t) = \gamma\sigma(t)\xi(t) - \lambda(K_i(t) - K_i^0), K_i(0) = K_i^0, \tag{7}$$

$$\dot{K}_p(t) = \gamma\sigma(t)\xi(t) - \lambda(K_p(t) - K_p^0), K_p(0) = K_p^0, \tag{8}$$

where γ is the adaptation coefficient, λ is the adaptation parametric feedback gain, K_i^0 and K_p^0 are the initial values of adjustable coefficients of the regulator.

To control the phase shift, by analogy with (5), (6), (7), and (8), it is proposed to introduce an adaptive control law with IRM into the phase control loop as follows:

$$\sigma_\psi(t) = \tau\xi_\psi(t) + e_\psi(t), \tag{9}$$

$$u_\psi(t) = -(K_{i\psi}(t)\xi_\psi(t) + K_{p\psi}(t)e_\psi(t)), \tag{10}$$

$$\dot{K}_{i\psi}(t) = \gamma\sigma(t)\xi_\psi(t) - \lambda(K_{i\psi}(t) - K_{i\psi}^0), K_{i\psi}(0) = K_{i\psi}^0, \tag{11}$$

$$\dot{K}_{p\psi}(t) = \gamma\sigma(t)\xi_\psi(t) - \lambda(K_{p\psi}(t) - K_{p\psi}^0), K_{p\psi}(0) = K_{p\psi}^0. \tag{12}$$

Thus, the resulting control signal for the left and right motors of the vibration machine, considering (10), is described as:

$$u_l(t) = u(t) + u_\psi(t), u_r(t) = u(t) + u_\psi(t). \tag{13}$$

For each rotor, a restriction on the control signal is introduced using the saturation function: $\text{sat}_u(u) = \text{sign}(u)\min\{|u|, u\}, u > 0$.

4. Results

Let us carry out a simulation and a physical experiment on a two-rotor vibrating machine using the adaptive control law (6)-(8), (10)-(13) model of the vibrating machine (3) for the frequency ratio of the right and left engines equal to $n = 1/2$ so that $\omega_r = 120$ rad/s, $\omega_l = 120$ rad/s with their antiphase rotation (Fig. 3). The parameters of the adaptive PI controller are chosen as follows: $\gamma = 1$, $\lambda = 0.01$, $\tau = 1$, $K_i^0 = 450$, $K_p^0 = 450$, $K_{i\psi}^0 = 450$, $K_{p\psi}^0 = 450$. The upper limit value of the control signal is $u = 40$ rad/s, the lower limit is 0.
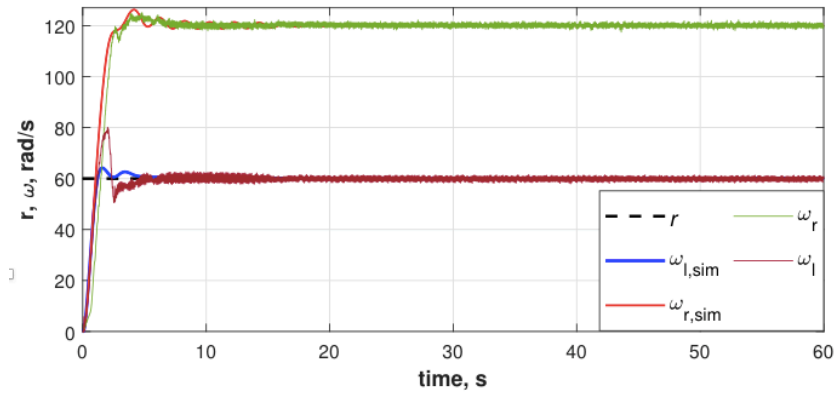
Fig. 2. Rotation speed
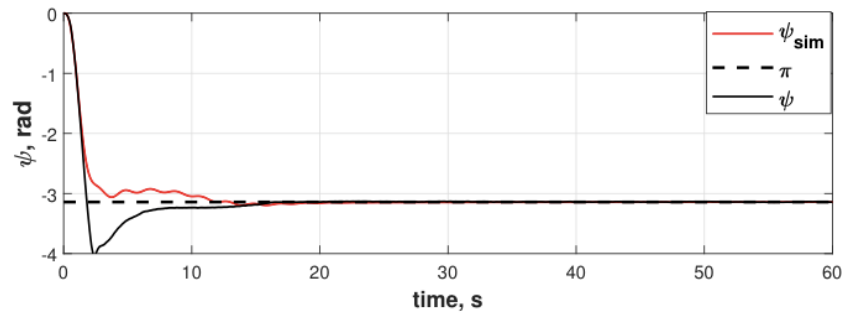
Fig. 3. Phase shift between rotors

From Figures 2 and 3 it can be seen that the adaptive control law maintains the given rotor speeds and phase shift. Figure 4 shows the process of adjusting the controller coefficients, from which it can be seen that the proportional coefficients K_p, K_i obtained experimentally coincide with the coefficients obtained from the simulation results. Figure 5 shows the change in the adaptation error for the speed loop of each rotor and the phase shift, which shows the agreement between the simulation and experiment results for the frequency control loop.
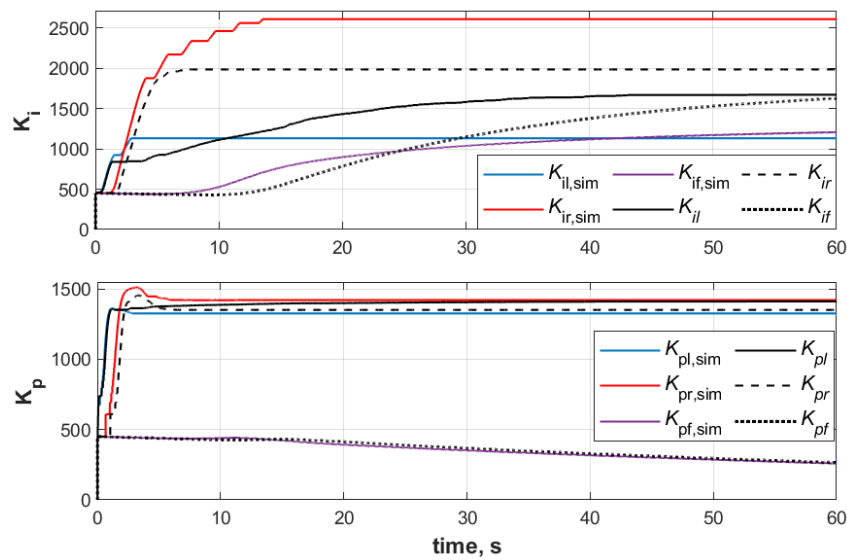
Fig. 4. Adaptation of controller gains
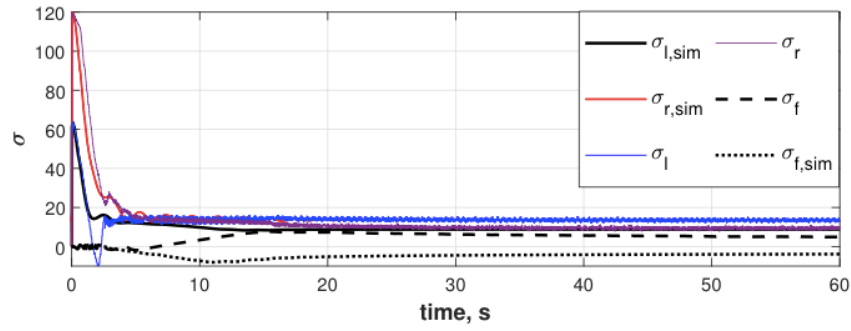
Fig. 5. Adaptation error

A similar experiment was carried out for rotor speeds of $\omega_r = 90$ and $\omega_l = 45$ rad/s (Fig. 6). The reference phase shift between rotors is equal to $\pi/2$. Figure 7 shows the phase shift between rotors via time, Fig. 8 – the adaptation of controller gains, and Fig. 9 – the adaptation error via time. Note that a further increase in the rotational speed of the rotors leads to a loss of phase shift control under the action of self-synchronization. The phase shift acquires a periodic dependence on time.
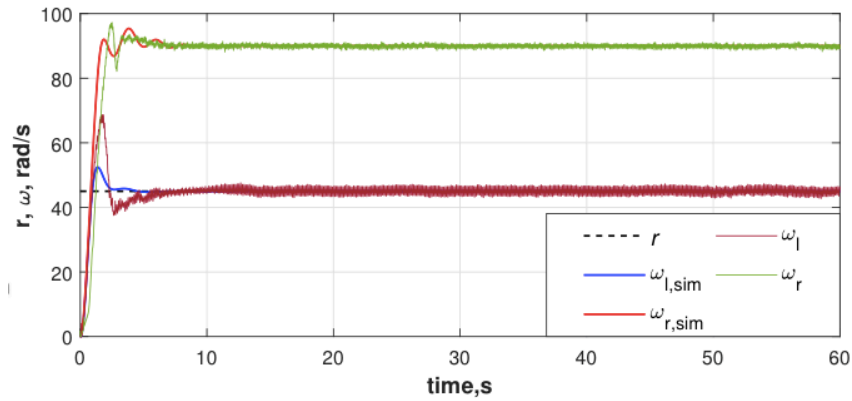
Fig. 6. Rotation speed
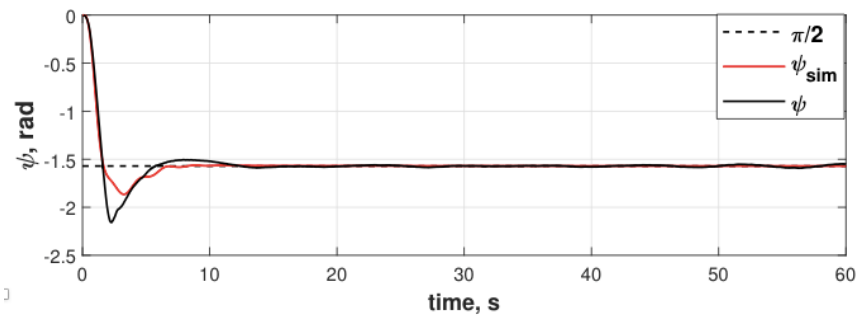
Fig. 7. Phase shift between rotors
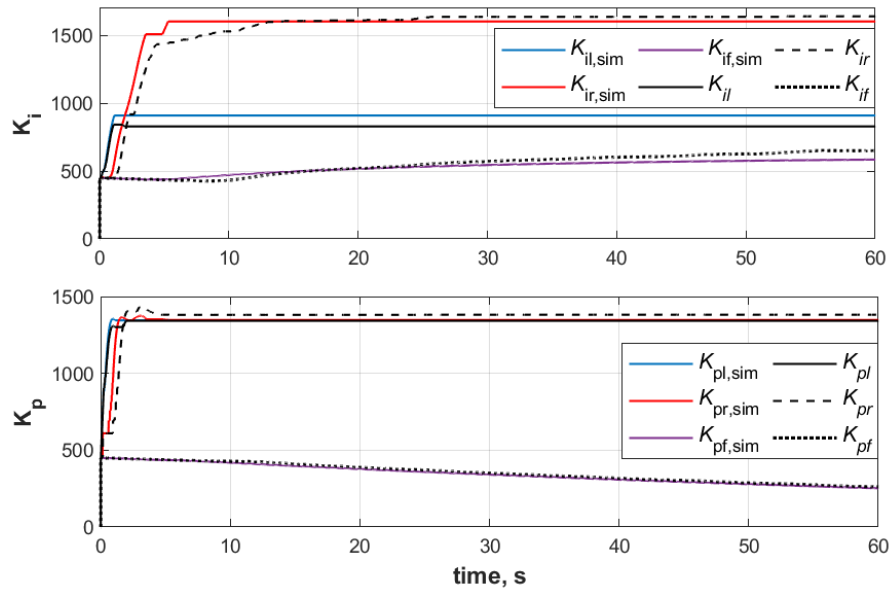
Fig. 8. Adaptation of controller gains
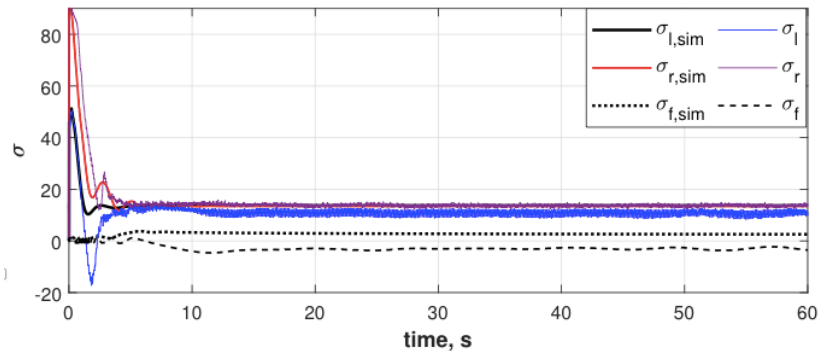
Fig. 9. Adaptation error

Also, experiments were carried out at a reference rotation speed of each rotor equal to 40 rad/s and applied phase shift between the rotors, given by the following periodic law: $\psi^*(t) = \pi \cdot \sin(0.3t)$. Figures 10-13 show the simulation and experimental results for this case.

Fig. 10. Rotation speed

Fig. 11. Phase shift between rotors

Fig. 12. Adaptation of controller gains

Fig. 13. Adaptation error

5. Conclusion
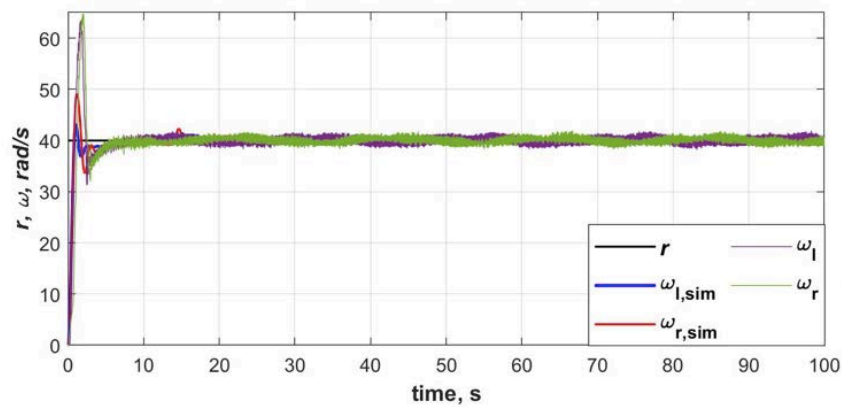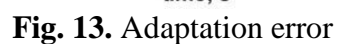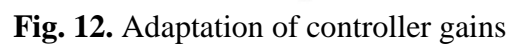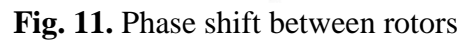
The paper proposes the use of an adaptive controller with IRM to control multiple synchronizations of a two-rotor vibratory machine. Simulation of a simplified model of the machine and an experiment were carried out, the results of which are close to each other,

except for the integral coefficients of the controller. An adaptive IRM controller allows expanding the range of controlled frequencies and phases compared to a standard PI-controller, and also allows running transients more smoothly.

References

1. Blekhman LI, Kremer EB, Vasilkov VB. Research on Vibration Processes and Devices: New Results and Applications. In: *Mechanics and Control of Solids and Structures*. Springer; 2022. p.75-90.

2. Vaisberg L. Vibration technology research achievements of the Mekhanobr scientific school and their practical implementation. *Vibroengineering PROCEDIA*. 2019;25: 76-82.

3. Andrievsky B, Zaitceva I. Methods of intelligent control in mechatronics and robotic engineering. *A survey. Electronics*. 2022;11(15): 2443.

4. Blekhman II. *Synchronization in science and technology*. New-York: ASME Press; 1988.

5. Blekhman I, Fradkov A, Nijmeijer A., Pogromsky A. On self-synchronization and controlled synchronization of dynamical systems. *Systems and Control Letters*. 1997;31(5): 299-306.

6. Blekhman I, Fradkov A, Tomchina O, Bogdanov D. Self-Synchronization and Controlled Synchronization: General Definition and Example Design. *Mathematics and Computers in Simulation*. 2002;58: 367-384.

7. Fradkov AL, Tomchina OP, Andrievsky B, Boikov VI. Control of Phase Shift in Two-Rotor Vibration Units. *IEEE Trans. Control Syst. Technol*. 2021;29(3): 1316-1323.

8. Andrievsky B, Fradkov AL, Tomchina OP, Boikov V. Angular velocity and phase shift control of mechatronic vibrational setup. *IFAC-PapersOnLine*. 2019;52(15): 436-441.

9. Andrievsky B, Boikov V. Bidirectional controlled multiple synchronization of unbalanced rotors and its experimental evaluation. *Cybernetics And Physics*. 2021;10(2): 63-74.

10. Fradkov AL. Speed-gradient scheme and its applications in adaptive control. *Autom. Remote Control*. 1979;40(9): 1333-1342.

11. Andrievsky B, Blekhman II, Blekhman LI, Boikov VI, Vasil'kov VB, Fradkov AL. Education and research mechatronic complex for studying vibration devices and processes. *J. Mach. Manuf. Reliab*. 2016;45(4): 369-374.

12. Andrievsky B, Boikov V. Experimental study of multiresonance mechatronic vibrational laboratory setup. *Cybernetics and Physics*. 2017;5(1): 5-11.

13. Andrievskii BR, Fradkov AL. Method of Passification in Adaptive Control, Estimation, and Synchronization. *Autom. Remote Control*. 2006;67(11): 1699-1731.

14. Fradkov A, Miroshnik I, Nikiforov V. *Nonlinear and Adaptive Control of Complex Systems*. Dordrecht: Kluwer; 1999.

15. Fradkov AL. Passification of nonsquare linear systems and Feedback Kalman-Yakubovich-Popov Lemma. *Europ. J. Contr*. 2003;9(11): 573-582.

16. Andrievsky B, Zaitceva I, Boikov VI. Digital Adaptive Control of Unbalanced Rotor Velocities with Anti-windup Augmentation. *IFAC-PapersOnLine. 14th IFAC Workshop on Adaptive and Learning Control Systems*. 2022;55(12): 258-263.

17. Andrievsky B, Zaitceva I, Li T, Fradkov AL. Adaptive Multiple Synchronization and Phase Shift Control for Mechatronic Vibrational Setup. *8th International Conference on Control, Decision and Information Technologies*. 2022: 611-616. Available from: doi: 10.1109/CoDIT55151.2022.9804086

THE AUTHORS

Zaitceva I.S.
e-mail: juliazaytsev@gmail.com
ORCID: 0000-0001-9957-022X

Andrievsky B.R.
e-mail: boris.andrievsky@gmail.com
ORCID: 0000-0001-6323-2931

Wave propagation under the influence of voids and non-free surfaces in a micropolar elastic medium

Sachin Kaushal[1✉], Rajneesh Kumar[2], Arun Kochar[1]

[1]Department of Mathematics, School of Chemical Engineering and Physical Sciences, Lovely Professional University, Phagwara, India

[2]Department of Mathematics, Kurukshetra University, Kurukshetra, India

✉ sachin_kuk@yahoo.co.in

Abstract. A problem of reflection of elastic wave in micropolar media with the void at non-free surface is considered. The governing equations are formulated for a specific model. The equations so obtained are put in two dimensions and converted into dimensionless form and then solved with the help of the reflection technique. Non-free boundary conditions are taken to obtain the amplitude ratios of different reflected waves i.e. Longitudinal displacement wave (LD-wave), Longitudinal void volume fraction wave (LVVF-wave), Transverse wave (T-wave), and Micro-rotational wave (MR-wave). These amplitude ratios are obtained numerically and also shown graphically for the non-free surface as well as for the free surface to depict the impact of stiffness and void. From the present study, certain cases are also deduced.

Keywords: wave propagation, non-free surface, micropolar, void, amplitude ratio

1. Introduction

When a plane wave traveling through an elastic medium comes across a boundary surface of the medium, it gets reflected into the medium. This phenomenon occurs in many situations, e.g. seismology, engineering, optics, etc. The investigation of the reflection problem of plane waves is an important tool to analyze various properties of the medium. For example, such problems find applications in the field of seismology as a method for determining the characteristics of the earth's internal structure as well as for the exploration of valuable materials. Various authors have contributed to the field of elasticity and wave propagation, notable of them are [1-8].

An elastic material that consists of small pores is defined as linear elastic material with voids. In the classical theory of elasticity, the volume of such pores is neglected which plays an important role as the volume of such pores is to be taken as an independent kinematic variable. Nunziato and Cowin [9] developed a theory that is based on non-linear elastic material having voids. Later on, Cowin and Nunziato [10] extended this to a linear elastic material having pores. Various authors have done different research on micropolar elastic material with void and notable them are [11-16].

In the context of micropolar porous media Marin [17] formulated a heat-flux theory that includes the heat-flux vector and an evolution equation for it. Lianngenga [18] studied the problem of attenuations and phase velocities of plane body waves and their reflection from a stress-free surface in the micropolar material with voids and also computed amplitude as well as energy ratios of reflected waves. Kumari and Kaliraman [19] observed variation in modulus of amplitude ratios of various reflected and refracted waves against incident waves traveling at high frequency as well as at low frequency in micropolar elastic solid with a void. Marin et al. [20] showed that the solution of mixed IBVP (initial boundary value problem) for porous micropolar bodies depends continuously on coefficients that couple the micropolar deformation equations. With the help of normal mode analysis, Alharbi et al. [21] obtained the expression for the components of stress, displacement components, microrotation components, and temperature field and also studied the effect of heat source on these expressions in the micropolar medium with void under the theory of the three-phase-lag model of thermoelasticity.

In the above-mentioned work, it is observed that the reflection of waves in micropolar elastic wave medium is usually taken over the free surface. However, In actual engineering problems due to accumulative damage, the interface may be imperfect and it will lead to a non-free surface with distributed elastic constraint or support. The study of the non-free surface is at the incubating stage. Zhang et al. [22] calculated energy flux ratios of reflected waves at the non-free surface of a micropolar elastic half-space. Singh [23] calculated reflection coefficients of thermoelastic waves by assuming different boundary conditions at the non-free surface.

The concept of a non-free surface is also used in various fields of Physics such as acoustics and electromagnetism therefore a problem on the boundary surface is considered as non-free with a micropolar elastic constraint with the void, where each mass point is subjected to the normal, tangential and rotational stiffnesses. The amplitude ratios of reflected waves are calculated for the desired boundary conditions at a non-free surface. The impact of voids and the influence of the non-free surface on amplitude ratios are shown graphically against the angle of incidence.

2. Governing equations
The field equations and constitutive relations in absence of body forces, body couples, and heat source (Eringen [24] and Iesan [25]) are as follows:

$$(\lambda + \mu)\nabla(\nabla.\vec{u}) + (\mu + K)\nabla^2\vec{u} + K(\nabla \times \vec{\phi}) + \beta^*\nabla q = \rho\frac{\partial^2\vec{u}}{\partial t^2}, \tag{1}$$

$$(\alpha + \beta)\nabla(\nabla.\vec{\phi}) + \gamma\nabla^2\vec{\phi} + K(\nabla \times \vec{u}) - 2K\vec{\phi} = \rho\hat{j}\frac{\partial^2\vec{\phi}}{\partial t^2}, \tag{2}$$

$$\alpha^*\nabla^2 q - \omega^*\dot{q} - \xi^* q - \beta^*(\nabla.\vec{u}) = \rho\kappa^*\frac{\partial^2 q}{\partial t^2}, \tag{3}$$

$$t_{ij} = \lambda u_{r,r}\delta_{ij} + \mu(u_{i,j} + u_{j,i}) + K(u_{j,i} - \varepsilon_{ijr}\phi_r) + \beta^* q\delta_{ij}, \tag{4}$$

$$m_{ij} = \alpha\phi_{r,r}\delta_{ij} + \beta\phi_{i,j} + \gamma\phi_{j,i}, \tag{5}$$

where λ, μ are Lame's constants, t is time, t_{ij} are stress components, q denotes volume fraction field, δ_{ij} is Kronecker delta, ρ is density, $\vec{u}$ is displacement vector, $\vec{\phi}$ denotes microrotation vector, ε_{ijr} is an alternating tensor, α, β, γ, K are micropolar constants, $\hat{j}$ denotes micro-inertia, m_{ij} denotes component of couple stress tensor, $\omega^*, \beta^*, \alpha^*, \xi^*, \kappa^*$ are material constants due to presence of voids, ∇^2 represents Laplacian operator.

3. Solution procedure
We consider a homogeneous, isotropic micropolar elastic half-space with the void at a non-free surface. The rectangular cartesian coordinate system (x_1, x_2, x_3) having an origin at

interface $x_3 = 0$ is considered along with x_3-axis pointing normally into the medium as shown in Fig. 1. Plane waves in x_1-x_3 plane are considered such that the wave-front is parallel to x_2-axis, therefore all the fields variable depend only on x_1, x_3, and t. Thus, the problem is considered two dimensional, so we take

$$\vec{u} = (u_1, 0, u_3), \vec{\phi} = (0, \phi_2, 0). \tag{6}$$
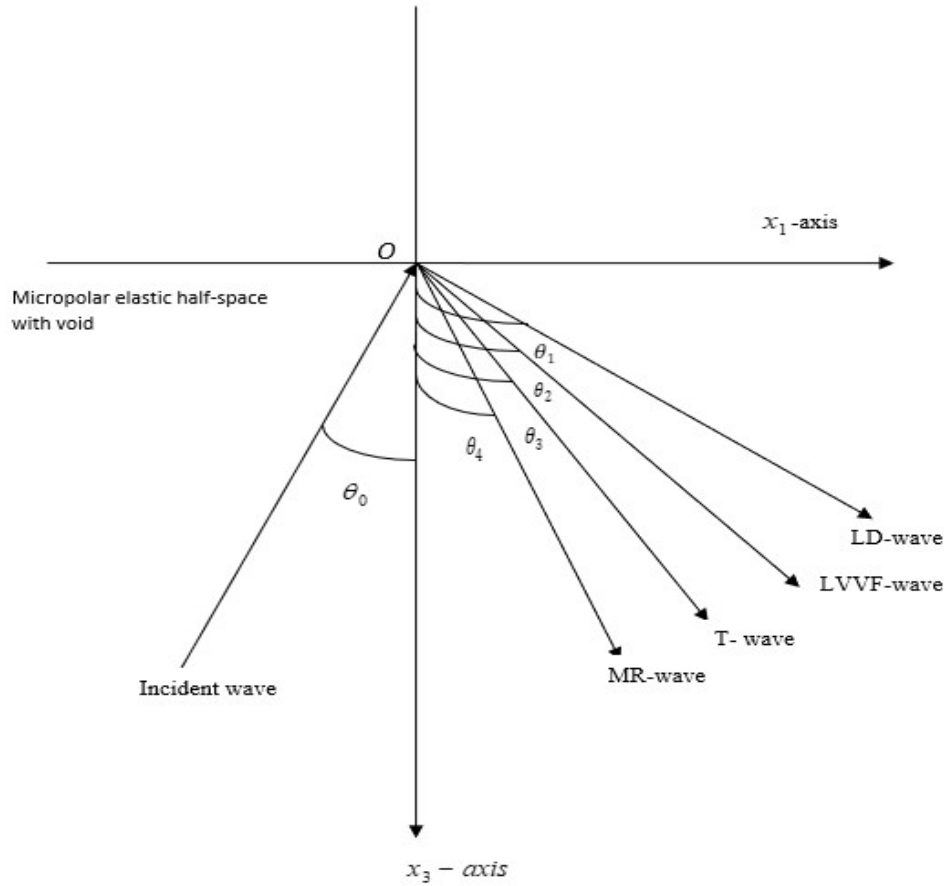
Fig. 1. Geometry of the problem

Dimensionless quantities are taken as

$$(x_i{}', u_i{}') = \frac{\omega_1}{c_1}(x_i, u_i), \; t'_{3i} = \frac{1}{\mu}t_{3i}, \; q' = \frac{K\omega_1{}^2}{c_1^2}q, \; t' = \omega_1 t, \; \phi'_2 = \frac{\hat{j}\omega_1{}^2}{c_1^2}\phi_2,$$

$$m'_{32} = \frac{\hat{j}\omega_1}{\gamma c_1}m_{32}, \; (i = 1,3) \tag{7}$$

where

$$c_1^2 = \frac{\lambda + 2\mu + K}{\rho} \text{ and } \omega_1{}^2 = \frac{K}{\rho\hat{j}}.$$

Making use of equations (6)-(7) in equations (1)-(5), we obtain

$$a_1\frac{\partial}{\partial x_1}\left(\frac{\partial u_1}{\partial x_1} + \frac{\partial u_3}{\partial x_3}\right) + a_2\nabla^2 u_1 - a_3\frac{\partial \phi_2}{\partial x_3} + a_4\frac{\partial q}{\partial x_1} = \frac{\partial^2 u_1}{\partial t^2}, \tag{8}$$

$$a_1\frac{\partial}{\partial x_3}\left(\frac{\partial u_1}{\partial x_1} + \frac{\partial u_3}{\partial x_3}\right) + a_2\nabla^2 u_3 + a_3\frac{\partial \phi_2}{\partial x_1} + a_4\frac{\partial q}{\partial x_3} = \frac{\partial^2 u_3}{\partial t^2}, \tag{9}$$

$$a_5\nabla^2\phi_2 + a_6\left(\frac{\partial u_1}{\partial x_3} - \frac{\partial u_3}{\partial x_1}\right) - a_7\phi_2 = \frac{\partial^2 \phi_2}{\partial t^2}, \tag{10}$$

$$a_{13}\nabla^2 q - a_{14}q - a_{15}\frac{\partial q}{\partial t} - a_{16}\left(\frac{\partial u_1}{\partial x_1} + \frac{\partial u_3}{\partial x_3}\right) = \frac{\partial^2 q}{\partial t^2}, \tag{11}$$

$$t_{33} = a_8\frac{\partial u_1}{\partial x_1} + a_9\frac{\partial u_3}{\partial x_3} + a_{10}q, \tag{12}$$

$$t_{31} = a_{11} \frac{\partial u_1}{\partial x_3} + \frac{\partial u_3}{\partial x_1} - a_{12}\phi_2, \tag{13}$$

$$m_{32} = \frac{\partial \phi_2}{\partial x_3}, \tag{14}$$

where

$$a_1 = \frac{\lambda+\mu}{\rho c_1^2}, a_2 = \frac{\mu+K}{\rho c_1^2}, a_3 = \frac{K}{\hat{\jmath}\rho\omega_1^2}, a_4 = \frac{\beta^*}{\omega_1\hat{\jmath}\rho}, a_5 = \frac{\gamma}{\rho c_1^2\hat{\jmath}}, a_6 = \frac{K}{\rho c_1^2}, a_7 = \frac{2K}{\hat{\jmath}\rho\omega_1^2}, a_8 = \frac{\lambda}{\mu}, a_9 = \frac{\lambda+2\mu+K}{\mu},$$

$$a_{10} = \frac{\beta^* c_1^2}{\mu\hat{\jmath}\omega_1^2}, a_{11} = \frac{\mu+K}{\mu}, a_{12} = \frac{Kc_1^2}{\mu\hat{\jmath}\omega_1^2}, a_{13} = \frac{\alpha^*}{\kappa^*\rho c_1^2}, a_{14} = \frac{\xi^*}{\kappa^*\rho\omega_1^2}, a_{15} = \frac{\omega^*}{\kappa^*\rho\omega_1^2}, a_{16} = \frac{\beta^*\hat{\jmath}}{\kappa^*\rho c_1^2}.$$

With the help of the expression given by Helmholtz decomposition, u_1 and u_3 can be expressed as

$$u_1 = \frac{\partial \varphi}{\partial x_1} - \frac{\partial \psi}{\partial x_3}, u_3 = \frac{\partial \varphi}{\partial x_3} + \frac{\partial \psi}{\partial x_1}. \tag{15}$$

By applying equation (15) in equations (8)-(11), we get

$$\left(\nabla^2 - \frac{\partial^2}{\partial t^2}\right)\varphi + a_4 q = 0, \tag{16}$$

$$\left(a_2\nabla^2 - \frac{\partial^2}{\partial t^2}\right)\psi + a_3\phi_2 = 0, \tag{17}$$

$$\left(a_5\nabla^2 - \frac{\partial^2}{\partial t^2} - a_7\right)\phi_2 - a_6\nabla^2\psi = 0, \tag{18}$$

$$\left(a_{13}\nabla^2 - \frac{\partial^2}{\partial t^2} - a_{14} - a_{15}\frac{\partial}{\partial t}\right)q - a_{16}\nabla^2\varphi = 0. \tag{19}$$

Assuming the motion to be harmonic and for solving the equations (16)-(19), we assume the solutions as

$$(\varphi, q, \psi, \phi_2) = (\varphi^o, q^o, \psi^o, \phi_2{}^o)e^{\iota\kappa(x_1\sin\theta_0 - x_3\cos\theta_0 + vt)}, \tag{20}$$

where κ denotes as a wave number, ι is known as iota, θ_0 is the angle of inclination, and quantities such as φ^o, q^o, ψ^o and $\phi_2{}^o$ are arbitrary constants. Using the values of $\varphi, q, \psi,$ and ϕ_2, we obtained the following equations

$$(v^4 + A_{01}v^2 + A_{02})(\varphi, q) = 0, \tag{21}$$

$$(v^4 + A_{03}v^2 + A_{04})(\psi, \phi_2) = 0, \tag{22}$$

where $v = \left(\frac{\omega}{\kappa}\right)$ denotes the velocity of waves, v_i $(i = 1-4)$ are velocities of the LD-wave, LVVF-wave, T-wave, and MR-wave respectively and

$$A_{01} = \frac{-(a_4 a_{16} - a_{14} + (a_{13}+1)\omega^2 + \iota\omega a_{15})}{\omega^2 - a_{14} + \iota\omega a_{15}}, A_{02} = \frac{a_{13}\omega^2}{\omega^2 - a_{14} + \iota\omega a_{15}}, A_{03} = \frac{a_2 a_7 - a_3 a_6 - (a_5 + a_2)\omega^2}{\omega^2 - a_7},$$

$$A_{04} = \frac{a_2 a_5 \omega^2}{\omega^2 - a_7}.$$

4. Boundary conditions

For the free surface, the component of stresses is zero but for the non-free surface, some finite values may exist and they are proportionate to the components of displacement as well as rotational components, and appropriate conditions at $x_3 = 0$ are

$$\text{(i) } t_{33} = -\iota S_1 u_3, \text{ (ii) } t_{31} = -\iota S_2 u_1, \text{ (iii) } m_{32} = -\iota S_3 \phi_2, \text{ (iv) } \frac{\partial q}{\partial x_3} = 0. \tag{23}$$

In equation (23) $S_1, S_2,$ and S_3 represent the stiffness along the normal component, tangential component, and rotational component. The stress field and displacement field are expressed in terms of complex quantities as it is observed that there is a phase shift between the stress field and displacement field due to the mathematical relation $u_{ij} = \iota\kappa_j u_i$ but actually, extra phase shift does not exist so to overcome this extra phase shift effect, we introduced a negative unit, $-\iota$ into the right side of equation (23).

5. Reflection at the non-free surface

To obtain amplitude ratio at non-free surface we consider $\varphi, q, \psi,$ and ϕ_2 as follows:

$$\varphi = \sum A_{0i} e^{\iota\kappa_0(x_1\sin\theta_0 - x_3\cos\theta_0) + \iota\omega t} + A_i e^{\iota\kappa_i(x_1\sin\theta_i + x_3\cos\theta_i) + \iota\omega t}, \tag{24}$$

$$q = \sum d_i \left(A_{0i} e^{\iota \kappa_0 (x_1 \sin \theta_0 - x_3 \cos \theta_0) + \iota \omega t} + A_i e^{\iota \kappa_i (x_1 \sin \theta_i + x_3 \cos \theta_i) + \iota \omega t} \right), \tag{25}$$

$$\psi = \sum B_{0i} \, e^{\iota \kappa_0 (x_1 \sin \theta_0 - x_3 \cos \theta_0) + \iota \omega t} + B_i e^{\iota \kappa_j (x_1 \sin \theta_j + x_3 \cos \theta_j) + \iota \omega t}, \tag{26}$$

$$\phi_2 = \sum f_i \left(B_{0i} e^{\iota \kappa_0 (x_1 \sin \theta_0 - x_3 \cos \theta_0) + \iota \omega t} + B_i e^{\iota \kappa_j (x_1 \sin \theta_j + x_3 \cos \theta_j) + \iota \omega t} \right), \tag{27}$$

where

$$d_i = \frac{\omega^2 - \kappa_i^{\ 2}}{a_4}, \; f_i = \frac{a_5 \kappa_j^2 + a_7 - \omega^2}{a_6 \kappa_j^2}, (i = 1,2), (j = 3,4),$$

where $A_{0i} \, (i = 1,2)$ are the amplitude of incident LD-wave, LVVF-wave, and $B_{0i}(i = 1,2)$ are the amplitude of incident T-wave and MR-wave. A_i are the amplitude of the reflected LD-wave and LVVF-wave. B_i are the amplitude of the reflected T-wave and reflected MR-wave. Snell's Law is given by

$$\frac{\sin \theta_0}{\upsilon_0} = \frac{\sin \theta_i}{\upsilon_i}, \tag{28}$$

where

$$\kappa_i \upsilon_i = \omega, \text{ at } x_3 = 0 \ (i = 1 - 4), \tag{29}$$

$$\upsilon_0 = \begin{cases} \upsilon_1, & \text{incident LD} - \text{wave} \\ \upsilon_2, & \text{incident LVVF} - \text{wave} \\ \upsilon_3, & \text{incident T} - \text{wave} \\ \upsilon_4, & \text{incident MR} - \text{wave} \end{cases}$$

Considering the phase of the reflected waves and using the equations (28)-(29), we can write,

$$\frac{\cos \theta_j}{\upsilon_j} = \left[\left(\frac{\upsilon_0}{\upsilon_j} \right)^2 - \sin^2 \theta_0 \right]^{\frac{1}{2}}. \tag{30}$$

As given by Schoenberg [26], we can write,

$$\frac{\cos \theta_j}{\upsilon_j} = \frac{\cos \overline{\theta}_j}{\overline{\upsilon}_j} + \iota \frac{c_j}{2\pi \upsilon_0}, \qquad (j = 1 - 4),$$

$$\frac{\cos \overline{\theta}_j}{\overline{\upsilon}_j} = \frac{1}{\upsilon_0} R_e \left\{ \left[\left(\frac{\upsilon_0}{\upsilon_j} \right)^2 - \sin^2 \theta_0 \right]^{\frac{1}{2}} \right\}, \quad c_j = 2\pi I_m \left[\left(\frac{\upsilon_0}{\upsilon_j} \right)^2 - \sin^2 \theta_0 \right]^{\frac{1}{2}},$$

where $\overline{\upsilon}_j$ and $\overline{\theta}_j$ denote the real phase speed and the angle of reflection respectively. c_j represent the attenuation in a depth and it is assumed to be equal to the wavelength of the incident wave i.e. $(2\pi \upsilon_0)/\omega$,

$$\frac{\overline{\upsilon}_j}{\upsilon_0} = \frac{\sin \overline{\theta}_j}{\sin \theta_0} \left[\sin^2 \theta_0 + \left[R_e \left([(\upsilon_0 \upsilon_4)^2 - \sin^2 \theta_0]^{\frac{1}{2}} \right) \right]^2 \right]^{\frac{-1}{2}}.$$

Invoking the boundary conditions (23) along the equations (12)-(14), (15) and using the values of $\varphi, q, \psi,$ and ϕ_2 from equations (24)-(27) along with equation (30), we obtained following system of equations as

$$\sum b_{ij} R_j = Y_j, \qquad (i, j = 1 - 4), \tag{31}$$

$$b_{1p} = -d_p \left[\left[a_8 \left(\frac{\upsilon_p}{\upsilon_0} \right)^2 \sin^2 \theta_0 + a_9 \left(\frac{\upsilon_p}{\upsilon_0} \right)^2 \left[\left(\frac{\upsilon_0}{\upsilon_p} \right)^2 - \sin^2 \theta_0 \right] \right] \kappa_p^2 + a_{10} - \kappa_p d_p S_1 \left[\left(\frac{\upsilon_0}{\upsilon_p} \right)^2 - \right. \right.$$

$$\left. \left. \sin^2 \theta_0 \right]^{\frac{1}{2}} \right],$$

$$b_{1q} = f_p \sin\theta_0 \left[\kappa_q^2 (a_8 - a_9) \left(\frac{\upsilon_q}{\upsilon_0}\right)^2 \left[\left(\frac{\upsilon_0}{\upsilon_q}\right)^2 - \sin^2\theta_0\right]^{\frac{1}{2}} - \kappa_q S_1 \frac{\upsilon_q}{\upsilon_0}\right],$$

$$b_{2p} = -d_p \kappa_p^2 \sin\theta_0 (a_{11} + 1) \left(\frac{\upsilon_p}{\upsilon_0}\right)^2 \left[\left(\frac{\upsilon_0}{\upsilon_p}\right)^2 - \sin^2\theta_0\right]^{\frac{1}{2}} - d_p \kappa_p S_2 \frac{\upsilon_p}{\upsilon_0} \sin\theta_0,$$

$$b_{2q} = f_p \kappa_q^2 \left[a_{11} \left(\frac{\upsilon_q}{\upsilon_0}\right)^2 \left[\left(\frac{\upsilon_0}{\upsilon_q}\right)^2 - \sin^2\theta_0\right] - \left(\frac{\upsilon_q}{\upsilon_0}\right)^2 \sin^2\theta_0 \right] - a_{12} + f_p \kappa_q S_2 \frac{\upsilon_q}{\upsilon_0} \left[\left(\frac{\upsilon_0}{\upsilon_q}\right)^2 - \right.$$

$$\left. \sin^2\theta_0\right]^{\frac{1}{2}},$$

$$b_{3p} = \iota\kappa_q \frac{\upsilon_q}{\upsilon_0} \left[\left(\frac{\upsilon_0}{\upsilon_q}\right)^2 - \sin^2\theta_0\right]^{\frac{1}{2}} + \iota S_3, \quad b_{3q} = 0,$$

$$b_{4p} = \iota\kappa_p \frac{\upsilon_p}{\upsilon_0} \left[\left(\frac{\upsilon_0}{\upsilon_p}\right)^2 - \sin^2\theta_0\right]^{\frac{1}{2}}, \quad b_{4q} = 0, \quad (p = 1,2), (q = 3,4),$$

where $R_1, R_2, R_3,$ and R_4 are the amplitude ratios of reflected LD-wave, LVVF-wave, T-wave, and MR-wave making an angle $\theta_1, \theta_2, \theta_3,$ and θ_4 respectively as shown in Fig. 1 and are given by

$$R_1 = \frac{A_1}{A^*}, \quad R_2 = \frac{A_2}{A^*}, \quad R_3 = \frac{B_1}{A^*}, \quad R_1 = \frac{B_2}{A^*}.$$

For incident LD-wave, $A^* = A_{01}$,
$$Y_1 = -b_{11}, \quad Y_2 = b_{21}, \quad Y_3 = b_{31}, \quad Y_4 = b_{41}.$$
For incident LVVF-wave, $A^* = A_{02}$,
$$Y_1 = -b_{12}, \quad Y_2 = b_{22}, \quad Y_3 = b_{32}, \quad Y_4 = b_{42}.$$
For incident T-wave, $A^* = B_{01}$,
$$Y_1 = b_{13}, \quad Y_2 = -b_{23}, \quad Y_3 = b_{33}, \quad Y_4 = b_{43}.$$
For incident MR-wave, $A^* = B_{02}$,
$$Y_1 = b_{14}, \quad Y_2 = -b_{24}, \quad Y_3 = b_{34}, \quad Y_4 = b_{44}.$$

6. Particular cases

Elastic medium with the void. If $\alpha = \beta = \gamma = K = 0$, then the above results reduce to elastic media with void having the following changes:
$$(v^4 + A_{01}v^2 + A_{02})(\varphi, q) = 0,$$
$$(v^2 - a_2)\psi = 0,$$
where
$$A_{01} = \frac{-(a_4 a_{16} - a_{14} + (a_{13} + 1)\omega^2 + \iota\omega a_{15})}{\omega^2 - a_{14} + \iota\omega a_{15}}, \quad A_{02} = \frac{a_{13}\omega^2}{\omega^2 - a_{14} + \iota\omega a_{15}}, \quad a_2 = \frac{\mu}{\rho c_1^2}, \quad a_9 = \frac{\lambda + 2\mu}{\mu}.$$

Micropolar elastic media. If $\alpha^* = \beta^* = \xi^* = \omega^* = \kappa^* = 0$, then results for reflected waves deduce for micropolar elastic media and following changes are observed,
$$(v^2 - 1)\varphi = 0,$$
$$(v^4 + A_{03}v^2 + A_{04})(\psi, \phi_2) = 0,$$
where
$$A_{03} = \frac{a_2 a_7 - a_3 a_6 - (a_5 + a_2)\omega^2}{\omega^2 - a_7}, \quad A_{04} = \frac{a_2 a_5 \omega^2}{\omega^2 - a_7}.$$

The above results tally with those obtained by Zhang et al. [22] after substituting appropriate values of the parameters.

7. **Numerical result and discussion**

Following are values of micropolar parameters for numerical computation given by Eringen [27], physical constants are given by [16],

$\lambda = 9.4 \times 10^{10} \text{Nm}^{-2}, \mu = 4 \times 10^{10} \text{Nm}^{-2}, \quad K = 1.0 \times 10^{10} \text{Nm}^{-2},$
$\gamma = 0.779 \times 10^{-9} \text{N}, \quad \hat{\jmath} = 0.2 \times 10^{-19} \text{m}^2, \rho = 1.74 \times 10^3 \text{ Kgm}^{-3}.$

The values of the void parameters are taken as

$\alpha^* = 3.688 \times 10^{-9} \text{ N}, \beta^* = 1.1384 \times 10^{10} \text{ Nm}^{-2}, \quad \xi^* = 1.147 \times 10^{10} \text{ Nm}^{-2},$
$\kappa^* = 1.175 \times 10^{-19} \text{m}^2, \omega^* = 0.0787 \times 10^{-1} \text{ Nsm}^{-2}.$

A comparison of values of the amplitude ratios of different reflected waves against the angle of incidence θ_0 is represented graphically for micropolar non-free surface i.e. $S_1 = S_2 = S_3 = 0.5$ (with the void and without void) and for free surface i.e. $S_1 = S_2 = S_3 = 0$ (with the void and without void). The computation for micropolar non-free surface (MNFS) without void is represented by a small dashed line and for micropolar non-free surface (MVNFS) with the void is represented by a small dashed line with center symbols triangle (Δ) respectively. The computation for micropolar free surface (MFS) without void is represented by a solid line and for micropolar free surface (MVFS) with the void is represented by solid with center symbols diamond ($\diamond$) respectively.

Longitudinal displacement (LD)-Wave. Figure 2 demonstrates the trend of $|\mathbf{R_1}|$ vs. θ_0. It is noticed that the magnitude of $|\mathbf{R_1}|$ shows steady state behavior for all the considered cases. It is also observed that in most of the intervals, the magnitude of the values of $|\mathbf{R_1}|$ is slightly greater for MVFS & MVNFS in comparison to MFS & MVFS which depicts the impact of void parameters on amplitude ratios.

Figure 3 depicts the variation of $|R_2|$ vs. θ_0. It is observed that at the beginning, the value of $|R_2|$ for MVFS & MVNFS have greater magnitude as compared with MFS & MNFS respectively but with an increase in θ_0, the trend reversed.

Figure 4 exhibits the plot of $|R_3|$ vs. θ_0. It is noticed that the behavior of $|R_3|$ for all the considered cases follows a similar trend with a significant difference in their magnitude but the magnitude of $|R_3|$ for MFS is higher as compared to other considered cases.

From Figure 5, it is noticed that the value of $|R_4|$ for MVFS and MVNFS increases in the first half of the interval, and later on, the value decreases, and the magnitude of $|R_4|$ is more for MVFS as compared to MVNFS and this difference in magnitude shows the impact of stiffnesses on amplitude ratios.

Fig. 2. Variation of Amplitude ratio $|R_1|$ for LD wave

Fig. 3. Variation of Amplitude ratio $|R_2|$ for LD wave
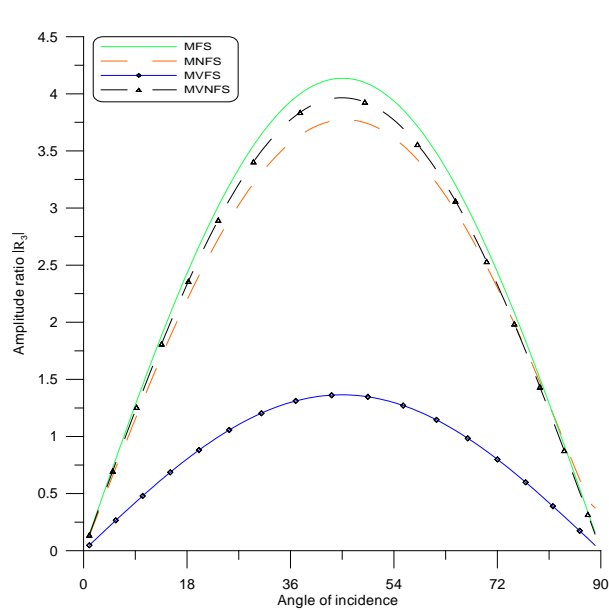
Fig. 4. Variation of Amplitude ratio $|R_3|$ for LD wave

Fig. 5. Variation of Amplitude ratio $|R_4|$ for LD wave

Longitudinal void volume fraction (LVVF)-Wave. The effect of the stiffnesses is notable on amplitude ratios from Fig. 6 in which the value of $|R_1|$ decreases for MVNFS and MVFS as θ_0 increases. It is also noticed that magnitude of $|R_1|$ is greater for MVNFS in comparison to those observed for MVFS.

Figure 7 depicts the variation of $|R_2|$ vs. θ_0. It is noticed that $|R_2|$ follows a similar trend for MVFS and MVNFS i.e. first increases and attains its maximum value at $\theta_0 = 24^o$, then starts decreasing as θ_0 increases. The magnitude of $|R_2|$ is more for MVNFS when compared with MVFS which depicts that stiffnesses play a vital role in amplitude ratios.
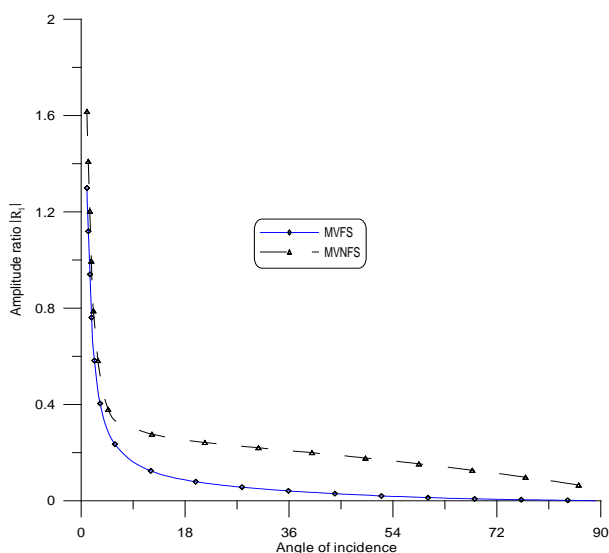
Fig. 6. Variation of Amplitude ratio $|R_1|$ for LVVF wave
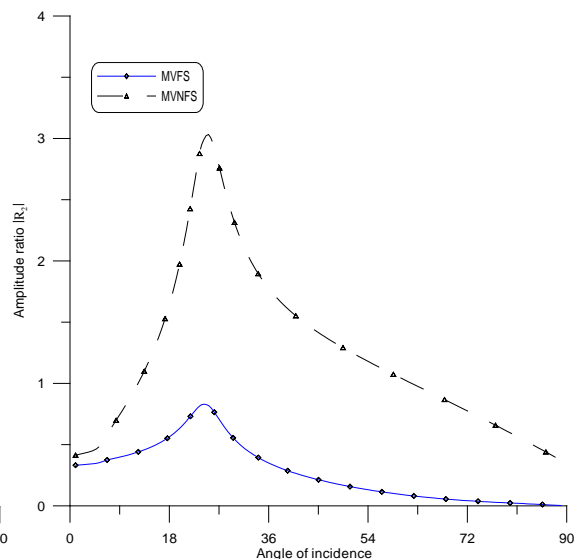
Fig. 7. Variation of Amplitude ratio $|R_2|$ for LVVF wave

Figure 8 shows the variation of amplitude ratio $|R_3|$ vs. θ_0. It is seen that the value of $|R_3|$ for MVNFS & MVFS decreases in the entire range except when $0^o \leq \theta_0 \leq 9^o$, the magnitude of the values of $|R_3|$ are greater for MVNFS in comparison to those obtained for MVFS.

From Figure 9 it is observed that the value of $|R_4|$ for MVNFS decreases for small values of θ_0 and as θ_0 increases, $|R_4|$ shows steady behavior for both MVFS & MVNFS. Due to the presence of stiffness the magnitude of the values of $|R_4|$ for MVNFS is smaller as compared to MVFS.
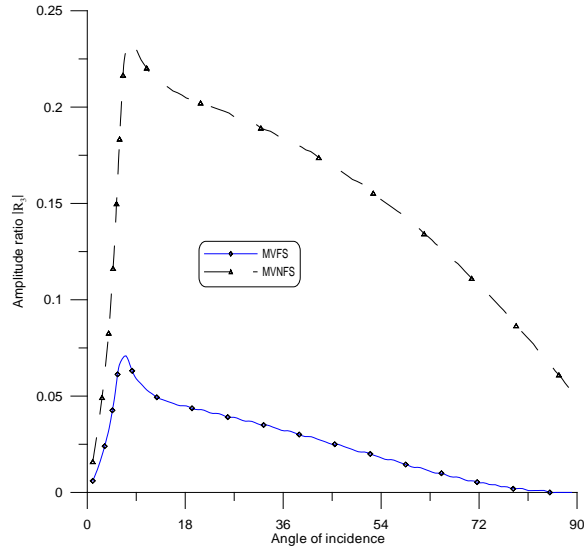
Fig. 8. Variation of Amplitude ratio $|R_3|$ for LVVF wave
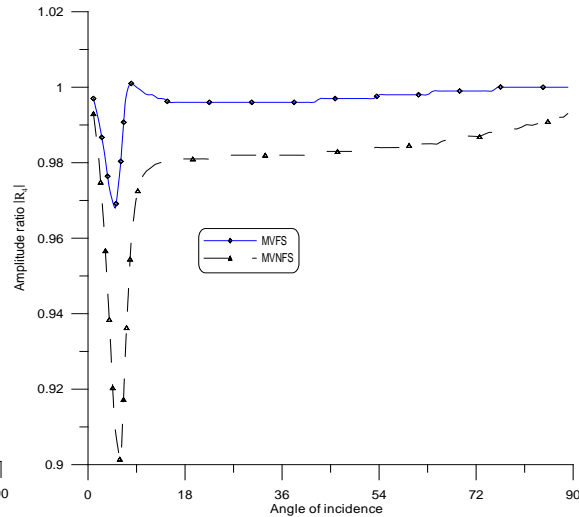
Fig. 9. Variation of Amplitude ratio $|R_4|$ for LVVF wave

Transverse (T)-Wave. Figure 10 depicts the variation of $|R_1|$ vs. θ_0. It is noticed that in absence of void effect i.e. for MFS & MNFS the value of $|R_1|$ shows a decreasing trend in the entire range whereas for MVFS and MVNFS, it shows a vice-versa trend in the entire interval except when $0^o \leq \theta_0 \leq 10^o$.

Figure 11 shows the variation of $|R_2|$ vs. θ_0. It is seen that $|R_2|$ shows ascending trend for MFS in the first half of the interval and vice-versa trends are noticed in the left over the interval whereas due to the presence of stiffnesses, $|R_2|$ for MNFS shows an increasing trend in $0^o \leq \theta_0 \leq 18^o$ and descending behavior in the rest of the interval. It is also observed that $|R_2|$ shows steady state behaviour for MVFS & MVNFS and increases sharply as $\theta_0 \geq 80^o$.
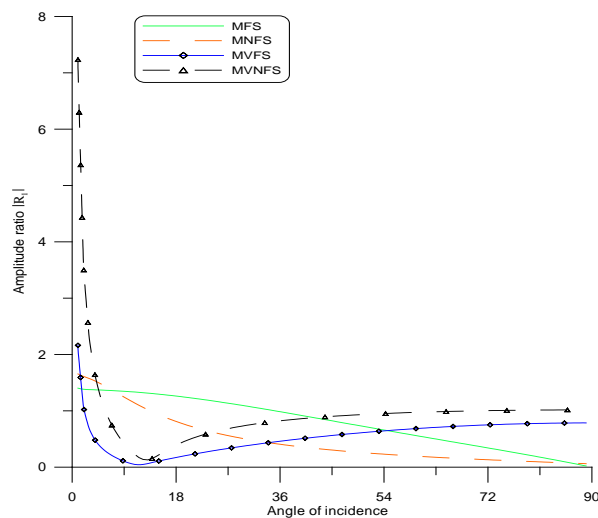
Fig. 10. Variation of Amplitude ratio $|R_1|$ for T wave
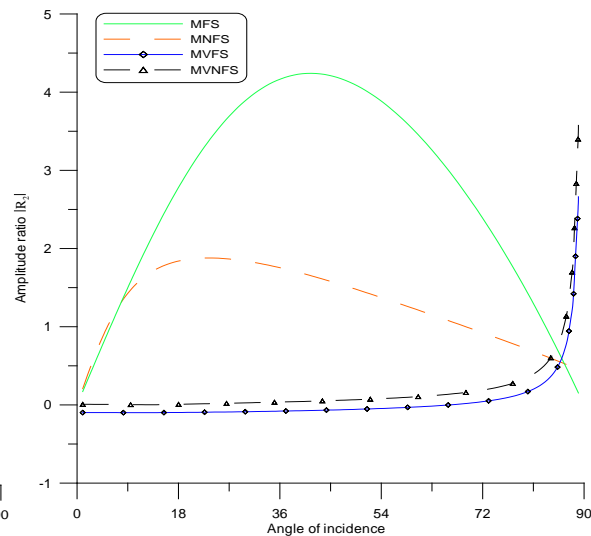
Fig. 11. Variation of Amplitude ratio $|R_2|$ for T wave

Figure 12 depicts the variation of $|R_3|$ vs. θ_0. The value of $|R_3|$ for MFS and MNFS shows descending behavior in the first half of the interval and then increases in the rest half of the interval, whereas $|R_3|$ follows a similar trend for MVFS and MVNFS i.e. increases near the boundary and decreases afterward, magnitude of $|R_3|$ is greater for MVFS.

From Figure 13, it is noticed that the value of $|R_4|$ for MVNFS and MVFS decreases for $0^\text{o} \leq \theta_0 \leq 10^\text{o}$, and the magnitude of $|R_4|$ for both the cases shows ascending trend for the rest of the interval. It is also noticed that the magnitude of $|R_4|$ for MVFS is more than that of MVNFS.
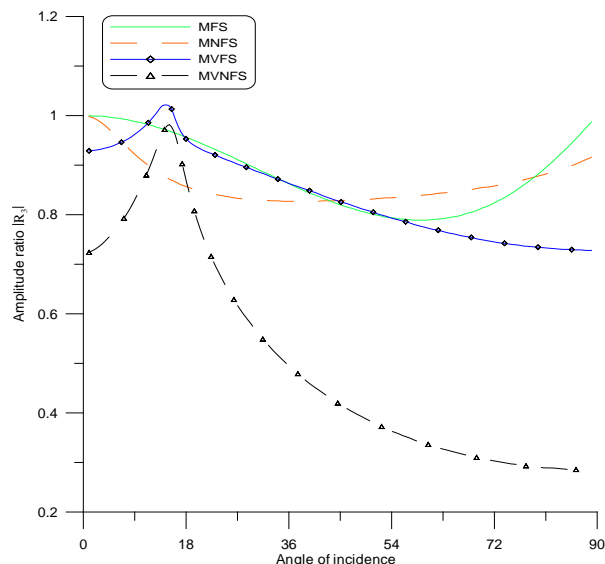
Fig. 12. Variation of Amplitude ratio $|R_3|$ for T wave
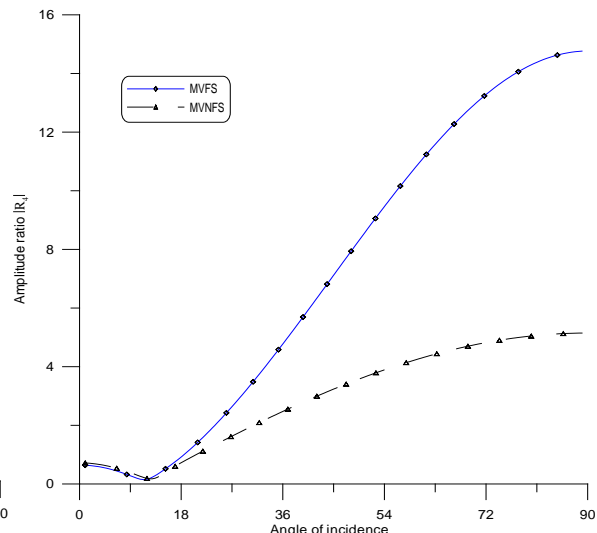
Fig. 13. Variation of Amplitude ratio $|R_4|$ for T wave

Micro-rotational (MR)-Wave. Figure 14 depicts the variation of $|R_1|$ vs. θ_0. It is observed that the value of $|R_1|$ for MFS and MNFS shows small variations about the origin in the interval $0^\text{o} \leq \theta_0 \leq 80^\text{o}$ and then increases left over the interval whereas the trend of $|R_1|$ for MVFS and MVNFS is increasing in nature due to the presence of stiffness parameters.

In Figure 15, it is noticed that the value of $|R_2|$ shows a steady state for all the considered cases in $0^\text{o} \leq \theta_0 \leq 50^\text{o}$ and as θ_0 increases, $|R_2|$ for MVFS & MVNFS shows decreasing behavior while $|R_2|$ for MFS & MNFS shows the opposite trend as observed for MVFS & MVNFS.

Figure 16 depicts the value of $|R_3|$ for MVNFS and MVFS increases in the $0^\text{o} \leq \theta_0 \leq 54^\text{o}$ and decreases in the remaining range, the magnitude of MVNFS is more than MVFS which reveals the impact of the non-free surface on amplitude ratios. A similar impact of stiffnesses can be observed for the values of MNFS and MFS as the magnitude of $|R_3|$ for MNFS is more than MFS with ascending behavior.

From Figure 17, it is noticed that initially the value of $|R_4|$ for MVFS and MVNFS increases and it reaches the maximum at $\theta_0 = 54^\text{o}$ and then decreases with an increase in θ_0, the magnitude of amplitude ratio $|R_4|$ for MVFS is more than that of MVNFS.
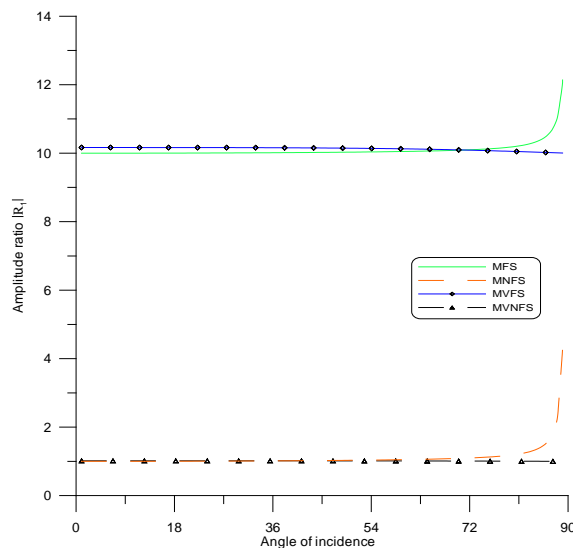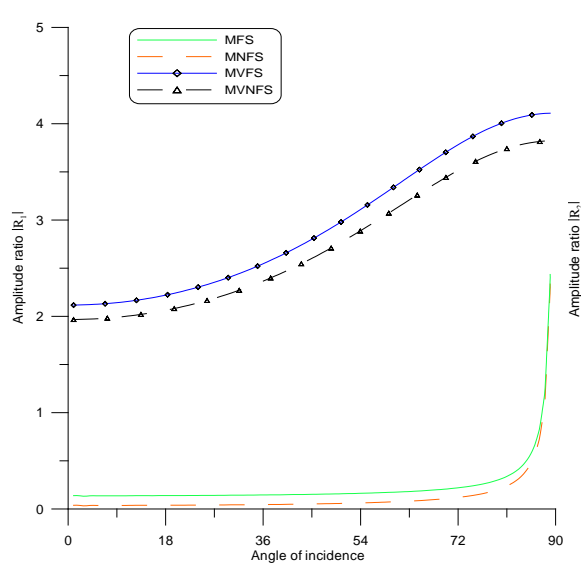
Fig. 14. Variation of Amplitude ratio $|R_1|$ for MR wave
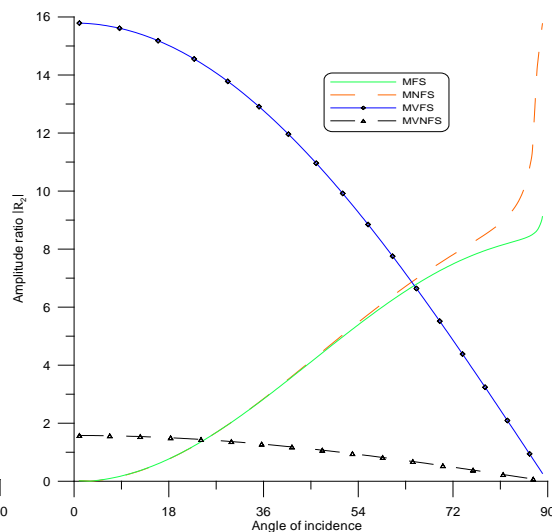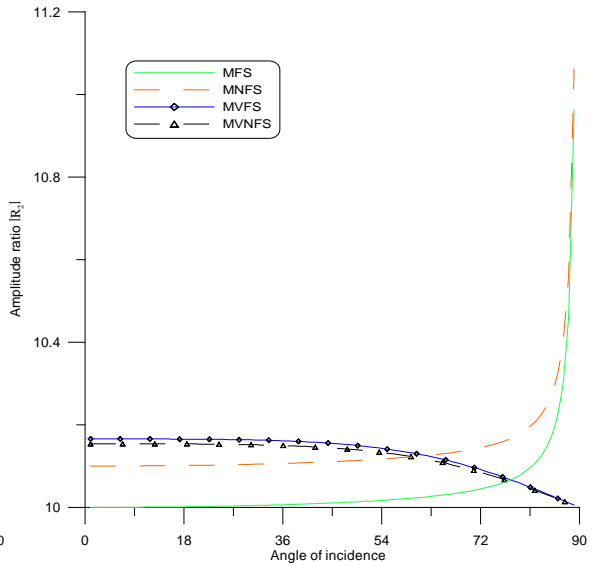

Fig. 15. Variation of Amplitude ratio $|R_2|$ for MR wave

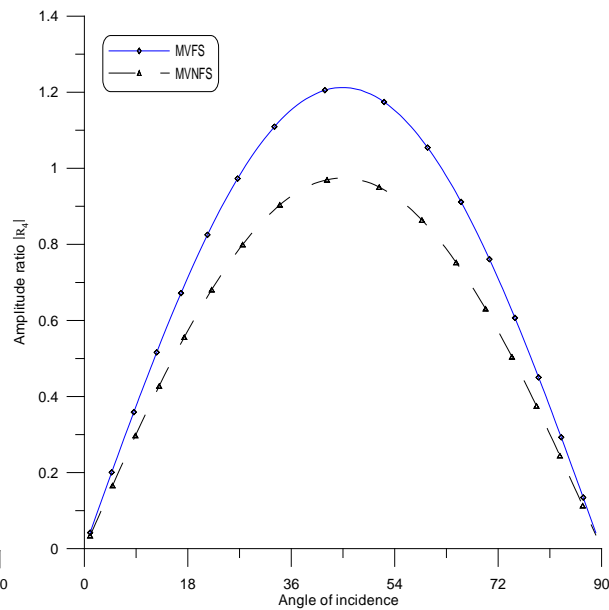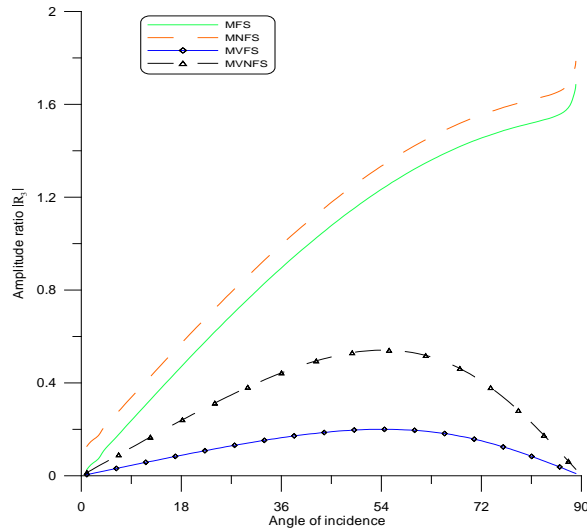**Fig. 16.** Variation of Amplitude ratio $|R_3|$ for MR wave
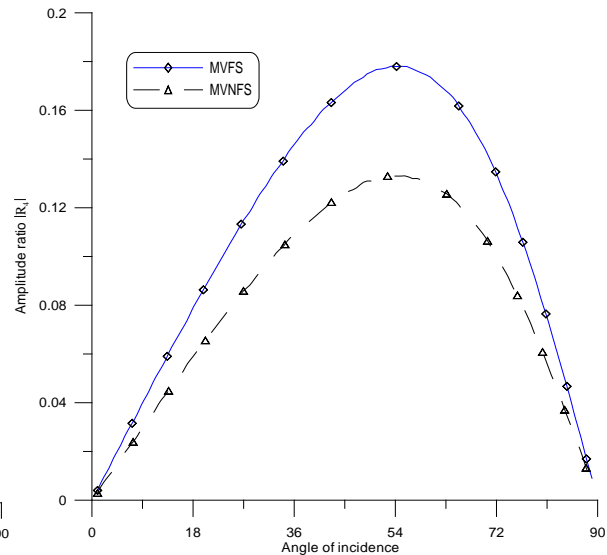
Fig. 17. Variation of Amplitude ratio $|R_4|$ for MR wave

8. Conclusion

In the present article, the phenomenon of reflection of the elastic wave at a non-free surface with a micropolar elastic constraint with void has been studied. The amplitude ratios of four reflected waves namely LD-wave, LVVF-wave, T-wave, and MR-wave are calculated numerically. The impact of stiffnesses and void parameters on these amplitude ratios are demonstrated graphically. From the numerically computed results following observations are made:

(a) The results indicate that due to the presence of stiffnesses, the magnitude of $|R_1|$ and $|R_2|$ is smaller as compared to those obtained for free surface, whereas in the case of $|R_3|$ and $|R_4|$, it shows similar oscillatory behaviour with a significant difference in their magnitude when LD-wave is incident.

(b) It is observed that when LVVF-wave is incident, the magnitudes of $|R_1|$, $|R_2|$, and $|R_3|$ in the case of free surface are smaller while $|R_4|$ shows a vice-versa trend which depicts the significant impact of stiffnesses on amplitude ratios.

(c) In the case of incident T-wave, it is observed that void parameters play a vital role in amplitude ratios as $|R_1|$ and $|R_2|$ show opposite behaviour for MVFS & MVNFS as compared to MFS & MNFS, while in the case of $|R_3|$ and $|R_4|$ they show similar behavior in the entire range.

(d) It is seen that when MR-wave is an incident, void and stiffness parameters play a major role as the magnitude of $|R_1|$, $|R_2|$, and $|R_4|$ for MVFS are greater as compared to MVNFS. It is also noticed that in absence of a void parameter trends are reversed i.e. values of $|R_2|$ and $|R_3|$ for the non-free surface are greater as compared to the free surface.

The physical application of this model can be found in the area of seismology where the results are helpful for the exploration of valuable materials such as minerals, crystals, and metals. The results are also useful in geophysics and earthquake engineering.

References

[1] Abd-Alla AN, Abbas IA. A problem of generalized Magneto-thermoelasticity for an infinitely long, perfectly conducting cylinder. *Journal of Thermal Stresses.* 2002;25(11): 1009-1025.

[2] Abbas IA, Abd-Alla, AN, Othman MIA. Generalized Magneto-thermoelasticity in a Fiber-Reinforced Anisotropic Half-Space. *International Journal of Thermophysics.* 2011;32: 1071-1085.

[3] Abbas IA, Abo-Dahab SM. On the Numerical Solution of Thermal Shock Problem for Generalized Magneto-Thermoelasticity for an Infinitely Long Annular Cylinder with Variable Thermal Conductivity. *Journal of Computational and Theoretical Nanoscience.* 2014;11(3): 607-618.

[4] Hobiny AD, Abbas IA. A study on photothermal waves in an unbounded semiconductor medium with cylindrical cavity. *Mechanics of Time-Dependent Materials.* 2017;21: 61-72.

[5] Hobiny A, Abbas IA. Analytical solutions of photo-thermo-elastic waves in a non-homogenous semiconducting material. *Results in Physics.* 2018;10: 385-390.

[6] Vlase S, Marin M, Ochsner A, Scutaru ML. Motion equation for a flexible one-dimensional element used in the dynamical analysis of a multibody system. *Continuum Mechanics and Thermodynamics.* 2019;31: 715-724.

[7] Omar AA, Shawagfeh N. Application of reproducing kernel algorithm for solving dirichlet time-fractional diffusion-gordon types equations in porous media. *Journal of Porous Media.* 2019;22(4): 411-434.

[8] Saeed T, Abbas IA, Marin M. A GL Model on Thermo-Elastic Interaction in a Poroelastic Material Using Finite Element Method. *Symmetry.* 2020;12(3): 488.

[9] Nunziato JW, Cowin SC. A non-linear theory of elastic material with voids. *Archives of Rational Mechanics and Analysis.* 1979;72: 175-201.

[10] Cowin SC, Nunzaito JW. Linear elastic material with voids. Journal of Elasticity 1984;13: 125-147.

[11] Kumar R, Choudhary S. Interaction due to mechanical sources in micropolar elastic medium with voids. *Journal of Sound and Vibration.* 2003;266: 889-904.

[12] Tomar SK. Wave propagation in a micropolar elastic plate with voids. *Journal of Vibration and Control.* 2005;11: 849-863.

[13] Mondal AK, Acharya DP. Surface waves in a micropolar elastic solid containing voids. *Acta Geophysica.* 2006;54(4): 430-452.

[14] Hsia SY, Cheng JW. Longitudinal plane wave propagation in elastic-micropolar porous media. *Japanese Journal of Applied Physics.* 2006;45(3A): 1743-1748.

[15] Mahmoud SR, Abd-Alla AM, El-Sheikh MA. Effect of the rotation on wave motion through cylindrical bore in a micropolar porous medium. *International Journal of Modern Physics B.* 2011;25(20): 2713-2728.

[16] Singh R, Singh K. Eigen value approach in micropolar elastic medium with voids. International. *Journal of Applied Mechanics and Engineering*. 2013;18(2): 521-536.

[17] Marin M. An approach of a heat-flux dependent theory for micropolar porous media. *Meccanica*. 2016;51: 1127-1133.

[18] Lianngenga, R.: Effect of inertial coefficients in the propagation of plane waves in micropolar porous materials. *International Journal of Computational Materials*. 2017;6(1): 1750007.

[19] Kumari N, Kaliraman V. Analysis of wave propagation at an imperfect boundary between micropolar elastic solid and micropolar porous elasticsolid. *International Journal of Mathematics Trends and Technology*. 2018;53(1): 22-37.

[20] Marin M, Chirila A, Ochsner A, Vlase S. About finite energy solutions in thermoelasticity of micropolar bodies with voids. *Boundary Value Problems*. 2019;2019: 89.

[21] Alharbi AM, Abd-Elaziz EM, Othman MIA. Effect of temperature-dependent and internal heat source on a micropolar thermoelastic medium with voids under 3PHL model. *ZAMM*. 2021;101(6): e202000185.

[22] Zhang P, Wei P, Tang Q. Reflection of micropolar elastic waves at the non-free surface of a micropolar elastic half-space. *Acta Mechanica*. 2015;226: 2925-2937.

[23] Singh B. Reflection of thermoelastic waves at a non-free thermally insulated surface. *International Journal of Applied Science and Engineering*. 2018;15(3): 149-161.

[24] Eringen AC. Theory of micropolar elasticity in fracture. *Academic Press*. 1968;2: 621-729.

[25] Iesan DA. Shock waves in micropolar elastic materials with voids. *Analele Stiintifice ale Universitatu Al. l. Cuzadin lasi Seria Noua Sectiunea la matematica*. 1985;31: 177-186.

[26] Schoenberg M. Transmission and reflection of plane waves at an elastic viscoelastic interface. *Geophysical Journal International*. 1971;25(1-3): 35-47.

[27] Eringen AC. Plane waves in non-local micropolar elasticity. *International Journal of Engineering Science*. 1984;22: 1113-1121.

THE AUTHORS

Kaushal Sachin
e-mail: sachin_kuk@yahoo.co.in
ORCID: 0000-0002-0873-0046

Kumar Rajneesh
e-mail: rajneesh_kuk@rediffmail.com
ORCID: 0000-0000-0000-0001

Kochar Arun
e-mail: arunkochar8@gmail.com
ORCID: 0000-0002-3527-8497

Comparative study of grain fragmentation in iron during cold and warm deformation by uniaxial tension

N.Yu. Zolotorevsky[1,3✉], V.V. Rybin[1,3], E.A. Ushanova[2,3], A.N. Matvienko[1,3],

V.N. Perevezentsev[3]

[1]Peter the Great St. Petersburg Polytechnic University, 29 Politechnicheskaya St., St. Petersburg, 195251, Russia

[2]NRC "Kurchatov Institute" - CRISM "Prometey", 49 Shpalernaya str., St. Petersburg, Russia, 191015

[3]Institute of mechanical engineering problems RAS – branch of the Federal State Budgetary Scientific

Institution "Federal Research Center Institute of Applied Physics of the Russian Academy of Science",

Belinskogo 85, 603024 Nizhny Novgorod

✉ zolotorevsky@phmf.spbstu.ru

Abstract. The microstructure fragmentation in iron tensile specimens deformed at room temperature and 600°C has been studied by means of EBSD. The aim of the research was to characterize and compare the patterns of fragmentation associated with the appearance and accumulation of deformation-induced high-angle boundaries (HABs). The microstructure was examined on the longitudinal section of necked specimens, in locations corresponding to various true strains from 0.5 to 1.6. It has been shown that a length of deformation-induced boundaries per unit area is characterized by rapid growth at small strains. With further straining, it ceases to grow in a low-angle interval of misorientations, whereas continues to grow in a high-angle interval. The accumulation of HABs occurs considerably faster during cold deformation, mainly through the formation of transition zones between grain-scale deformation bands.
Keywords: iron, plastic deformation, dynamic recrystallization, microstructure, EBSD

1. Introduction

Large plastic deformation of metals leading to their fragmentation [1-3], i.e. the subdivision of initial grains into misoriented fragments, has gained a lot of interest, being a promising approach to obtaining a structural state with extraordinary mechanical properties [4-5]. As a result, a huge number of studies have been carried out in order to characterize ultrafine-grained microstructures produced by various methods of severe plastic deformation [4,6]. At the same time, an initial stage of fragmentation, at which the first deformation-induced high angle boundaries (HABs) appear and start to accumulate, has received much less attention in research.

According to studies by Rybin and co-workers [1], the first fragment boundaries stand up against previously formed cellular substructure because of their relatively high misorientations and more dense constitution. It has been shown that misorientations of cell boundaries remain at the level of a few degrees, whereas misorientations of the fragment boundaries progressively increase with strain so that HABs are formed eventually [1,7,8]. Given that different lattice rotations of neighboring fragments are caused by different slip systems activity occurring inside them, the fragment boundaries are called geometrically necessary boundaries (GNBs) [9]; these two terms are further used as equivalents. The evolution of misorientation angle distribution both at cell and fragment boundaries has been extensively studied by Hughes and Hansen et al [7,10].

The above results were obtained using transmission electron microscopy (TEM), which has been useful in characterizing dislocation structures, in particular, in distinguishing cell and fragment boundaries by their morphology. However, the nature, and especially the scale, of the fragmentation process are often better suited to the investigation by electron backscatter diffraction (EBSD). The latter method gives a panoramic view of grain-scale heterogeneity, which is very characteristic of the microstructure evolution [11-13], and provides much better statistics than TEM when studying crystallographic parameters of the fragmented structures. During the last two decades, the development of microstructural heterogeneity, including the grain-scale orientation gradients and geometrically necessary dislocations, has been extensively examined using EBSD for strains of not more than ~0.5 [14-18]. Meanwhile, the range of true strains from ~0.5 to 2, where the deformation-induced HABs begin to form, has been far less studied, in particular with respect to the effect of deformation temperature [19,20]. The goal of the present study is to move ahead on this issue. The earlier developed method [21], which allows isolating the contribution of deformation-induced HABs to the overall boundary misorientation distribution, has proven useful in addressing this challenge.

Pure iron deformed by tension has been chosen for the present research. The variation of plastic strain along the neck of the specimens allowed us to study the fragmentation developed in the strain range of interest. We examined the microstructure evolution under conditions of cold and warm deformation, at room temperature and 600°C, respectively. The latter temperature was chosen for the warm deformation taking into consideration that, according to the study by Glover and Sellars [22], notable dynamic recrystallization was observed in α-iron only at temperatures above 600°C. Therefore, when making this choice, we expected to avoid the significant influence of discontinuous recrystallization [23] on the microstructure evolution.

2. Materials and Methods

The material used in this study was a commercially pure iron containing ~0.01% of S and ~0.01% Si in solid solutions as well as particles of manganese sulfides and oxides ranging in size from about 0.1 to 1 μm. The cylindrical specimens were deformed in tension at a strain rate of $5 \cdot 10^{-4}$ c^{-1} until fracture, at room temperature (using testing machine 2167 P-50) and at 600°C (using universal hydraulic testing machine BiSS, model Nano). The initial diameters of the gauge region of the specimens were 6 mm and 5 mm for deformation at room temperature and 600°C, respectively. Engineering stress-strain curves are shown in Fig. 1. The yield stress is approximately 155 and 76 MPa for room temperature and 600°C, respectively.

The specimens for microstructure examination were cut along the tensile direction (TD), and further, the longitudinal sections were studied. Figure 2 shows these sections represented schematically. Local true strains in the neck of the specimens were estimated from the local diameter D using the equation $\varepsilon = 2 log \frac{D_0}{D}$, where D_0 is the initial diameter of the specimen. Finite element modeling showed that the local strain near the specimen axis in the first approximation is equal to the average strain of the given section [24].

EBSD mapping was carried out in a scanning electron microscope LYRA 3 XMN RL using Oxford HKL AZtec™ software, on the equipment of the Centre of Shared Use of Scientific Equipment "Composition, structure and properties of structural and functional materials of NRC "Kurchatov Institute" – CRISM "Prometey". Orientation maps represented in what follows are the inverse pole figure (IPF) maps plotted with respect to TD. The analysis of the maps was performed with the help of MTEX software [25]. The percentage of non-indexed points in the EBSD data presented below was less than 18% for the cold deformation and less than 7% for the warm deformation which enabled the sufficiently reliable reconstruction of the deformation structure. The size of the panoramic maps varied from about 350×350 μm to 150×150 μm, while the scanning step size was reduced from 350 nm down to 200 nm with increasing strain. The examined areas are indicated in Fig. 2 by squares together with corresponding local strains. The statistics associated in what follows with the strain "~1" were obtained by averaging the data from the scans related to strains 0.95 and 1.15, while the ones associated with the strain "~1.5" – from the scans related to strains 1.4 and 1.55.
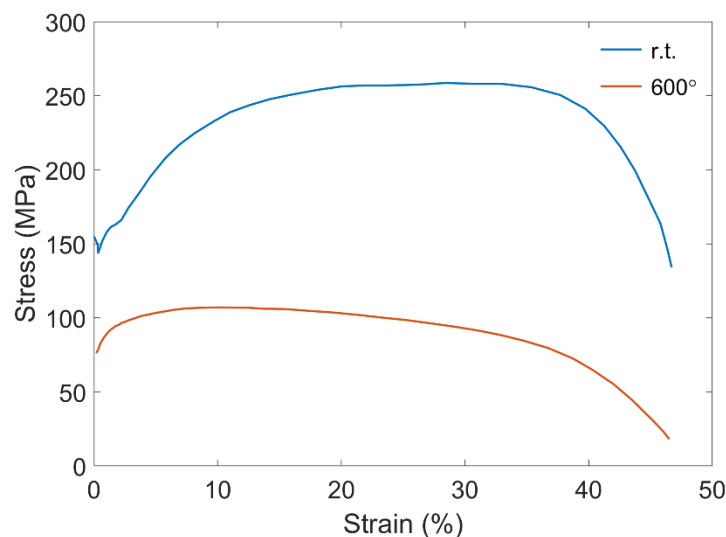
Fig. 1. Engineering stress-strain curves for tensile deformation of iron at room temperature (r.t.) and 600°C. Only plastic strain range is depicted
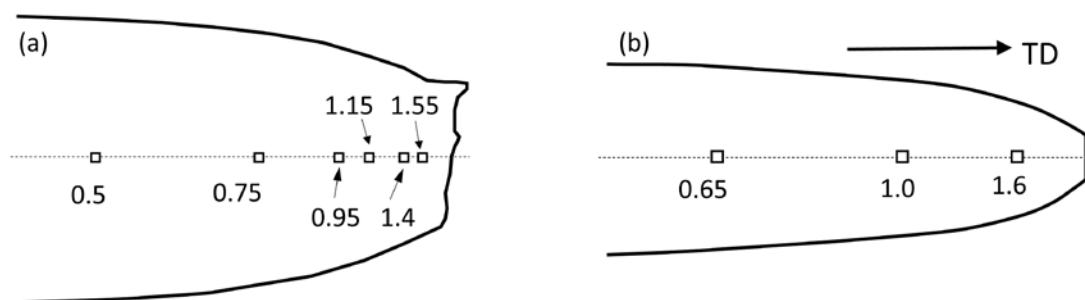
Fig. 2. Schematic drawing of the longitudinal sections of the specimens deformed at room temperature (a) and 600°C (b). Examined regions are depicted by squares, near which local strains are indicated

In order to analyze the evolution of misorientations at deformation-induced boundaries as well as to estimate the fraction of deformation-induced HABs, the earlier proposed method [21] has been used allowing separation of the contribution from the deformation-induced boundaries to the overall misorientation distribution. Its usage is essential for the present

study since it allows assessing the fraction of deformation-induced HABs even when this is of the same order as the fraction of original grain boundaries. The method included the following steps: (i) determination of the misorientation distribution of all boundaries, $l_{tot}(\theta)$, in terms of the boundary length per unit area, (ii) separation of original grain boundaries and determination of their misorientation distribution, $l_0(\theta)$, (iii) obtaining finally the misorientation distribution of DIBs, $l_{DIB}(\theta)$, by subtracting $l_0(\theta)$ from $l_{tot}(\theta)$. This procedure was considered in detail elsewhere [21].

3. Results

Initial microstructure. The as-received condition exhibits nearly equiaxed grains with no deformation substructure inside them (Fig. 3a). The grains are almost randomly oriented (Fig. 3b). An average grain size determined by the linear-intercept method was about 54 μm. Fig. 3a shows that multiple Σ3 boundaries (60° around <111> axis) occur in the undeformed iron. From the 60°-peak in the misorientation angle distribution (Fig. 3b), one can conclude that a fraction of such boundaries in the microstructure is about 12%. The morphology of these "twins" differs, however, from the annealing twins observed in FCC metals, which usually appear as flat grain boundaries or intragranular plates. It should be noted that although annealing twins were previously detected in α-iron, which has been passed slowly through the critical range during cooling, as well as in iron deformed and then recrystallized [26], this phenomenon is still poorly investigated.
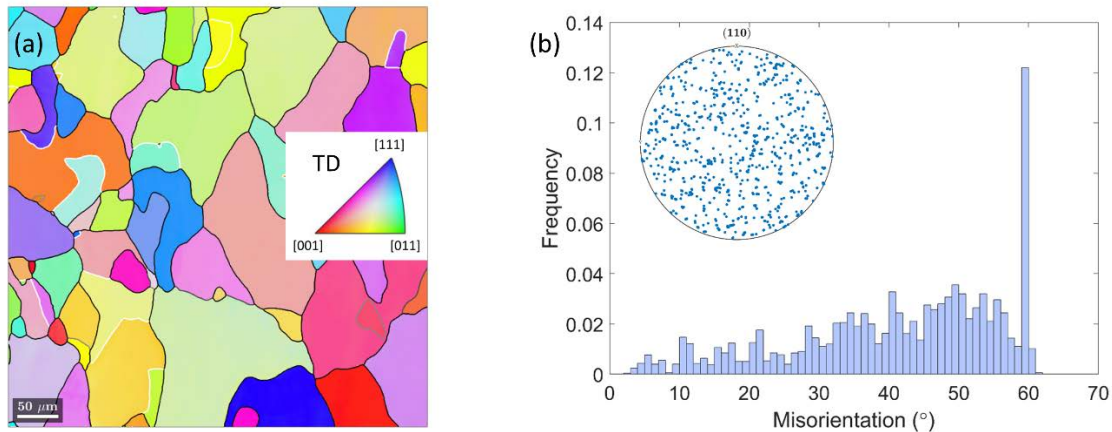
Fig. 3. Typical microstructure of undeformed iron: the inverse pole figure (IPF) map of the microstructure colored with respect to TD (a); the misorientation angle distribution and the texture represented using discrete pole figure (b). Color coding of grain boundaries on the map: random grain boundaries, black; Σ3 boundaries, white

General characterization of microstructures evolution. Figures 4a and 4b show typical deformation microstructures developed at room temperature. A pronounced axial <110> texture develops during tension. It is for this reason that IPF maps colored with respect to TD have a rather uniform coloring in spite of highly misoriented microstructure. The original Σ3 boundaries present in the initial microstructure are strongly distorted by the plastic deformation, however, some of their segments retain a near-twin misorientation in terms of Brandon criterion, that is, their angular deviation from the ideal Σ3 misorientation is smaller than $15°/\sqrt{\Sigma} = 8.66°$. At a strain of 0.5, tension leads to a considerable grain-scale orientation heterogeneity (Fig. 4a). With increasing strain, such a heterogeneity manifests itself in the form of deformation bands [23,27-30] separated from each other by zones of high orientation

gradient, often referred to as "transition bands" [27]. Though the latter is usually the locations where low-angle boundaries are concentrated [28], high-angle ones also form there. At a strain of 1.4 (Fig. 4b), the borders between the deformation bands are mostly HABs, and it is not always easy to distinguish them from the original grain boundaries. Some structural peculiarities associated with the formation of HABs as a result of deformation banding will be considered in the next section.

Compared with cold deformation, dynamic recovery has a much greater impact on the microstructure evolution at 600°C (Figs. 4c and 4d). Nevertheless, for a smaller strain, the morphology of the deformation microstructure looks like that observed after cold deformation, in particular, the grain-scale orientation heterogeneity occurs as well, although to a lesser extent (Fig. 4c). New features evidencing dynamic recrystallization appear at strains of $\varepsilon = 1$ and larger: (i) original grain boundaries develop serrations, and (ii) small new grains form. A region where such grains are concentrated is marked by the rectangle in Fig. 4d.
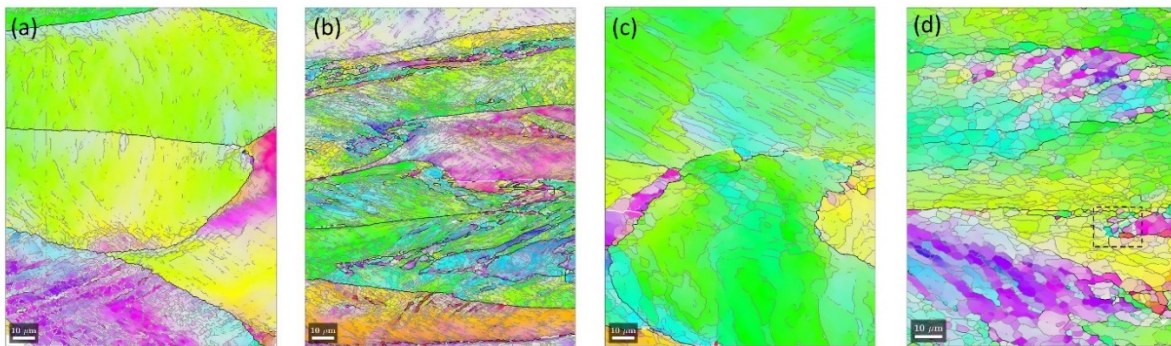
Fig. 4. IPF maps of iron deformed to a strain of 0.5 (a) and 1.4 (b) at room temperature, and to a strain of 0.65 (c) and 1.6 (d) at 600°C. Color-coding of boundaries: $1° < \theta < 45°$, grey; $\theta > 45°$, black; $\Sigma 3$ boundaries according to Brandon criterion, white.
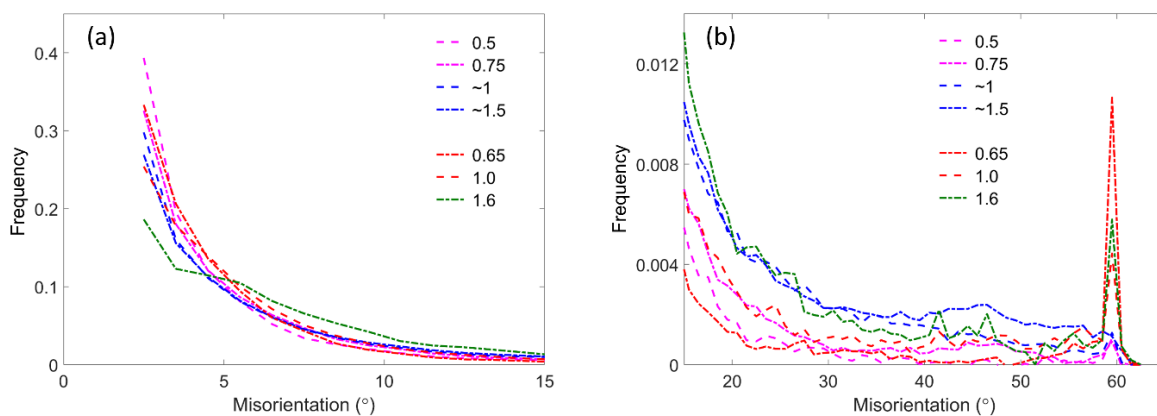
Fig. 5. Effect of strain on misorientation frequency distribution for deformation-induced boundaries in iron deformed by tension at room temperature (blue lines) and 600°C (red lines). True strains are indicated in the legend

The effect of strain on the distribution of misorientations across deformation-induced boundaries is shown in Fig. 5 in the usual way using the frequency $f_{DIB}(\theta)$. The latter was calculated here as $l_{DIB}(\theta)/L_{DIB}$, where $l_{DIB}(\theta)$ is the length of the boundaries having misorientations within the interval $(\theta, \theta+1°)$, and L_{DIB} is the length of all deformation-induced boundaries per unit area. For ease of consideration on one plot, the distributions are shown

using line graphs instead of histograms. Besides, the plot is divided into the low-angle (Fig. 5a) and high-angle parts (Fig. 5b). One can see that the distribution of low-angle boundaries is little dependent on strain, except for the case of warm deformation to $\varepsilon = 1.6$. At the same time, the relative fraction of HABs increases with strain significantly. The integral characteristic of its growth is shown in Fig. 6.
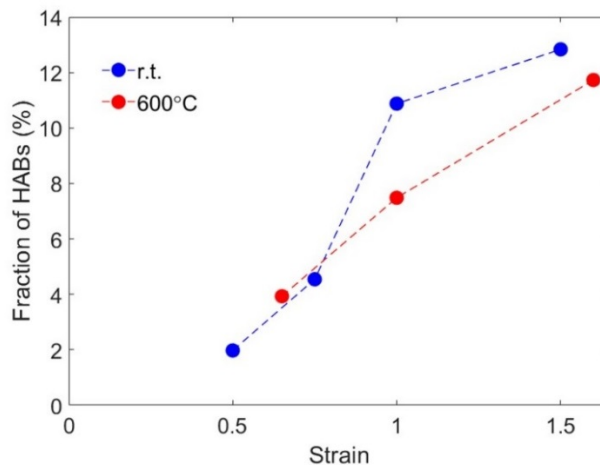
Fig. 6. Effect of strain on the fraction of deformation-induced high-angle boundaries (HABs) in iron deformed by tension at room temperature (r.t.) and 600°C

Figure 7 shows the evolution of misorientation angle distribution represented in terms of the boundary length, $l_{DIB}(\theta)$. This way of presentation allows assessing the total length per unit area ("the specific length") of the boundaries, which fall in a certain angular interval, and not just their relative fraction. One can see that, during cold deformation, $l_{DIB}(\theta)$ increases significantly for all θ at $\varepsilon < 0.75$, but with further straining it almost ceases to grow for $\theta < 15°$. Note that the evolution of the cell structure is well known to stagnate at large strains [1,10], however, in the present case, we are looking at GNB rather than cell wall misorientation distribution. Only for the highest angles of disorientation, $\theta > 40°$, $l_{DIB}(\theta)$ continues to grow substantially at all considered strains. Therefore, the gradual increase of fragment misorientations comes to replace the formation of new fragments as the primary mechanism for fragmentation. The broad peak appearing at angles $\theta > 40°$ at $\varepsilon \sim 1.5$ seems to emerge because mutual lattice rotations of adjacent crystallites exceed the maximal disorientation angle[1] at some boundaries. It is worth noting that, although the relative fraction of deformation-induced HABs reaches only a level of about 12 % (Fig. 6), a ratio of their length to the length of grain boundaries in the initial polycrystalline iron, $L_{DI\ HAB}/L_0$, becomes ~ 3.5 (Fig. 8).

Though the specific length of the boundaries developed at 600°C is considerably lower than after cold deformation, the shape of misorientation angle distribution remains similar up to a strain of 1 (Fig. 7). It changes qualitatively at $\varepsilon = 1.6$ owing to a decrease in the specific length of subboundaries with angles $\theta < 5°$. This occurs, apparently, because of accelerated dynamic recovery that leads to the coarsening of subgrain structure. The specific length of deformation-induced HABs is close to that of original grain boundaries at $\theta > 40°$. At the same time, a peak appears in the misorientation distribution at $\theta \approx 60°$. This peak cannot be related to the original $\Sigma 3$-boundaries, since corresponding 60°-peak (see Fig. 3b) spreads

---

[1] The "disorientation" is defined as a minimum angle relationship between crystallites with regard to all 24 cubic symmetry operations. The highest possible disorientation angle varies from 45 to 62.8° depending on the axis of rotation [31].

owing to additional misorientations induced by a strain [32-34]. Hence, its appearance is an indication of some kind of twinning, which takes place during warm deformation.
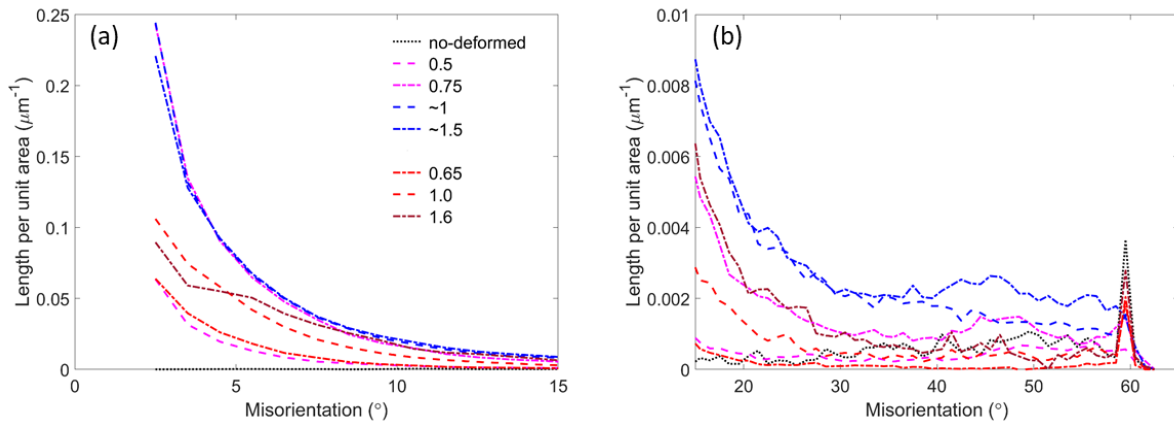
Fig. 7. Effect of strain on misorientation distribution at deformation-induced boundaries represented in terms of boundary length per unit area, in iron deformed by tension at room temperature (blue lines) and 600°C (red lines). The distribution for the initial polycrystalline iron is also presented. True strains are indicated in the legend
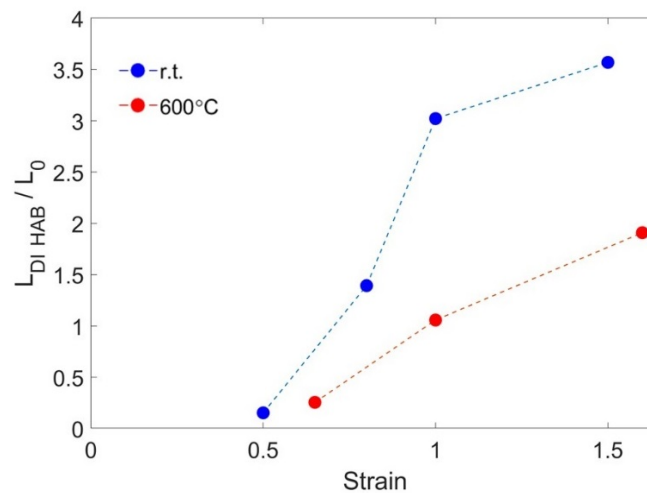
Fig. 8. Effect of strain on the accumulation of HABs in iron deformed by tension at room temperature (r.t.) and 600°C: the ratio of the length of deformation-induced HABs ($L_{DI\ HAB}$) to the length of grain boundaries in the initial polycrystalline iron (L_0)

In general, the accumulation of deformation-induced HABs occurs considerably faster at room temperature than at 600°C in the examined strain range, which is well seen in Fig. 8. In the following sections, the main patterns of HAB formation are considered.

Deformation-induced HABs evolved at room temperature. As noted above, a considerable fraction of HABs is formed within the transition zones developed between the grain-scale deformation bands. It has been shown previously that transition zones of different types occur in tensile strained iron [29,30]. Zones of the first type are similar to ordinary transition bands consisting of low-angle subboundaries, which together provide a high-angle rotation across the band [27]. At the same time, distinct HABs are observed in some parts of such bands. One can suggest that subboundaries appear within the transition band first, and then they merge forming a HAB. In contrast to such narrow transition bands, zones of the second type are wider and more strongly fragmented [30].

Arrays of microbands are also an effective source of deformation-induced HABs in iron according to an assessment made in our earlier work [29]. Unlike so-called microshear bands [8,35], these microbands keep the directionality of the preformed low-angle subboundaries [30], similar to those observed previously in a cold rolled steel [36] or in tantalum alloy [37]. Individual microbands of this type or their small groups can be found in many grains, e.g. Fig. 4b, however, in some grains, such a banding may be the dominant way of in-grain structure evolution. As an example, an array of microbands formed at $\varepsilon = 0.75$ is shown in Fig. 9a (in order to better reproduce the fine structure of this region, it was mapped with a scanning step of 50 μm). These microbands do not propagate through the whole grain but form a peculiar transition zone between regions of relatively uniform but different orientations ("deformation bands"). It is worth noting that misorientation angles up to ~50° are reached at the boundaries crossed by line scan EF (Fig. 9b), despite the quite small strain.
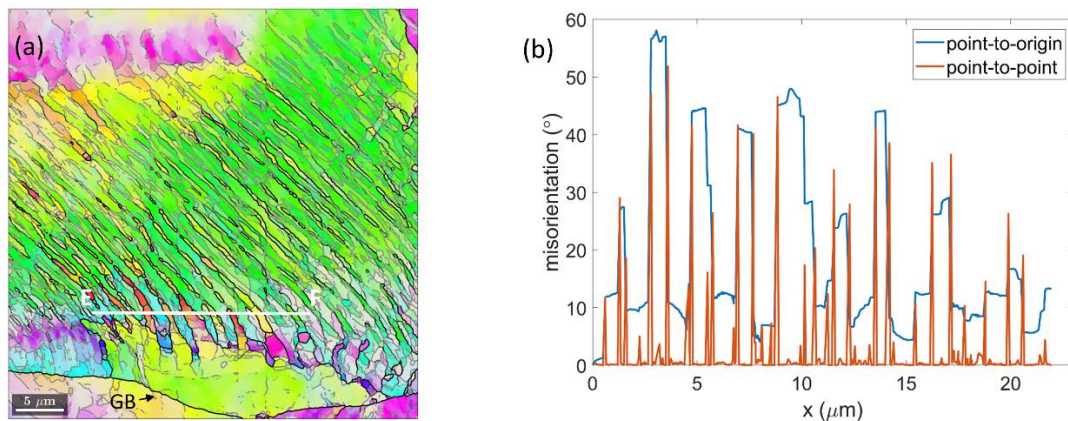
Fig. 9. IPF map of iron deformed at room temperature to a strain of 0.75 (a) and misorientation distribution along segment EF (b). Color-coding of boundaries is the same as in Fig. 4

Deformation-induced HABs evolved at 600°C. Figure 10 shows a region, where characteristic manifestations of dynamic recrystallization take place; some of them are indicated by arrows on the map. The bulging, which is accompanied by the formation of new small grains, is particularly prominent at a grain boundary located on the top of the map (GB1). Such a strong bulging, however, seems to be rare under these deformation conditions. The more usual pattern of nucleation is found at the grain boundary located a little lower (GB2), where a new small grain appears with a limited local migration of the interface. In addition, agglomerations of grains/subgrains with high-angle boundaries form near some original grain boundaries, in particular near grain junctions; one can see an example of such a formation in the lower part of the map in Fig. 10. In these cases, the nucleation of recrystallized grains is rather a result of the evolution of subgrains, namely, the deformation-induced increase in subboundary misorientation. The latter, in its turn, leads to an increase in subboundary mobility and to its local migration [23]. The fundamental fact is that there is no transfer to a long-range growth of new grains: their sizes remain in the order of the neighboring subgrain sizes. Hence, this process may be characterized as continuous dynamic recrystallization [23,38,39].

With increased strain from 1 to 1.6, the character of the microstructure remains the same (Fig. 4), despite the evolution of misorientation distribution (Fig. 7). Namely, the majority of the original grain volume still contains subgrain structure, whereas the sites where new fine grains are concentrated occupy relatively small regions. Such a group of new grains with high-angle boundaries is marked by a rectangle in Fig. 4d. A peak near 60° has been

noted in section 3.1, which remains in the misorientation distribution at all strains. The structural features responsible for this peak can also be found in the area marked in Fig. 4d. They look just like the annealing twins form in the region where dynamic recrystallization occurs. However, these are not plate-like twins specific to dynamic recrystallization of FCC metals [39]. According to Field et al. [40], similar twins were observed during recrystallization when the growth of grains became stagnant. If this mechanism occurs in the present case, the twinning is a manifestation of discontinuous dynamic recrystallization. At the same time, the observation of annealing twins in iron is rather unexpected, so a further study of this phenomenon is necessary.
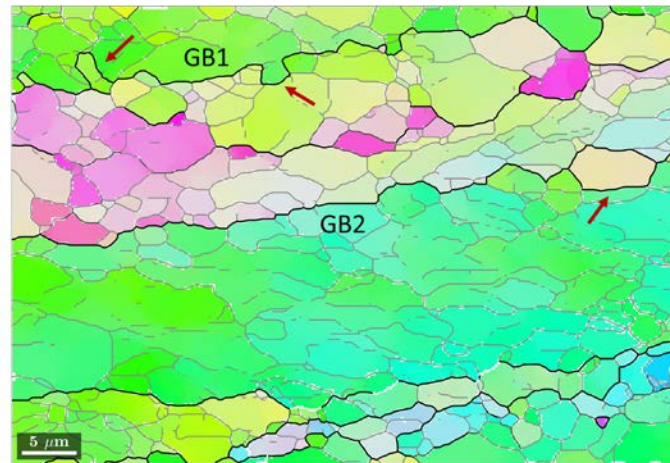
Fig. 10. IPF map of iron deformed at 600°C to strain of 1. Color-coding of boundaries is the same as in Fig. 4

4. Discussion

Despite the significant differences in the patterns of structure evolution, the increase of misorientations at previously formed deformation-induced boundaries is becoming a major mechanism for grain refinement at large strains, both at room temperature and at 600°C. That does not mean, of course, that the formation of new dislocation subboundaries becomes impossible. A dynamic balance seems rather occur between their creation and disappearance. As a result, at the maximum strains studied, the specific length of the lowest-angle subboundaries even decreases: slightly during cold deformation, and significantly during warm deformation. A similar reduction of the low-angle peak, which indicates progress of dynamic recovery, has been frequently observed at sufficiently large strains previously, for example, in steels subjected to cold [41] and warm [20] deformation. Note that the evolution of structure during continuous recrystallization is expected to include the disappearance of some subboundaries [23]. Hence, the recrystallization can also contribute to the reduction of the low-angle peak at 600°C.

As opposed to low-angle boundaries, HABs accumulate steadily with straining, in an approximately linear way for both temperatures (Fig. 8). The fact that the length of deformation-induced boundaries per unit area increases faster at room temperature than at 600°C may be partly associated with the scale, at which the fragmentation process develops. GNBs usually occur at previously formed cell/subgrain boundaries (IDBs) [1,2]. This is likely because the IDBs, despite being penetrable to gliding dislocations [42], can hinder them and thereby contribute to the subdivision of grain into regions, in which different slip systems operate or a different partitioning of the same slip systems occurs [43]. Thus, when cells become smaller with decreasing temperature, a specific length of GNBs is supposed to

increase. At the same time, the main factor is, in our view, the effect of grain-scale deformation banding, which is very pronounced at room temperature, on the formation of HABs. Since different combinations of slip systems operate in neighboring deformation bands from the very beginning of their development, an angle of misorientation between them appears to be on the order of true strain [1,3]. Therefore, at strains of ~1 to 1.5, the deformation banding would have to produce HABs with misorientation angles close to the highest possible disorientation. Indeed, the excess length of the deformation-induced HABs formed at room temperature over the one formed at 600°C is maximal at disorientation angles of ~40° and higher.

5. Conclusions

The process of grain fragmentation in iron subjected to tension at room temperature and 600°C has been studied by means of EBSD analysis. The following conclusions can be drawn from the present investigation.

    1. The character of the boundary misorientation distribution remains the same during the early stages of fragmentation, both at room temperature and 600°C. Only after warm deformation up to a strain of 1.6, the shape of the distribution changes considerably owing to the intensification of dynamic recovery and continuous recrystallization.

    2. The length of deformation-induced boundaries per unit area ceases to grow with strain in the low-angle range of misorientations, however, it continues to grow in the high-angle range.

    3. The relative fraction as well as the length per unit area of deformation-induced HABs increase approximately linearly with strain. The HABs appear and then evolve primarily by way of the gradual increase of misorientations between fragments. The dynamic recrystallization occurring at 600°C gives a relatively small contribution to the grain refinement.

    4. Within the examined strain interval, the accumulation of HABs occurs faster at room temperature than at 600°C. This impact of the temperature lowering is mainly due to the more intensive grain-scale deformation banding associated with the formation of transition zones, where HABs are concentrated.

References

1. Rybin VV. *Large plastic deformations and fracture of metals.* Moscow: Metallurgy; 1986. (In Russian)
2. Hansen N, Juul Jensen D. Development of microstructure in FCC metals during cold work. *Phil. Trans. R. Soc. Lond. A.* 1999;357(1756): 1447-1470.
3. Gil Sevillano J, Van Houtte P, Aernoudt E. Large strain work hardening and texture. *Progress in Mater. Sci.* 1980;25(2-4): 69-412.
4. Valiev RZ Langdon TG. Principles of equal-channel angular pressing as a processing tool for grain refinement. *Progress in Mater. Sci.* 2006;51(7): 881-981.
5. Mulyukov RR, Imayev RM, Nazarov AA. Production, properties and application prospects of bulk nanostructured materials. *J. Mater. Sci.* 2008;43: 7257-7263.
6. Estrin Y, Vinogradov A. Extreme grain refinement by severe plastic deformation: A wealth of challenging science. *Acta Mater.* 2013;61(3): 782-817.
7. Hughes DA, Hansen N, High angle boundaries formed by grain subdivision mechanisms. *Acta Mater.* 1997;45(9): 3871-3886.
8. Hurley PJ, Humphreys FJ. The application of EBSD to the study of substructural development in a cold rolled single-phase aluminium alloy. *Acta Mater.* 2003;51(4): 1087-1102.

9. Kuhlmann-Wilsdorf D, Hansen N. Geometrically necessary, incidental and subgrain boundaries. *Scripta Metall. Mater.* 1991;25(7): 1557-1562.

10. Hughes DA, Liu Q, Chrzan DC, Hansen N. Scalling of microsructural parameters: misorientations of deformation induced boundaries. *Acta Mater.* 1997;45(1): 105-112.

11. Delannay L, Mishin OV, Juul Jensen D, Van Houtte P. Quantitative analysis of grain subdivision in cold rolled aluminium. *Acta Mater.* 2001;49(13): 2441-2451.

12. He W, Ma W, Pantleon W. Orientation inhomogeneities within individual grains in cold-rolled aluminium resolved by electron backscatter diffraction. *Mater. Science and Engineering A*. 2008;483-484: 668-671.

13. Hurley PJ, Humphreys FJ. Characterizing the deformed state in Al-0.1Mg alloy using high-resolution electron bacscattered diffraction. *J. Microsc.* 2002;205(3): 218-225.

14. Allain-Bonasso N, Wagner F, Berbenni S, Field DP. A study of the heterogeneity of plastic deformation in IF steel by EBSD. *Mater. Science and Engineering A*. 2012;548: 56-63.

15. Subedi S, Pokharel R, Rollett AD. Orientation gradients in relation to grain boundaries at varying strain level and spatial resolution. *Mater. Science and Engineering A*. 2015;638: 348-356.

16. De Vincentis NS, Roatta A, Bolmaro RE, Signorelli JW. EBSD analysis of orientation gradients developed near grin boundaries. *Materials Research.* 2019;22(1): e20180412.

17. Kundu A, Field DP. Influence of microstructural heterogeneity and plastic strain on geometrically necessary dislocation structure evolution in single-phase and two-phase alloys. *Materials Characterization.* 2020;170: 110690.

18. Liu M, Liu Y, Li H. Deformation mechanism of ferrite in a low carbon Al-killed steel: Slip behavior, grain boundary evolution and GND development. *Mater. Science and Engineering A*. 2022;842: 143093.

19. Humphreys FJ, Bate PS. The microstructures of polycrystalline Al–0.1Mg after hot plane strain compression. *Acta Mater.* 2007;55(16): 5630-5645.

20. Yanushkevich Z, Belyakov A, Kaibyshev R. Microstructural evolution of a 304-type austenitic stainless steel during rolling at temperatures of 773–1273 K. *Acta Mater.* 2015;82: 244-254.

21. Zolotorevsky NY, Rybin VV., Matvienko AN, Ushanova EA, Philippov SA. Misorientation angle distribution of deformation-induced boundaries provided by their EBSD-based separation from original grain boundaries: Case study of copper deformed by compression. *Mater. Characterization*. 2019;147: 184-192.

22. Glover G, Sellars CM, Recovery and recrystallization during high temperature deformation of a-iron. *Metall. Trans.* 1973;4: 765-775.

23. Humphreys FJ, Hatherly M. *Recrystallization and related annealing phenomena, second edition.* Elsevier Science Ltd, Pergamon; 2004.

24. Kuroda M, Uenishi A, Yoshida H, Igarashi A. Ductility of interstitial-free steel under high strain rate tension: Experiments and macroscopic modeling with a physically-based consideration. *International Journal of Solids and Structures.* 2006;43(14-15): 4465-4483.

25. Hielscher R, Silbermann CB, Schmidl E, Ihlemann J. Denoising of crystal orientation maps. *J. Appl. Cryst.* 2019;52: 984-996.

26. Greninger AB. Twinning in alpha iron. *Nature.* 1935;June: 916-917.

27. Dillamore IL, Morris PL, Smith CJE, Hutchinson WB. Transition bands and recrystallization in metals. *Proc. Roy. Soc. A.* 1972;329(1579): 405-420.

28. Kreisler A, Doherty RD. Structure of well-defined deformation bands and formation of recrystallization nuclei in aluminium. *Metal Science.* 1978;12(12): 551-560.

29. Zolotorevsky N, Ushanova E, Rybin V, Perevezentsev V. Characterization of fragmented structure developed during necking of iron tensile specimen. *Letters on Materials.* 2021;11(4): 503-507.

30. Zolotorevsky N, Rybin V, Ushanova E, Ermakova N, Perevezentsev V. Large-scale fragmentation of grains in plastically deformed polycrystalline iron. *Materials Today Communications*. 2022;31: 103816.

31. Gertsman VY, Zhilyaev AP, Pshenichnyuk AI, Valiev RZ. Modelling of grain boundary misorientation spectrum in polycrystals with crystallographic texture. *Acta Metal. Mater.* 1992;40(6): 1433-1441.

32. Rybin VV, Zisman AA, Zolotorevsky NY. Junction disclinations in plastically deformed crystals. *Acta metall. mater.* 1993;41(7): 2211-2217.

33. Cizek P, Whiteman A, Rainforth M. EBSD and TEM investigation of the hot deformation substructure characteristics of a type 316L austenitic stainless steel. *Journal of Microscopy.* 2004;213(3): 285-295.

34. Zolotorevsky NY, Ermakova NY, Sizova VS, Ushanova EA, Rybin VV. Experimental characterization and modeling of misorientations induced by plastic deformation at boundaries of annealing twins in austenitic steel. *J. Mater. Sci.* 2017;52: 4172-4181.

35. Li BL, Godfrey A, Meng QC, Liu Q, Hansen N. Microstructural evolution of IF-steel during cold rolling. *Acta Mater.* 2004;52(4): 1069-1081.

36. Afrin N, Quadir MdZ, Munroe PR, Ferry M, Unusual crystallographic aspects of microband boundaries within {111}<110> oriented grains in a cold rolled interstitial free steel. *ISIJ International.* 2014;54(6): 1346-1352.

37. Ma G, Hughes DA, Godfrey AW, Chen Q, Hansen N, Wu G. Microstructure and strength of a tantalum-tungsten alloy after cold rolling from small to large strains. *J. Mater. Sci. Technol.* 2021;83: 34-48.

38. Sakai T, Belyakov A, Kaibyshev R, Miura H, Jonas JJ. Dynamic and post-dynamic recrystallization under hot, cold and severe plastic deformation conditions. *Progress in Materials Science*. 2014;60: 130-207.

39. Belyakov A, Dudova N, Tikhonova M, Sakai T, Tsuzaki K, Kaibyshev R. Dynamic recrystallization mechanisms operating under different processing conditions. *Materials Science Forum.* 2012;706-709: 2704-2709.

40. Field DP, Bradford LT, Nowell MM, Lillo TM. The role of annealing twins during recrystallization of Cu. *Acta Mater.* 2007;55(12): 4233-4241.

41. Belyakov A, Tsuzaki K, Kimura Y, Regularities of deformation microstructures in ferritic stainless steels during large strain cold working. *ISIJ International.* 2008;48(8): 1071-1079.

42. Gil Sevillano J. Flow stress and work hardening. In: Mughrabi H. (ed.) *Plastic Deformation and Fracture of Materials. Materials Science and Technology, a Comprehensive Treatment*. Weinheim: VCH; 1993. p.19-88.

43. Pantleon W. The evolution of disorientations for several types of boundaries. *Mater. Sci. and Eng. A*. 2001;319-321: 211-215.

THE AUTHORS

Zolotorevsky N.Yu.
e-mail: zolotorevsky@phmf.spbstu.ru
ORCID: 0000-0002-0185-5452

Rybin V.V.
e-mail: rybinvv@mail.com
ORCID: 0000-0003-1619-309X

Ushanova E.A.
e-mail: elinaus@mail.ru
ORCID: 0000-0003-3094-8559

Matvienko A.N.
e-mail: matvienko_an@spbstu.ru
ORCID: 0000-0002-3012-1407

Perevezentsev V.N.
e-mail: v.n.perevezentsev@gmail.com
ORCID: 0000-0002-0437-8540

Macroscopic quantum effects of electromagnetic induction in silicon nanostructures

L.E. Klyachkin$^{\boxtimes}$, N.T. Bagraev, A.M. Malyarenko

Ioffe Physical Technical Institute of the Russian Academy of Sciences, 26, Polytekhnicheskaya St.,

St. Petersburg, 194021, Russia

$\boxtimes$ leonid.klyachkin@gmail.com

Abstract. At room temperature, a macroscopic quantum galvanomagnetic effect of Faraday electromagnetic induction was demonstrated under conditions of the capture of single magnetic flux quanta in the edge channels, confined by chains of negative-U centers, in a silicon nanostructure heavily doped with boron, prepared in Hall geometry on an n-type Si (100) substrate. It is shown that this effect leads to the appearance of an induction current when only a constant magnetic field is applied in the absence of an externally applied voltage or a stabilized current. The experimental dependences of U_{xx}, U_{xy}, and U_{pn} on the magnitude of the external magnetic field in its various directions demonstrate both the Hall staircase of conductivity and the Shubnikov–de Haas oscillations.

Keywords: silicon nanostructure, negative-U centers, electromagnetic induction, Hall staircases of conductivity, Shubnikov-de Haas oscillations

Citation: Klyachkin LE, Bagraev NT, Malyarenko AM. Macroscopic quantum effects of electromagnetic induction in silicon nanostructures. *Materials Physics and Mechanics.* 2022;50(2): 252-265. DOI: 10.18149/MPM.5022022_6.

1. Introduction
In recent years, the creation of various types of nanostructures has led to the intensive development of nanoelectronics. During research in this area, a number of macroscopic quantum phenomena were discovered, which manifest themselves at high temperatures up to room temperature. Such phenomena include high-temperature oscillations of Shubnikov–de Haas, de Haas–van Alphen, Aharonov–Bohm, Hall quantum resistance staircase, longitudinal conductivity quantum ladder, and Faraday electromagnetic induction under conditions of the capture of single magnetic flux quanta. Such effects have been observed in graphene, as well as in similar topological insulators and superconductors [1-3]. In addition, high-temperature quantum phenomena have been detected in silicon nanostructures (SNSs) based on single-crystal silicon, 6H-SiC, and CdF_2 containing quantum wells (QWs) with edge channels formed from chains of centers with a negative correlation energy (negative-U). It was experimentally found that these nanostructures exhibit the properties of topological insulators [4-7]. It should be noted that negative-U centers can have a different nature: in particular, in

single-crystal silicon and CdF_2 based SNSs they are formed on the basis of B^+–B^- boron dipoles oriented in the (111) direction under conditions of heavy doping, while in 6H-SiC based nanostructures negative-U centers have a vacancy nature [8]. It was shown that under compression conditions, due to high pressure of the order of hundreds of GPa [9], in such nanostructures, an edge channel with a cross-section of 2×2 nm appears on the surface of the QW limited by negative-U centers, which leads to an increase in the carrier relaxation time [10], due to the suppression of electron-electron interaction (EEI). Note that in a number of works, the neutralization of EEI in edge channels was predicted in cases when they are limited by chains of d- or f-elements [11,12]. Thus, it was experimentally demonstrated that layers consisting of negative-U dipole centers that form edge channels on the QW surface determine the possibility of observing macroscopic quantum phenomena at high temperatures up to room temperature [4-7].

Among the observed macroscopic quantum phenomena in the SNSs, one should especially highlight the Faraday electromagnetic induction (FEMI) under the conditions of the capture of single magnetic flux quanta [13]. It was found [7,14] that during the longitudinal current flow in a system with an edge channel, single magnetic flux quanta are captured by single charge carriers in the edge channel and the effect of electromagnetic induction is realized, which manifests itself in electrical measurements, and also leads to intense radiation in far IR, THz and GHz wavelengths. Taking into account the results of the above experiments, one should expect the manifestation of a galvanomagnetic effect in such nanostructures, namely, the appearance of an induction current when only a constant magnetic field is applied in the absence of an externally applied voltage or the transmission of a stabilized current. In this case, the capture of single quanta of the magnetic flux on single carriers in the edge channels will be determined only by varying the magnitude and direction of the magnetic field. It is expected that in this case, the effect will manifest itself when studying the dependences of U_{xx}, U_{xy}, and U_{pn} on the magnitude of the external magnetic field in a nanostructure formed in the Hall geometry.

2. Experimental methodology

SNS is an ultra-narrow p-type silicon quantum well bounded by δ-barriers heavily doped with boron (5×10^{21} cm^{-3}) on the surface of n-silicon (100) (Fig. 1). Boron atoms in δ-barriers form trigonal dipole centers with negative correlation energy (B^+–B^-) due to the negative-U reaction: $2B_0 \rightarrow B^+ + B^-$ [5] limiting edge channels. Thanks to this circumstance, the EEI is significantly suppressed in such an edge channel, as a result of which the carriers have a long relaxation time, which, in turn, makes it possible to observe macroscopic quantum processes at high temperatures up to room temperature.

The studies of the de Haas–van Alphen (dHvA) [4] and Shubnikov–de Haas (SdH) effects, as well as the quantum Hall effect (QHE) [5], showed that in these experimental SNSs, the two-dimensional concentration p_{2D} of single charge carriers in the edge channel bound by chains of negative-U centers is 3×10^{13} m^{-2}. Their behavior is characterized by a long relaxation time and a low value of the effective mass [15,16]. When studying dHvA in these experimental SNSs, it was shown that as the magnetic field increases, the static magnetic susceptibility begins to reveal dHvA oscillations due to the creation of Landau levels, $E_\nu = \hbar\omega_c(\nu+1/2)$, ν is the number of the Landau level. In particular, the condition of covering the edge channel with single magnetic flux quanta turns out to be satisfied at an external magnetic field strength ΔB = 124.6 mT, which follows from the relation $\Phi_0 = \Delta BS$ and corresponds to the filling of the first Landau level, $\nu_1 = 1$, $\nu_1 = p_{2D}h/eB$, where $\Phi_0 = h/e$ (or $h/2e$) is the magnetic flux quantum, and S is the area on which the capture is made. Based

on the foregoing, it is possible to estimate the longitudinal size l_0 of the region of the edge channel, in which the interference of a single carrier occurs:

$$l_0 = \frac{\Phi_0}{\Delta B d_0}, \tag{1}$$

where $\Delta B = 124.6$ mT; $d_0 = 2$ nm is the width of the edge channel [5] since this value is the characteristic distance between the barriers containing negative-U centers that form the edge channels bounding the QW. From here, we get the value $l_0 \approx 16$ μm. It can be said with confidence that the edge channel of the investigated nanostructure consists of regions of interference of single carriers, taking into account the value of their two-dimensional density, determined from Hall measurements, 3×10^{13} m^{-2}. This value of the two-dimensional density corresponds to the distance between carriers (holes) in the edge channel of approximately 16 μm. In other words, each region of the edge channel, in which a single carrier ('pixel') is located, consists of layers containing boron dipoles with an area of $S_{pixel} = 16$ μm $\times$ 2 nm, along which the carrier tunnels. The quantum well is limited by these two layers with a width and height of approximately 2 nm, which is consistent with the depth of the diffusion profile [17].
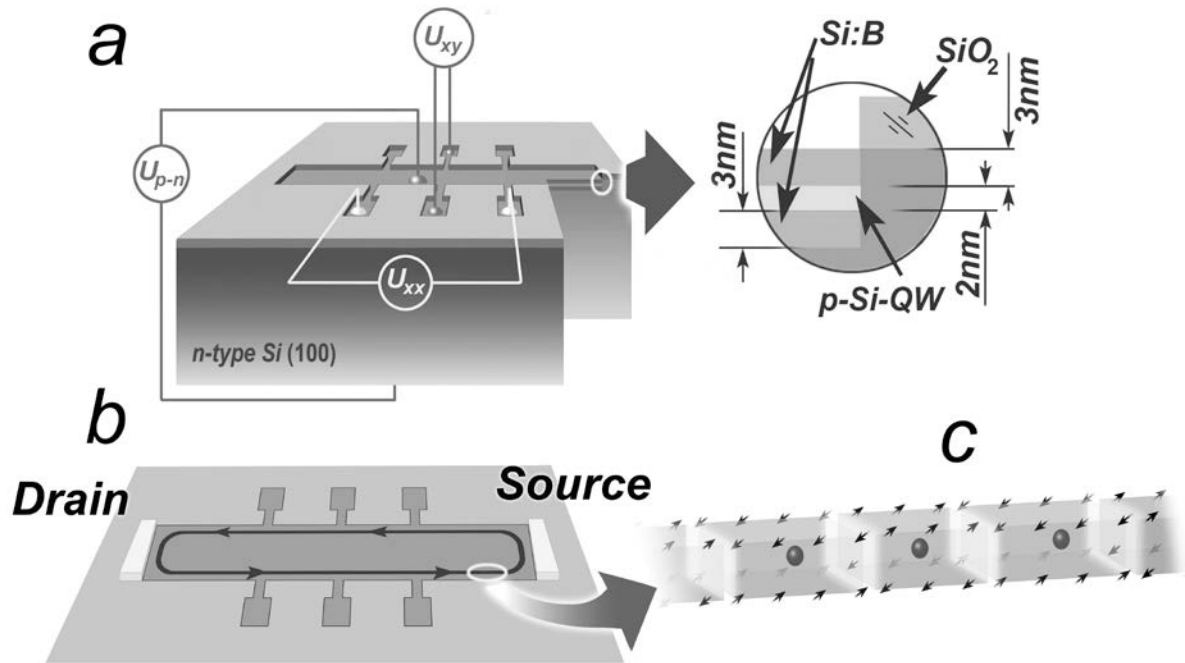
Fig. 1. Silicon nanostructure (a) containing a heavily doped silicon quantum well bounded by δ-barriers consisting of negative-U dipole boron centers and forming an edge channel (b) with ballistic conductivity in it. Fragment of the edge channel (c), consisting of a sequence of regions of interference of single carriers (pixels)

Thus, due to the FEMI, the quantum interference of single carriers occurs inside the pixels of the edge channel, and, in accordance with the classical FEMI relation, it is possible to estimate the induction current I_{ind} arising due to the application of an external magnetic field:

$$I_{ind} = \frac{\Delta E}{\Delta \Phi} = \frac{neV_g}{m\Phi_0}, \tag{2}$$

where ΔE is the change in energy when varying the magnitude of the magnetic flux in the region of quantum interference; $\Delta\Phi = \Delta BS$; ΔB is the change in the external magnetic field inside the region of quantum interference with area S; n is the number of single charge carriers in the region of quantum interference; m is the number of magnetic flux quanta captured in the region of quantum interference; V_g is the control voltage applied to the edge channel [16]. In particular, if we consider quantum interference and I_{ind} in a single pixel containing a charge carrier, then $n = 1$, m is the number of magnetic flux quanta captured by a single pixel, and the resulting conductivity value in e^2/h units is greater than one. At the same time, under conditions of quantum interference, fractional conductivity values with $\nu > 1$ ($\nu = n/m$) can appear on an area larger than the area of one pixel [5]. With an increase in the magnetic field, quantum interference occurs exclusively in single pixels of small size. In this case, one should expect the capture of several magnetic flux quanta per pixel, and, accordingly, fractional conductivity values with $\nu < 1$, which manifests itself when registering the Hall staircase of conductivity [5].

Hence, it follows that the FEMI can play an important role in the observation of macroscopic quantum effects in SNSs. In addition, it becomes possible to implement device structures based on the application of a control voltage to edge channels, an example of which is a spin transistor [18]. This device can operate under the conditions of transport of single carriers when registering both longitudinal and transverse voltage drops. Such an effect can only be obtained by applying an external magnetic field, which is the cause of the induction current. It should be noted that the proposed version of the FEMI quantum effect can occur even in the absence of a specified source-drain current in the Hall geometry since a change in the external magnetic field is sufficient to generate I_{ind}. Thus, macroscopic quantum phenomena can be detected using galvanomagnetic techniques.

The idea of the presence of the FEMI in quantum-well structures was first proposed by Laughlin [19], who suggested using a special wave function, within which the electron-electron interaction is suppressed, which makes it possible to explain the appearance of the fractional Hall conductivity staircase [20]. In this case, it was not required to divide the edge channel into pixels with forced localization of single carriers in them [19,21]. However, the methods used to register the fractional QHE revealed some contradiction with the condition of its observation in a system with a free gas of carriers, namely, for the experimental implementation of the fractional QHE, pre-illumination with monochromatic light at low temperatures were used, as well as the application of voltage to the gate during cooling of the samples [20,22]. Moreover, selective illumination satisfied the condition of recharging DX centers and other negative-U centers with their transition to the dipole state [5,22-26]. That is, the preliminary preparation of the sample for the registration of macroscopic quantum effects probably corresponded to the creation of conditions for suppressing the electron-electron interaction even at a high carrier density.

Thus, in accordance with expression (2), integer and fractional quantum phenomena can occur in experiments with SNSs under conditions of varying filling of pixels with different numbers of magnetic flux quanta. Using the scaling effect, i.e. by changing the distances between the contacts (using different contacts of the SNS made in the Hall geometry for the research), it is possible to change the number of carriers in the edge channel and obtain fractional values both greater and less than one [5].

It should be taken into account that in the investigated SNS on the area of the edge channel S_{xx} between the XX contacts ($S_{xx} = 2$ mm $\times$ 2 nm $= 4\times10^{-12}$m^2) there are approximately 125 single carriers, which corresponds to the value of the two-dimensional

density $p_{2D} \approx 3 \times 10^{13}$ m^{-2}. The results of measurements of the field dependences of the magnetic susceptibility [4] and Hall measurements [5] are in good agreement with this value.

The above-described SNSs containing edge channels consisting of pixels exhibit the property of quantized conductivity [4]. As a result, we can consider the edge channel as a ballistic one, in which each of the pixels is characterized by a resistance equal to the resistance quantum h/e^2. In addition, it was shown [7] that in such edge channels it is possible to form double-length pixels with a resistance $h/2e^2$ containing a pair of carriers with the probable implementation of a Josephson transition near the pixel boundary.

In the framework of this study, the detection of inductive current when only a magnetic field is applied is performed by measuring the voltage that occurs under the influence of a magnetic field on the contacts XX (U_{xx}), XY(U_{xy}), and on the gate contacts (U_{pn}). In this case, the induction current is determined from a simple expression:

$$U = I_{ind}R,\qquad(3)$$

where R is the resistance of the section of the edge channel between the measuring contacts, and U is the voltage that occurs on these contacts.

The SNSs studied within this paper are made in the Hall geometry (Figure 1), so their edge channels, in which the induction current (I_{ind}) is induced, are located in the XX direction. Previously, it was found [5] that during the technological process of QW formation, the SNS surface is covered with a field of fractal-type pyramids with an apex angle of 55°, which are oriented in the (111) direction. These pyramids are an ordered accumulation of their own interstitial silicon atoms and are separated from each other by vacancies, which, in turn, are transformed in the process of doping into the above described trigonal negative-U dipole centers, also oriented in the (111) direction. Previously, it was shown [4] that the chains of such trigonal negative-U centers, which form δ-barriers that limit the edge channel, are oriented in the (011) direction.

In addition, studies of the dHvA effect [4] and spin-dependent transport [27] in SNSs showed that the characteristics of ballistic carrier transfer in the edge channel in the XX direction are identical to the XY direction.

It follows from the foregoing that it is necessary to conduct experimental studies of U_{xx}, U_{xy}, and U_{pn} on the magnitude of the external magnetic field at different orientations of the magnetic field in a plane parallel to the XY direction. Therefore, four orientations of the magnetic field were chosen in these experiments: 1) Hall (the magnetic field is perpendicular to the SNS); 2) the magnetic field is parallel to the SNS and XY contacts; 3,4) intermediate cases with a deviation of the direction of the magnetic field from the Hall direction by 35° and 55°.

The magnetic field was sweeping in the range of 0–520 mT with a step of about 0.05 mT, then turned off, and then the measurements were repeated with the opposite polarity of the magnetic field. On the experimental dependences presented below, for the definite direction of the magnetic field, we showed both as B^+ (the magnetic field is directed towards the SNS) and B^- (the magnetic field is directed away from the SNS).

The U_{xx}, U_{xy} and U_{pn} values were measured using KEITLEY 2182A and Agilent 34420A nanovoltmeters.

3. Experimental results

Since I_{ind} arises in each pixel as a result of the capture of magnetic flux quanta, and the connection between pixels is carried out by tunneling single carriers through dipole centers in the barriers limiting them, parallel connection of pixels is realized in the edge channels. Thus,

it can be expected that the value of the longitudinal registered voltage will correspond to the value $U_{ind} = I_{ind}(h/e^2) \cdot (1/k)$, where k is the number of pixels containing single charge carriers between the measuring contacts, and the corresponding I_{ind} is determined from Faraday relation (2).

The above consideration makes it possible to describe the presence of a conductivity (resistance) staircase that arises when the magnitude of the external magnetic field changes within the framework of the Hall geometry of the experiment. The presence of such a staircase is expected both when registering U_{xy} in the perpendicular orientation of the external magnetic field and, accordingly, when registering U_{xx} when the field is oriented along the SNS plane parallel to the XY contacts, and also when registering U_{pn} (at the p-n junction on the gate-substrate contacts) in both of the above-mentioned field directions.

However, the contribution to the measured quantities can give the SdH effect. Then the role of the resistance in expression (3) will be determined by the Landau size quantization, which gives an oscillatory dependence of the resistance: if the Fermi level coincides with the Landau level, the resistance peaks, and if they do not coincide, the resistance cancels out [28]. In this case, characteristic oscillations are expected in the U_{xx} dependences at a perpendicular orientation of the external magnetic field.

Note that the position of the Landau level peaks corresponds to the middle step of the Hall resistance staircase [28].

It follows from the above that it is expedient to use the interrelationship of U_{xx} and U_{xy}, namely $R_{xx} = R_{xy}/k$, where k is the number of pixels between the measurement contacts XX. Since R_{xy} is determined by the resistance of a pixel containing a single carrier (h/e^2), the behavior of R_{xx} with a change in the magnetic field follows the corresponding dependence of R_{xy}, and $U_{xx} = I_{ind}R_{xx} = I_{ind}R_{xy}/k$.

Magnetic field perpendicular to the SNS. Figure 2 shows the experimental dependences of U_{xx}, U_{xy}, and U_{pn} on the magnitude of the external magnetic field oriented perpendicular to the SNS plane. U_{xx} dependences (Fig. 2a) demonstrate pronounced SdH oscillations, which are determined, first of all, by the mechanism of successive capture of magnetic flux quanta on the pixels of the edge channel with successive generation of induced current. Moreover, on each of the presented dependences, several periods of oscillations are observed. Previous studies of the dHvA [4], SdH, and QHE [5] effects showed that the period of oscillations when a magnetic flux quantum is captured by a single pixel with an area $S_{pix} = 16.6\mu m \times 2$ nm $= 33.2 \ 10^{-15} m^2$ is $\Delta B = 124.6$ mT. All curves shown in Fig. 2a demonstrate oscillations at 124.6 mT, and in addition, all of them have additional sets of oscillation periods, which are determined by more complex combinations of pixels, including those associated with SNS defects, which cannot be calculated.

U_{xy} (Fig. 2b) and U_{pn} (Fig. 2c) dependences demonstrate a stepwise character, which indicates the dominance of the QHE in comparison with the SdH effect for a given direction of the external magnetic field. However, along with the steps, these dependences also exhibit weak SdH oscillations, which most likely indicates the implementation of a mixed regime with the presence of both of the above effects. Note that the change in the polarity of the magnetic field in the study of the dependence $U_{xy} = f(B)$ leads to a pronounced Zeeman effect (Fig. 2b).

Since the SNS is only affected by the magnetic field (neither a bias voltage nor a stabilized current I_{ds} are applied to it), we can estimate the current induced by the magnetic

field, since it is known that a pixel, under the influence of a current, is a radiation generator at its resonant frequency of 2.6 THz [6]. The quantum energy $h\nu$ will be determined by the formula:

$$h\nu = I_{ind}\Delta\Phi,\qquad(4)$$

where ν is the generation frequency, $\Delta\Phi$ is the change in the magnetic flux through the pixel. The frequency of generation can be predicted by knowing the dimensions of the resonator.

Taking into account the Wulff–Bragg relation $2nd = \lambda$, (where d is the resonator length, i.e. the pixel length, n is the refractive index, λ is the radiation wavelength), I_{ind} can be estimated using the formula:

$$I_{ind} = \frac{ch}{2dn\Delta\Phi}.\qquad(5)$$

Fig. 2. U_{xx} (*a*), U_{xy} (*b*), and U_{pn} (*c*) dependencies on the magnitude of the external magnetic field oriented perpendicular to the plane of the silicon nanostructure.
Dependencies: 1 – the field is directed to the surface of the SNS; 2 – the field is directed away from the SNS surface. T = 300 K

Then, knowing that the pixel length is 16.4 μm, assuming that the refractive index is close to the refractive index of silicon 3.4, and the change in the magnetic flux for the SNS at a magnetic field of 124 mT is equal to the magnetic flux quantum $\Phi_0 = h/e$ (or $h/2e$), we obtain I_{ind} values of approximately 0.4 and 0.8 μA, respectively, for two values of Φ_0.

It is necessary to take into account the contribution of two more components to the induced current: 1) the Josephson induced current I_{indJ} [29,30] and 2) the superconducting induced current I_{indS} arising due to the presence of the superconducting gap [13], which can be calculated by the formula:

$$I_{indJS} = e\Delta/h. \tag{6}$$

Note that in the case of the Josephson-induced current, a pair of single carriers must be considered, in which case the pixel size is doubled.

In this case, I_{indJ} is approximately equal to 0.2 μA, considering that $\nu = 2.6$ THz and I_{indS} is approximately equal to 0.8 μA, considering that Δ the width of the superconducting gap, is equal to 22 meV.

Now, knowing I_{ind}, we can obtain the calculated values of U_{xy} using the formulas:

$$U_{xy} = 2I_{ind}\left(\frac{h}{e^2}\right) \tag{7a}$$

or

$$U_{xy} = 2I_{ind}\left(\frac{h}{2e^2}\right). \tag{7b}$$

Taking into account all the components of the inductive current, and also that their superposition can both be added up and subtracted, we obtain the calculated U_{xy} values of the same order as the experimental ones, which are shown in Fig. 2b.

The magnetic field in the SNS plane parallel to the XY contacts. Figure 3 shows the experimental dependences of U_{xx}, U_{xy}, and U_{pn} on the magnitude of the external magnetic field oriented in the SNS plane parallel to the XY contacts. In this case, the size and orientation of the edge channel pixels are preserved. However, compared to the previous orientation of the magnetic field, the carriers rotate along the field in a transverse plane relative to the SNS plane. In this case, additional compression of the carrier trajectory from below by the p-n junction field occurs, as a result of which the spread of parameters is smaller compared to the previous case.

U_{xx} (Fig. 3a), U_{xy} (Fig. 3b), and U_{pn} (Fig. 3c) dependences, in the case of application of an external magnetic field in the SNS plane parallel to the XY contacts, demonstrate a stepwise character, which indicates a clear dominance of the QHE.

Note that the experimental values of U_{xx} and U_{pn} are 1-2 orders of magnitude higher than the values of U_{xy}, although when measuring the classical and quantum Hall effect, namely when applying a longitudinal stabilized current I_{ds} to the SNS the measured voltage U_{xx} is always significantly lower (by several orders of magnitude) than U_{xy}. In these experiments, when $I_{ds}=0$, U_{xx} is approximately 2 orders of magnitude higher than the U_{xy} values measured under the same conditions. This is explained by the appearance of strong polarization due to the Zeeman effect, which contributes to the U_{xx} values by several orders of magnitude greater than the magnetic field-induced voltage $U_{xx\,ind}$ since the Zeeman polarization coefficient depends exponentially on the magnetic field. The same circumstance

also explains the monotonic growth of the experimental dependences of U_{xx} on the magnetic field strength.

Taking this into account, it is possible to estimate the magnitude of the voltage U_{xxind} induced by the magnetic field using the following formula:

$$U_{xxind} = U_{XX} \exp\left(-\frac{2eB\hbar}{kTm^*}\right), \qquad (8)$$

where e is the electron charge, B is the magnitude of the magnetic field, k is the Boltzmann constant, T is the temperature, m^* is the effective mass of charge carriers. If m^* is assumed to be approximately 10^{-34} kg (previously it was shown in [15] that in SNS it is about $10^{-3} m_0$ at room temperature), then with a magnetic field $B = 124.6$ mT and at room temperature, the exponent will be 4.5×10^{-5} and the value of U_{xxind} will be about 10 nV.
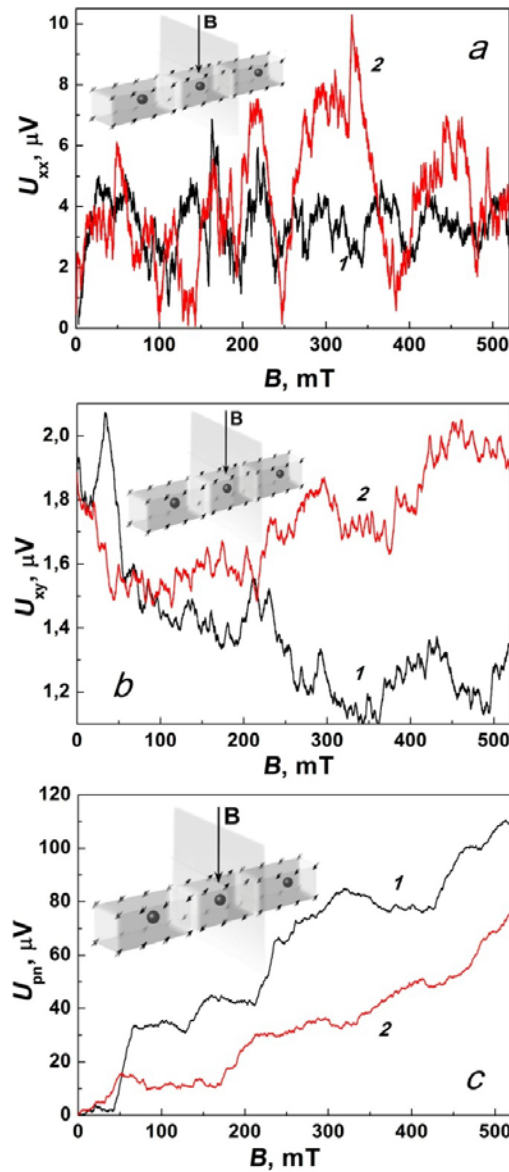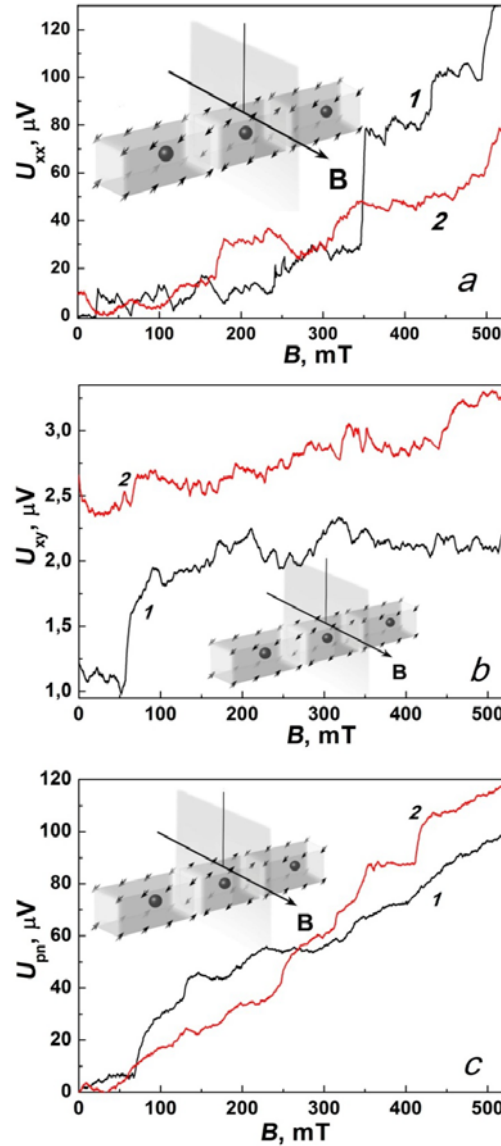

Fig. 3. U_{xx} (*a*), U_{xy} (*b*), and U_{pn} (*c*) dependencies on the magnitude of the external magnetic field oriented along the plane of the silicon nanostructure parallel to the XY contacts. The field for dependencies (1) is directly opposite to the field for dependencies (2). T = 300 K

Taking into account the pronounced stepwise nature of the experimental dependences, it is possible to estimate the coincidence of the position of the steps in the $U_{xx} = f(B_{xy})$ and $U_{pn} = f(B_{xy})$ with integer and basic fractional values of the pixel resistance R_{xx} calculated in h/e^2 units according to the formula:

$$R_{xx} = \frac{\Phi}{ne} = \frac{BS}{ne}[Ohm] = \frac{BS}{ne}\frac{e^2}{h}\left[\frac{h}{e^2}\right], \qquad (9)$$

where $n = 1$; $S = 33.2 \times 10^{-15} m^2$.

The results presented in Fig. 4 show good agreement.
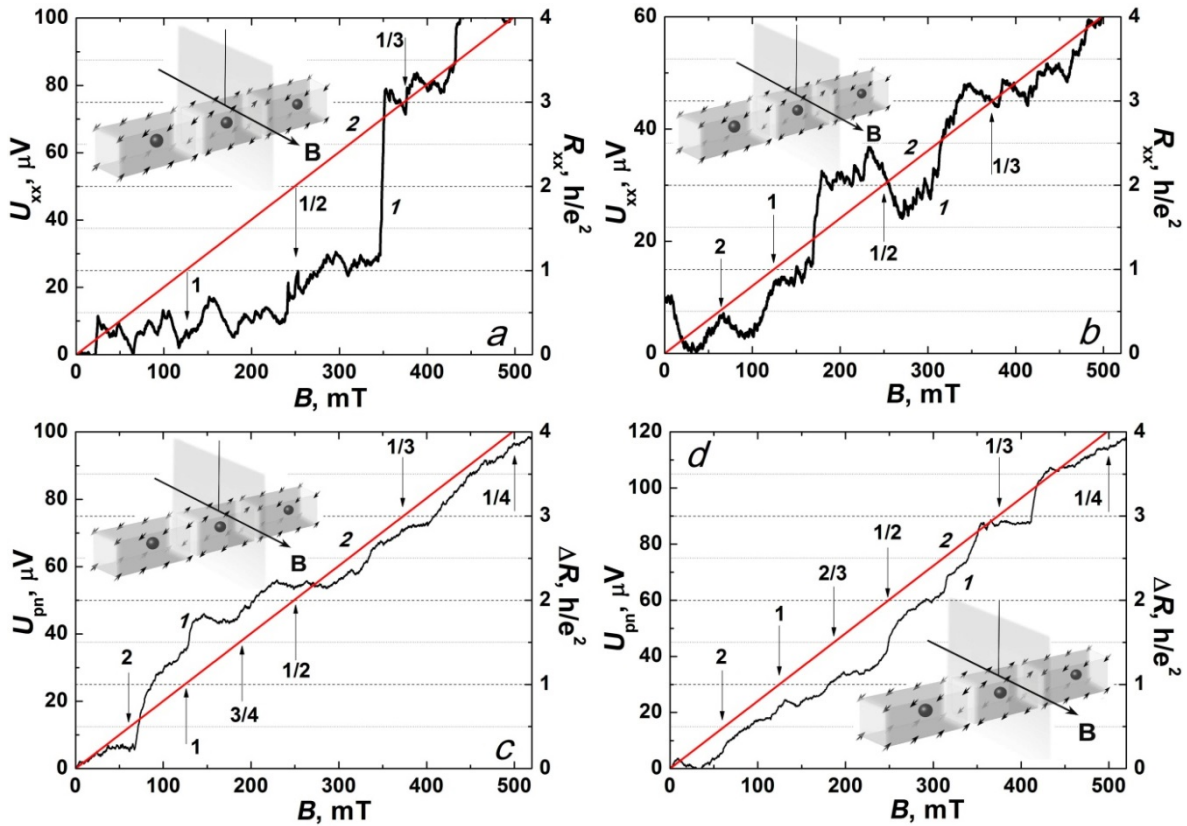
Fig. 4. Comparison of the position of the steps in the dependences (*a*, *b*, curves *1*) $U_{xx} = f(B_{xy})$ and (*c*, *d*, curves *1*) $U_{pn} = f(B_{xy})$ with integer and basic fractional calculated values of the pixel resistance R_{xx} in h/e^2 units (straight lines *2*). The fields (a) and (b), (c), and (d), respectively, have the opposite direction. T = 300 K

The magnetic field in intermediate positions between the perpendicular to the SNS plane and parallel XY contacts. In this section, we consider cases of intermediate angles of the direction of the magnetic field relative to the SNS surface with a deviation of the direction of the magnetic field from the Hall direction by 35° and 55° in the plane perpendicular to the surface of the SNS and parallel to the XY contacts. Figure 5 shows the $U_{xx} = f(B)$ dependences, which have a mixed oscillatory-stepwise character.

We will consider the magnitude of such a deflected magnetic field as a superposition of two components: the Hall field (B_{Hall}) and the field directed along the SNS surface parallel to the XY contacts ($B_{H\|XY}$). It is obvious that the component of the magnetic field B_{Hall} determines the oscillating nature corresponding to the SdH effect, while the other component

of the magnetic field $B_{H\|XY}$ determines the stepwise nature of the $U_{xx} = f(B)$ dependences as a result of the dominance of the QHE. In Figure 5, the values of both components of the magnetic field are presented on additional abscissa axes. It can be seen that in the case when the B_{Hall} component increases faster than $B_{H\|XY}$ with the increasing magnetic field (Fig. 5a), the U_{xx} dependences are stepwise due to the dominance of the QHE. In the opposite case, when the $B_{H\|XY}$ component increases faster than B_{Hall} with increasing magnetic field (Fig. 5b), at low fields the SdH effect dominates, and at higher fields a mixed regime occurs, in which both SdH and QHE effects are manifested.

In addition, in Figure 5 (line *3*), the positions of the pixel resistance R_{xx} are indicated in h/e^2 units with integer and basic fractional calculated values depending on the value of $B_{H\|XY}$. The results obtained correlate well with the experimental dependences described above for various variants of applying a magnetic field in the cases considered above.
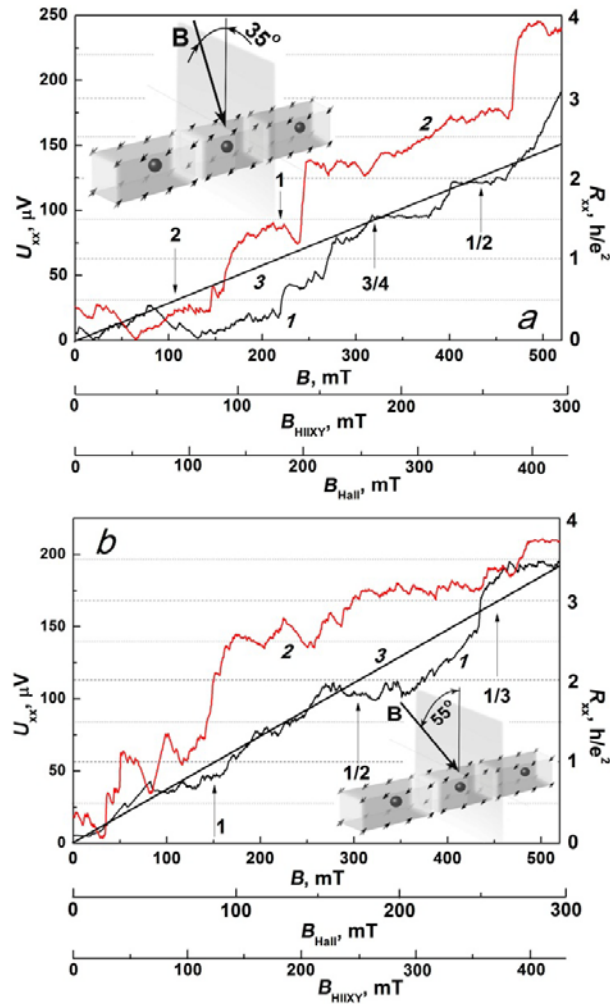
Fig. 5. Comparison of the position of the steps in the $U_{xx} = f(B)$ dependences (curves *1* and *2*) obtained with a deviation of the magnetic field direction in the plane perpendicular to the SNS surface and parallel to the XY contacts from the Hall direction by (a) 35° and (b) 55°, with integer and basic fractional calculated values of the pixel resistance R_{xx} in h/e^2 units (straight lines *3*). For dependencies (*1*) and (*2*), the direction of the field is directly opposite. $T = 300$ K

4. Conclusions

The suppression of the electron-electron interaction, which leads to an increase in the relaxation time due to the presence of negative-U centers limiting the QW edge channels, makes it possible to detect macroscopic quantum effects, the Hall staircase of conductivity, and SdH oscillations at high temperatures up to room temperature. These effects arise due to FEMI under conditions of the capture of single quanta of the magnetic flux. In this case, integer and fractional values of the plateau and steps of the Hall conductivity staircase are determined by the sizes of the sections of the edge channels containing single charge carriers.

Due to the presence of negative-U centers limiting the edge channels, macroscopic quantum phenomena are observed at different orientations of the external magnetic field when the U_{xx}, U_{xy} voltage, and the U_{pn} voltage are registered perpendicular to the QW plane studied in the framework of the Hall geometry, since in the cases under consideration the size quantization condition is satisfied.

An important role of edge channels in the detection of macroscopic quantum phenomena using galvanomagnetic techniques is manifested by varying the direction of the external magnetic field in the plane perpendicular to the SNS surface and parallel to the XY contacts from the Hall direction by an angle of 35° or 55°. In this case, both SdH oscillations and the Hall conductivity staircase are simultaneously observed, and the dominance of one or the other effect depends on the prevalence of either the Hall component of the external magnetic field or parallel to the XY contacts.

References

1. Novoselov KS, Jiang Z, Zhang Y, Morozov SV, Stormer HL, Zeitler U, Maan JC, Boebinger GS, KimP, Geim AK. Room-Temperature Quantum Hall Effect in Graphene. *Science*. 2007;315(5817): 1379.
2. Hasan MZ, Kane CL. Topological insulators. *Reviews of Modern Physics*. 2010;82(4): 3045-3067.
3. Yan B, Zhang SC. Topological materials. *Rep. Prog. Phys*. 2012;75: 096501.
4. Bagraev NT, Grigoryev VY, Klyachkin LE, Malyarenko AM, Mashkov VA, Romanov VV. Room Temperature de Haas–van Alphen Effect in Silicon Nano sandwiches. *Semiconductors*. 2016;50(8): 1025-1033.
5. Bagraev NT, Grigoryev VY, Klyachkin LE, Malyarenko AM, MashkovVA, Rul NI. High-temperature quantum kinetic effect in silicon nanosandwiches. *Low Temperature Physics*. 2017;43(1): 110.
6. Taranets KB, Fomin MA, Klyachkin LE, Malyarenko AM, BagraevNT, Chernev AL. Terahertz resonance response of biological tissue placed on a silicon nanostructure. *Journal of Applied Physics*. 2019;125(22): 225702.
7. Bagrayev NT, Golovin PA, Klyachkin LE, Malyarenko AM, Presnukhina AP, Reukov AS, Khromov VS. Therapy of covid complications with terahertz irradiation. *Technical Physics*. 2022;92(7): 943-950.
8. Bagrayev NT, Kukushkin SA, Osipov AV, Klyachkin LE, Malyarenko AM, Khromov VS. Terahertz irradiation from silicon carbide nanostructures. *Semiconductors*. 2021;55(11): 1027-1033
9. Kukushkin SA, Osipov AV. Theory and practice of SiC growth on Si and its applications to wide-gap semiconductor films. *J. Phys. D: Appl. Phys*. 2014;47: 313001.
10. Gehlhoff W, Bagraev NT, Klyachkin LE. Cyclotron Resonance in Heavily Doped Silicon Quantum Wells. *Solid St. Phenomena*. 1995;47-48: 589-594.
11. Klinovaja J, Stano P, Yazdani A, Loss D. Topological Superconductivity and Majorana Fermions in RKKY Systems. *Physical Review Letters*. 2013;111(5): 186805.

12. Zyuzin AA, Loss D. RKKY interaction on surfaces of topological insulators with superconducting proximity effect. *Physical Review B*. 2014;90(12): 125443.

13. Aronov AG, Sharvin YV. Magnetic flux effects in disordered conductors. *Reviews of Modern Physics*. 1987;59(3): 755-779.

14. Bagrayev NT, Klyachkin LE, Malyarenko AM, Novikov BA. Application of silicon sources of terahertz radiation in medicine. *Biotekhnosfera*. 2015;5: 64-79.

15. Bagraev NT, Galkin NG, Gehlhoff W, Klyachkin LE, Malyarenko AM. Phase and amplitude response of the '0.7 feature' caused by holes in silicon one-dimensional wires and rings. *J. Phys.: Condens. Matter*. 2008;20: 164202-164212.

16. Bagraev NT, Gehlhoff W, Klyachkin LE, Kudryavtsev AA, Malyarenko AM, Romanov VV. Spin-Dependent Transport Of Holes In Silicon Quantum Wells Confined By Superconductor Barriers. *AIP Conference Proceedings*. 2010;1199(1): 4314-432.

17. Bagraev NT, Gehlhoff W, Klyachkin LE, Naeser A, Rykov S. Quantum-Well Boron and Phosphorus Diffusion Profiles in Silicon. *Defect and Diffusion Forum*. 1997;143-147: 1003-1008.

18. Rul NI, Golovin PA, Bagrayev NT, Klyachkin LE, Malyarenko AM. Optoelectric phase characteristics of silicon nanosandwiches with negative correlation energy. *NTV SPbGPU Fiziko-matematicheskiye nauki*. 2021;14(4): 9-20.

19. Laughlin RB. Quantized Hall conductivity in two dimensions. *Phys. Rev. B*. 1981;23: 5632-5633.

20. Willett R, Eisenstein JP, Störmer HL, Tsui DC, Gossard AC, English JH. Observation of an even-denominator quantum number in the fractional quantum Hall effect. *Phys. Rev. Lett.* 1987;59: 1776-1779.

21. Halperin BI. Theory of the quantized Hall conductance. *Helvetica Phys. Acta*. 1983;56: 75-102.

22. Kukushkin IV, von Klitzing K, Ploog K, Kirpichev VE, Shepel BN. Reduction of the electron density in GaAs-AlxGa1−xAs single heterojunctions by continuous photoexcitation *Phys. Rev. B*. 1989;40: 4179-4182.

23. Zazoui M, Feng SL, Bourgoin JC. Nature of the DX center in Ga1−xAlxAs. *Phys. Rev. B*. 1991;44: 10898-10900.

24. Peale RE, Mochizuki Y, Sun H, Watkins GD. Magnetic circular dichroism of the DX center in Al0.35Ga0.65As:Te. *Phys. Rev. B*. 1992;45: 5933-5943.

25. Alt HCh. Experimental evidence for a negative-U center in gallium arsenide related to oxygen. *Phys. Rev. Lett*. 1990;65: 3421-3424.

26. Bagraev N.T. The EL2 center in GaAs: symmetry and metastability. *J. Phys. I France*. 1991;1(10): 1511-1527.

27. Bagraev NT, Gehlhoff W, Klyachkin LE, Kudryavtsev AA, Malyarenko AM, Oganesyan GA, Poloskin DS, Romanov VV. Spin-dependent transport of holes in silicon quantum wells confined by superconductor barriers. *Physica C*. 2008;468: 840-842.

28. Shoenberg D. *Magnetic oscillations in metals*. Cambridge: Cambridge University Press; 1984.

29. Bagraev NT, Klyachkin LE, Kudryavtsev AA, Malyarenko AM, Romanov VV. Superconducting properties of silicon nanostructures. *Semiconductors*. 2009;43(11): 1441-1454.

30. Bagraev NT, Klyachkin LE, Kudryavtsev AA, Malyarenko AM, Oganesyan GA, Poloskin DS. Quantum supercurrent and Andreev reflection in silicon nanostructures. *Semiconductors*. 2009;43(11): 1496-1506.

THE AUTHORS

Klyachkin L.E.
e-mail: leonid.klyachkin@gmail.com
ORCID: 0000-0001-7577-1262

Bagraev N.T.
e-mail: bagraev@mail.ioffe.ru
ORCID: 0000-0001-8286-3472

Malyarenko A.M.
e-mail: annamalyarenko@mail.ru
ORCID: 0000-0002-4667-7004

Using products of polyethylene recycling for the production of holding tanks

L.N. Shafigullin[1✉], N.V. Romanova[1], V.T. Erofeev[2], A.T. Gabdrakhmanov[3], A.A. Bobryshev[1]

[1]Kazan (Volga region) Federal University, 18, Kremlyovskaya St., Kazan, Republic of Tatarstan, 420008, Russia

[2]Ogarev National Research Mordovia State University, 430005, Republic of Mordovia, Saransk, 68 Bolshevistskaya street, Russia

[3]Kazan National Research Technical University named after A.N. Tupolev, 420111, Kazan, st. K. Marx, 10, Russia

✉ misharin_82@mail.ru

Abstract. In this paper, the influence of recovered high-density polyethylene on the tensile strength at break, elongation at break, hardness Shore D, flexural strength, and charpy impact energy of the polymer compositions has been studied, as well as the process has been developed for rotational moulding of holding tanks made of products of polyethylene recycling. The developed compositions have satisfactory physical-mechanical properties, and they can be used effectively to make holding tanks from products of polyethylene recycling with modifying plasticizer. Notably, the products have a lower cost as compared to products made of virgin polyethylene. The developed technology of holding tank production from products of polyethylene recycling addresses the important environmental problem regarding the management of polymer waste and the transition to a circular economy.
Keywords: polyethylene recycling, holding tanks, rotational moulding, waste management

Citation: Shafigullin LN, Romanova NV, Erofeev VT, Gabdrakhmanov AT, Bobryshev AA. Using products of polyethylene recycling for the production of holding tanks. *Materials Physics and Mechanics*. 2022;50(2): 266-274. DOI: 10.18149/MPM.5022022_7.

1. Introduction
Nowadays, the consumption of polymer materials is continuing to grow. Thus far, the worldwide consumption of large-tonnage polymer materials exceeds 265 million tons. Polyolefins account for more than 65 % of the demand.

Recycling of used plastics is a major issue in the polymer industry [1-17]. As estimated by NITsPURO (Research and Development Center for Management of Resource Saving and Waste, Russia), 34 % of polymer waste in Russia is polyethylene (PE), 20.4 % – polyethylene terephthalate (PET), 13.6 % – polyvinyl chloride (PVC), 7.6 % - polystyrene (PS), 7.4 % – polypropylene (PP), and 17 % – mixed materials on paper or board base.

Notably, PE waste has the highest collection and recycling rate (20 %), next are PP (up to 17 %), PET (12 %), PS (12 %), PVC (no more than 10 %) [18]. These materials can be stored in natural conditions for a long period of time due to their high environmental resistance. However, the recovery of polymer waste can be considered an important economic factor in terms of its environmental impact since the energy and materials are reused.

Polymer materials fit completely within the concept of a circular economy: the energy needed for the production of recycled granulate from waste averages only 10 % of the energy required for the production of virgin granulate. In this regard, the best polymers are polyethylene terephthalate and polystyrene, and the most challenging are polyolefins. An increase in the consumption of polyolefins and corresponding waste makes recycling a vital task in materials engineering.

2. Materials and methods

The components of the polymer compound were polymer composition RotoPol M115CB for rotational moulding (supplied by Polymer Corporation, Kazan, Russia) (Table 1); plasticizing masterbatchRevtol, grade PF0010/1-PE (made by the scientific and production company BARS-2, Saint Petersburg, Russia) (Table 2); recycled polymer composition RotoPol M115CB for rotational moulding (Fig. 1); pigment Iron Oxide Black 722 (made in PRC) (Table 3). The recycled composition was prepared in the following order: a collection of waste (used holding tanks and plastic water-filled barriers); washing of the waste to remove any external contaminations; crushing of the waste in the crusher (the size of a particle was 1-10 mm); grinding of the waste in MF-500 miller (the size of a particle was 0.1-0.5 mm); weighing of the components on the industrial scales. The recycled polymer composition consists of ground waste and pigment Iron Oxide Black 722; the components of the recycled polymer composition were mixed in the stirrer.

Table 1. Physical and mechanical properties of the polymer composition RotoPolM115CB

Index	Measurement method	Meaning
Melt flow index (190°C, 2.16 kg) g/10 min	ASTM D 1238	3.8
Density, g/cm^3	ASTM D 1505	0.938
Modulus of elasticity in bending, kgf/cm^2, not less than	ASTMD790	800
Izod impact strength at 23°C, J/m, not less than	ASTMD256	does not collapse

Fig. 1. Secondary polymer composition for rotational molding RotoPolM115CB (RotoPol M115CB) after grinding on a mixer

Table 2. Material properties: concentrate "BASCO"

The name of indicators	Norms according to TU 20.16.59-001-23124265-2018 with amendments. No. 7	Results
Granulometric composition	It is allowed to have granules smaller than 2 mm and more than 5 mm in amounts up to 1%	corresponds
Color (shade) of the colored polymer	Must match the color of a sample from an approved range or a control sample agreed upon between the manufacturer and the consumer	corresponds
Quality of staining	The sample must be evenly colored in tone without streaks and inclusions	corresponds
Bulk density of concentrate, g/cm^3	0.40-1.60	0.54
Conditions for determining the melt flow index of the concentrate		M-2.16 kgf, T-190°C, nozzle 2.095 mm
Melt flow rate g/10 min, not less	2,0	11
Heat resistance, °C, not less	200	240

Table 3. Physical and chemical parameters of iron oxide black pigment (IronOxideBlack 722)

The name of indicators	Specification
Appearance	Uniform black powder
Mass fraction of iron compounds in terms of Fe2O3, %	91.3
Mass fraction of substances soluble in water,%,	0.4
pH of water extract	5.0-8.0
Mass fraction of volatile substances, %	1.2
Residue after screening through a sieve No. 325, %	0.3
Light fastness	8 points
Relative coloring power, %	98.0

Six (6) different holding tank samples were made to study the properties of rotationally moulded products made of recycled polyethylene; to develop the best possible compositions to compensate for the shortcomings of recycled polyethylene; to develop the best possible rotational moulding process. Their compositions are given in Table 4. The amount of pigment for all the studied tanks was 15 g per tank (14 kg). The influence of pigment on the properties of the resulting materials was assumed as insignificant due to its small amount.

The holding tanks were made by rotational moulding using POLIVINIL rotational moulding machine. The optimum conditions of rotational processing were chosen empirically: primary starting rotational velocity within an oven was 3.7 rpm; primary secondary rotational velocity within an oven was 3.0 rpm; end primary rotational velocity within an oven was 3.7 rpm; end secondary rotational velocity within an oven was 3.7 rpm; clockwise rotation time was 3 minutes; counterclockwise rotation time was 3 minutes; moulding time was 43 minutes; moulding temperature was 260°C.

The following properties of the studied samples were determined: tensile strength at break, MPa (GOST 11262-2017 [19]); elongation at break, % (GOST 11262-2017 [19]); hardness, Shore D units (GOST 24621-2015 (ISO 868:2003) [20]); flexural strength, MPa (GOST 4648-2014 [21]); Charpy impact energy, kJ/m^2 (GOST 4647-15 [22]).

Testing for tensile strength at break and elongation at break according to GOST 11262 was performed on the samples of type 2. The tests were carried out using the universal testing machine LRXPlus. Testing for flexural strength according to GOST 4648 was performed on the samples of the recommended type: a length (*l*) of 80±2 mm, a width (*b*) of 10.0±0.2 mm, and a thickness (*h*) of 4.0±0.2 mm. The tests were carried out using the universal testing machine LRXPlus. Testing for Charpy impact energy according to GOST 4647 was performed on the unnotched samples of type 2. The tests were carried out using the impact test machine HIT 25P. Testing for Shore D hardness according to GOST 24621 was performed on the square samples of 30×30 mm. The tests were carried out using the hardness tester DigiTest. The structure of the samples was analyzed using the digital microscope Levenhuk DTX 700 LCD.

3. Results and discussion

One of the main problems with plastic waste is the presence of various additives: dyes, stabilizers, plasticizers, and special additives containing metals, mercury, lead, and cadmium. Incineration cannot solve the problem of disposal into the environment. Recycling may solve this problem. The main recycling methods are mechanical recycling, chemical recycling, and energy recovery. Land disposal restrictions play a significant role: landfill bans are in force in eight European countries out of eighteen where the polymer recycling rates are above the European average (28 %). In Japan, up to 83 % of polymer waste is recycled, mainly using energy recovery. In Russia, only 5-15 % of all household waste is subjected to recycling. The share of sorted useful fractions does not exceed 10-15 %, and one-fifth of them are polymers. In total, maximum of 350 kt of polymers go into recycling and more than 4.5 are buried. The ongoing reform of the legislation (amendments to Federal Law No. 89-FZ on Production and Consumption Waste) is promising fundamental changes in the management of municipal solid waste.

One of the base polymers is polyolefins – polymers of ethylene (PE). Products made of polyolefins are widely used in the construction and renovation of residential and non-residential buildings, as finish materials, for interior finishing of buildings and structures, for power and water supply utilities, for fabrication of various containers, and medical products. Polymer pipes are widely used in the public utility sector, pipeline construction, etc. Food and non-food packaging is an important application of polymers. The main methods of PE reprocessing into end products are injection moulding, extrusion moulding, rotational moulding, etc.

Holding tanks for portable toiler cubicles were selected as test objects. These tanks were made of PE, manufactured by rotational moulding, and had a capacity of a maximum of 250 l. Typically, these products are made from rotational moulding grades of virgin PE. The products shall meet the following requirements: satisfactory physical-mechanical properties; an operating temperature range of ±40°C; resistance to water and chemical media (human waste, detergents); light weight; high structural load capacity.

Recycled materials are known [1] to have different mechanical properties and ageing resistance as compared to virgin ones. Both recycled and virgin materials feature the same mechanism of degradation when subjected to mechanical forces, and physical and chemical effects, but with different reaction rates. For that reason, recycled materials are more sensitive to degradation when processed.

In view of this, the objective of this paper was to study the influence of recovered PE content in rotationally moulded compositions on the physical-mechanical properties, as well as to develop a process of rotational moulding for holding tanks using PE recycling products.

Table 4. Formulation and physical-mechanical properties of the studied samples
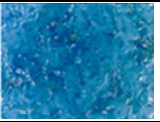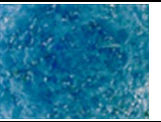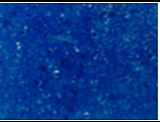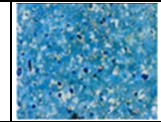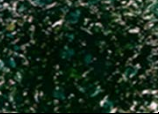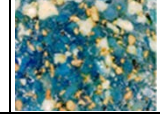
Sample	1	2	3	4	5	6
Formulation, mass fractions						
Virgin PE (RotoPol M115CB)	100	70	50	-	-	-
Recycled PR (RotoPol M115CB)	-	30	50	100	100	100
Plasticizing masterbatchRevtol, grade PF0010/1-PE 4	-	-	-	5	4	-
Physical mechanical properties						
Tensile strength at break (MPa)	16	16	16	16	16	15
Elongation at break (%)	81	80	74	73	74	28
Hardness (Shore D units)	22	22	22	22	22	22
Flexural strength (MPa)	16	16	18	17	18	20
Charpy impact energy (kJ/m^2)	51	51	42	46	52	35 Failure

Mechanical processing of PE is a very important segment of the recycling industry. The final properties and economic value of PE depend on the level of degradation during first use and on the recycling conditions. The main source of recovered high-density polyethylene (HDPE) is liquid containers. In this case, the molecular mass of used HDPE products remains quite high because degradation of materials of this type is rather low during short-term use. This factor means that the properties of recycled materials are close to the properties of virgin polymers.

Table 4 gives the formulations of the virgin and recycled HDPE compositions and their physical-mechanical properties.

The analysis of the macrostructures of the resulting compositions (Table 5) showed the formation of a heterogeneous structure for the recycled PE compositions (samples 4-6) as compared with the virgin PE samples.

Table 5. Micrographs of the sample surface

Sample	1	2	3	4	5	6
Outer side						
Inner side						

It is observed that the surface of the recycled PE samples has voids and air holes (samples 5 and 6), as well as different coloured inclusions, which may indicate the formation of a faulted macrostructure. Sample 6 has large different coloured inclusions, which is associated with the formation of a heterogeneous structure. Therefore, the important factor in getting high-quality recycled PE products is the introduction of additives to improve processing qualities and compatibility of broken-down particles.

Hence, mixtures of virgin and recycled polymers and mixtures to go to the waste are heterogeneous systems, which explains lower mechanical properties as compared to virgin materials. Phase separation in the melt and after cooling results from a poor interface between the components and local stress concentrations. Compatibilizers reduce interfacial tension in the melt by modifying the boundaries or by forming links between the phases. It induces the stabilization of a dispersed phase through its growth and agglomerating, increases the adhesion at the interface, and limits the phase separation in the solid state.

Table 4 shows that the majority of the physical-mechanical properties have relatively similar values as a result of the absence of significant degradation during production. Besides, there is a considerable difference in the elongation at break and the impact energy.

The properties-content curves for the mixtures of virgin PE/recycled PE were assessed. Figure 2 shows the dependence of the elongation at break, flexural strength, and Charpy impact energy on the content of recycled PE in the mixture. It should be noted that the values of both properties lie significantly lower than the values which have been calculated according to the rule of mixtures. It means that small quantities of recycled PE can cause a significant decrease in PE properties. It is known that the primary factors responsible for deviation from the rule of mixtures are the presence of other components in recycled PE, and differences in the morphology of the crystalline phase. Lower elongation at break (Fig. 2a) results from the degradation of PE, and weakening and discontinuity of the system followed by a negative impact on the properties. The impact properties (Fig. 2c) are more sensitive to the breakdown of polymer chains, which changes the morphology and causes a significant decrease in the impact properties. Notably, the products made of 100% recycled PE feature a catastrophic decrease in impact strength. The flexural strength increases slightly, which is associated with the formation of partially cross-linked structures (Fig. 2b).

a)

b)

c)
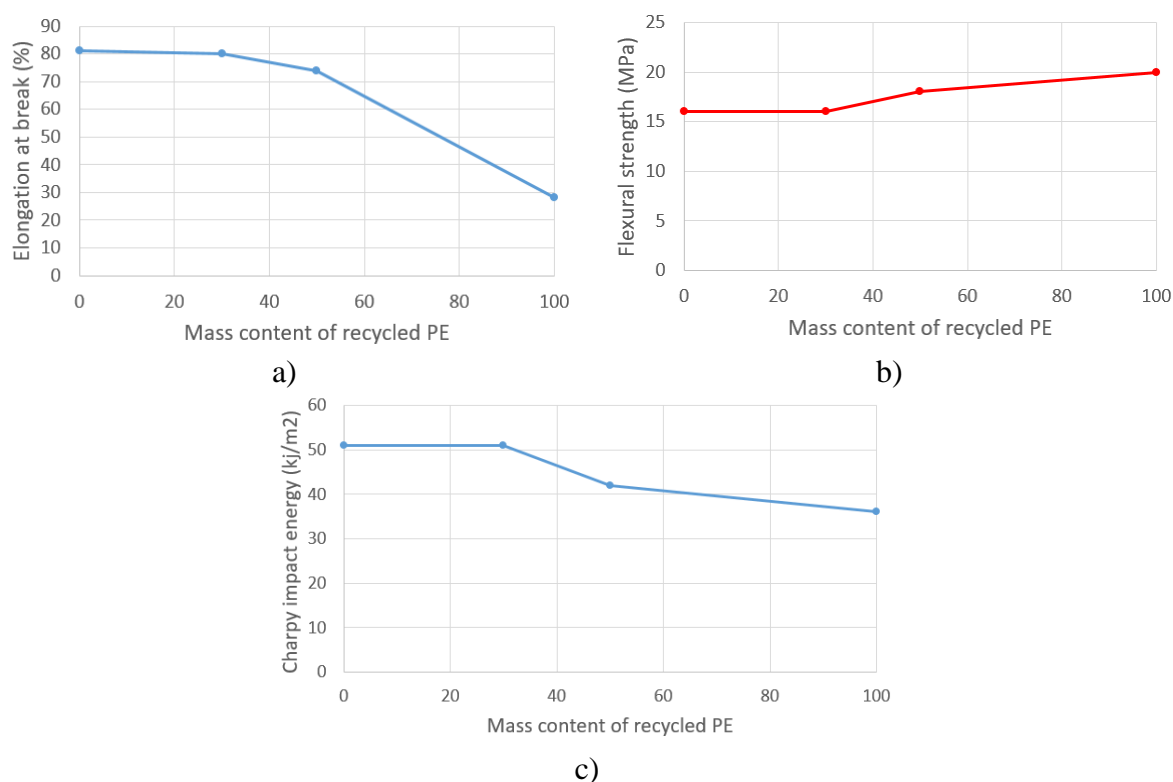
Fig. 2. Change in the properties due to an increase in the content of recycled PE:
a) elongation at break; b) flexural strength; c) Charpy impact energy

Therefore, the differences in the physical-mechanical properties depending on the content of recycled PE result from the changes in the structure and morphology.

The addition of the compatibilizer by BARS-2 (plasticizing masterbatchRevtol, grade PF0010/1-PE 4) showed the effectiveness of this system. Notably, the physical-mechanical properties of the product made from recycled PE with 5 parts by weight of plasticizer (sample 5, Table 4) are not inferior to those of the products made of virgin PE (sample 1, Table 4).

The addition of the compatibilizer by BARS-2 (plasticizing masterbatch Revtol, grade PF0010/1-PE 4) showed the effectiveness of this system. Notably, the physical-mechanical properties of the product made from recycled PE with 5 parts by weight of plasticizer (sample 5, Table 4) are not inferior to those of the products made of virgin PE (sample 1, Table 4).

4. Conclusions

The comprehensive studies showed that it was possible to make holding tanks from recycled PE using modifying plasticizer (sample 4). The physical-mechanical properties of sample 4 are not inferior to those of samples 1-3 which were made from virgin PE. Ina ddition, sample 4 has high application properties. The specialists of Polymiz-Tara LLC (Russian Federation, Kazan) decided to introduce a polymer composition (sample 4) into the technology for manufacturing storage tanks from recycled PE by rotational molding (Fig. 3).

Fig. 3. Storage Tank (sample 4)

Therefore, the developed technology of holding tank production by rotational moulding using products of polyethylene recycling ensures high-quality products, a lower product cost as compared to the products made of virgin polyethylene, and addresses the important environmental problem regarding the management of polymer waste and transition to a circular economy.

References
1. LA Mantle F. *Recycling of plastics*. Saint Petersburg: Profession; 2007.
2. Kuvardin NV, Ageeva LS, Kireeva NE. Solving the problems of polymer recycling within the framework of the trends of modern technology development. In: *Fundamental and Applied Research in Chemistry and Ecology - 2021. Collection of scientific articles of the International Scientific and Practical Conference of Students, Postgraduates and Young Scientists*. Kursk: Southwestern State University; 2021. p.96-99. (In Russian)
3. Cruz F, Lanza S, Boudaoud H, Hoppe S, Camargo M. Polymer recycling and additive manufacturing in the context of open source software: process optimization and methods. *Environmental economics*. 2018;5: 112-129. (In Russian)
4. Shapovalov VM, Grigoriev AY. Recycling and utilization of multicomponent polymer systems based on secondary thermoplastics. *Polymeric Materials and Technologies*. 2021;7(3): 6-19. (In Russian)
5. Bobovich BB, Popova EV. Utilization of automotive components made of plastics. *Life Safety.* 2020;4(232): 37-40. (In Russian)
6. Timofeenko AA, Shapovalov VM. Polyurethanes: market analysis, problems and prospects of recycling. *Polymeric Materials and Technologies*. 2021;7(4): 6-16. (In Russian)

7. Chursova LV, Tsybin AI, Grebeneva TA, Panina NN. Recycling of epoxy binders and polymer composite materials based on them (review). *News of Materials Science. Science and Technology.* 2018;5-6(31): 55-64. (In Russian)

8. Panfilov DA. Chemical recycling of polyethylene terephthalate as a method for obtaining effective modifiers of polymeric materials. *Plastic Masses.* 2021;7-8: 25-30. (In Russian)

9. Shafigullin LN, Romanova NV, Sokolova YA, Aloyan RM, Mirgasimov II, Akulova MV. Secondary processing of products from polyurethane foam. *Izvestiya Vysshikh Uchebnykh Zavedenii, Seriya Teknologiya Tekstil'noi Promyshlennosti.* 2019;6: 90-93.

10. Shafigullin LN,. Romanova NV, Gabdrakhmanov AT, Korchagin OP, Agashkin DA. Recycling components made of polyurethane foam. *IOP Conf. Series: Materials Science and Engineering.* 2020;915: 012051.

11. Thompson RC, Moore CJ, Saal FS, Swan SH, Plastics, the environment and human health: Current consensus and future trends. *Philosophical Transactions of the Royal Society B: Biological Sciences.* 2009;364(1526): 2153-2166.

12. Al-Salem SM, Lettieri P, Baeyens J. Recycling and recovery routes of plastic solid waste (PSW): A review. *Waste Management.* 2009;29(10): 2625-2643.

13. Hahladakis JN,. Velis CA, Weber R, Iacovidou E, Purnell P. An overview of chemical additives present in plastics: Migration, release, fate and environmental impact during their use, disposal and recycling. *Journal of Hazardous Materials.* 2018;344: 179-199.

14. Ragaert K, Delva L, Van Geem K. Mechanical and chemical recycling of solid plastic waste. *Waste Management.* 2017;69: 24-58

15. Siddique R, Khatib J, Kaur I. Use of recycled plastic in concrete: A review. *Waste Management.* 2008;28(10): 1835-1852.

16. Paszun D, Spychaj T. Chemical Recycling of Poly(ethylene terephthalate). *Industrial and Engineering Chemistry Research.* 1997;36(4): 1373-1383.

17. Singh N, Hui D, Singh R, Ahuja IPS, Feo L, Fraternali F. Recycling of plastic solid waste: A state of art review and future applications. *Composites Part B: Engineering.* 2017;115: 409-422.

18. Gaev FF, Devyatkin VV. *Problems of recycling polymer waste in Russia.* Available from: https://www.waste.ru/modules/section/item.php?itemid=8&keywords=%D0%93%D0%B0% D0%B5%D0%B2+%D0%A4.%D0%A4.+%D0%94%D0%B5%D0%B2%D1%8F%D1%82% D0%BA%D0%B8%D0%BD+%D0%92.%D0%92. (In Russian) [Accessed 04th March 2005].

19. Standard GOST 11262-2017 (ISO 527-2:20212). *Plastics. Tensile test method.* Moscow; Standartinform Publ.; 2018. (In Russian)

20. Standard GOST 24621-91. *Plastics and ebonite. Determination of indentation hardness by means of a durometer (Shore hardness).* Moscow: Izdatelstvo standartov Publ.; 1992. (In Russian)

21. Standard GOST 4648-2014 (ISO 178:2010). *Plastics. Method of static bending test.* Moscow: Standartinform Publ; 2015.

22. Standard GOST 4647-15 (ISO 179-1:2010, NEQ). *Plastics. Method for determination of Charpy impact strength.* Moscow: Standartinform Publ; 2017.

23. Standard GOSTR 56724-2015 (ISO 11357-3:2011).*Plastics. Differential scanning calorimetry (DSC). Part 3. Determination of temperature and enthalpy of melting and crystallization.* Moscow: StandartinformPubl; 2016.

THE AUTHORS

Shafigullin L.N.
e-mail: misharin_82@mail.ru
ORCID: 0000-0002-7947-801X

Romanova N.V.
e-mail: romnatav@yandex.ru
ORCID: 0000-0003-2484-346X

Erofeev V.T.
e-mail: fac-build@adm.mrsu.ru
ORCID: 0000-0001-8407-8144

Gabdrakhmanov A.T.
e-mail: veyron000@mail.ru
ORCID: 0000-0003-4667-8311

BobryshevA.A.
e-mail: borisov800@mail.ru
ORCID: 0000-0003-2106-6271

Synthesis and characterization of polymeric hydrogel-based nanoporous composite and investigation of its temperature-dependent drug release activity

Akhilesh Kumar Maurya, Shagun Varshney, Nidhi Mishra[✉]

Department of Applied Sciences, Indian Institute of Information Technology, Allahabad, Prayagraj, Uttar Pradesh, 211012, India

[✉] nidhimishra@iiita.ac.in

Abstract. Hydrogels are 3-dimensional polymeric networks that undergo swelling when placed in an aqueous medium. The hydrogel-based polymers can respond to changes in the surrounding like temperature, pressure, pH, etc. Widespread cross-linking in hydrogels provides it with robustness, propensity for water, and better mechanical properties. The present work reports the one-pot chemical synthesis of a co-polymeric hydrogel-based composite using 2-HEMA (hydroxyethyl methacrylate), PEGMA (Polyethylene glycol), and PNIPAM (Poly (N-isopropyl acrylamide)). Extensive water retention ability and biocompatibility are some distinguishing features that enable it to be used for various biomedical applications. The hydrogel was characterized using X-ray diffraction analysis for its crystalline nature, scanning electron microscopy for surface morphology and pore size, and Fourier transform infrared spectroscopy for functional group analysis. Drug loading and release activity was performed and analyzed by Ultraviolet-Visible spectroscopy.
Keywords: composite, characterization, drug loading, hydrogel, thermos-responsive polymer

Citation: Akhilesh Kumar Maurya, Shagun Varshney, Nidhi Mishra. Synthesis and characterization of polymeric hydrogel-based nanoporous composite and investigation of its temperature-dependent drug release activity. *Materials Physics and Mechanics*. 2022;50(2): 275-286. DOI: 10.18149/MPM.5022022_8.

1. Introduction
Hydrogels are a network of polymer(s) that can absorb water and still can remain insoluble in water. They show swelling behavior after imbibing water in their pores [1-4]. Permeability and water retention properties are the characteristic features of such hydrogels. They undergo hydration due to the presence of hydrophilic groups and are also observed to exhibit viscoelastic properties [5]. The extensive cross-linking between the groups makes them insoluble and gives them a robust structure and enhanced mechanical properties [6-8]. The cross-linking may be due to the chemical and or physical interaction between the covalent bonds. The water retention properties of hydrogels make them excellent biocompatible agents [9,10], where their hydrophilic, rubber-like nature causes negligible tissue irritation. It also

prevents them from adhering to the surface of cells and proteins [11,12]. Hydrogels may be chemically stable or degrade depending on the chemical composition and cross-linking extent [13]. Natural polymers such as gelatin, chitosan, agar, etc., and synthetic polymers like polyacrylamide, methacrylate esters, etc., can prepare such hydrogels. They can be synthesized using polymer-polymer cross-linking, copolymerization, and reactive precursors [14-17]. Hydrogels can be classified as homopolymer (single monomer), copolymer (more than one monomer), and multi-polymer (more than one polymer) [18-20].

Hydrogels are responsive to stimuli like pressure, pH, reagent concentration, and temperature [21-23]. The behavior of polymers adapting to structural changes in response to physical or chemical stimuli makes them suitable for synthesizing smart polymers. Thermo-responsive and pH-sensitive polymeric hydrogels are one of the essential identities being used for several applications [24-27]. Thermo-responsive polymers belong to the class of smart polymers that respond to temperature changes. This makes them readily available for controlled drug delivery and other medical applications. Thermo-responsive polymers may either collapse or expand around their critical temperature. PNIPAM (Poly (N- isopropyl acrylamide)) is a thermo-responsive polymer that has been used for drug delivery for decades [28-30]. It transitions from hydration to dehydration at a lower critical solution temperature (LCST) of 32ºC. Below the LCST, PNIPAM exists in a fully swollen state, but above the LCST, it shrinks [31-34].

HEMA (Poly-hydroxy-ethyl-methacrylate) is a hydrophilic and stable polymer formed from the monomer hydroxyethyl methacrylate. It has received considerable recognition for years owing to its simple synthesis and applications in biomedical engineering [35-38]. PEGMA (Polyethylene glycol) does not initiate an immune response and even does not adhere to proteins in the body [39]. Although hydrophobic, it becomes hydrophilic and swells up by water absorption by side groups. This polymer has been reported to have excellent biocompatibility and properties similar to living tissues [40-42]. It also has a hydroxyl functional group that can be utilized for protein conjugation. The conjugation of PNIPAM is done with methacrylate to enhance the mechanical property of the hydrogels [43-46]. Hydrogels have been used in medical applications [47-50], which include the preparation of contact lenses [51,52], tissue engineering [53,54], drug delivery [55-57], etc.

In the present study, one-pot synthesis of hydrogel-based polymeric composite has been carried out using 2-HEMA, PEGMA, and PNIPAM as the starting precursors. The synthesis and characterization of the hydrogel are also accompanied by the investigation of the drug release activity of curcumin observed in the simulated body fluid (SBF). Several characterization techniques, including X-ray diffraction (XRD), Scanning Electron Microscopy (SEM), Fourier transform infrared spectroscopy (FTIR), and Ultraviolet-Visible (UV-Vis) Spectroscopy, have been used to analyze the structural, morphological, and physio-chemical characteristics of the synthesized composite.

2. Material and methods

For the synthesis of hydrogel, the chemical reagents required were 2-HEMA (2-Hydroxy-methacrylate, 99% assay), NIPAM (N-Isopropylacrylamide, 99% assay), PEGMA (poly (ethylene glycol) methacrylate, 99.5% assay), APS (Ammonium persulfate, 99% assay), MBA (N, N'-Methylene Bis(acrylamide), 99% assay), and nitrogen gas. For the preparation of simulated body fluid, NaCl (Sodium chloride, 99% assay), $NaHCO_3$ (Sodium bicarbonate, 99.5% assay), KCl (Potassium chloride, 99% assay), Na_2HPO_4 (Sodium phosphate, 99% assay), $MgCl_2.6H_2O$ (Magnesium chloride hexahydrate, 99% assay), HCl (hydrochloric acid, 99% assay), $CaCl_2.2H_2O$ (Calcium chloride dehydrate, 99% assay), Na_2SO_4 (Sodium sulfate, 99.5% assay), TRIS tris(hydroxymethyl)aminomethane (99.5% assay), and Curcumin (99.5% assay) were used for investigating the drug release activity. All chemicals used were of

analytical grade and were purchased from Merck. & Co. Double-distilled water was used throughout the experiment.

Synthesis of hydrogel-based polymeric composite. NIPAM (1.13 g), 2-HEMA (1.2 mL), and PEGMA (3.26 mL) were mixed in a round bottom flask under continuous stirring. After some time, 1% APS solution (60 µL) was added as an indicator for reaction, and 5% of MBA (280 µL) was added as a cross-linking agent. The flask was sealed under the continuous flow of nitrogen gas (to provide an inert atmosphere for reaction). Flask was then transferred to the water bath at 80 ℃ for 3.5 h. to promote the polymerization reaction. After synthesis, the hydrogel was placed in deionized water for three days, and the water was periodically replaced with fresh double-distilled water. The experimental setup for the synthesis of hydrogel is shown in Fig. 1.
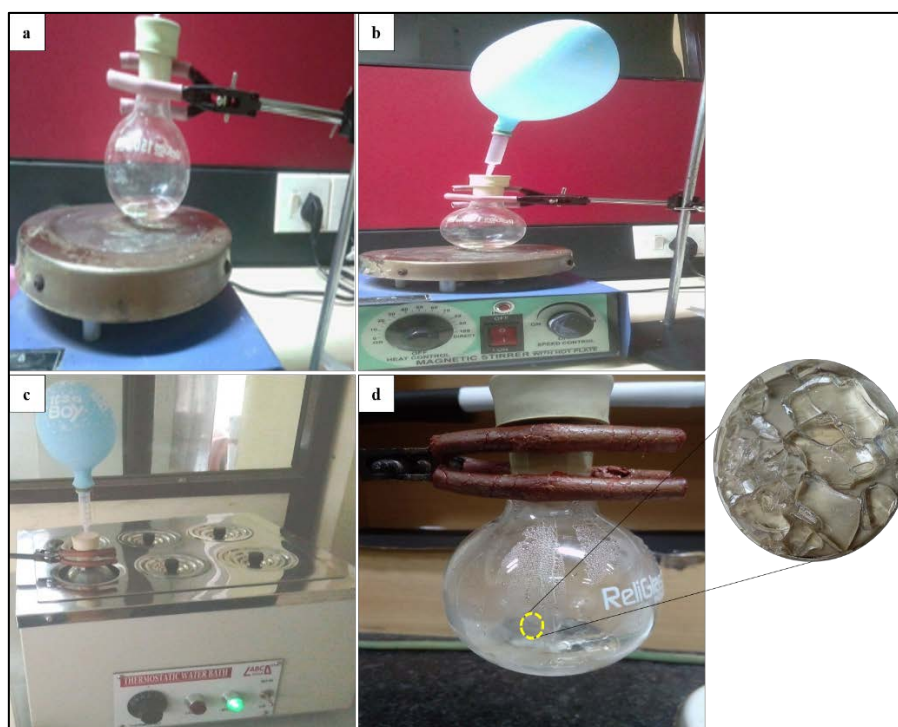
Fig. 1. (a), (b), (c), and (d) Laboratory synthesis of polymeric hydrogel

Preparation of simulated body fluid. NaCl (3.3 g), NaHCO$_3$ (1.1 g), KCl (0.19 g), Na$_2$HPO$_4$ (0.09 g), and MgCl$_2$.6H$_2$O (0.15 g) were added to a flask, and mixed, thoroughly in 350 mL of double distilled water. After that, 7.5 mL of HCl was added to the above mixture, followed by the addition of CaCl$_2$.2H$_2$O (0.18 g), Na$_2$SO$_4$ (0.04 g), and TRIS (3.03 g). HCl (12.5 mL) was added to maintain the desired pH of SBF. The flowchart for the synthesis of SBF is shown in Fig. 2.

Drug loading and release analysis. Curcumin (100 mg) was dissolved in 5 mL of acetone solution, and 20 mg of synthesized hydrogel was added to the solution and kept for 24 h. to load the curcumin into the hydrogel. The percentage of drug-loaded was evaluated by taking the weight of the loaded hydrogel. The flowchart for loading drugs into the hydrogel composite is shown in Fig. 3.

The drug-hydrogel complex was placed in 20 mL of SBF for 30 min under continuous stirring for a definite time interval. After that, the absorption of SBF was analyzed by UV-Vis spectroscopy. The mixture temperature was increased by 10 ℃ for the next reading. Further, the temperature was raised by 5 ℃ up to 50 ℃, and the readings were again recorded. The experimental setup for loading the drug is shown in Fig. 4.

```
┌─────────────────────────────────────────────┐
│           Deionized water (350 ml)           │
└─────────────────────────────────────────────┘
                        ↓
┌─────────────────────────────────────────────┐
│ NaCl, NaHCO₃, KCl, Na₂HPO₄, MgCl₂.6H₂O added to water │
└─────────────────────────────────────────────┘
                        ↓
┌─────────────────────────────────────────────┐
│                Addition of HCl               │
└─────────────────────────────────────────────┘
                        ↓
┌─────────────────────────────────────────────┐
│   Addition of CaCl₂.2H₂O, Na₂SO₄ and TRIS    │
└─────────────────────────────────────────────┘
                        ↓
┌─────────────────────────────────────────────┐
│          Temperature increased to 37 °C      │
└─────────────────────────────────────────────┘
                        ↓
┌─────────────────────────────────────────────┐
│            Addition of left-over HCL         │
└─────────────────────────────────────────────┘
                        ↓
┌─────────────────────────────────────────────┐
│        Addition of left-over water (150 ml)  │
└─────────────────────────────────────────────┘
                        ↓
┌─────────────────────────────────────────────┐
│        Stored in refrigerator for further use│
└─────────────────────────────────────────────┘
```
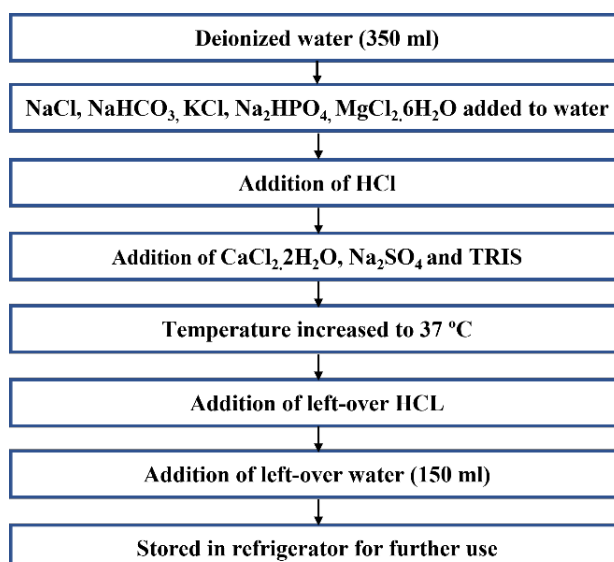
Fig. 2. Flowchart for the synthesis of simulated body fluid

```
┌─────────────────────────────────────────────┐
│               Hydrogel (20 mg)               │
└─────────────────────────────────────────────┘
                        ↓
┌─────────────────────────────────────────────┐
│          Measured amount of curcumin         │
└─────────────────────────────────────────────┘
                        ↓
┌─────────────────────────────────────────────┐
│          Curcumin dissolved in acetone       │
└─────────────────────────────────────────────┘
                        ↓
┌─────────────────────────────────────────────┐
│     Hydrogel placed in curcumin for 24 hours │
└─────────────────────────────────────────────┘
                        ↓
┌─────────────────────────────────────────────┐
│ Drug loading observed by measuring the increase in weight │
└─────────────────────────────────────────────┘
```
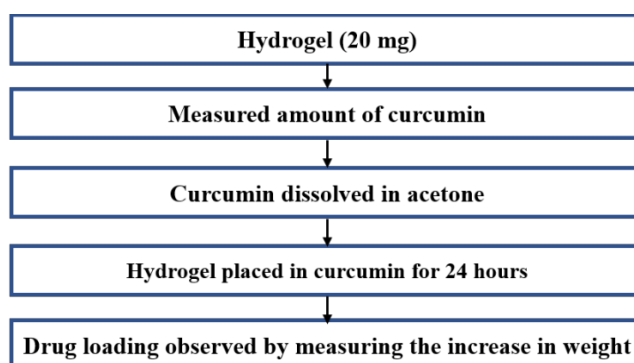
Fig. 3. Flowchart for drug loading and release analysis
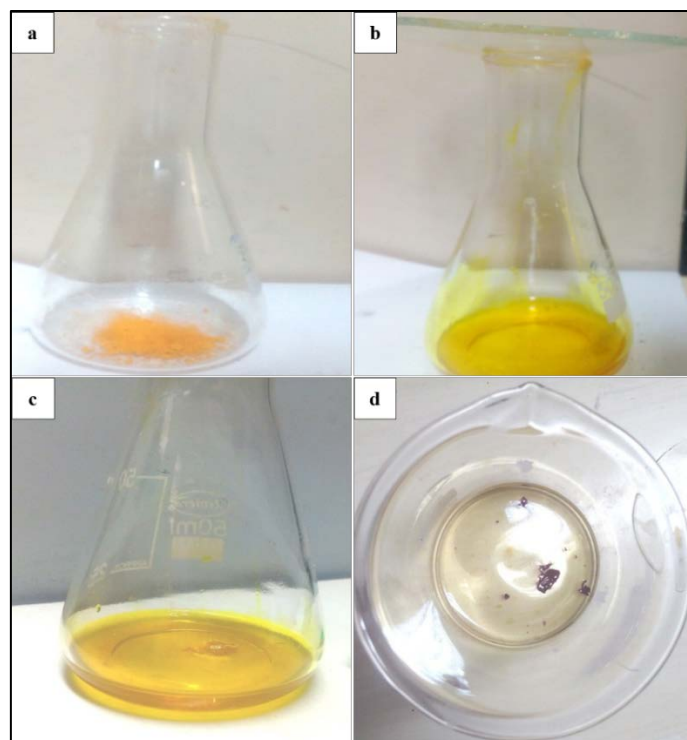
Fig. 4. Experimental setup for the loading of drug

3. Results and discussion

X-Ray diffraction analysis. The most frequent type of XRD used to examine solid-state materials is powder diffraction, which may accept samples in powder, thin film, or even in bulk form. Most investigations on supramolecular hydrogels have concentrated on this feature of XRD, which is an excellent technique for aiding in the analysis of crystalline materials in general [58]. It is worth noting that there are other varieties of XRD, including wide-angle X-ray diffraction and small-angle X-ray scattering, which are being increasingly utilized to analyze the structure of biological macromolecules, including hydrogels [59]. XRD analysis was performed to investigate the crystalline and structural characteristics of the hydrogel composite (Model: Rigaku Miniflex 600 Desktop X-Ray Diffraction System). The diffraction pattern of the hydrogel composite is shown in Fig. 5. The intensity of diffraction for the samples was recorded at a wavelength of 1.541 Å with a diffraction angle (2θ) ranging from $0°$ to $80°$ with a scanning rate of $5°$/ min. A pure sample of synthesized hydrogel does not exhibit any sharp peaks, as shown in the diffraction patterns. The absence of sharp crystalline peaks reveals the amorphous nature of the synthesized composite. A single broad peak at a $2\theta = 20°$ angle attributes to the synthesized hydrogel polymeric network, which is in accordance with Varaprasad *et al.* [60].
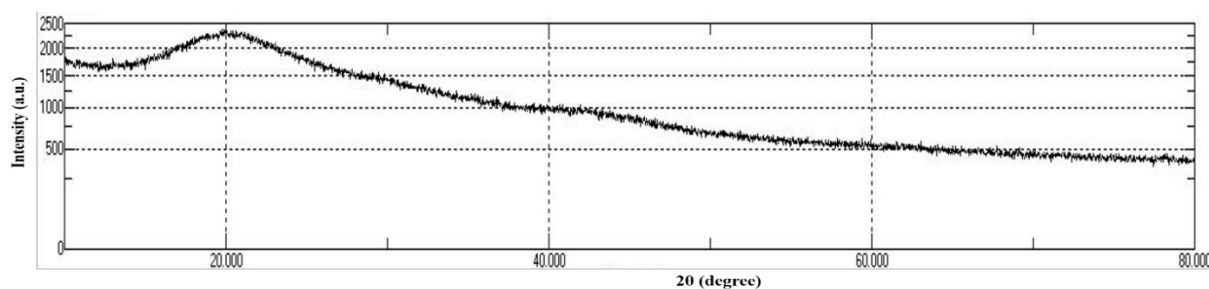
Fig. 5. Diffraction patterns for the synthesized hydrogel composite

Scanning electron microscopy analysis. Electron microscopes use a stream of electrons to provide high-resolution pictures of materials. However, the analyte might be damaged as a result. To eliminate beam interference, a vacuum is required, which implies samples must be dried before imaging. Although it is less detailed and only gives surface imaging of materials, the method does not need considerable sample preparation for frequent usage. While SEM offers information about the surface of hydrogel, focused ion beam -SEM can be employed for obtaining a 3D image for the same. The surface morphology and pore size of the hydrogel composite were analyzed by SEM (Model: JSM-6490LV, JEOL, JAPAN). The surface morphology of hydrogel depicted the compactness of structure and arrangement of monomers for polymer synthesis. As seen in Figures 6, (a), (b), (c), and (d), porous structure with rough surface morphology can be observed. The hydrogel was observed to have well cross-linked monomers to form a polymeric network. At a much higher magnification, pore size with an average diameter between 23-104 nm for the synthesized hydrogel can be observed in Fig. 6 (d). The pores allow water, drug, and other molecules to be absorbed in the swollen state. When dried, water molecules get evaporated, and the entrapment of the drug takes place in the hydrogel.
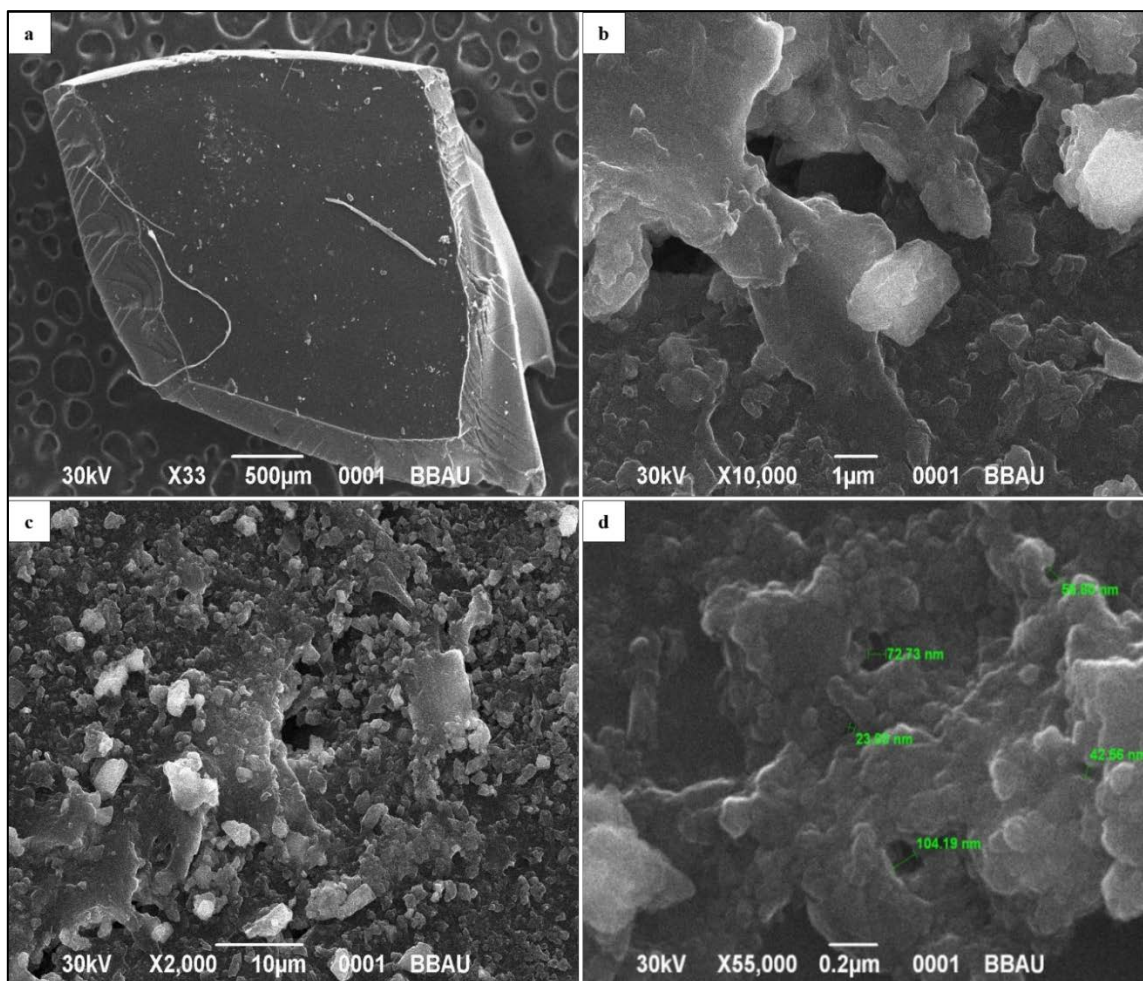
Fig. 6. Scanning electron micrographs for morphological analysis of the synthesized hydrogel

Fourier transform infrared spectroscopy analysis. Although it uses infrared light, FTIR spectroscopy works similarly to UV–vis spectroscopy. FTIR infers the absorbance spectrum precisely by applying the Fourier transform process to absorbance measurements of numerous wavelengths of light at the same time. Certain stretching vibrations on FTIR spectra correlate to certain functional groups, allowing the approach to describe the atomic structure of the hydrogel or solution or establish its composition in other ways [61]. FTIR spectroscopy (Model: NicoletTM6700, Thermo Scientific, USA) in attenuated total reflection mode in the range from 4000 to 500 cm^{-1} with 4 cm^{-1} as the resolution. The FTIR spectrum reveals the different functional groups in the synthesized hydrogel composite. The FTIR spectrum exhibited different peaks at 3429.7 cm^{-1}, 2915.3 cm^{-1}, 1725.6 cm^{-1}, 1643.5 cm^{-1}, 1552.8 cm^{-1}, 1425.5 cm^{-1}, 1358.8 cm^{-1}, 1161.6 cm^{-1}, 1067.5 cm^{-1} and 605.1 cm^{-1} is shown in Fig. 7. The peak at 3429.7 cm^{-1} is a characteristic of the hydroxyl-based copolymer, indicating the presence of 2-HEMA. The peak at 2915.3 cm^{-1} is attributed to carboxylic acid in the monomers. The peak at 1725.6 cm^{-1} corresponds to the carbonyl group present in all monomers. The peak at 1643.5 cm^{-1} represents the stretching in alkenes (C=C). The peak at 1552.8 cm^{-1} indicates the stretching of C=C aromatic/conjugate units, revealing the presence of aromatic groups in the hydrogel. The peak at 1425.5 cm^{-1} depicts the stretching of alkane in the polymeric network. 1358.8 cm^{-1} indicates the presence of (C-N) stretch of PNIPAM. The peak value of 1161.6 cm^{-1} and 1067.5 cm^{-1} represents O-H groups present in PEGMA. The functional groups' monomers are attracted to each other and form polymeric networks with the pores, which can absorb/entrap the molecules and release them to the desired place.
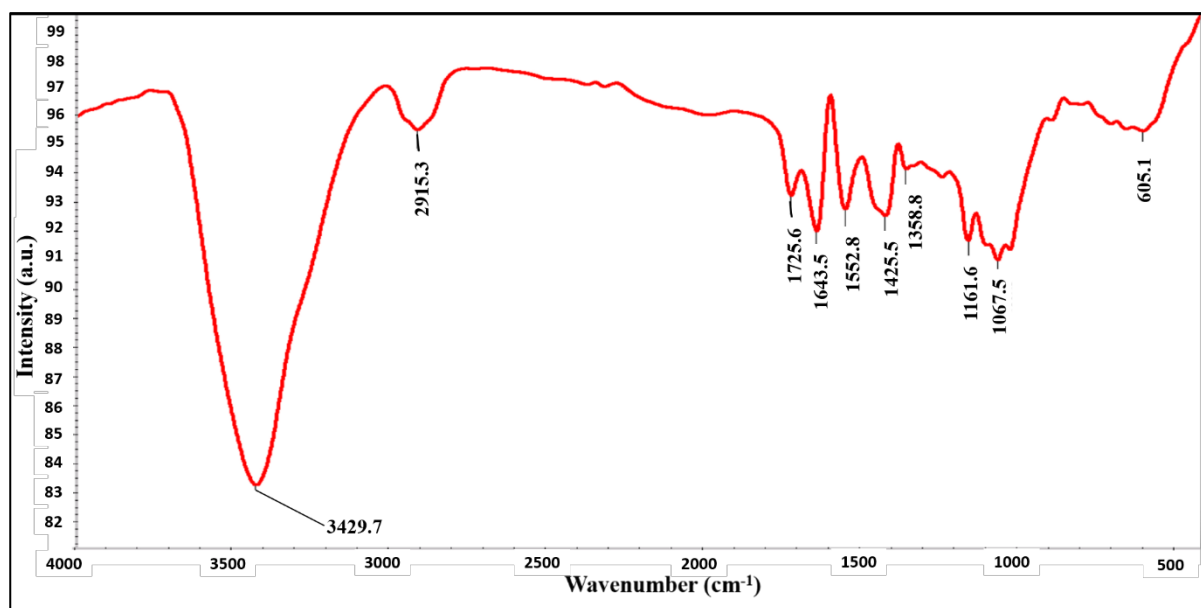
Fig. 7. Infrared spectrum for the analysis of functional groups in the synthesized hydrogel

Swelling behavior, drug loading, and drug release profile analysis. Swelling behavior studies were performed on the synthesized hydrogel composite. The dry weight of hydrogel was 20 mg; after incorporating water within its network, the weight increased to 50 mg. Thus, using the formula for calculating the swelling percentage, the degree of swelling of the hydrogel sample was found to be 75%. After the polymerization reaction, the hydrogel was soaked in water, and a slow increase in the volume was observed. When the swollen hydrogel was dried in an oven at 50 ºC, the polymeric network of hydrogel collapsed, releasing the retained water molecules, and a shrinking in size was observed. The dry weight of hydrogel was taken, which was observed to be 20 mg. Then after placing it in curcumin solution in acetone for 24 h, the weight increased to 32 mg. The percentage Loading efficiency is computed to be around 60% by using the formula below.

$$Drug\ loading\ \% = \frac{HD-HO}{HO} \times 100.$$

In the above equation, HO – weight of the dry hydrogel, HD – weight of the drug-loaded hydrogel. UV-Vis analysis for drug release is shown in Fig. 8, and the temperature-dependent drug release profile is shown in Fig. 9.
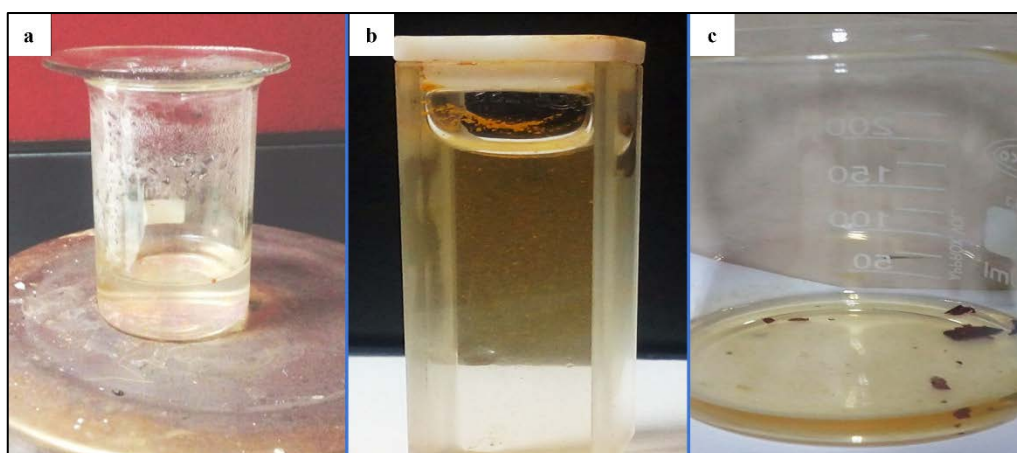
Fig. 8. Ultraviolet-Visible analysis for the release of drug by hydrogel composite
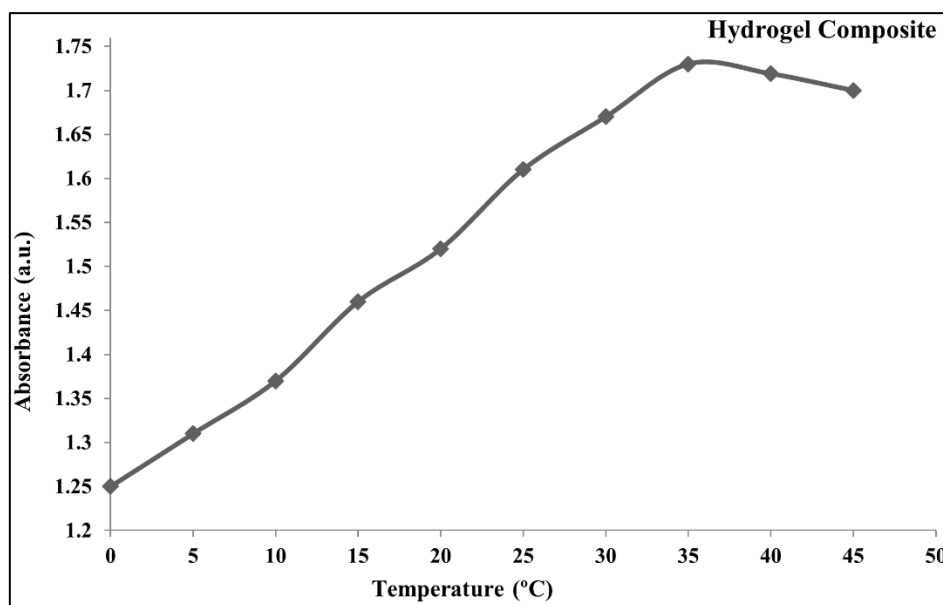
Fig. 9. Temperature-dependent drug release profile for hydrogel composite

The hydrogel was placed in SBF for releasing the drug and calculating its drug release percentage. Absorbance readings were taken at different temperatures. The hydrogel composite started to remove the drug as soon as it was placed in SBF. The absorbance value was observed to increase, indicating the release of curcumin slowly until the temperature reached 35 °C. Above 35 °C, absorbance reading almost became stagnant. Thus, the release percentage was computed and found to be around 26.47 %. Therefore, further studies can be carried out to optimize the efficacy of drug release. The release percentage was calculated by using the formula below:

$$Release \% = \frac{\text{Absorbance at final temperature} - \text{Absorbance at initial temperature}}{\text{Absorbance at final temperature}} \times 100.$$

4. Conclusions

Hydrogel composite was successfully synthesized using monomer of 2-HEMA, PEGMA, and NIPAM with pores lying within the nanometer range. Synthesized hydrogel responded to external stimuli like pH, temperature, etc. Hydrogels with cross-linked structures and amorphous nature were observed to have various functional groups. A study on the swelling behavior was also performed on the hydrogel by soaking it in an aqueous solution, and it exhibited a swelling percentage of 75%. Curcumin, an anti-cancer drug, was successfully loaded into the hydrogel, and the release characteristics were observed in SBF. Hydrogel composite showed sustained release of curcumin in SBF. Therefore, it can be further tailored to increase the loading and release efficiency of the drug. It can also be used for delivering therapeutic medications to targeted sites shortly.

References

1. Motamedi E, Motesharezedeh B, Shirinfekr A, Samar SM. Synthesis and swelling behavior of environmentally friendly starch-based superabsorbent hydrogels reinforced with natural char nano/micro particles. *Journal of Environmental Chemical Engineering.* 2020;8(1): 103583.
2. Shoukat H, Buksh K, Noreen S, Pervaiz F, Maqbool I. Hydrogels as potential drug-delivery systems: Network design and applications. *Therapeutic Delivery.* 2021;12(5): 375-396.

3. Ahmadi M, Zholobko O, Wu XF. Inhomogeneous swelling behavior of a bi-layered spherical hydrogel containing a hard core. *Journal of Applied Physics.* 2020;128(4): 044703.

4. Rehman TU, Bibi S, Khan M, Ali I, Shah LA, Khan A, Ateeq M. Fabrication of stable superabsorbent hydrogels for successful removal of crystal violet from waste water. *RSC Advances.* 2019;9(68): 40051-40061.

5. McKenzie M, Betts D, Suh A, Bui K, Kim LD, Cho H. Hydrogel-based drug delivery systems for poorly water-soluble drugs. *Molecules.* 2015;20(11): 20397-20408.

6. Kopecek J. Hydrogels: From soft contact lenses and implants to self-assembled nanomaterials. *Journal of Polymer Science Part A: Polymer Chemistry.* 2009;47(22): 5929-5946.

7. Bao Z, Xian C, Yuan Q, Liu G, Wu J. Natural polymer-based hydrogels with enhanced mechanical performances: preparation, structure, and property. *Advanced Healthcare Materials.* 2019;8(17): 1900670.

8. Ali A, Ahmed S. Recent advances in edible polymer based hydrogels as a sustainable alternative to conventional polymers. *Journal of Agricultural and Food Chemistry.* 2018;66(27): 6940-6967.

9. Zander ZK, Hua G, Wiener CG, Vogt BD, Becker ML. Control of Mesh Size and Modulus by Kinetically Dependent Cross-Linking in Hydrogels. *Advanced Materials.* 2015;27(40): 6283-6288.

10. Zhang D, Tang Y, Zhang Y, Yang F, Liu Y, Wang X, Yang J, Gong X, Zheng J. Highly stretchable, self-adhesive, biocompatible, conductive hydrogels as fully polymeric strain sensors. *Journal of Materials Chemistry A.* 2020;8(39): 20474-20485.

11. Kamath KR, Park K. Biodegradable hydrogels in drug delivery. *Advanced Drug Delivery Reviews.* 1993;11(1-2): 59-84.

12. Yu J, Wang K, Fan C, Zhao X, Gao J, Jing W, Zhang X, Li J, Li Y, Yang J, Liu W. An Ultrasoft Self-Fused Supramolecular Polymer Hydrogel for Completely Preventing Postoperative Tissue Adhesion. *Advanced Materials.* 2021;33(16): 2008395.

13. Hoare TR, Kohane DS. Hydrogels in drug delivery: Progress and challenges. *Polymer.* 2008;49(8): 1993-2007.

14. Elmehbad NY, Mohamed NA. Terephthalohydrazido cross-linked chitosan hydrogels: Synthesis, characterization and applications. *International Journal of Polymeric Materials and Polymeric Biomaterials.* 2022;71(13): 969-982.

15. Li S, Wang L, Yu X, Wang C, Wang Z. Synthesis and characterization of a novel double cross-linked hydrogel based on Diels-Alder click reaction and coordination bonding. *Materials Science and Engineering: C.* 2018;82: 299-309.

16. Elsayed MM. Hydrogel preparation technologies: relevance kinetics, thermodynamics and scaling up aspects. *Journal of Polymers and the Environment.* 2019;27(4): 871-891.

17. Zainal SH, Mohd NH, Suhaili N, Anuar FH, Lazim AM, Othaman R. Preparation of cellulose-based hydrogel: A review. *Journal of Materials Research and Technology.* 2021;10: 935-952.

18. Hua J, Ng PF, Fei B. High-strength hydrogels: Microstructure design, characterization and applications. *Inc. J. Polym. Sci., Part B: Polym. Phys.* 2018;56: 1325-1335.

19. Sharma S, Tiwari S. A review on biomacromolecular hydrogel classification and its applications. *International Journal of Biological Macromolecules.* 2020;162: 737-747.

20. Bashir S, Hina M, Iqbal J, Rajpar AH, Mujtaba MA, Alghamdi NA, Wageh S, Ramesh K, Ramesh S. Fundamental concepts of hydrogels: Synthesis, properties, and their applications. *Polymers.* 2020;12(11): 2702.

21. Deen GR, Loh XJ. Stimuli-responsive cationic hydrogels in drug delivery applications. *Gels.* 2018;4(1): 13.

22. Roy A, Manna K, Pal S. Recent advances in various stimuli-responsive hydrogels: from synthetic designs to emerging healthcare applications. *Materials Chemistry Frontiers.* 2022;6(17): 2338-2385

23. Lim WJ, Ooi BS. Applications of responsive hydrogel to enhance the water recovery via membrane distillation and forward osmosis: A review. *Journal of Water Process Engineering.* 2022;47: 102828.

24. Aswathy SH, Narendrakumar U, Manjubala I. Commercial hydrogels for biomedical applications. *Heliyon.* 2020;6(4): e03719.

25. Radvar E, Azevedo HS. Supramolecular peptide/polymer hybrid hydrogels for biomedical applications. *Macromolecular Bioscience.* 2019;19(1): 1800221.

26. Pasparakis G, Tsitsilianis C. LCST polymers: Thermoresponsive nanostructured assemblies towards bioapplications. *Polymer.* 2020;211: 123146.

27. Sarwan T, Kumar P, Choonara YE, Pillay V. Hybrid thermo-responsive polymer systems and their biomedical applications. *Frontiers in Materials.* 2020;7: 73.

28. Cao M, Wang Y, Hu X, Gong H, Li R, Cox H, Zhang J, Waigh TA, Xu H, Lu JR. Reversible thermoresponsive peptide–PNIPAM hydrogels for controlled drug delivery. *Biomacromolecules.* 2019;20(9): 3601-3610.

29. Doberenz F, Zeng K, Willems C, Zhang K, Groth T. Thermoresponsive polymers and their biomedical application in tissue engineering–a review. *Journal of Materials Chemistry B.* 2020;8(4): 607-628.

30. Xu X, Liu Y, Fu W, Yao M, Ding Z, Xuan J, Li D, Wang S, Xia Y, Cao M. Poly (N-isopropylacrylamide)-based thermoresponsive composite hydrogels for biomedical applications. *Polymers.* 2020;12(3): 580.

31. Chen Z, Chen Y, Chen C, Zheng X, Li H, Liu H. Dual-gradient PNIPAM-based hydrogel capable of rapid response and tunable actuation. *Chemical Engineering Journal.* 2021;424: 130562.

32. Tang L, Wang L, Yang X, Feng Y, Li Y, Feng W. Poly (N-isopropylacrylamide)-based smart hydrogels: Design, properties and applications. *Progress in Materials Science.* 2021;115: 100702.

33. Wang L, Liu F, Qian J, Wu Z, Xiao R. Multi-responsive PNIPAM–PEGDA hydrogel composite. *Soft Matter.* 2021;17(46): 10421-10427.

34. Harrer J, Rey M, Ciarella S, Löwen H, Janssen LM, Vogel N. Stimuli-responsive behavior of PNiPAm microgels under interfacial confinement. *Langmuir.* 2019;35(32): 10512-10521.

35. Singhal P, Vashisht H, Nisar S, Mehra S, Rattan S. Stimulus responsive soy-protein based hydrogels through grafting HEMA for biomedical applications. *Industrial Crops and Products.* 2022;178: 114621.

36. Yilmaz B, Ozay O. Synthesis, Characterization and Biomedical Applications of p (HEMA-co-APTMACI) Hydrogels Crosslinked with Modified Silica Nanoparticles. *Biointerface Res. Appl. Chem.* 2022;12: 3664-3680.

37. Gopanna A, Rajan KP, Thomas SP, Chavali M. Polyethylene and polypropylene matrix composites for biomedical applications. In: *Materials for Biomedical Engineering.* Elsevier; 2019. p.175-216.

38. Egbo MK. A fundamental review on composite materials and some of their applications in biomedical engineering. *Journal of King Saud University-Engineering Sciences.* 2021;33(8): 557-568.

39. Tarno H, Qi H, Endoh R, Kobayashi M, Goto H, Futai K. Types of frass produced by the ambrosia beetle Platypus quercivorus during gallery construction, and host suitability of five tree species for the beetle. *Journal of Forest Research.* 2011;16(1): 68-75.

40. Chen SL, Fu RH, Liao SF, Liu SP, Lin SZ, Wang YC. A PEG-based hydrogel for effective wound care management. *Cell Transplantation.* 2018;27(2): 275-284.

41. Shi J, Yu L, Ding J. PEG-based thermosensitive and biodegradable hydrogels. *Acta biomaterialia.* 2021;128: 42-59.

42. Han Y, Tang J, Liu S, Zhao X, Wang R, Xia J, Qin C, Chen H, Lin Q. Cellular microenvironment-sensitive drug eluting coating on intraocular lens for enhanced posterior capsular opacification prevention and in vivo biocompatibility. *ACS Applied Bio Materials.* 2020;3(6): 3582-3593.

43. Ross M, Hicks EA, Rambarran T, Sheardown H. Thermo-sensitivity and erosion of chitosan crosslinked poly [N-isopropylacrylamide-co-(acrylic acid)-co-(methyl methacrylate)] hydrogels for application to the inferior fornix. *Acta Biomaterialia.* 2022;141: 151-163.

44. Gao D, Duan L, Wu M, Wang X, Sun Z, Zhang Y, Li Y, He P. Preparation of thermo/redox/pH-stimulative poly (N-isopropylacrylamide-co-N, N′-dimethylaminoethyl methacrylate) nanogels and their DOX release behaviors. *Journal of Biomedical Materials Research Part A.* 2019;107(6): 1195-1203.

45. Mohammadi M, Arabi L, Alibolandi M. Doxorubicin-loaded composite nanogels for cancer treatment. *Journal of Controlled Release.* 2020;328: 171-191.

46. Ko CH, Henschel C, Meledam GP, Schroer MA, Müller-Buschbaum P, Laschewsky A, Papadakis CM. Self-assembled micelles from thermoresponsive poly (methyl methacrylate)-b-poly (N-isopropylacrylamide) diblock copolymers in aqueous solution. *Macromolecules.* 2020;54(1): 384-397.

47. Saylan Y, Denizli A. Supermacroporous composite cryogels in biomedical applications. *Gels.* 2019;5(2): 20.

48. Yazdanpanah G, Jiang Y, Rabiee B, Omidi M, Rosenblatt MI, Shokuhfar T, Pan Y, Naba A, Djalilian AR. Fabrication, Rheological, and Compositional Characterization of Thermoresponsive Hydrogel from Cornea. *Tissue Engineering Part C: Methods.* 2021;27(5): 307-321.

49. Vasile C, Pamfil D, Stoleru E, Baican M. New developments in medical applications of hybrid hydrogels containing natural polymers. *Molecules.* 2020;25(7): 1539.

50. Chen G, Tang W, Wang X, Zhao X, Chen C, Zhu Z. Applications of hydrogels with special physical properties in biomedicine. *Polymers.* 2019;11(9): 1420.

51. Musgrave CS, Fang F. Contact lens materials: a materials science perspective. *Materials.* 2019;12(2): 261.

52. Driest PJ, Allijn IE, Dijkstra DJ, Stamatialis D, Grijpma DW. Poly (ethylene glycol)-based poly (urethane isocyanurate) hydrogels for contact lens applications. *Polymer International.* 2020;69(2): 131-139.

53. Zhao H, Liu M, Zhang Y, Yin J, Pei R. Nanocomposite hydrogels for tissue engineering applications. *Nanoscale.* 2020;12(28): 14976-14995.

54. Jiang L, Wang Y, Liu Z, Ma C, Yan H, Xu N, Gang F, Wang X, Zhao L, Sun X. Three-dimensional printing and injectable conductive hydrogels for tissue engineering application. *Tissue Engineering Part B: Reviews.* 2019;25(5): 398-411.

55. Wang Q, Li S, Wang Z, Liu H, Li C. Preparation and characterization of a positive thermoresponsive hydrogel for drug loading and release. *Journal of Applied Polymer Science.* 2009;111(3): 1417-1425.

56. Sun Y, Nan D, Jin H, Qu X. Recent advances of injectable hydrogels for drug delivery and tissue engineering applications. *Polymer Testing.* 2020;81: 106283.

57. Abasalizadeh F, Moghaddam SV, Alizadeh E, Kashani E, Fazljou SM, Torbati M, Akbarzadeh A. Alginate-based hydrogels as drug delivery vehicles in cancer treatment and their applications in wound dressing and 3D bioprinting. *Journal of Biological Engineering.* 2020;14(1): 1-22.

58. Etter M, Dinnebier RE. A century of powder diffraction: a brief history. *Zeitschrift für anorganische und allgemeine Chemie.* 2014;640(15): 3015-3028.

59. Graewert MA, Svergun DI. Impact and progress in small and wide angle X-ray scattering (SAXS and WAXS). *Current Opinion in Structural Biology.* 2013;23(5): 748-754.

60. Varaprasad K, Mohan YM, Ravindra S, Reddy NN, Vimala K, Monika K, Sreedhar B, Raju KM. Hydrogel–silver nanoparticle composites: a new generation of antimicrobials. *Journal of Applied Polymer Science.* 2010;115(2): 1199-1207.

61. Denzer BR, Kulchar RJ, Huang RB, Patterson J. Advanced Methods for the Characterization of Supramolecular Hydrogels. *Gels.* 2021;7(4): 158.

THE AUTHORS

Nidhi Mishra
e-mail: nidhimishra@iiita.ac.in
ORCID: 0000-0002-6028-7723

Akhilesh Kumar Maurya
e-mail: rss2018504@iiita.ac.in
ORCID: 0000-0003-3281-532X

Shagun Varshney
e-mail: shagun3733@gmail.com
ORCID: 0000-0002-3248-5925

Hybrid modeling of gas-dynamic processes in AC plasma torches

N.Y. Bykov[1,2], N.V. Obraztsov[1,2 ✉], A.A. Hvatov[2], M.A. Maslyaev[2], A.V. Surov[2,3]

[1]Peter the Great St. Petersburg Polytechnic University, 29 Politechnicheskaya st., St. Petersburg, 195251, Russia

[2]ITMO University, 49 Kronversky av., St. Petersburg, 197101, Russia

[3]Institute for Electrophysics and Electric Power RAS, 18 Dvortsovaya emb., St. Petersburg, 191186, Russia

✉ nikita.obrazcov@mail.ru

Abstract. A model of plasma-forming gas flows in AC plasma torches was proposed for the range of operating parameters typical for technologies for the synthesis of perspective materials. It assumes the solution of the Navier-Stokes equations together with the equation for the electric field potential and includes a model of arc root motion. The law of the motion was restored by the method of generative model design from the available experimental data. The COMSOL Multiphysics[R] package was used for simulations. An additional analysis of the applicability of various package modules for modeling essentially subsonic compressible flows with energy release was carried out. Recommendations were given for the simulation of flows in AC plasma torches. The influence of the arc root motion on the flow pattern was studied and the significant asymmetry in the gas-dynamic parameter distributions was shown.

Keywords: AC plasma torch, model of plasma-forming gas flow, arc root motion, method of generative model design, energy release into flow

Citation: Bykov NY, Obraztsov NV, Hvatov AA, Maslyaev MA, Surov SA. Hybrid modeling of gas-dynamic processes in AC plasma torches. *Materials Physics and Mechanics*. 2022;50(2): 287-303. DOI: 10.18149/MPM.5022022_9.

1. Introduction

The development of technologies for the synthesis and processing of new materials is associated with the engineering of complex technical devices. Such devices include plasma torches [1-3]. Plasma torches are used for the synthesis of different carbon structures and metal nanoparticles, obtaining dispersed materials including refractory and hard-metal powders, waste processing, as well as for melting, cutting, and heat treatment [3-13]. Alternative current (AC) plasma torches hold a special place in plasma technologies. The possibility of use in industrial premises with no specially developed complex power sources, the ability to work on multispecies plasma-forming media, and the high service life of electrodes are the main advantages of the AC plasma torches [14].

The efficiency of plasma technologies depends on the parameters of the plasma flow that affect the yield of the synthesized material, the quality of welds, the porosity and adhesion of sprayed coatings, the percentage of waste destruction, etc. Optimization of existing and development of new plasma technologies require a tool for estimating the gas-dynamic parameters of the plasma flow (temperature, velocity, density) in the "working" volume. Depending on the type of technology, the "working" volume can serve the internal channels of the plasma torch, the region of jet expansion in the reactor external with respect to the channels, or both regions simultaneously [15]. An experimental study of high-enthalpy flows is difficult due to high gas temperatures in the arc and reactor. Simulation of plasmodynamic processes is associated with a number of computational problems. It is necessary to consider a hybrid problem involving at least three related subproblems: gas-dynamic, thermal, and electromagnetic.

COMSOL Multiphysics, ANSYS Fluent, Code_Saturne, and OpenFOAM are the most frequently used software products for plasmodynamic process simulation [16-21]. The development of existing scenarios for calculating processes in AC plasma torches using these packages requires an understanding of physical aspects, the correct choice of calculation modules, and subsequent fine matching of computational parameters.

An important feature of modeling flows with energy release, namely, Joule heating, is the need for correct consideration of the effects of medium compressibility. In the COMSOL Multiphysics environment, it is possible to use the Laminar/Turbulent Flow modules with the Compressible Flow option, or the High Mach Number Flow module [22] to take into account the compressibility of the flow. In the context of solving the problem with the COMSOL Multiphysics package, a comparative analysis of the results of applying these modules is required. Carrying out such an analysis is one of the goals of this work.

An important element of the hybrid model describing plasmodynamic processes is the arc root motion model. The movement of the arc root depends on many parameters, among the swirling of the gas flow at the channel inlet and the action of an external magnetic field can be distinguished. In the case of a direct current (DC) plasma torch, accounting for the motion of the arc root results in the asymmetry of the instantaneous distributions of parameters in the cross sections of the plasma flow in the channel. In this case, the averaging of spatially asymmetric profiles over time leads to the Gaussian form of the distribution of parameters along the radial coordinate [23]. For an AC plasma torch, the influence of the arc attachment motion on the flow pattern, both in the channel and in the region of jet expansion in the reactor zone, is more complex and insufficiently studied.

To calculate the motion of the arc attachment in the general case, it is additionally necessary to consider the electrical problem for the electrode itself [23], the processes in the near-electrode plasma layer [24], etc. Thus, the solution of the complete problem requires additional computational resources. One of the alternative approaches is the method proposed in this paper for including the law of motion of the arc root into the hybrid model. The law of motion can be reconstructed from the available experimental data using generative model design (GMD) methods in the form of a differential equation (DE) [25-27]. This approach has been implemented and discussed in this paper.

The aim of the work is to develop a model of an AC plasma torch for the simulation of gas-dynamic and electrical parameters in the volume of channels and in the region of gas expansion using the COMSOL Multiphysics package. The proposed study consists of several parts: an analysis of the parameters of a compressible flow in the presence of an energy release, a consideration of the general formulation of the problem, a description of the application of the GMD method to the problem of restoring the law of motion of an arc root in the form of a DE, a discussion of the results of modeling the compressible flow of a plasma-forming gas using various approaches in the COMSOL Multiphysics environment, analysis of

the results of the 3D simulation with regard to the motion of the arc root along the surface of the electrode.

2. Compressibility of the medium in the simulation of AC plasma torches

To estimate the change in pressure, density, and velocity of a medium during its heating in a given temperature range, it is worth having approximate theoretical expressions presented in this section.

It is known that for an isentropic flow, a variation in the Mach number in the range from 0 to 0.14 results in a change in the gas density by 1%. The gas can approximately be considered an incompressible medium with $\rho = const$. In the case of the gas flow in the plasma torch channel, the medium is heated due to the release of Joule heat, and the flow as a whole is significantly non-isentropic. A simplified one-dimensional model of gas flow in a channel, which assumes energy release into the flow in a certain very small spatial region, is considered in [28]. Before and after the energy deposition region, the flow is assumed to be isentropic. Assuming that in area 1 before the heating zone and in area 2 after it, the flow remains substantially subsonic, i.e. corresponding Mach numbers $M_1 << 1, M_2 << 1$, using the theory [28], we have simple relations

$$\frac{M_2}{M_1} \approx \sqrt{\frac{T_2}{T_1}}, \quad \frac{p_2}{p_1} \approx 1, \quad \frac{\rho_2}{\rho_1} \approx \frac{T_1}{T_2}, \tag{1}$$

where T_i, p_i, ρ_i are the temperature, pressure, and density in area i of the channel.

Air heating in AC plasma torches is accompanied by an increase in temperature above 3500-4000K, which is necessary for sufficient conductivity of the medium. Assuming air heating from $T_1 = 300\ K$ to $T_2 = 6000\ K$ in the arc, i.e.

$$\frac{T_2}{T_1} = 20, \quad \sqrt{\frac{T_2}{T_1}} = 4.47$$

we get

$$\frac{\rho_2}{\rho_1} \approx \frac{T_1}{T_2} = 0.05.$$

With such a significant change in density, the compressibility of the gas cannot be neglected. With the indicated increase in temperature for a one-dimensional flow, a proportional increase in velocity and a decrease in density occurs

$$\frac{u_2}{u_1} = \frac{\rho_1}{\rho_2} \approx \frac{T_2}{T_1} = 20.$$

The compressibility of a medium in the COMSOL Multiphysics 6.0 environment can be taken into account by the modules (a) Single phase flow, compressible flow, non-isothermal flow (hereinafter referred to as the LF approach), or (b) High Mach number flow (hereinafter referred to as the HM approach). The LF approach is used to calculate a compressible medium at Mach numbers less than 0.3 (which corresponds to the flow conditions in a plasma torch). It is assumed that the medium is "dynamically" weakly compressible, i.e. the change in density due to a change in pressure in the flow does not exceed 5%. In this case, the density may change due to temperature dependence. The implemented numerical schemes for the LF approach do not enable us to determine accurately the propagation of pressure waves [29]. The HM approach can be used to calculate a compressible medium at any Mach number. Spasmodic and sharp parameter changes are permissible. The HM module implements a special solution stabilization algorithm [29].

Analysis of the features of the application of these approaches to solving the problem of modeling the flow in an AC plasma torch is one of the goals of this work.

3. Statement of the problem

The geometry of the problem. The paper considers two geometries of the plasma torch (Fig. 1). In scheme 1, the plasma torch channel contains a cylindrical body, and the end surface AB is the first electrode. In scheme 2, the first electrode is hollow and its surface AB coincides with the inner surface of the channel. The second grounded electrode is in the jet expansion region.

Channel radius is $R_c = 16\ mm$, channel length is 330 mm, and distance from the outlet section of the channel to the electrode in the channel is 240 mm. In the case of a hollow electrode (scheme 2), this is the distance from the outlet section to point B of the hollow electrode. The distance between the electrodes is $L_e = 560\ mm$. For scheme 1 inner cylinder radius is $R_e = 10\ mm$. Jet expansion region has dimensions $L_R = 60R_c$ and $H = 50R_c$ for scheme 1, and $L_R = 20R_c$ and $H = 12.5R_c$ for scheme 2.

Scheme 1 assumes an axisymmetric formulation of the problem, scheme 2 assumes a 3D formulation of the problem by taking into account arc root motion (see subsection below).

Table 1 shows the data on the simulation cases, including the average gas velocity at the channel inlet, the flow rate of the plasma-forming gas (air), and the Reynolds number values.

Table 1. Simulation cases

Case	Electrode	Arc root	Scenario	Scheme	I_0, A	V_{x_in}, m/s	T_{in}, K	Re	G, g/s
A	Cylinder face	Fixed	LF	1	10	1	300	~450	0.568
B	Cylinder face	Fixed	HM	1	10	1.075	300	~480	0.578
C	Hollow	Moving	HM	2	10	1.075	300	~1290	0.975
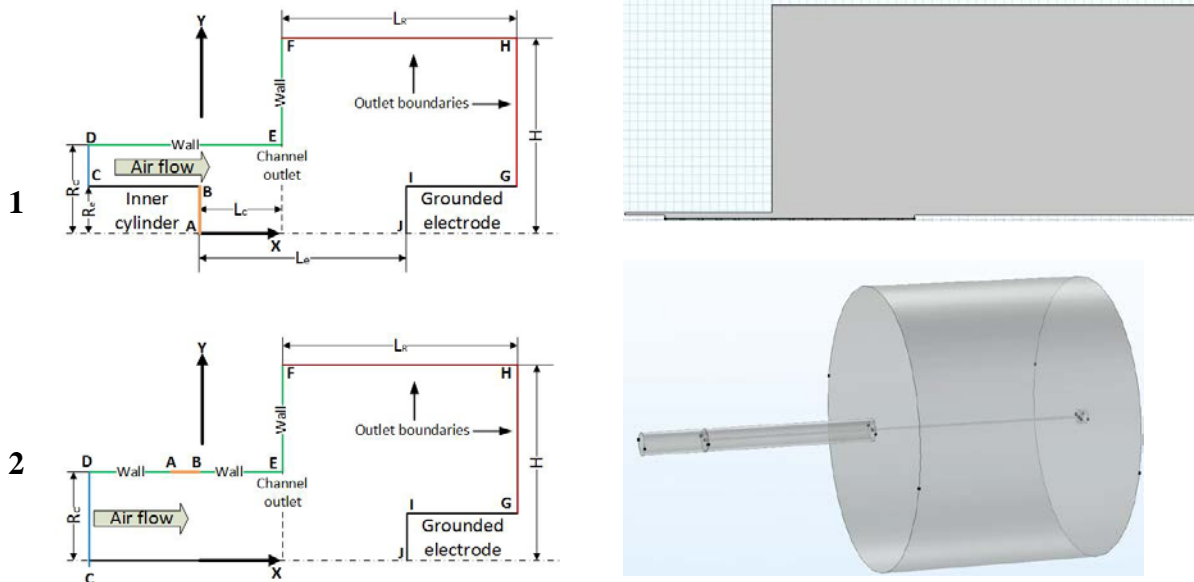
Fig. 1. The geometry of the problem

Mathematical model. The laminar flow of a compressible viscous heat-conducting medium (air) in an alternating electric field is considered. The dynamics of the medium is described by the system of Navier-Stokes equations [22]:

$$\frac{\partial \rho}{\partial t} + \nabla \cdot (\rho \mathbf{u}) = 0,$$ (2)

$$\rho\left(\frac{\partial \mathbf{u}}{\partial t} + (\mathbf{u} \cdot \nabla)\mathbf{u}\right) = \nabla \cdot (-p\mathbf{I} + \tau),$$ (3)

$$\tau = \mu(\nabla \mathbf{u} + (\nabla \mathbf{u})^T) - \frac{2}{3}\mu(\nabla \cdot \mathbf{u})\mathbf{I},$$

$$\rho C_p \left(\frac{\partial T}{\partial t} + (\mathbf{u} \cdot \nabla)T\right) = -(\nabla \cdot \mathbf{q}) + \tau : \mathbf{S} - \frac{T}{\rho}\frac{\partial \rho}{\partial T}\bigg|_p \left(\frac{\partial p}{\partial t} + (\mathbf{u} \cdot \nabla)p\right) + Q_J, \qquad (4)$$

$$\mathbf{q} = -\lambda \nabla T,$$

where t is the time; $\mathbf{u}$ is the velocity; ρ, p, and T are the density, pressure, and temperature of the medium, respectively; τ is the viscous stress tensor; $\mathbf{q}$ is the heat flow vector; $\mathbf{S}$ is the strain-rate tensor: $\mathbf{S} = (\nabla \mathbf{u} + (\nabla \mathbf{u})^T)$; $Q_J = \mathbf{j} \cdot \mathbf{E}$ is the Joule heating power ($\mathbf{j}$ is the current density, $\mathbf{E}$ is the electric field strength); C_p is the heat capacity at constant pressure, μ is viscosity and λ is heat conduction coefficient.

Equation (4) accounts for the work of viscous friction forces and pressure forces. Radiation of heated air in the considered temperature range is disregarded. Air is considered in the single-fluid approximation. The molar mass of air M_a and its other thermophysical parameters (thermal conductivity, heat capacity) are functions of temperature. Density, pressure, and temperature are related by the equation of the state of an ideal gas:

$$p = \rho R T / M_a, \qquad (5)$$

where R is the universal gas constant.

For small values of the current in the arc (see Table 1) and the absence of an external magnetic field, to describe the electrical part, it is enough to consider the equation for the electric field potential φ [17]:

$$-\nabla \cdot \left(\sigma(T)\nabla\varphi + \frac{\partial(\varepsilon_0\varepsilon_r\nabla\varphi)}{\partial t}\right) = 0, \qquad (6)$$

where $\sigma(T)$ is the temperature-dependent electric conductivity, ε_0 is the electrical constant, and ε is the relative permittivity. Relationship between potential and electric field strength $\mathbf{E} = -\nabla\varphi$, current density is defined as $\mathbf{j} = \sigma(T)\mathbf{E}$.

Boundary conditions and initial conditions. Depending on the simulation scenario (LF or HM), two types of setting the boundary conditions for equations (2)-(4) at the input boundary CD are considered. For both approaches, the inlet flow is not swirling and it is assumed that only the x component of the velocity $V_{x,in}$, perpendicular to the inlet section is nonzero.

For the LF approach, a velocity profile is set at the CD boundary corresponding to the steady flow between cylinders with the average velocity $V_{x,av}$ [28]. The gas temperature T_{in} is set too.

In the HM approach, disturbances from the downstream flow region can influence the solution at the subsonic inlet boundary [22,30,31]. Thus, the solution at the boundary is determined both by the given conditions and by the solution for the downstream flow field. In COMSOL Multiphysics, setting boundary conditions in this form correspond to the characteristics-based flow condition option. The specified boundary conditions include the values of the static pressure p_{in} and temperature T_{in}, as well as the Mach number at the boundary:

$$\mathrm{M}_{in} = V_{x,in}/\sqrt{\gamma R_g T_{in}}, \qquad (7)$$

where γ is the specific heat ratio, R_g is the gas constant.

It should be noted that in order to match the flow rates of the plasma-forming gas for cases A and B through the inlet section (with accuracy of more than 98%), the velocity values differed for the LF and HM approaches. For the LF approach $V_{x,av} = 1$ m/s, for the HM approach $V_{x,in} = 1.075\frac{\mathrm{m}}{\mathrm{s}}$, $\mathrm{M}_{in} = 0.0031$.

The characteristic Reynolds numbers are given in Table 1. For cases A and B, Re is determined by the characteristic height of the inlet $H = R_c - R_e = 6\ mm$, and for case C by the channel radius R_c.

At the exit boundary, for all approaches, the static pressure $p_{out} = 1\ atm$ was considered known, and the change in temperature along the normal n to the surface was assumed to be zero

$$\left.\frac{\partial T}{\partial n}\right|_{out} = 0. \tag{8}$$

All solid surfaces (channel walls, electrode surfaces, channel end in the expansion area) were considered to be thermally insulated.

For calculation cases A and B (Table 1), a two-dimensional axisymmetric problem is considered. One of the electrodes is the end surface of the cylinder located in the channel. The end surface area of the cylinder is $S_E = 0.0314\ m^2$. The arc is "rigidly" attached to the electrode at the AB boundary. On this boundary, the condition is set

$$\int_S \mathbf{j} \cdot \mathbf{n_u}\ dS = I. \tag{9}$$

Here, $\mathbf{n_u}$ is the unit normal, and S is the surface area of the electrode. The second electrode is grounded. The current strength changes according to the law

$$I = I_0 \cdot \sqrt{2} \sin(2\pi f_0 t), \tag{10}$$

where I_0 is the current RMS, $f_0 = 50\ Hz$.

For case C, the problem is three-dimensional. The electrode is a ring (see Fig. 1, AB boundary in scheme 2) on the inner surface of the channel. In this case, the only arc root is the "working" part, not the whole ring. The root area is $S_s = 0.0004\ m^2$. The current density is assumed to be constant over the root area and equal to $\mathbf{J}$. According to (9) $\mathbf{J} = I/S_s$. The current changes according to (10). The root moves according to the law discussed in the section below. One complete revolution takes approximately 100 ms.

Arc root motion in the 3D setting. In the absence of an external magnetic field, the typical value of the angular velocity of arc root rotation is $\omega \sim 60$ rad/s. A typical set of experimental data on the change in the arc root angle ϕ with time is shown in Fig. 2. For each time interval of 10 ms, the root rotates by about 36 degrees, making a complete revolution in about 100 ms. The law of angle change with time is repeated every 10 ms and is essentially non-linear (Fig. 2) due to an additional hopping movement of the attachment by about 0.2 rad (not shown in the figure).

The hybrid simulation algorithm includes a differential equation of motion of the arc root, describing the averaged experimental data. A differential equation of the arc root motion has been obtained using the modified algorithm of generative model design [25].

GMD involves the use of a multi-criteria evolutionary optimization algorithm to select the equation that most accurately reproduces the data. The algorithm contains single-criteria and multi-criteria steps.

The single-criteria step operates with a set of tokens representing possible "building blocks" of the future equation. Tokens are parameterized functions, for example, trigonometric, and differential operators of different orders.

The crossing and mutation and regularization operators are defined for a single-criteria algorithm. The crossing operator is the exchange of terms between equations-individuals. The mutation is represented by two operators – replacement of the whole term in the equation or one factor with a given probability. The cross-over operator is the terms exchanged between the equation-individuals. The regularization operator uses sparse regression to determine the shortest expression from a given set of terms with minimal discrepancy. At the same time, terms with a coefficient less than the specified one are removed from the equation. The single-criteria algorithm works for each of the equations on the Pareto front of the multi-criteria algorithm.
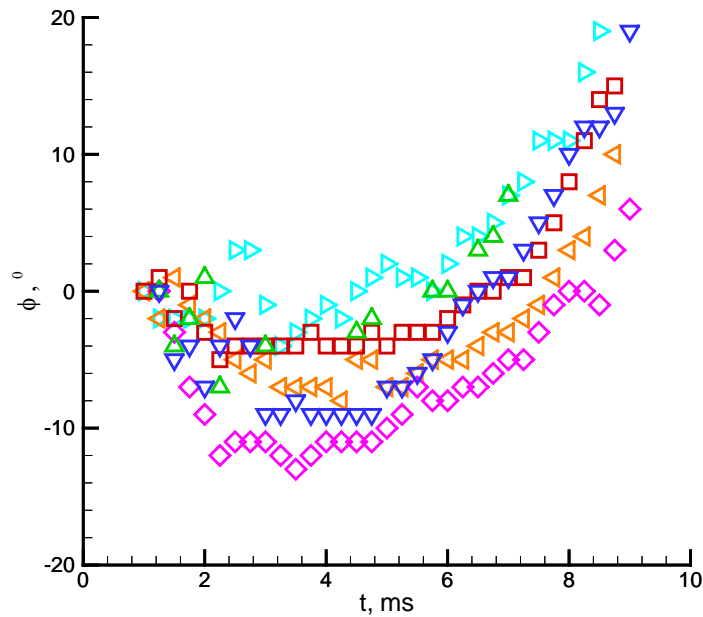
Fig. 2. An example of experimental data on the motion of an arc root. Different symbols and colors correspond to different measurements

A multi-criteria step is an update of a set of Pareto-nondominable solutions in the space of accuracy and complexity criteria. Accuracy in this case is the difference between a randomly selected term and all the others, that is, an analogue of the discrepancy. The second criterion is complexity, the number of non–zero terms in the equation. Thus, an equation with a minimum discrepancy is chosen for each number of terms from a given interval. After the construction of the Pareto fronts, a given number of nondominable levels is saved (the level, in this case, is the ordinal number of the equation sorted by discrepancy for a given number of terms) and a single-criterion step is performed for each equation, followed by the reconstruction of the front at the completion of all single-criterion steps.
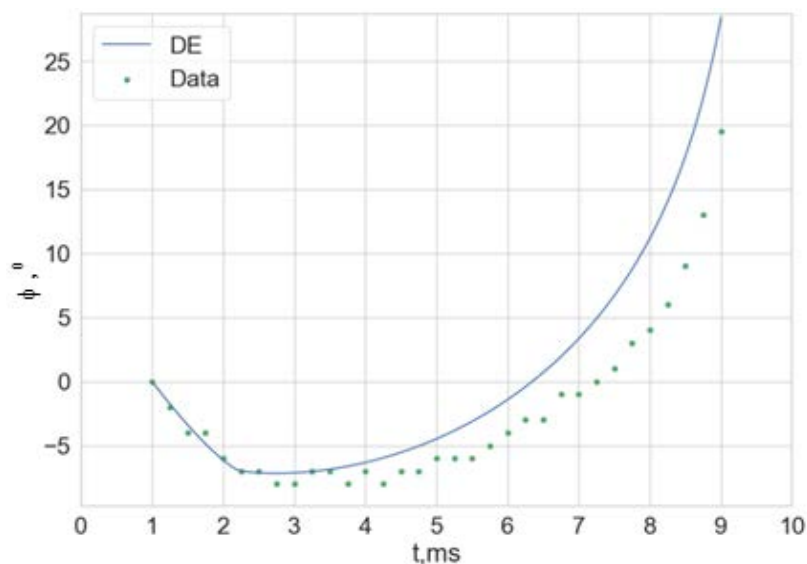
Fig. 3. Data (points) and solutions of the obtained differential equations (12)

For the equation of arc motion, the equation was sought in the form of a second-order equation

$$F(\phi'', \phi', \phi, t, f) = 0. \tag{11}$$

With due regard to the impact of external factors $f_1 = sin(2\pi f_0 t)$ or $f_2 = cos(2\pi f_0 t)$.

To restore the arc equation, median values of the angular deviation distribution at each moment of time were taken for the entire series of experiments. The median arc for restoring the equation is shown in Fig. 3.

The restored equation has the form

$$0.375181\phi' + 251.559\phi + 150.584\phi \, cos(2\pi f_0 t) + 47.4799 = sin(2\pi f_0 t)\phi' \qquad (12)$$

The equation (12) solution was obtained using the scipy.odeint package is shown in Fig. 3.

Equation (12) is included in a hybrid model for calculating a plasma torch implemented in the COMSOL Multiphysics environment. In order to reduce the computational time, the solution of equation (12) is divided into two-time intervals, each of which is approximated by a polynomial of power 11.

Features of numerical implementation of the model in COMSOL Multiphysics environment. The COMSOL Multiphysics 6.0 package has been used to solve the hybrid problem of the flow in an AC plasma torch. The main computation parameters are summarized in Table 2.

Table 2 Computation parameters

| Case	Time step, s	DOFs	Mesh elements	Damping factor	Tolerance	Computation time, h
A	2e-4	855265	195805	0.9	0.005	24
B	2e-4	855265	195805	Automatic	0.005	53
C	Automatic	95172	71794	1 (E) 0.8 (GH)	0.01	148

The finite element method is used to discretize differential equations by spatial coordinates in the COMSOL Multiphysics program. First order polynomials are used to calculate the weight and interpolation functions when processing both gas-dynamic variables (equations (2)-(4)) and electric potential (equation (6)). An implicit finite-difference scheme is used to discretize time derivatives. The calculations employ an IDA (Implicit Differential-Algebraic) solver based on the BDF (Backward differentiation formula) approach. The second-order time approximation is set in the settings. Time step selection option for case C is automatic. For cases A and B, the time step parameters and the mesh size were chosen on the basis of previous calculations [17] and an additional study of the influence of these parameters on the resulting solution. The damping factor in the Newton-Raphson method for solving the nonlinear problems is indicated in Table 2. A Fully Coupled approach is used for cases A and B, based on the Jacobian calculation for the general system of equations (2)-(4). In calculation C, the Segregated setting is used, which assumes the calculation of the Jacobian separately for the gas-dynamic together with the thermal (GH) part and electrical (E) part of the problem. The solution of algebraic equations is performed by the Pardiso solver. The calculations were carried out by the resources of the supercomputer cluster of the SCC "Polytechnic" on one computing node containing two Intel Xeon E5–2697 v3 CPUs.

An artificial conductivity of 235 S/m was used to initialize the arc discharge between the electrodes in cases A and B. By 10 milliseconds, its contribution to the total conductivity was zero. In case C, a volumetric energy source with a power of 500 W was set. Using the step function, this source was turned off 0.05 seconds after the start. The total time of the physical process was 1.5s.

4. Flow in a plasma torch with an end electrode

This section presents the results of simulations for cases A and B of the axisymmetric problem, which differ in the scenarios for modeling the flow of a compressible medium in the COMSOL Multiphysics package. Case A assumes using the Laminar Flow module with the Compressible Flow option. Case B involves using the High Mach Number Flow module. Figure 4 shows the maximum value of overpressure (over atmospheric pressure) in the flow area. It is seen that the maximum pressure deviation from the atmospheric pressure set at the boundary does not exceed 0.4%. At the same time, the maximum pressure values for case B are somewhat lower.
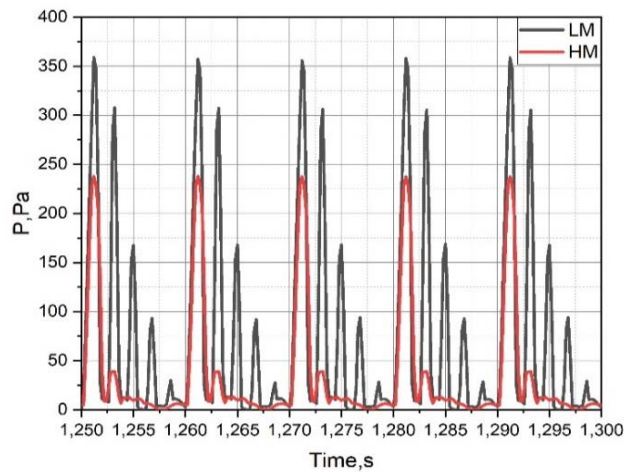
Fig. 4. The maximum value of overpressure in the flow area for simulation cases A (LM legend) and B (HM legend)

Figure 5 shows the axial distributions of temperature (Fig. 5a) and velocity (Fig. 5b) for cases A and B corresponding to the times when the value of the current in the arc is minimal $I=0$ and maximal $I=\sqrt{2}I_0$. At the moment of the maximum current, the temperature in the channel rises to 6500K. In the region of the channel, the temperature weakly depends on the longitudinal coordinate. The discrepancy between calculation cases A and B in terms of the maximum temperature observed in the flow region does not exceed 2%. In the jet expansion region behind the plasma torch channel, the gas temperature and velocity oscillate in space [17,32]. The positions of the maxima and minima on the axial temperature distribution are close but do not coincide for cases A and B.

As discussed in Section 2, with an increase in temperature from 300 (inlet) to 6500 K for a simplified formulation of the problem, an increase in the flow velocity by a factor of 21.7 can be expected. The inlet velocity is near 1m/s (see Table 1). The maximum observed velocity is 20.7 m/s in case A and 17.5 m/s in case B. The maximum velocity is reached in the vicinity of the channel outlet. The velocity distributions in the cases under consideration are similar by quality. The most significant difference is manifested for the moment of minimum current in the region of the channel adjacent to the electrode. For case A, a stagnation point with zero velocity appears on the velocity profile. The velocity field shows an "instantaneous" circulation area at the given time behind the electrode. For other moments of time, the area of backward flow is lacking [32]. For case B, this area is not observed for any moments.

The fields of velocity and temperature for cases A and B and the moment of maximum current are shown in Figs. 6 and 7. It can be seen that the spatial variations of the parameters in both cases are close.
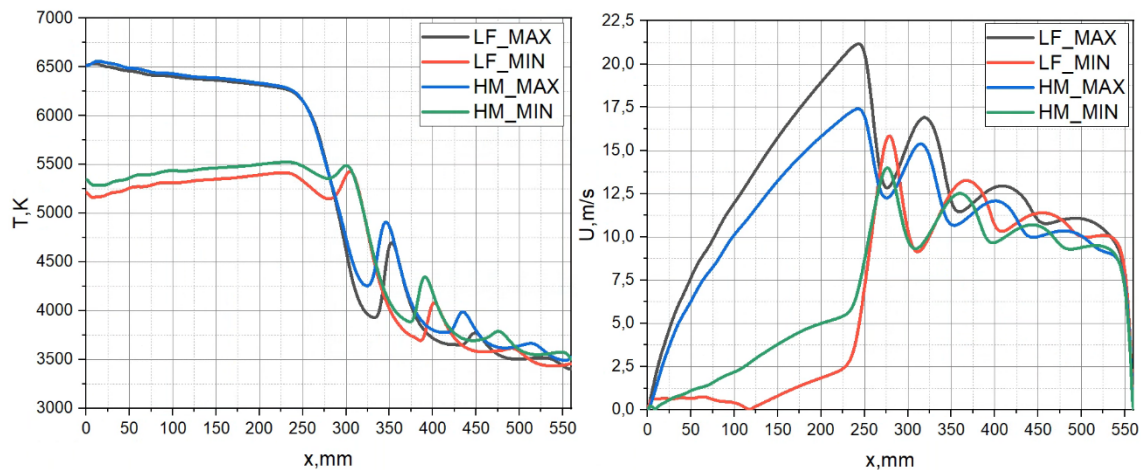
Fig. 5. Axial distributions of temperature (a) and velocity (b) for cases A (LF legend) and B (HM legend) corresponding to the moments of the minimal and maximal current value in the arc (MIN and MAX legends).
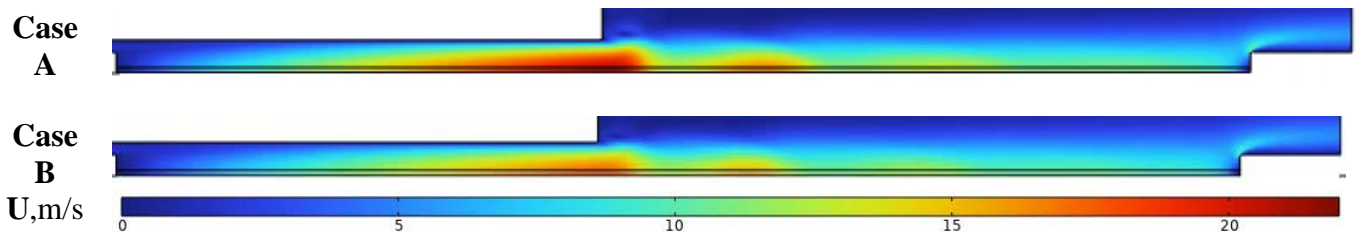
Fig. 6. Velocity fields for cases A and B and the moment of maximum current
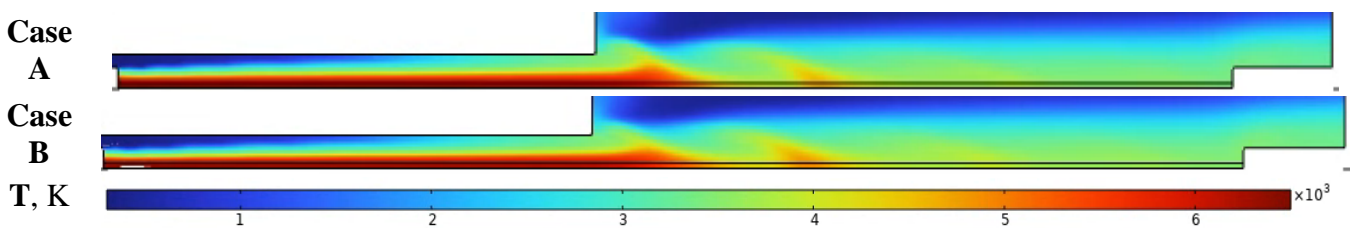
Fig. 7. Temperature fields for cases A and B and the moment of maximum current

The main difference between cases A and B is the behavior of the velocity at the inlet boundary. For case A (LF approach), the velocity value does not fluctuate, while in case B (HM approach), the fluctuations are significant. The latter is related to the specific character of the HM approach [22] and boundary conditions settings (see section 3). The internal tests show that the presence of such fluctuations is independent of the mesh size. For the problem under consideration with a nonstationary energy supply resulting in a significant change in temperature in space and time, such oscillations of parameters in a subsonic flow can be physical but require experimental verification.

Thus, to estimate the flow parameters both in the channel (except the region adjacent to the inlet boundary) and in the jet expansion region, any of the discussed approaches (LF or HM) can be used. However, the experience of solving similar problems in the COMSOL Multiphysics environment with different data (different values of velocity and gas flow rate at the inlet boundary) suggests that the simulation using the HM approach is more stable from a computational point of view.
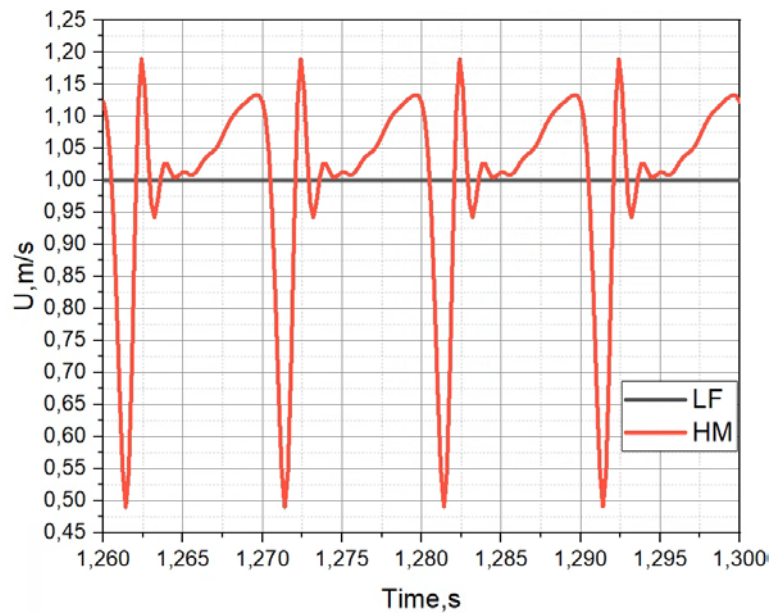
Fig. 8. Average velocity over the section at the inlet boundary for cases A (LM legend) and B (HM legend)

5. The flow in the plasma torch with regard to the arc root movement

In the previous section, the flow in the plasma torch, one of the electrodes of which is the end face of an inner cylinder with a radius of 10 mm (see Fig. 1), had been considered. The arc root is "rigidly" attached to the electrode surface (case B, Table 1). This formulation of the problem predetermines the symmetry of the variation in parameters relative to the axis. The statement of the problem in case C (Table 1) is more complex, assuming that (i) the electrode surface coincides with the surface of the cylindrical channel with a radius of 16 mm (see Fig. 1) and (ii) the arc root moves along this surface according to equation (12). Taking into account the displacement of the arc root effects a significant change in the gas-dynamic flow pattern.

Figure 9 shows the temperature distribution for different time moments in section X=0, which coincides with the electrode for case B and with the end of the hollow electrode for case C. As noted above, for case B, the picture is symmetrical about the axis with a maximum temperature of about 6500K. For case C, the location of the temperature maximum coincides with the location of the center of the arc root. The maximum temperature in the vicinity of the root center exceeds 8000 K. The temperature difference for cases B and C is explained mainly by the difference in current density and partially by the difference in flow rate (see Table 1). The flow rate affects the arc voltage drop [32]. The current density for case C turns out to be higher due to the smaller root area (Fig. 10), respectively, and the Joule heating of the arc near such a root is also higher. In the remaining sections of the channel downstream, the temperature distributions for case C retain their asymmetric form (Fig. 11). In sections X=120mm (middle of the channel) and X=240mm (outlet from the channel), the maximum observed temperature values are close to case B. In the outlet section of the channel, the temperature value averaged over the entire section is close to case B (Table 3) and is about 3900K.

Table 3. Average values of parameters in the section X=240 (outlet of the channel)

	Velocity, m/s	Temperature, K
Case B	10.283	3982.7
Case C	16.879	3874.7
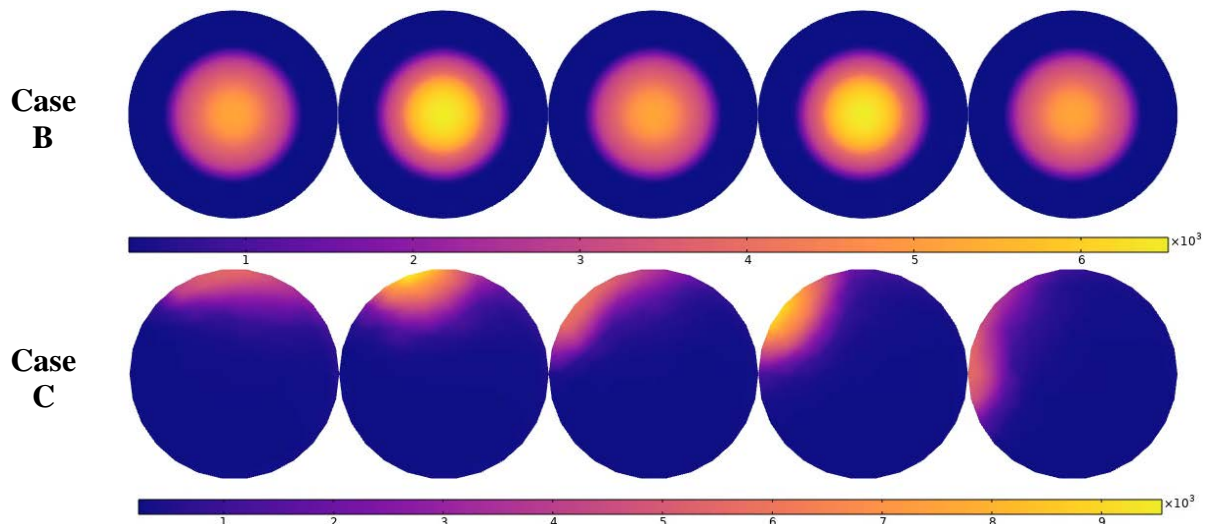
Fig. 9. Distribution of gas temperature (K) in section X=0 for different moments of time (t=0, t=T_0/4, t=T_0/2, t=3T_0/4, t=T_0. T_0 = 0,02 s.). Case B on the top, case C on the bottom
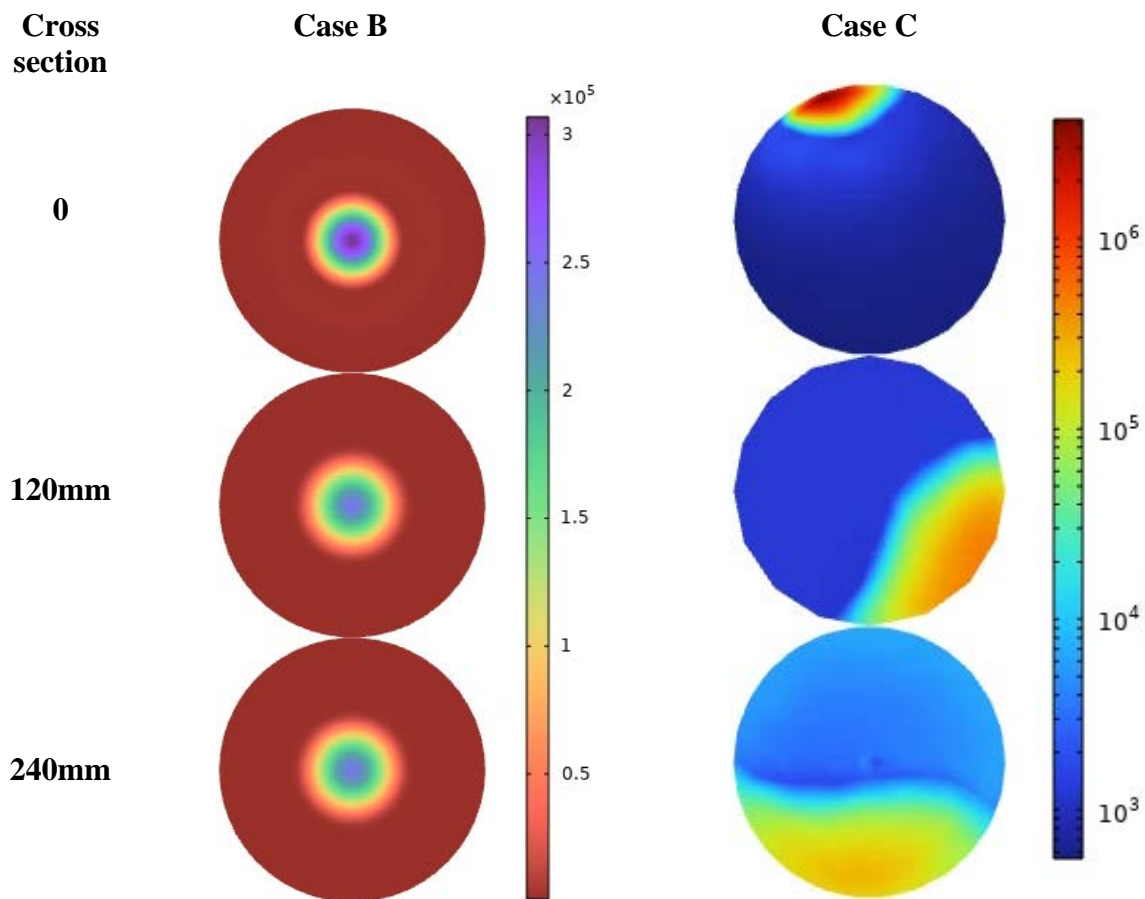
Fig. 10. Current density (A/m^2) at the moment of the maximum current in the sections X=0, X=120mm, X=240mm (exit from the channel). Case B is on the left, case C on the right.

The distributions of the remaining parameters for the calculation case C are also asymmetric (e.g. Fig. 10). The gas velocity in section X=0 in the vicinity of the arc attachment spot exceeds 15 m/s, in most of the sections the velocity is less than 5 m/s. The maximum velocity averaged over the cross-section is reached at the outlet of the channel (Table 3). For case B the velocity distributions in the sections are symmetrical, and the

maximum velocity in the outlet section is lower compared to case C. This difference is due to the difference in flow rates for cases B and C (see Table 1).
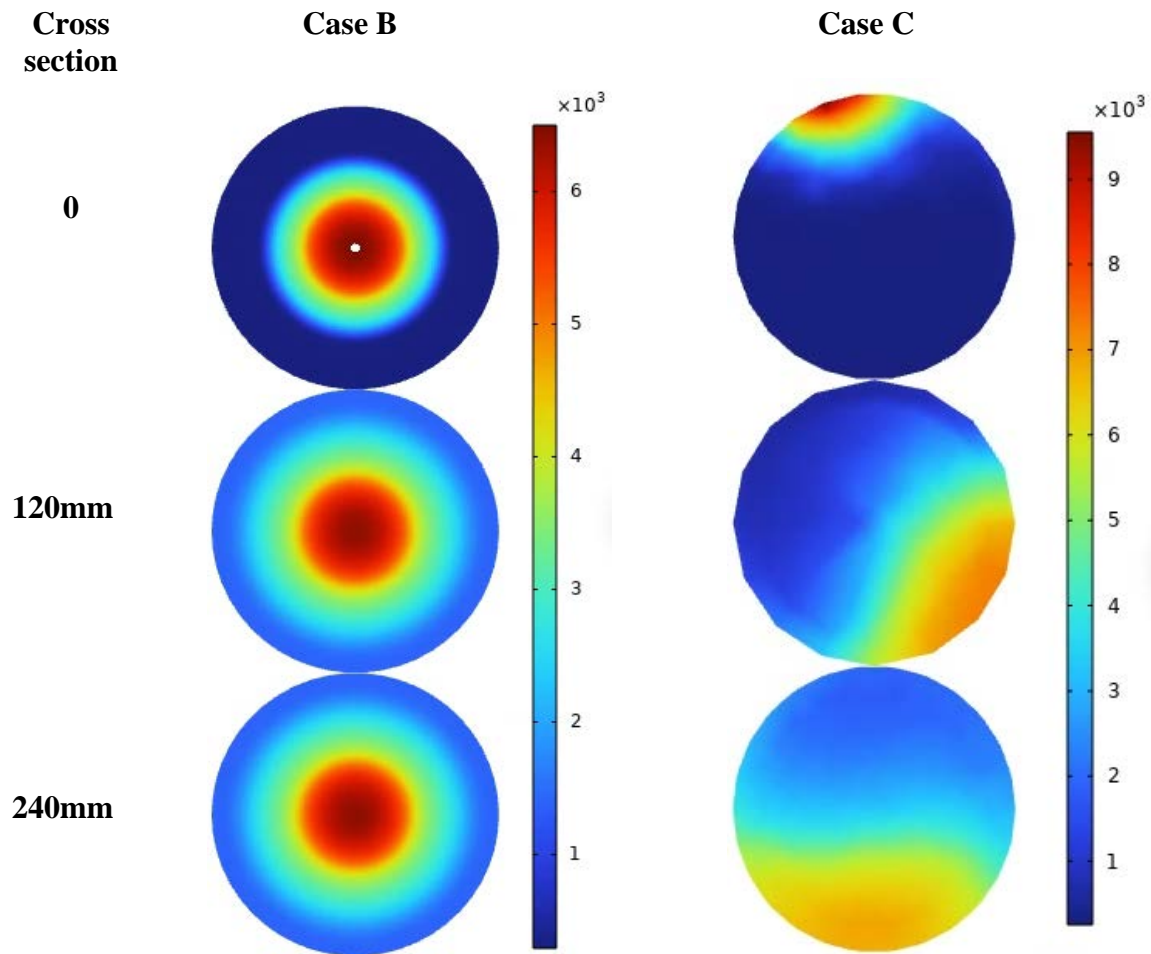
Fig. 11. Gas temperature (K) at the moment of the maximum current in the sections X=0, X=120mm, X=240mm (exit from the channel). Case B is on the left, case C on the right
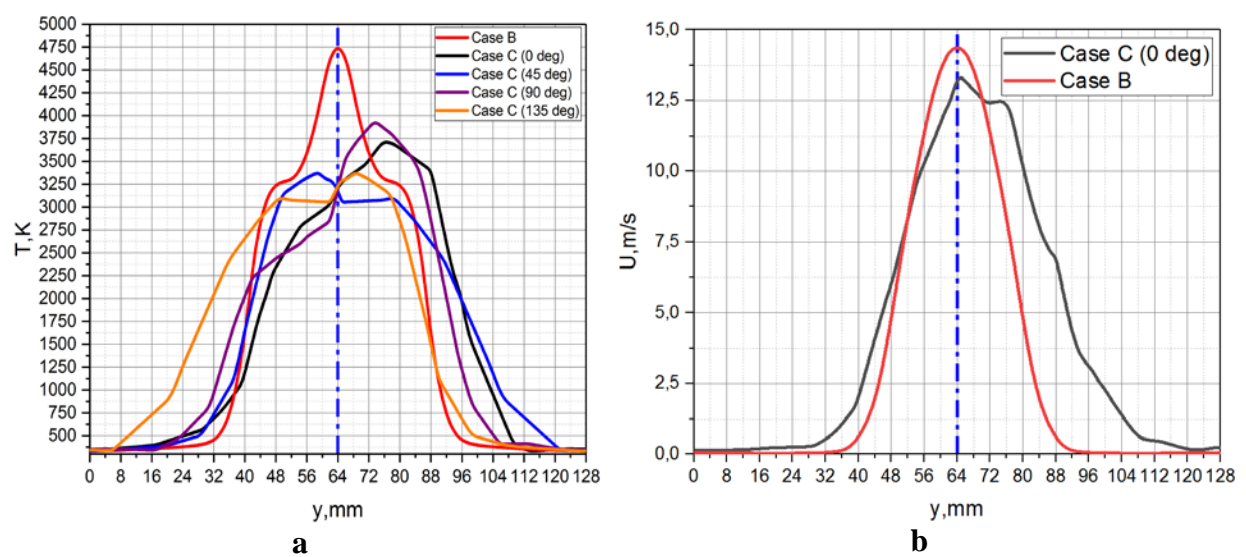
Fig. 12. Radial distribution of temperature (a) and velocity (b) in section X=300 mm

From the point of view of plasma chemistry and technologies for the synthesis of nanostructured materials, the parameters of the heated gas, including the jet dimensions in the expansion region outside the channel are of great importance. For case B, the temperature in the jet on the axis does not fall below 3500K, the characteristic transverse size of the jet Y_{ch} in section X=300mm (Fig. 12a), corresponding to the temperature drop to 1000K, is about $1.6R_c$. Rotation of the arc root leads to broader distribution of temperature with a lower maximum. The characteristic transverse size of the jet is about $Y_{ch}=2R_c$. The radial distribution of velocity is also broader (Fig. 12b).

6. Conclusions

Thermal plasma generators are in demand for many modern technologies for the synthesis of nanostructured and powder materials, as well as materials with special performance properties. Alternating current electric arc plasma torches are promising sources of thermal plasma.

The development of electric arc plasma torches for each specific technology requires an assessment of the plasma parameters. The description of the processes of heating the plasma-forming gas by alternating electric current, its ionization, gas-dynamic acceleration in the plasma torch channel, and the outflow of a high-enthalpy jet into the background gas is a non-trivial problem that can only be solved by numerical methods. Taking into account the complexity of the problem, the development of the corresponding computational model is carried out in stages.

In this paper, we continue the development of a hybrid model of an AC plasma torch in the COMSOL Multiphysics environment proposed in [17]. The model involves calculating the parameters of the electric field, determining the heating power of the plasma-forming medium, and solving the system of Navier-Stokes equations to determine the density, velocity, and temperature of the gas. The electrical and gas-dynamic subproblems are related through the temperature-dependent conductivity of the medium, which affects the local current density and Joule heating. Air is considered a plasma-forming medium, the thermophysical parameters of which, including the molar mass, depending on temperature.

In the presented study, special attention is paid to the correct consideration of the compressibility factor of the plasma-forming gas. The compressibility of a medium can be taken into account within the COMSOL Multiphysics package using the Laminar/Turbulent Flow module with the Compressible Flow option, or the High Mach Number Flow module. For the first time, the results of applying these modules to solve the problem of essentially subsonic flow of a compressible gas with energy release into the flow are compared. It is shown that the results obtained using different computational scenarios are close to each other. The temperature distributions in the flow region practically coincide. The gas velocity distributions are close, however, the maximum value of the flow velocity achieved at the moment of maximum current differs by 17%. Thus, both approaches (modules) can be used to estimate the flow parameters. However, the use of the High Mach Number Flow module showed greater computational stability of the computational algorithm implemented in it when the set of initial data changes.

As an element of the hybrid model, the present paper takes into account the process of arc root motion along the electrode surface. For the first time, to describe this process, it is proposed to use the differential equation of motion of the arc root, reconstructed from the available experimental data using the generative model design method. Taking into account the root motion required the solution of a three-dimensional problem. The results of calculating the spatial parameter distributions differ significantly from the symmetric distributions observed when the motion of the arc root is not taken into account. Asymmetry in the parameter distributions is observed both along the entire length of the channel and in

the region of jet expansion. Accounting for the arc root motion is an important element of the plasma torch model, bringing the simulation results closer to the flow pattern observed in reality.

References
1. Mostaghimi J, Boulos MI. Thermal Plasma Sources: How Well are They Adopted to Process Needs? *Plasma Chem Plasma Process.* 2015;35: 421-436.
2. Fulcheri L, Fabry F, Takali S, Rohani V. Three-phase AC arc plasma systems: a review. *Plasma Chem Plasma Proc.* 2015;35: 565-85.
3. Klimenko GK, Kuzenov VV, Lyapin AA, Ryzhkov SV. *Calculation, modeling and design of low-temperature plasma generators.* Publishing House of MSTU; 2021. (In Russian)
4. Gautier M, Rohani V, Fulcheri L, Direct decarbonization of methane by thermal plasma for the production of hydrogen and high value-added carbon black. *International Journal of Hydrogen Energy.* 2017;42(47): 28140-28156.
5. Jensen R, van der Eijk C, Wærnes AN. Production of Sustainable Hydrogen and Carbon for the Metallurgical Industry. *Mater. Proc.* 2021;5(1): 67.
6. Juan L, Fangfang H, Yiwen L, Yongxiang Y, Xiaoyan D, Xu L. A New Grade Carbon Black Produced by Thermal Plasma Process. *Plasma Science & Technology.* 2003;5(3): 1815-1819.
7. Xie Z, Tang Z, Zhang D, Kang N, Su X, Yang B, Dai Y, Liang F. Hydrogen arc plasma promotes the purification and nanoparticle preparation of tungsten. *Int. J. Refract. Met. Hard Mater.* 2022;105: 105815.
8. Shekhovtsov VV, Skripnikova NK, Volokitin OG. Phase transitions in SiO2 nanopowder synthesized by electric arc plasma. *IEEE transactions on plasma science.* 2021;49(9): 2618-2623.
9. Rat V, Chazelas C, Goutier S, Keromnes A, Mariaux G, Vardelle A. In-flight mechanisms in suspension plasma spraying: issues and perspectives. *J. Therm. Spray Tech.* 2022;31: 699-715.
10. Wang H, Zeng M, Liu J et al. One-step synthesis of ultrafine WC-10Co hardmetals with VC/V2O5 addition by plasma assistedmilling, *Int. J. Refract.Met. HardMater.* 2015;48: 97-101.
11. Wei CB, Song XY, Fu J et al. Microstructure and properties of ultrafine cemented carbides-differences in spark plasma sintering and sinter-HIP. *Mater. Sci. Eng. A.* 2012;552: 427-433.
12. Sivaprahasam D, Chandrasekar SB, Sundaresan R. Microstructure and mechanical properties of nanocrystalline WC-Co consolidated by spark plasma sintering. *Int. J. Refract. Met. Hard Mater.* 2007;25(2): 144-152.
13. Qi J, Luo Y, Yin Y, Dai X. Preparation of Ultra-fine Aluminum Nitride in Thermal Plasma. *Plasma Science & Technology.* 2002;4(4): 1417.
14. Surov AV, Popov SD, Popov VE, Subbotin DI, Serba EO, Spodobin VA, Nakonechny GhV, Pavlov AV. Multi-gas AC plasma torches for gasification of organic substances. *Fuel.* 2017;203: 1007-1014.
15. Rutberg PhG, Nakonechny GhV, Pavlov AV, Popov SD, Serba EO, Surov AV. AC plasma torch with a H2O/CO2/CH4 mix as the working gas for methane reforming. *J. Phys. D: Appl. Phys.* 2015;48(24): 245204.
16. Baeva M, Benilov MS, Almeida NS, Uhrlandt D. Novel nonequilibrium modelling of a DC electric arc in argon. *J. Phys. D: Appl. Phys.* 2016;49(24): 245205.
17. Bykov NY, Obraztsov NV, Kobelev AA, Surov AV. Modeling of an AC Plasma Torch - Part I: Electrical Parameters and Flow Temperature. *IEEE Transactions on Plasma Science.* 2021;49(3): 1017-1022.

18. Ivanov DV, Zverev SG. Mathematical Simulation of Plasma Processes in a Radio Frequency Inductively Coupled Plasma Torch in ANSYS Fluent and COMSOL Multiphysics Software Packages. *IEEE Transactions on Plasma Science*. 2022;50(6): 1700-1709.

19. Ivanov DV, Zverev SG. Mathematical Simulation of Processes in Air ICP/RF Plasma Torch for High-Power Applications. *IEEE Transactions on Plasma Science*. 2020;48(2): 338-342.

20. Rehmet C, Fabry F, Rohani V, Cauneau F, Fulcheri L. A comparison between MHD modeling and experimental results in a 3-phase AC arc plasma torch: influence of the electrode tip geometry. *Plasma Chem. Plasma Process*. 2014;34: 975-996.

21. Zhou X, Chen X, Ye T, Zhu M. Large eddy simulation on the flow characteristics of an argon thermal plasma jet. *Plasma Sci. Technol*. 2021;23(12): 125405.

22. *COMSOL AB, COMSOL Multiphysics-CFD Module, User's Guide*. 2022.

23. Sambou F, Gonzalez JJ, Benmouffok M, Freton P. Theoretical study of the arc motion in the hollow cathode of a dc thermal plasma torch. *J. Phys. D: Appl. Phys*. 2022;55(2): 025201.

24. Benilov MS. Understanding and modeling plasma–electrode interaction in high pressure arc discharges: a review. *Phys. D: Appl. Phys*. 2008;41(14): 144001.

25. Maslyaev M, Hvatov A, Kalyuzhnaya AV. Partial differential equations discovery with EPDE framework: Application for real and synthetic data. *Journal of Computer Science.* 2021;53: 101345.

26. Bykov NY, Hvatov AA, Kalyuzhnaya AV, Boukhanovsky AV. A method for reconstructing models of heat and mass transfer from the spatio-temporal distribution of parameters. *Technical Physics Letters*. 2021;47: 9-12. (In Russian)

27. Bykov N, Hvatov A, Kalyuzhnaya A, Boukhanovsky A. A method of generative model design based on irregular data in application to heat transfer problems. *Journal of Physics: Conference Series.* 2021;1959: 012012.

28. Loitsyansky LG. *Mechanics Fluid Gas*. Moscow: Nauka; 1973. (In Russian)

29. *Calculation of near- and supersonic technologies in COMSOL Multiphysics*. Available from: https://www.COMSOL.ru/video/sub-and-supersonic-flows-in-COMSOL-webinar-ru. [Accessed 18th July 2022] (in Russian).

30. Poinsot T, Veynante D. *Theoretical and Numerical Combustion.* Edwards; 2005.

31. Larsson J. *Numerical Simulation of Turbulent Flows for Turbine Blade Heat Transfer Applications*. *Ph.D. thesis.* Chalmers University of Technology; 1998.

32. Bykov NY, Obraztsov NV, Kobelev AA, Surov AV. Modeling of an AC Plasma Torch – Part II: Gasdynamic Pattern and Effect of Flow Rate. *IEEE transactions on plasma science*. 2021;49(3): 1023-1027.

THE AUTHORS

Obraztsov N.V.
e-mail: nikita.obrazcov@mail.ru
ORCID: 0000-0003-1107-3259

Bykov N.Y.
e-mail: nbykov2006@yandex.ru
ORCID: 0000-0003-0041-9971

Hvatov H.A.
e-mail: alex_hvatov@itmo.ru
ORCID: 0000-0002-5222-583X

Maslyaev M.M.
e-mail: mikemaslyaev@itmo.ru
ORCID: 0000-0001-5595-0802

Surov A.V.
e-mail: alex_surov@mail.ru
ORCID: 0000-0003-4671-5741

Processing and wear behavior optimization of B_4C and rice husk ash dual particles reinforced ADC12 alloy composites using Taguchi method

R. Murali Mohan[1], U.N. Kempaiah[2], B. Manjunatha[3], Madeva Nagaral[4✉], V. Auradi[5]

[1]Government Engineering College, Hassan, 573202, India

[2]University Visveswaraya College of Engineering Bangalore, Bangalore 560001, India

[3]Acharya Institute of Technology, Bangalore 560107, India

[4]Aircraft Research and Design Centre, Hindustan Aeronautics Limited, Marathahalli, Bangalore, India

[5]Siddaganga Institute of Technology Tumkur, Tumkur 572103, India

✉ madev.nagaral@gmail.com

Abstract. The composite material comprises either two or more constituents having dissimilar physical and chemical properties. The composite is prepared by various techniques, but the stir casting method has been widely used, as it is simple and cost-effective. In the present work, the composites from ADC12 Aluminum Alloy-Boron Carbide (B_4C) (wt.5%) and varied wt % of Rice Husk Ash (RHA) were developed with the help of the stir cast technique. Composite having 3, 6, 9 wt.% of RHA were considered for the wear analysis. The wear analysis of hybrid composites was studied with the help of Taguchi method and also optimum values were determined. The tribological study was conducted on the Pin on disk testing apparatus under dry sliding conditions. The L27 orthogonal array has been preferred in the present work to include three factors and three levels. The selected factors are Speed (N), Load (W), RHA, and wear depth as system output (yield). Analysis of variance has been carried out to know the parameters' influence and level of contribution to the wear loss. For, the validation of the analysis results the experimental test was carried out for the optimum values. To understand the wear mechanism in composites the samples were analyzed using Scanning Electron Microscopic (SEM) and it has been observed that both abrasive, as well as adhesive wear, did occur on the contact surface of the specimens.
Keywords: ADC12 Alloy, B_4C, rice husk ash, microstructure, wear, optimization, Taguchi

1. Introduction

More recently, extensive research work has been conducted on agro based waste products because these agro-waste products are easily available, less dense, have reduced cost and are environmentally friendly. Several research studies show that Agro based waste byproducts

like maize stalk ash, bamboo leaf ash, corn cob ash, RHA, bagasse ash, and bean shell waste ash have been used as reinforcing materials to increase the Wear and Mechanical characteristics of aluminium-based composites. The latest sophisticated materials are an aluminium alloy matrix supplemented with SiC and B_4C particulate [1,2]. Hard materials are commonly used as reinforcements due to their ability to improve qualities such as tensile and compression strengths, as well as their advantages in tribological applications. Reinforcements with appropriate particles are commonly used to improve mechanical qualities. B_4C and RHA fibres have also been used as reinforcing materials in MMC because of their high strength and low density. Aluminium MMCs made by solidification processes with these particulates as reinforcing material represent a class of low-cost, suitable materials for a variety of engineering applications in the automobile industry, such as brake pads, bushes, and bearings [3,4]. The aluminium metal matrix material reinforced with B_4C has the potential to develop a material with improved thermal conductivity, incredible mechanical capabilities, and good damping behaviour at high temperatures [5]. However, there is a wettability problem between aluminium and the B_4C-RHA reinforcements, and oxidation of the particles at high temperatures causes industrial problems and material cavitation.

At increased temperatures, current research on AMMC with ceramic reinforcement particles has revealed an increase in wear resistance and improvements in mechanical properties [6,7]. Due to the presence of B_4C, matrix deformation, load distribution, and micro defects that frequently occur along the friction track could be effectively prevented.

From the literature, it is clear that numerous investigators conceded the investigations on hybrid composites using aluminium alloys of different series such as 1xxx -7xxx as matrix material but from literature, it is very rarely seen that usage of aluminium alloy ADC12 as matrix material. Further combination of reinforcements like boron carbide and agro waste product RHA containing oxide in the development and characterization of hybrid MMCs was not done.

In the present work, samples of ADC12 Aluminum Alloy-B_4C-RHA composites were prepared using stir casting. For the preparation of composites ADC12 aluminum alloy is used as matrix material, B_4C particles, and RHA particles were used as reinforcing materials. The tribological properties of ADC12 aluminum alloy-B_4C-RHA AMCs were studied by Taguchi's technique. It has been understood that the rate of wear in composites was influenced by the amount of RHA (reinforcing material) used and wear parameters like the sliding speed and applied load. Pin on Disk wears testing apparatus was used to find out the wear of the composite samples which were initially developed by stir casting method [8,9]. The design of experiments was planned and conducted as per the L27orthogonal array by Taguchi technique. The agro-waste derivatives were found very much influential as reinforcing materials [10] on properties of composites materials and also promising resources for the aluminium based metal composites on a large scale. In recent times, several investigations were aimed at the optimization of the production parameters and wear parameters.

2. Taguchi method

Taguchi method [11-13] is a powerful technique for designing of experiments to obtain a high yield from the process or system using orthogonal arrays (OA). Taguchi techniques are strategically ordered experiments to minimize deviations in the desired quality. It is a logical and easy statistical approach to finding popular designs for better execution, high quality, and less expensive. The Signal-to-Noise Ratio (S/N Ratio) is determined from the output response in Taguchi technique (experimental results-wear loss). The signal-to-noise ratios were calculated with the following goals in mind: smaller is better, nominal is best, and larger is

best. The research in this work was carried out with the goal of making the wear depth as small as possible, and the equations employed are listed below [14].

$$S/N = -10 \times log\left(\sum \frac{Y^2}{n}\right).$$

Here Y – result output at a certain level of combination and n – Number of result output at a certain level of combination.

The Taguchi method uses the problem's objective to obtain the Signal to Noise (S/N) ratio values. With the help of obtained S/N ratio values, the ideal combinations of variables have been presented. Analysis of variance technique has been utilized to know the statistically required factor and its contribution. To crosscheck the obtained ideal parameters a validation test was also conducted.

3. Experimentation

Materials used and composites preparation. A wide range of metals are utilized in MMCs and the decision of the substance relies on the sort of utilization. Henceforth alloy frameworks, for example, aluminium, copper, iron, magnesium, titanium, and nickel have been used as the base. It is observed that Fe-based car parts in the long run all be supplanted with more lightweight metals, e.g., aluminium combinations. ADC12 Alloy is Al-Si-Cu-based cast amalgams that have high mechanical properties and great castability so these composites have been utilized for automotive parts, for example, chamber blocks, transmission cases, carburettors, brake cushions, and so forth. For the current work grid material picked is ADC12 Alloy. Table 1 is showing the chemistry of ADC12 alloy. Some important physical, mechanical and thermal properties of ADC12 alloy are shown in Table 2.

Table 1. Chemistry of ADC12 alloy

Elements (wt. %)	ADC12 (Standard wt. %)	ADC12 (Actual wt. %)
Si	9.60-12.00	10.60
Fe	1.30 Max.	0.84
Cu	1.50-3.50	2.13
Mn	0.50	0.09
Mg	0.30 Max.	0.07
Zn	1.00 Max.	0.89
Ni	0.50 Max.	0.07
Pb	0.30 Max.	0.02
Ti	0.20 Max	0.05
Aluminium	Balance	Balance

Table 2. Properties of ADC12 alloy

Density (g/cc)	2.7
Melting point (°C)	660
Poisson's Ratio	0.33
Modulus of Elasticity (GPa)	70-80
Hardness (HV)	70
Tensile Strength (MPa)	165-331
Co-efficient of Thermal Expansion(mm / K^{-1})	31.1×10^{-6}

Boron synthetically combined with carbon results in a very hard ceramic known as boron-carbide, B_4C being the 3rd hardest material after cubic boron nitride (CBN) and

diamond is used as abrasion material and to combat wear. Because of its high hardness and low density, the material can be used in aluminium matrix alloy in the form of particulates to produce composition material. In the present work, B_4C particulates with 40 micron size are used which were brought from Speed-Fam Ltd., Chennai. The SEM analysis of B_4C particulates has been carried out at BMSCE, Bangalore, Karnataka, India. Figure 1 shows the micro B_4C particles. The composition of B_4C particles is shown in Table 3. Further, Table 4 indicates the different physical and mechanical properties of B_4C.

Table 3. Composition of B_4C particles

Elements	Composition wt. %
Boron (B)	63.68
Carbon (C)	36.32
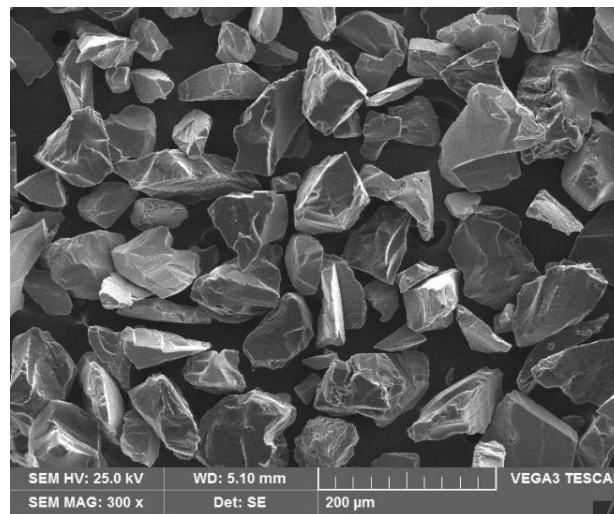
Fig. 1. Scanning Electron Microphotograph of B_4C particles

Table 4. Physical and mechanical properties of B_4C

Crystallography	Rhombo-hedral
Color	Black
Specific Gravity	2.52
Knoop 100 hardness	2900 - 3580
Shape	Blacky-Angular
Melting Point °C	2350
Density (g/cc)	2.52
Young's Modulus (GPa)	450-470
Thermal Conductivity (at 25°C W/m – K)	30-42

RHA is one of the farming waste substances and is characteristic fortification material. An enormous measure of rice husk is produced over the world consistently. This amount of waste is a challenge to dispose of. The momentum research focused to change over the RHA squander into valuable support material by getting Si through rice husk flakes. The concoction synthesis of arranged RHA is shown in Table 5. The normal molecule size of utilized RHA is 30 µm. Figure 2 is the SEM image of RHA particles and properties are available in Table 6.

Fig. 2. Scanning Electron Microphotograph of RHA particles

Table 5. Chemistry of RHA

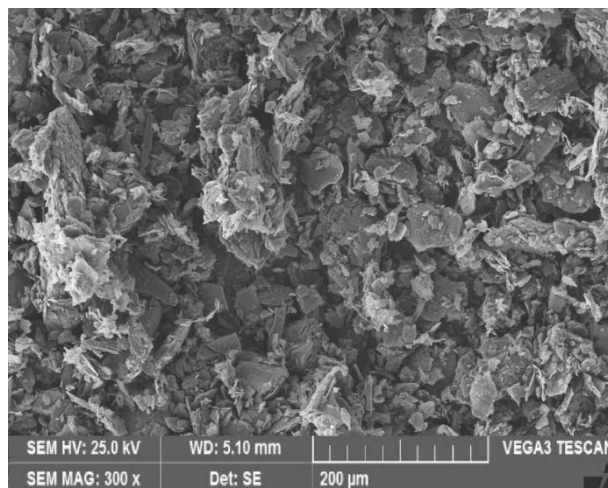| Elements	SiO_2	K_2O	CaO	MgO	Fe_2O_3	Al_2O_3	C	Na_2O	LOI*
Wt. (%)	93.1	1.28	1.1	0.56	0.49	0.47	0.33	0.6	2.61

*LOI-Loss of Ignition

Table 6. Physical and mechanical properties of RHA

Crystallography	Rhombo-hedral
Color	Black
Specific Gravity	2.52
Knoop 100 hardness	2900 - 3580
Shape	Blacky-Angular
Melting Point °C	2350
Density (g/cc)	2.52
Young's Modulus (GPa)	450-470
Thermal Conductivity (at 25°C W/m – K)	30-42

The cost-effective and uncomplicated stir casting was selected for the fabrication of the composites in the current research. ADC12 aluminum Alloy-B_4C-Rice Husk Ash hybrid composites with a varying weight percentage of Rice husk ash were fabricated with the help of the stir casting technique. During the development of Aluminum alloy based composite, ADC12 Aluminum Alloy was reinforced within B_4C-Rice husk ash material. The different hybrid composites were prepared having B_4C fixed wt5% and Rice husk ash particulates varied with wt.% 3,6,9. Initially, the compact chunks of ADC12 Aluminum Alloy were placed in a crucible, and the temperature was raised up to 750°C in a furnace. Parallelly, B_4C particles of 40μm and Rice husk ash powder particles of 30μm were heated in an oven whose temperature was set to 300°C this preheating was carried out in order to remove trapped moisture or any unwanted organic elements. Now, the calculated amount of preheated B_4C particles and RHA powder were introduced within the molten metal of aluminum alloy, and brisk stirring of molten metal is carried out using an electric motor stirrer until there is a formation of a vortex. The stirring speed was maintained in the range of 500±25 rpm with the help of a tachometer. Continuous stirring for 5-7 minutes was conducted so that each and every B_4C and RHA particles were mixed in the molten metal thoroughly and 1% wt of magnesium chips were added to the molten mixture to improve the wettability of the composite mixture. Now, the thoroughly mixed molten composite mixture is poured into a

graphite-coated metal mould die at room temperature. Once the molten metal mix solidifies it is ejected carefully from the dies and machined to ASTM standards for the conduction of wear tests.

Design of experiment (DOE). Many orthogonal arrays available for the design of experiments are based on several parameters at their respective levels. For the optimization of parameter levels along with the reduction in cost and time of experimentation, the selection of a perfect orthogonal array is very important. Orthogonal design helps us in knowing the effect of multiple factors on wear depth. For determining the wear behavior in the present work, the three design factors chosen are Speed (N), Load (W), and RHA at three levels as in Table 7.

Table 7. Design factors and their levels

Levels	Design Factors		
	Speed N, (rpm)	Load W, (N)	RHA (wt.%)
1	250	10	3
2	500	20	6
3	750	30	9

The values of design factors obtained at three different levels are shown in Table 4 above. The software "Minitab" helps in improving factor interaction along with accuracy by selecting design factors, levels, and L27 orthogonal array during analysis. L27 is the number of trial runs i.e., 27 runs are carried out during experimentation. Each column is assigned to the respective factor and interconnected factors.

Table 8 below represents L27 orthogonal array. Each of the columns is assigned with a respective parameter. Speed (N) is assigned to the first column similarly, the second and fifth columns are assigned to Load (W) and RHA respectively. The rest of the columns assign themselves to the errors and interrelated factors. The trial runs were conducted based on L27 orthogonal array and the degree of design factors represented in each row is shown in Table 8.

To diminish the wear depth S/N ratios were calculated by considering the objective as smaller is the better. The analysis of variance ANOVA for experiment results was applied to find the contribution of each factor in the output.

Wear test. Pin on Disk machine (Ducom-20) was used to analyze the wear characteristics and behavior of Al/B4C/RHA hybrid composite under dry conditions. ASTM G99 wear test standards were considered for the conduction of experiments over a circular specimen with diameter of 10 mm and length of 15 mm. Under dry sliding conditions, By considering the parameters like varying load of 10N, 20N, 30N, and sliding distance of 1000 m also keeping track diameter of 50 mm wear rate was found out. The developed hybrid composite comprising of Al/B_4C/RHA standard test specimens was forced against a revolving steel disk whose hardness is 55 HRC and a part of wear testing machine i.e., steel disk revolved and the pin (specimen) is secured by a holder clamp. The required input data like speed, time, load setting, etc. were entered into the system software also the required manual application of load was carried out. Now as per the orthogonal array the wear tests was conducted for each set of the specimen by varying the speeds from 250 RPM to 750 RPM. After the wear test, wear loss was determined from the depth of the sample by the weighing machine as system response, and digital data were collected. Analysis was done by digital data collected from the experimentation used as an output response as in Table 9.

Table 8. Orthogonal array L27 (3^{13}) of Taguchi

Experiment No.	1	2	3	4	5	6	7	8	9	10	11	12	13
1	1	1	1	1	1	1	1	1	1	1	1	1	1
2	1	1	1	1	2	2	2	2	2	2	2	2	2
3	1	1	1	1	3	3	3	3	3	3	3	3	3
4	1	2	2	2	1	1	1	2	2	2	3	3	3
5	1	2	2	2	2	2	2	3	3	3	1	1	1
6	1	2	2	2	3	3	3	1	1	1	2	2	2
7	1	3	3	3	1	1	1	3	3	3	2	2	2
8	1	3	3	3	2	2	2	1	1	1	3	3	3
9	1	3	3	3	3	3	3	2	2	2	1	1	1
10	2	1	2	3	1	2	3	1	2	3	1	2	3
11	2	1	2	3	2	3	1	2	3	1	2	3	1
12	2	1	2	3	3	1	2	3	1	2	3	1	2
13	2	2	3	1	1	2	3	2	3	1	3	1	2
14	2	2	3	1	2	3	1	3	1	2	1	2	3
15	2	2	3	1	3	1	2	1	2	3	2	3	1
16	2	3	1	2	1	2	3	3	1	2	2	3	1
17	2	3	1	2	2	3	1	1	2	3	3	1	2
18	2	3	1	2	3	1	2	2	3	1	1	2	3
19	3	1	3	2	1	3	2	1	3	2	1	3	2
20	3	1	3	2	2	1	3	2	1	3	2	1	3
21	3	1	3	2	3	2	1	3	2	1	3	2	1
22	3	2	1	3	1	3	2	2	1	3	3	2	1
23	3	2	1	3	2	1	3	3	2	1	1	3	2
24	3	2	1	3	3	2	1	1	3	2	2	1	3
25	3	3	2	1	1	3	1	3	2	1	2	1	3
26	3	3	2	1	2	1	3	1	3	2	3	2	1
27	3	3	2	1	3	2	1	2	1	3	1	3	1

4. Results and discussion

Microstructural analysis. The microstructural characterizations of specimens are inspected by SEM equipment. Figure 3 shows the SEM micrographs of ADC12 material with B_4C and RHA micro particulates reinforced composites without heat treatment. Figure 3 (a) shows the SEM of pure ADC12 material. Figure 3 (b-e) shows the SEM images of ADC12 alloy with a constant 5 wt. % of B_4C and 3, 6, 9 and 12 wt. % of RHA hybrid composites respectively. The SEM micrograph of as-cast ADC12 is free from particulates as it is an unreinforced alloy. Since the ADC12 alloy contains Si as the key alloying element, the presence of silicon is clearly represented by the leafy structure in the matrix. In addition, Figure 3 (b-e) shows that the B_4C and RHA particles in the produced hybrid composites are homogeneous. The enhanced reinforcing content in the ADC12 alloy composites is also visible in the microphotographs. As can be observed in Fig. 3 (e), adding 5 wt. percent B_4C microparticles and 12 wt. percent RHA particulates to the ADC12 matrix in two stages improved the microstructure of the composite significantly. The prepared samples with 5 wt. % of B_4C and 3, 6, and 9 wt. % of RHA particulates composites are free from clustering as in Fig. 3 (b-d). As wt. % of RHA particulates increased to 12 wt. % in ADC12 with 5 wt. % of B_4C, agglomeration is observed in the hybrid composites due to higher wt. % of low-density

particles. It is also noted in Fig. 3 (b-e) that the micro B_4C and RHA particles are distinct and show a good bonding between the ADC12 alloys.

Table 9. Wear test and S/N ratio results

Experiment No.	Speed (RPM	Load (N)	RHA (%)	Wear (mm^3/m)	S/N Ratio
1	250	10	3	0.0055981	45.0393
2	250	10	6	0.0041500	47.6390
3	**250**	**10**	**9**	**0.0022882**	**52.8103**
4	250	20	3	0.0130621	37.6797
5	250	20	6	0.0105636	39.5237
6	250	20	9	0.0072458	42.7982
7	250	30	3	0.0216458	33.2925
8	250	30	6	0.0192409	34.3155
9	250	30	9	0.0141103	37.0093
10	500	10	3	0.0108229	39.3131
11	500	10	6	0.0083000	41.6184
12	500	10	9	0.0053390	45.4508
13	500	20	3	0.0246315	32.1702
14	500	20	6	0.0211273	33.5031
15	500	20	9	0.0156357	36.1176
16	500	30	3	0.0373204	28.5611
17	500	30	6	0.0339546	29.3820
18	500	30	9	0.0263138	31.5963
19	750	10	3	0.0171674	35.3059
20	750	10	6	0.0139591	37.1028
21	750	10	9	0.0102967	39.7460
22	750	20	3	0.0369472	28.6484
23	750	20	6	0.0324455	29.7769
24	750	20	9	0.0240256	32.3865
25	750	30	3	0.0541146	25.3337
26	750	30	6	0.0498000	26.0554
27	750	30	9	0.0392800	28.1166

Analysis of S/N ratio. The S/N ratio for several numbers of the experiment is achieved from wear loss test conducted and in order to obtain as less as possible wear depth for ADC12 Al alloy/B_4C/RHA hybrid MMC using Taguchi technique. Small is always a good objective which in turn is used to obtain the S/N ratio. The values obtained for the wear test and the respective S/N ratio results are shown in Table 9 above.

Table 10 depicts the response table of means of wear loss and Table 11 S/N ratios being smaller is better for speed (N), Load (W), and wt.% of RHA (RHA). The difference between maximum response value and minimum response value for a certain factor at different levels is called a delta value. Also, based on these delta values ranking are assigned to each factor in the wear loss response table. The Load (L) factor has the highest delta value so it is assigned as rank 1. Similarly, the Sliding speed (S) factor and wt. % of RHA factors are allocated as second and third rank based on delta values.
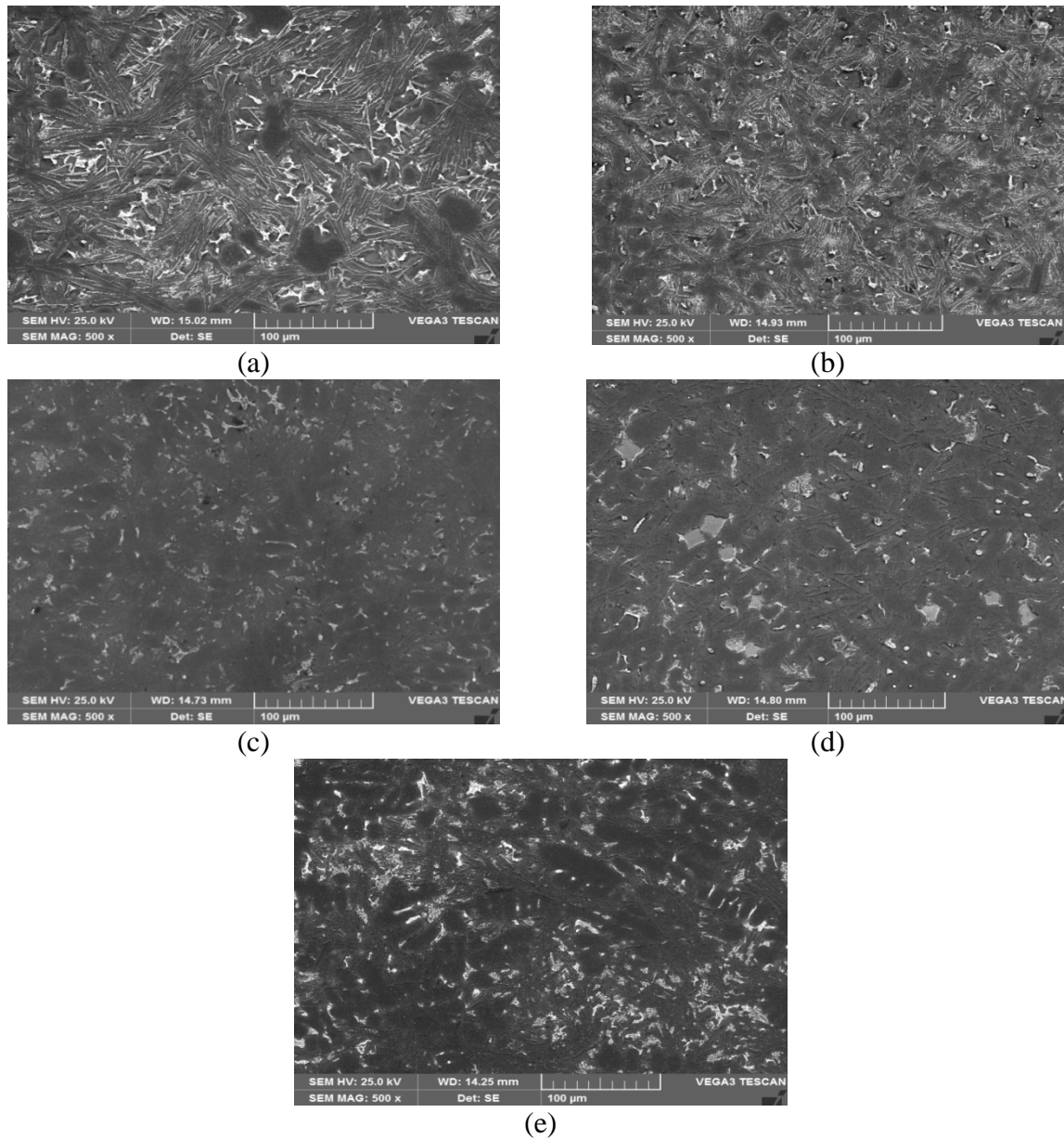
(a)

(b)

(c)

(d)

(e)

Fig. 3. (a-e) Scanning electron microphotographs of (a) ADC12 alloy (b) ADC12 Alloy-5% B_4C-3% RHA (c) ADC12 Alloy-5%-B_4C-6% RHA (d) ADC12 Alloy-5% B_4C-9% RHA (e) ADC12 Alloy-5% B_4C-12% RHA composites

Table 10. Response table for means of wear loss

Means of wear loss			
Level	Speed	Load	RHA
1	0.010878	0.008658	0.024590
2	0.020383	0.020632	0.021505
3	0.030893	0.032864	0.016059
Delta	0.020015	0.024207	0.008531
Rank	2	1	3

Table 11. Response table for S/N ratios smaller is better

S/N Ratios Smaller is better			
Level	Speed	Load	RHA
1	41.12	42.67	33.93
2	35.30	34.73	35.44
3	31.39	30.41	38.45
Delta	9.74	12.26	4.52
Rank	2	1	3
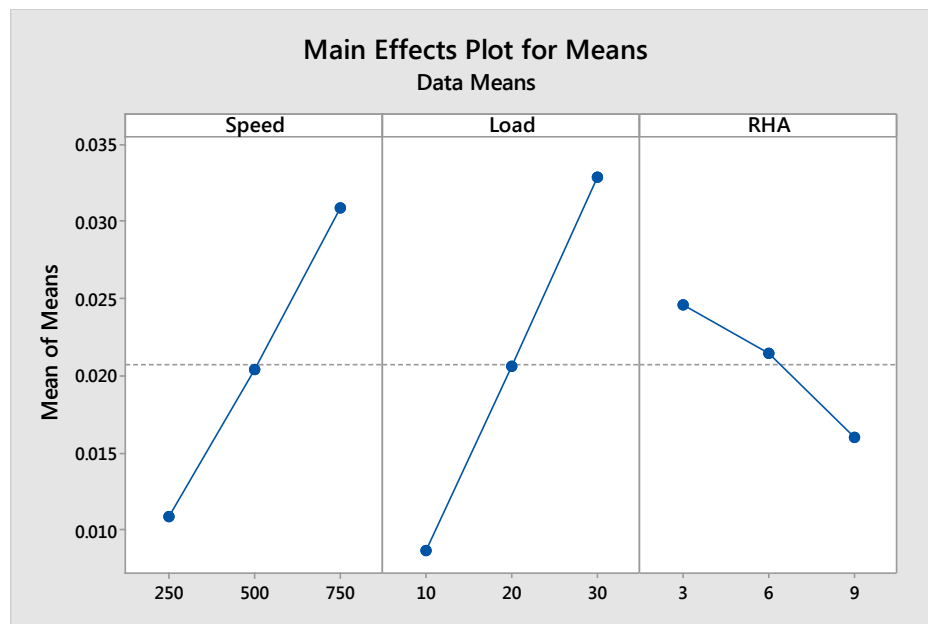
Fig. 4. Main Effects plot for Means of Means
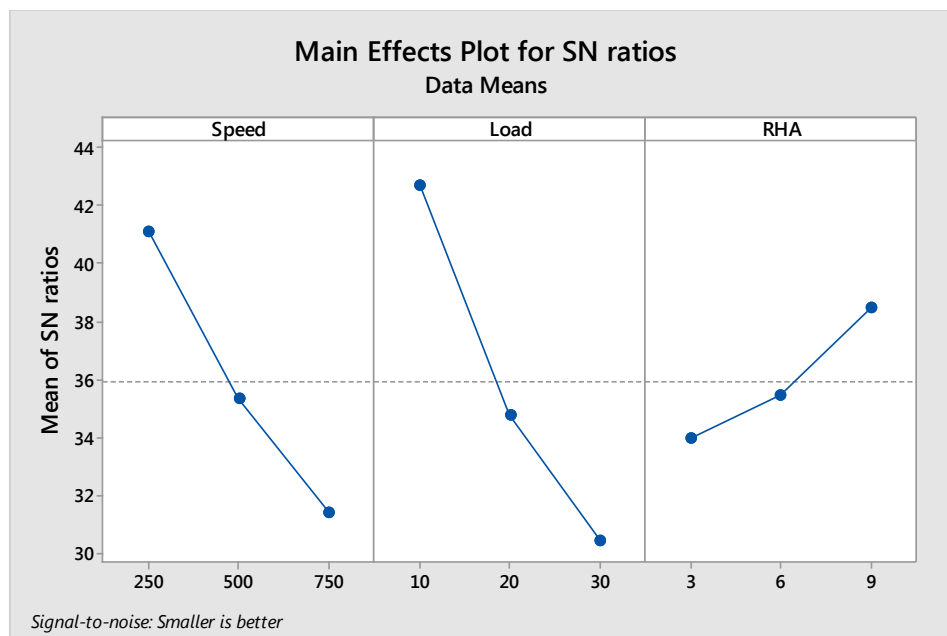
Fig. 5. Main Effects plot for Data SN ratio

Figures 4 and 5 main effects plot for mean and S/N ratio, each factor at different levels consisting of the maximum value of S/N ratio represents the significant level. The results indicate the maximum S/N ratio value is achieved by Speed (N) at level 1. Load (L) and wt.

% of RHA are at level 1 and Level 3 respectively. For Least wear, the ideal combination for experimentation is N1W1RHA3 (i.e., Speed= 250 rpm, Load = 10 N, wt. % of RHA = 9%).

Analysis of variance for wear. Variance test analysis is conducted to know the critical values which contribute largely to wear loss, and the interaction result on the hybrid composite samples along with the percent influence of each feature and factors interaction on ADC12 Aluminum Alloy-B_4C-RHA. Table 12 below indicates that the very critical parameter is Sliding speed (N) with the maximum contribution of 35.17%, along with Load (L) factor and wt. % of RHA whose contribution is 51.41% and 6.55% respectively towards hybrid composite specimen's wear loss. Among factors interactions, significant factors were speed (N) and load (S), have a contribution of 5.65 %.

Table 12. Analysis of variance for means

Source	DF	Seq SS	Adj MS	F Value	Contribution (%)
Speed	2	0.001804	0.000902	2470.37	35.17
Load	2	0.002637	0.001318	3610.65	51.41
RHA	2	0.000336	0.000168	459.83	6.55
Speed*Load	4	0.000290	0.000073	198.58	5.65
Speed*RHA	4	0.000028	0.000007	19.26	0.55
Load*RHA	4	0.000031	0.000008	21.38	0.60
Error	8	0.000003	0.000000		0.06
Total	26	0.005129			100.00

Confirmation test. For validation of analysis results, the regression technique was used. Using this technique, the relationship between the factors-interacting factors also output variable as a fitted equation to observed results.

Table 13. Analysis of variance for S/N ratio

Source	DF	Seq SS	Adj MS	F Value	P-value
Regression	6	1210.07	201.678	134.88	0.000
Speed	1	39.87	38.866	25.99	0.000
Load	1	50.39	50.390	33.70	0.000
RHA	1	30.20	30.201	20.20	0.000
Speed*Load	1	5.63	5.634	3.77	0.066
Speed*RHA	1	2.66	2.656	1.78	0.198
Load*RHA	1	6.47	6.474	4.33	0.051
Error	20	29.90	1.495		
Total	26	1239.97			

Table 13 depicts the analysis of variance for S/N ratio values used in developing the regression equation for the critical and interacting factors which resulted from the analysis of variance. Thus, the equation for S/N ratios obtained from regression analysis is

$$\text{S/N Ratio} = 51.34 - 0.02119(S) - 0.603(L) + 1.557(RHA) + 0.000274 \times (S \times L) - 0.000627 \times (S \times RHA) - 0.0245 \times (L \times RHA)$$

Table 14 below gives the validation of test results under ideal conditions. When we compare the different values of S/N ratio for both experimental wear loss and the one calculated using the regression equation it's just -1.715. Therefore, the calculated and experimental results for S/N ratio values very close to each other are having the least difference.

Table 14. Confirmation test results at optimum conditions

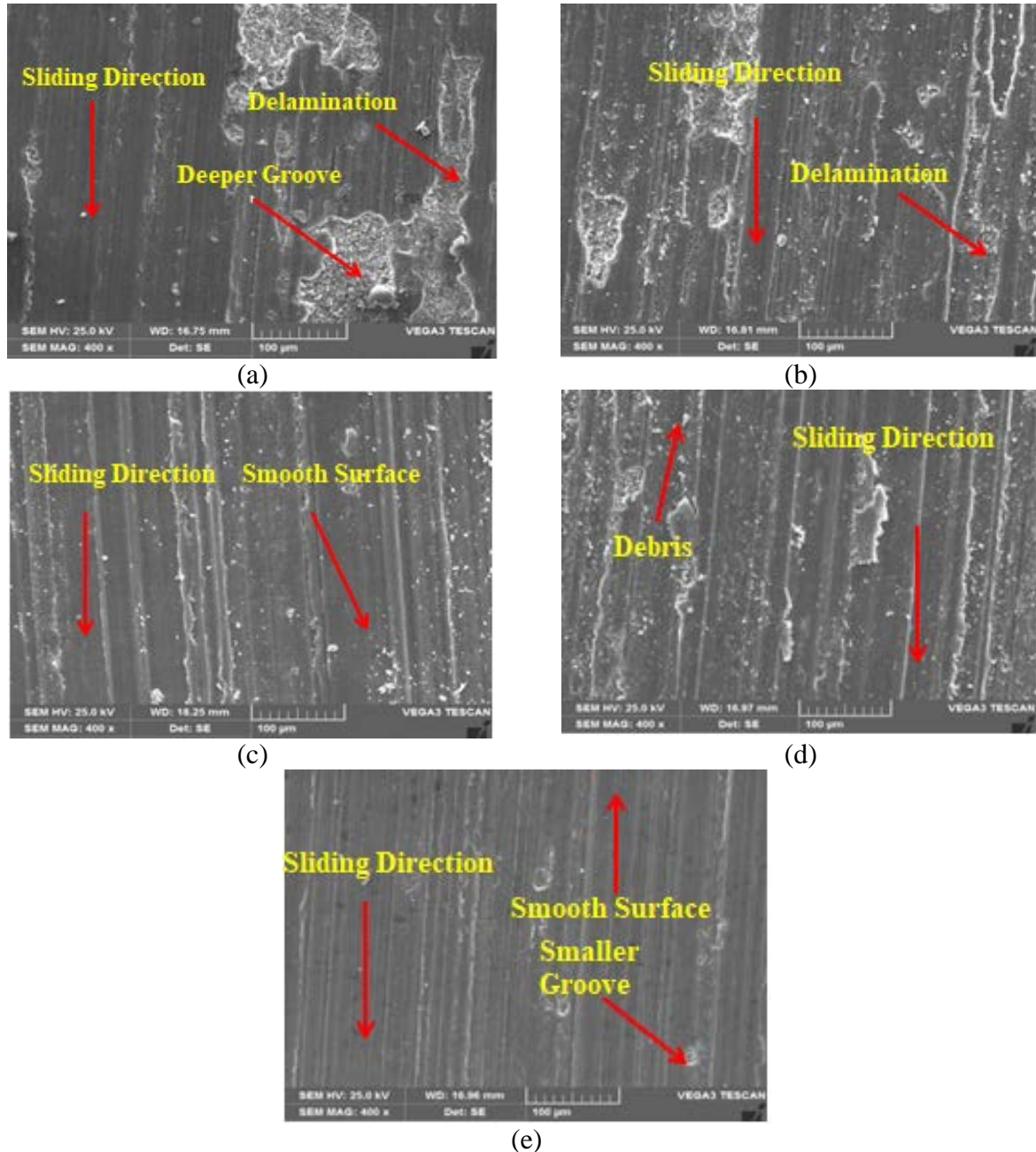| Sl. No.	Speed	Load	RHA	Wear (mm^3/m)	S/N Ratio	Regression equation S/N ratio	Difference
1	250	10	9	0.0022882	**52.8103**	51.09475	-1.71555

(a)

(b)

(c)

(d)

(e)

Fig. 6. Wear worn surfaces SEM images of (a) ADC12 alloy (b) ADC12-5 wt. % B$_4$C-3 wt. % of RHA (c) ADC12-5 wt. % B$_4$C-6 wt. % of RHA (d) ADC12-5 wt. % B$_4$C-9wt. % of RHA (e) ADC12-5 wt. % B$_4$C-12 wt. % of RHA composites

Worn surface analysis. Figure 6 is addressing the wear surfaces of ADC12 composite, ADC12 with 5 wt. % B$_4$C and 3 wt. % RHA, ADC12 combination with 5 wt. % B$_4$C and 6 wt. % RHA, ADC12 composite with 5 wt. % B$_4$C and 9 wt. % RHA and ADC12 compound with 5 wt. % B$_4$C and 12 wt. % RHA composites at the most extreme speed of 750 rpm and greatest loading condition of 30 N for 1000 m sliding distance. It is important to consider the

worn surface morphology of ADC12 and its B_4C and RHA particulates composites as it shows the kind of wear the materials with various creations have gone through. During sliding, the ADC12 composite network is milder than the scouring circle material and consequently shows the thick progression of aluminum lattice, which is a pin causing plastic disfigurement of the example surface, bringing about high material misfortune [15,16]. As shown in Fig. 6 (a), the ragged surface of ADC12 compound contains sections, small pits, and a broken oxide layer, all of which contributed to the extension of wear problems. Large grooved regions on the worn surface of the ADC12 alloy are visible in Fig. 6 (a). Deeper adhesive grooves in ADC12 alloy, cracks on the worn surface, and scratches cause plastic deformation of unreinforced material. Continual wear grooves and a few damaged spots are visible, as shown in Fig. 6 (a). The frictional heat has softened the ADC12 alloy matrix, as evidenced by a large adhesive groove. More material was lost in those spots because they were chipped away under a heavier load and faster speed and over a longer sliding distance. In as-cast ADC12 alloy, the adhesive wear is most noticeable in the wide or larger delaminated region.

Lesser depressions and scores may be seen in Fig. 6 (b-e), indicating that the area is protected from wear. Figure 6 (b-e) shows the parallel groove which indicates the abrasive wear as formed by the intrusion of the hard boron carbide and RHA particles into a smooth surface. The scored grooves formed on the track disc in addition to the impact of the wear-hardened deposits. The presence of B_4C and RHA particles in the ADC12 alloy acts as a barrier for plastic deformation during the wear process. These particles are hard in nature which contributes a reduction in material loss during wear tests. Fig. 6 (e) is showing the worn surface of ADC12 alloy with 5 wt.% of B_4C and 12 wt.% of RHA particle reinforced composites. The worn surface is smooth due to the presence of hard particles; very small groves are visible on the surface.

5. Conclusions

ADC12 alloy with 5 wt. % of constant B_4C particles and 3, 6, 9, and 12 varying wt. % of RHA particles reinforced hybrid composites were prepared by the stir cast method. Scanning electron micrographs indicated the through the distribution of dual particles in the ADC12 alloy. From the Taguchi analysis and wear experimentation ofADC12 Aluminum Alloy-B_4C-RHA Composite samples, the following conclusions were drawn.

- The wear characteristics of ADC12 Aluminum Alloy-B_4C-RHA composites were studied by Taguchi technique.
- The ideal combination for experimentation with the least wear depth is known to be S1W1RHA3, i.e., Speed250 rpm, load 10 N, and Sliding wt.9% RHA. From the analysis of variance, the factors speed (N), Load (W), and wt. % RHA are found to affect the wear significantly.
- However, load (W) and speed (N) are important factors with a contribution of 86.58%. Among the interaction factors, Speed (S) * Load (W) and Speed * RHA has the contribution of 6.2% found to be the most significant interaction. Further, worn surface analysis exhibited various wear mechanisms under load and sliding velocity conditions.

References

1. Nagaral M, Auradi V, Kori SA. Microstructure and Mechanical Properties of Al6061-graphite Composites Fabricated by Stir-Casting Process. *Applied Mechanics and Materials*. 2015;766-767: 308-314.

2. Matti S, Shivakumar BP, Shashidhar S, Nagaral M. Dry sliding wear behavior of mica, fly ash and red mud particles reinforced Al7075 alloy hybrid metal matrix composites. *Indian Journal of Science and Technology*. 2021;14 (4): 310-318.

3. Murali Mohan R, Kempaiah UN, Seenappa, Nagaral M. Processing and mechanical characterization of ADC12 alloy-B4C-RHA hybrid compositesю International. *Journal of Engineering and Advanced Technology*. 2019;9(2): 2239-2244.

4. Nagaral M, Auradi V, Kori SA. Vijayakumar Hiremath. Investigations on mechanical and wear behavior of nano Al2O3 particulates reinforced AA7475 alloy composites. *Journal of Mechanical Engineering and Sciences*. 2019;13(1): 4623-4635.

5. Zhou H, Yao P, Gong T, Xiao Y, Zhang Z, Zhao L, Fan K, Deng M. Effects of ZrO2 crystal structure on the tribological properties of copper metal matrix composites. *Tribology International*. 2019;138: 380-391.

6. Ram Prabhu T, Varma VK, Vedantam S. Tribological and mechanical behavior of multilayer Cu-SiC and Gr hybrid composites for brake friction material applications. *Wear*. 2014;317: 201-212.

7. Rjadhav P, Sridhar BR, Nagaral M, Harti JI. Mechanical behavior and fractography of graphite and boron carbide particulates reinforced A356 alloy hybrid metal matrix composites. *Advanced Composites and Hybrid Materials*. 2020;3: 114-119.

8. Nagaral M, Auradi V, Kori SA, Shivaprasad V. Mechanical characterization and wear behavior of nano TiO2 particulates reinforced Al7075 alloy composites. *Mechanics of Advanced Composite Structures*. 2020;7(1): 71-78.

9. Nagaral M, Kalgudi S, Auradi V, Kori S. Mechanical characterization of ceramic nano B4C-Al2618 alloy composites synthesized by semi solid processing. *Transactions of the Indian Ceramic Society*. 2018;77(3): 1-4.

10. Taguchi G. *Introduction to Quality Engineering*. Asian Productivity Organization; 1990.

11. Ross PJ. *Taguchi Technique for Quality Engineering*. 2nd ed. New York: McGraw-Hill; 1996.

12. Roy RK. *A Primer on Taguchi Method*. New York: Van Nostraid Reinhold; 1990.

13. *Minitab User Manual (Release 13.2), Making Data Analysis Easier*. PA, USA: MINITAB State College; 2001.

14. Manjunatha B, Niranjan HB, Satyanarayana KG. Effect of mechanical and thermal loading on boron carbide particles reinforced Al-6061 alloy. *Materials Science and Engineering: A*. 2015;632: 147-155.

15. Gopal Krishna UB, Vasudeva B, Auradi V, Nagaral M. Effect of percentage variation on wear behaviour of tungsten carbide and cobalt reinforced Al7075 matrix composites synthesized by melt stirring method. *Journal of Bio and Tribo Corrosion*. 2021;7(3): 1-8.

16. Nagaral M, Deshapande RG, Auradi V, Boppana SB, Dayanand S, Anilkumar MR. Mechanical and wear characterization of ceramic boron carbide-reinforced al2024 alloy metal composites. *Journal of Bio-and Tribo-Corrosion*. 2021;7(1): 1-12.

THE AUTHORS

Murali Mohan R.
e-mail: mmyuktha@gmail.com
ORCID: -

Kempaiah U.N.
e-mail: unkemp@rediffmail.com
ORCID: -

Manjunatha B.
e-mail: manjunathab.ait@gmail.com
ORCID: -

Nagaral Madeva
e-mail: madev.nagaral@gmail.com
ORCID: 0000-0002-8248-7603

Auradi V.
e-mail: vsauradi@gmail.com
ORCID: 0000-0001-6549-6340

Finite element algorithm for implementing variants of physically nonlinear defining equations in the calculation of an ellipsoidal shell

A.Sh. Dzhabrailov[1 ✉], A.P. Nikolaev[1], Yu.V. Klochkov[1], N.A. Gureyeva[2]

[1] FGBOU VPO Volgograd state agrarian University, 400002, Volgograd, PR. University, d. 26, Russia

Financial University under the Government of the Russian Federation, Moscow, Russia

✉ arsen82@yandex.ru

Abstract. The defining equations at the loading step are obtained in three variants. In the first variant, the relations between strain increments and stress increments are obtained by differentiating the equations of the theory of small elastic-plastic deformations using the hypothesis of plastic incompressibility of the material. In the second variant, the assumption of plastic incompressibility was not used. The relations between the first invariants of stress and strain tensors were considered to be known from the extension test. In the third variant, the defining equations at the loading step are obtained without dividing the strain increments into elastic and plastic parts based on the hypothesis of proportionality of the components of the strain increment deviators and the components of the stress increment deviators using the relations between the first invariants of the stress and strain increment tensors determined experimentally. The numerical example shows the preference of the third variant of the defining equations.

Keywords: shell, strain tensor, finite element, displacement vector, physical nonlinearity, plasticity matrix, stress tensor

1. Introduction

At present, the theory of shells has a fairly complete outline [1,2,3,4]. Obtaining analytical solutions for the vast majority of problems in engineering practice is not possible due to the complexity of the equations. Therefore, the development and improvement of numerical methods for strength calculations of engineering structures is an urgent task at the present time. One of the priority directions of the world's leading researchers in the field of studying thin-walled shell structures is taking into account the physical nonlinearity of the material used [5-15]. The most effective among modern methods used in the design of thin-walled structures is the finite element method (FEM). The development of the FEM is devoted to the works of many domestic and foreign authors [16-25]. When taking into account the physical nonlinearity, the above-mentioned works use the classical assumption of the invariance of the

volume as a result of elastic-plastic deformations, which does not quite correspond to the physical meaning of the deformation process and in some cases can lead to significant errors. Moreover, in physically nonlinear calculations, it is customary to divide the strain increments at the loading step into elastic and plastic parts. In the presented work, using the assumption that the components of the deviators of the increments of strains are proportional to the components of the deviators of the increments of stresses, the authors obtained new constitutive equations in which the above separation of strains at the loading step is absent.

2. Materials and methods

Basic relations. The position of the point M^0 of the middle surface of the ellipsoid is determined by the radius vector [26]

$$\mathbf{R^0} = asinT\mathbf{i} + bcosTsint\mathbf{j} + ccosTcost\mathbf{k}, \tag{1}$$

where a,b,c – segments cut off on the OX, OY, OZ axes; $\mathbf{i}, \mathbf{j}, \mathbf{k}$ – orts the Cartesian coordinate system; T – ellipse parameter in the OZ plane; t – ellipse parameter in the plane perpendicular to the OX axis.

The basis vectors at the point M^0 can be found as follows (1):

$$\mathbf{a}_1^0 = \mathbf{R^0}_{,T} = acosT\mathbf{i} - bsinTsint\mathbf{j} - csinTcost\mathbf{k}; \tag{2}$$
$$\mathbf{a}_2^0 = \mathbf{R^0}_{,t} = bcosTcost\mathbf{j} - ccosTsint\mathbf{k}.$$

The normal to the middle surface is determined by the vector product:

$$\mathbf{a}_3^0 = \frac{\mathbf{a}_1^0 \times \mathbf{a}_2^0}{|\mathbf{a}_1^0 \times \mathbf{a}_2^0|} = \frac{u_1}{u}\mathbf{i} + \frac{u_2}{u}\mathbf{j} + \frac{u_3}{u}\mathbf{k}, \tag{3}$$

where $u_1 = bcsinTcosT$; $u_2 = acsintcos^2T$; $u_3 = abcostcos^2T$; $u = \sqrt{u_1^2 + u_2^2 + u_3^2}$.

Dependencies (2) and (3) are presented in the following form:

$$\{\mathbf{a}^0\} = [\tau(T,t)]\{\mathbf{i}\}; \quad \{\mathbf{i}\} = [\tau(T,t)]^{-1}\{\mathbf{a}^0\}, \tag{4}$$
$$\underset{3\times1}{} \quad \underset{3\times3}{} \quad \underset{3\times1}{} \quad \underset{3\times1}{} \quad \underset{3\times3}{} \quad \underset{3\times1}{}$$

where $\{\mathbf{a}^0\}^T = \{\mathbf{a}_1^0 \mathbf{a}_2^0 \mathbf{a}_3^0\}$; $\{\mathbf{i}\}^T = \{\mathbf{ijk}\}$.
$\underset{1\times3}{} \qquad\qquad\qquad \underset{1\times3}{}$

Differentiating the basis vectors (4) of an arbitrary point of the middle surface, we express them by the components of the same basis:

$$\{\mathbf{a}^0_{,T}\} = [\tau(T,t)_{,T}]\{\mathbf{i}\} = [\tau(T,t)_{,T}][\tau(T,t)]^{-1}\{\mathbf{a}^0\} = [M]\{\mathbf{a}^0\};$$
$$\underset{3\times1}{} \quad \underset{3\times3}{} \quad \underset{3\times1}{} \quad \underset{3\times3}{} \quad \underset{3\times3}{} \quad \underset{3\times1}{} \quad \underset{3\times3}{}\underset{3\times1}{}$$
$$\{\mathbf{a}^0_{,t}\} = [\tau(T,t)_{,t}]\{\mathbf{i}\} = [\tau(T,t)_{,t}][\tau(T,t)]^{-1}\{\mathbf{a}^0\} = [N]\{\mathbf{a}^0\}, \tag{5}$$
$$\underset{3\times1}{} \quad \underset{3\times3}{} \quad \underset{3\times1}{} \quad \underset{3\times3}{} \quad \underset{3\times3}{} \quad \underset{3\times1}{} \quad \underset{3\times3}{}\underset{3\times1}{}$$

where $\{\mathbf{a}^0_{,T}\}^T = \{\mathbf{a}_{1,T}^0 \mathbf{a}_{2,T}^0 \mathbf{a}_{3,T}^0\}$; $\{\mathbf{a}^0_{,t}\}^T = \{\mathbf{a}_{1,t}^0 \mathbf{a}_{2,t}^0 \mathbf{a}_{3,t}^0\}$.
$\underset{1\times3}{} \qquad\qquad\qquad\qquad \underset{1\times3}{}$

Consider several main positions of the points of the middle surface of the shell during deformation: the deformed position after $(j-1)$ loading steps (point M, displacement vector $\mathbf{v}$) and the position after the jth loading step (point M^*, displacement vector $\Delta\mathbf{v}$). The points of an arbitrary layer of the shell, spaced at a distance of ξ from the median line, are denoted by the symbols $M^{0\xi}$, M^ξ, and $M^{*\xi}$ corresponding to the indicated states.

Radius vectors of the points M, M^*, $M^{0\xi}$, M^ξ, and $M^{*\xi}$ are determined as follows:

$$\mathbf{R}^{0\xi} = \mathbf{R}^0 + \xi\mathbf{a}_3^0; \quad \mathbf{R} = \mathbf{R}^0 + \mathbf{v}; \quad \mathbf{R}^* = \mathbf{R} + \Delta\mathbf{v}; \tag{6}$$
$$\mathbf{R}^\xi = \mathbf{R}^{0\xi} + \mathbf{v} + \xi(\mathbf{a}_3 - \mathbf{a}_3^0); \quad \mathbf{R}^{*\xi} = \mathbf{R}^\xi + \Delta\mathbf{v} + \xi(\mathbf{a}_3^* - \mathbf{a}_3),$$

where $\mathbf{a}_3$ and $\mathbf{a}_3^*$ – normalized vectors to the middle surface of the shell at the points M and M^*.

The components of the displacement vectors $\mathbf{v}$ and $\Delta\mathbf{v}$ included in (6) are determined on the initial basis of the point M^0:

$$\mathbf{v} = v^i\mathbf{a}_i^0; \quad \Delta\mathbf{v} = \Delta v^i\mathbf{a}_i^0. \tag{7}$$

The basis vectors at the points $M^{0\xi}$, M^ξ, and $M^{*\xi}$ are found by differentiating (6) and taking into account (5):

$$\mathbf{g}_1^0 = \mathbf{R}_{,T}^{0\xi}; \quad \mathbf{g}_1 = \mathbf{R}_{,T}^\xi + \mathbf{v}_{,T} + \xi(\mathbf{a}_{3,T} - \mathbf{a}_{3,T}^0);$$

$$\mathbf{g}_1^* = \mathbf{R},_T^* = \mathbf{g}_1 + \Delta\mathbf{v},_T + \xi\left(\boldsymbol{a}_{3,T}^* - \boldsymbol{a}_{3,T}\right); \tag{8}$$
$$\mathbf{g}_2^0 = \mathbf{R},_t^{0\xi}; \mathbf{g}_2 = \mathbf{R},_t^\xi + \mathbf{v},_t + \xi\left(\mathbf{a}_{3,t} - \mathbf{a}_{3,t}^0\right);$$
$$\mathbf{g}_2^* = \mathbf{R},_t^* = \mathbf{g}_2 + \Delta\mathbf{v},_t + \xi\left(\boldsymbol{a}_{3,t}^* - \boldsymbol{a}_{3,t}\right).$$

The derivatives of the vectors $\mathbf{v}$ and $\Delta\mathbf{v}$ can be obtained by differentiating (7) and taking into account (5):

$$\mathbf{v},_\alpha = z_\alpha^m \mathbf{a}_m^0; \mathbf{v},_{\alpha\beta} = z_{\alpha\beta}^m \mathbf{a}_m^0$$
$$\Delta\mathbf{v},_\alpha = f_\alpha^m \mathbf{a}_m^0; \Delta\mathbf{v},_{\alpha\beta} = f_{\alpha\beta}^m \mathbf{a}_m^0, \tag{9}$$

where z_α^m and $z_{\alpha\beta}^m$ – functions of the displacement vector components $\mathbf{v}$ and their derivatives; f_α^m, $f_{\alpha\beta}^m$ – functions of the displacement vector components $\Delta\mathbf{v}$ and their derivatives; for $\alpha=1$ we understand the derivative with respect to the parameter T; for $\alpha=2$ – differentiation with respect to the parameter t.

The unit normal vectors at the points M and M^* can be represented by the vector products of the corresponding basis vectors tangent to the middle surface of the ellipsoid at the points under consideration. When calculating in a geometrically linear formulation, these unit vectors can be represented by the expressions:

$$\mathbf{a}_3 = \frac{\mathbf{a}_1 \times \mathbf{a}_2}{\sqrt{a}}; \mathbf{a}_3^* = \frac{\mathbf{a}_1^* \times \mathbf{a}_2^*}{\sqrt{a}}, \tag{10}$$

where $\mathbf{a}_1 = (\mathbf{R}^0 + \mathbf{v}),_T$; $\mathbf{a}_2 = (\mathbf{R}^0 + \mathbf{v}),_t$; $\mathbf{a}_1^* = (\mathbf{R} + \Delta\mathbf{v}),_T$; $\mathbf{a}_2^* = (\mathbf{R} + \Delta\mathbf{v}),_t$; $a = a_{11}a_{22} - a_{12}a_{21}$ – determinant of the metric tensor at a point M.

When determining the curvature in an arbitrary shell layer spaced at a distance ξ from the median line, one can apply the equations of continuum mechanics [27]:

$$\varepsilon_{\alpha\beta}^\xi = \frac{1}{2}\left(g_{\alpha\beta} - g_{\alpha\beta}^0\right); \Delta\varepsilon_{\alpha\beta}^\xi = \frac{1}{2}\left(g_{\alpha\beta}^* - g_{\alpha\beta}\right), \tag{11}$$

where $g_{\alpha\beta}^0 = \mathbf{g}_\alpha^0 \mathbf{g}_\beta^0$; $g_{\alpha\beta} = \mathbf{g}_\alpha \mathbf{g}_\beta$; $g_{\alpha\beta}^* = \mathbf{g}_\alpha^* \mathbf{g}_\beta^*$ – covariant components of metric tensors at corresponding points.

When using (8), (9), and (10), the deformations at an arbitrary point of the shell (11) are represented by the expressions:

$$\varepsilon_{\alpha\beta}^\xi = \varepsilon_{\alpha\beta} + \xi\chi_{\alpha\beta}; \Delta\varepsilon_{\alpha\beta}^\xi = \Delta\varepsilon_{\alpha\beta} + \xi\Delta\chi_{\alpha\beta}, \tag{12}$$

where $\varepsilon_{\alpha\beta}^\xi$, $\chi_{\alpha\beta}$ – deformation and curvature of the middle surface of the shell at the point M; $\Delta\varepsilon_{\alpha\beta}$, $\Delta\chi_{\alpha\beta}$ – increments of deformations and curvature of the middle surface at a point M^*.

At the loading step, the deformation parameters of the middle surface in a linear formulation are determined by the expressions:

$$\Delta\varepsilon_{\alpha\beta} = \frac{1}{2}\left(\mathbf{a}_\alpha^0 \Delta\mathbf{v},_\beta + \mathbf{a}_\beta^0 \Delta\mathbf{v},_\alpha\right); \tag{13}$$
$$\Delta\chi_{\alpha\beta} = \frac{1}{2}\left(\mathbf{a}_\alpha^0 \Delta\mathbf{v},_\beta + \mathbf{a}_\beta^0 \Delta\mathbf{v},_\alpha + \mathbf{a}_\alpha^0 (\mathbf{a}_3^* - \mathbf{a}_3),_\beta + \mathbf{a}_\beta^0 (\mathbf{a}_3^* - \mathbf{a}_3),_\alpha\right).$$

Expressions (12) and (13) taking into account (8), (9) and (10) are presented in matrix form:

$$\underset{3\times1}{\{\varepsilon^\xi\}} = \underset{3\times6}{[G]}\underset{6\times1}{\{\varepsilon\}} = \underset{3\times6}{[G]}\underset{6\times33}{[L]}\underset{33\times1}{\{v\}}; \underset{3\times1}{\{\Delta\varepsilon^\xi\}} = \underset{3\times6}{[G]}\underset{6\times1}{\{\Delta\varepsilon\}} = \underset{3\times6}{[G]}\underset{6\times3}{[L]}\underset{3\times1}{\{\Delta v\}}, \tag{14}$$

where $\{\varepsilon^\xi\}^T = \left\{\varepsilon_{11}^\xi \varepsilon_{22}^\xi 2\varepsilon_{12}^\xi\right\}$; $\{\Delta\varepsilon^\xi\}^T = \left\{\Delta\varepsilon_{11}^\xi \Delta\varepsilon_{22}^\xi 2\Delta\varepsilon_{12}^\xi\right\}$;
$\{\varepsilon\}^T = \{\varepsilon_{11}; \varepsilon_{22}; 2\varepsilon_{12}; \chi_{11}; \chi_{22}; 2\chi_{12}\}$; $\{v\}^T = \{v^1; v^2; v^3\}$;
$\{\Delta v\}^T = \{\Delta v^1; \Delta v^2; \Delta v^3\}$; $\{\Delta\varepsilon\}^T = \{\Delta\varepsilon_{11}; \Delta\varepsilon_{22}; 2\Delta\varepsilon_{12}; \Delta\chi_{11}; \Delta\chi_{22}; 2\Delta\chi_{12}\}$;
$[L]$ – transformation matrix.

Discretization element at the loading step. An arbitrary quadrangular fragment of the middle surface of the shell with nodes i, j, k, and l is taken as a finite element. To perform the numerical integration procedure, this fragment is approximated by a square with local coordinates ζ and η, varying within $-1 \leq \zeta, \eta \leq 1$. The mapping is implemented using bilinear functions:

$$\lambda = \{f(\zeta,\eta)\}^T_{1\times4}\{\lambda_y\}_{4\times1}, \tag{15}$$

where $\{\lambda_y\}^T = \{\lambda^i \lambda^j \lambda^k \lambda^l\}$, and the symbol λ means the values of the nodal parameters T and t, which are further denoted by the symbols θ^1 and θ^2, respectively.

After the derivatives (15) are found, the coordinates θ^α in the system $\zeta, \eta (\theta^\alpha_{,\zeta}, \theta^\alpha_{,\eta})$ and local coordinates ζ, η are differentiated with respect to the global unknowns θ^α $(\zeta_{,\alpha}, \eta_{,\alpha}, \zeta_{,\alpha\beta}, \eta_{,\alpha\beta})$.

As nodal variable parameters for (j-1) previous steps, the components of the displacement vector and their derivatives in local and global coordinate systems are selected:

$$\{v^n_l\}^T_{1\times12} = \left\{ v^{ni} v^{nj} v^{nk} v^{nl} v^{ni}_{,\zeta}\ v^{nj}_{,\zeta}\ v^{nk}_{,\zeta}\ v^{nl}_{,\zeta}\ v^{ni}_{,\eta}\ v^{nj}_{,\eta}\ v^{nk}_{,\eta}\ v^{nl}_{,\eta} \right\}; \tag{16}$$

$$\{v^n_g\}^T_{1\times12} = \left\{ v^{ni} v^{nj} v^{nk} v^{nl} v^{ni}_{,\theta^1}\ v^{nj}_{,\theta^1}\ v^{nk}_{,\theta^1}\ v^{nl}_{,\theta^1}\ v^{ni}_{,\theta^2}\ v^{nj}_{,\theta^2}\ v^{nk}_{,\theta^2}\ v^{nl}_{,\theta^2} \right\},$$

where $n=1,2,3$.

Similarly, at the jth loading step

$$\{\Delta v^n_l\}^T_{1\times12} = \left\{ \Delta v^{ni} \Delta v^{nj} \Delta v^{nk} \Delta v^{nl} \Delta v^{ni}_{,\zeta}\ \Delta v^{nj}_{,\zeta}\ \Delta v^{nk}_{,\zeta}\ \ldots\ldots \Delta v^{nk}_{,\eta}\ \Delta v^{nl}_{,\eta} \right\}; \tag{17}$$

$$\{\Delta v^n_g\}^T_{1\times12} = \left\{ \Delta v^{ni} \Delta v^{nj} \Delta v^{nk} \Delta v^{nl} \Delta v^{ni}_{,\theta^1} \ldots\ldots \Delta v^{nj}_{,\theta^2} \Delta v^{nk}_{,\theta^2} \Delta v^{nl}_{,\theta^2} \right\}.$$

The local basis nodal vectors of the finite element (FE) at the loading step can be represented as:

$$\{\Delta V^l_y\}^T_{1\times36} = \left\{ \{\Delta v^{1l}\}^T_{1\times12} \{\Delta v^{2l}\}^T_{1\times12} \{\Delta v^{3l}\}^T_{1\times12} \right\}; \{\Delta V^g_y\}^T_{1\times36} = \left\{ \{\Delta v^{1g}\}^T_{1\times12} \{\Delta v^{2g}\}^T_{1\times12} \{\Delta v^{3g}\}^T_{1\times12} \right\}. \tag{18}$$

When using differential dependencies

$$v^n_{,\zeta} = v^n_{,\theta^1} \theta^1_{,\zeta} + v^n_{,\theta^2} \theta^2_{,\zeta}; v^n_{,\eta} = v^n_{,\theta^1} \theta^1_{,\eta} + v^n_{,\theta^2} \theta^2_{,\eta} ; (n = 1,2,3) \tag{19}$$

between nodal unknowns in local and global coordinate systems, the following matrix relation takes place:

$$\{\Delta V^l_y\}_{36\times1} = [H]_{36\times36} \{\Delta V^g_y\}_{36\times1}. \tag{20}$$

As a result of deformation, the position of the internal point of the FE can be determined through the nodal unknowns using the expressions:

$$v^n = \{\varphi\}^T_{1\times12}\{v^{nl}\}_{12\times1}; \Delta v^n = \{\varphi\}^T_{1\times12}\{\Delta v^{nl}\}_{12\times1}; \quad n = 1,2,3, \tag{21}$$

where the structure $\{\varphi\}^T$ includes Hermite polynomials of the third degree [28].

Based on (14), increments of step strain, taking into account (21), will take the form:

$$\{\Delta \varepsilon^\xi\}_{3\times1} = [G]_{3\times6}[L]_{6\times3}\{\Delta v\}_{3\times1} = [G]_{3\times6}[L]_{6\times3}[A]_{3\times36}\{\Delta V^l_y\}_{36\times1} = [G]_{3\times6}[B]_{6\times36}\{\Delta V^l_y\}_{36\times1}, \tag{22}$$

where $[A]_{3\times36} = \begin{bmatrix} \{\varphi\}^T_{1\times12} & \{0\}^T_{1\times12} & \{0\}^T_{1\times12} \\ \{0\}^T_{1\times12} & \{\varphi\}^T_{1\times12} & \{0\}^T_{1\times12} \\ \{0\}^T_{1\times12} & \{0\}^T_{1\times12} & \{\varphi\}^T_{1\times12} \end{bmatrix}.$

Relationships between strain increments and stress increments at the loading step.
The constitutive equations of the theory of small elastoplastic deformations in a curvilinear coordinate system are written as [29]:

$$\varepsilon^\xi_{\alpha\beta} - \frac{1}{3} g_{\alpha\beta} P^\xi_\varepsilon = \frac{3}{2} \frac{\varepsilon_i}{\sigma_i} \left(\sigma_{\alpha\beta} - \frac{1}{3} g_{\alpha\beta} P_\sigma \right), \tag{23}$$

where $\varepsilon^\xi_{\alpha\beta}$ – covariant strain tensor components; $P^\xi_\varepsilon = \varepsilon^\xi_{\alpha\beta} g^{\alpha\beta}$ – the first invariant of the strain tensor; $g_{\alpha\beta}, g^{\alpha\beta}$ – covariant and contravariant components of the metric tensor; $\sigma_{\alpha\beta}$ –

covariant stress tensor components; $P_\sigma = \sigma_{\alpha\beta} g^{\alpha\beta}$ – the first invariant of the stress tensor; ε_i – strain intensity; σ_i – stress intensity.

The dependence between the first invariants of the strain and stress tensor, taking into account the hypothesis of the incompressibility of the material, is written as [30]:

$$P_\varepsilon^\xi = \frac{1-2\mu}{E} P_\sigma = K_1 P_\sigma, \qquad (24)$$

where μ – the transverse strain coefficient; E – elasticity modulus of the material.

If we disregard the hypothesis about the incompressibility of the material, then relation (24) can be represented as follows:

$$P_\varepsilon^\xi = K_2 P_\sigma = \frac{3}{2} \frac{(1-2\mu)}{(1+\mu)} \frac{1}{E_{sd}} P_\sigma, \qquad (25)$$

where the coefficient K_2 is determined on the basis of experience with a simple tension of the rod; E_{sd} – secant modulus of the deformation diagram.

Taking into account (24) and (25) dependences (23) can be rewritten as:

$$\varepsilon_{\alpha\beta}^\xi = \frac{3}{2} \frac{\varepsilon_i}{\sigma_i} \sigma_{\alpha\beta} + \frac{1}{3} g_{\alpha\beta} P_\sigma \left(-\frac{3}{2} \frac{\varepsilon_i}{\sigma_i} + K_m \right), \qquad (26)$$

where $m = 1, 2$.

Dependences between strain increments and stress increments at the loading step are determined by differentiation of (26):

$$\Delta\varepsilon_{\alpha\beta}^\xi = \frac{\partial \varepsilon_{\alpha\beta}^\xi}{\partial \sigma_{11}} \Delta\sigma_{11} + \frac{\partial \varepsilon_{\alpha\beta}^\xi}{\partial \sigma_{22}} \Delta\sigma_{22} + \frac{\partial \varepsilon_{\alpha\beta}^\xi}{\partial \sigma_{12}} \Delta\sigma_{12}, \qquad (27)$$

where the coefficients K_m at the loading step are considered unchanged.

Based on (27), a matrix relation is formed:

$$\{\Delta\varepsilon^\xi\} = [D_m]\{\Delta\sigma_{\alpha\beta}\}, \qquad (28)$$
$$\underset{3\times1}{} \quad \underset{3\times3}{} \underset{3\times1}{}$$

where $\{\Delta\sigma_{\alpha\beta}\}^T = \{\Delta\sigma_{11} \Delta\sigma_{22} \Delta\sigma_{12}\}$ – string of stress increments at the loading step; $m = 1, 2$ depending on the coefficient K_m used.

The author's version of the relationship between increments of strains and stresses suggests using the assumption that the components of the deviator of increments of strains are proportional to the components of the deviator of increments of stresses:

$$\Delta\varepsilon_{\alpha\beta}^\xi - \frac{1}{3} g_{\alpha\beta} P_{\Delta\varepsilon}^\xi = \frac{3}{2} \frac{\varepsilon_i^\Delta}{\sigma_i^\Delta} \left(\Delta\sigma_{\alpha\beta} - \frac{1}{3} g_{\alpha\beta} P_{\Delta\sigma} \right), \qquad (29)$$

where $\Delta\varepsilon_{\alpha\beta}^\xi$ – covariant components of the strain increment tensor; $P_{\Delta\varepsilon}^\xi = \Delta\varepsilon_{\alpha\beta}^\xi g^{\alpha\beta}$ – the first invariant of the strain increment tensor; $\Delta\sigma_{\alpha\beta}$ – covariant components of the stress increment tensor; $P_{\Delta\sigma} = \Delta\sigma_{\alpha\beta} g^{\alpha\beta}$ – first invariant of the stress increment tensor; ε_i^Δ – intensity of strain increments; σ_i^Δ – intensity of stress increments.

In practical use in relations (29) it is assumed that the ratio of the intensities of strain increments and stress increments is equal to the ratio of increments of strain and stress intensities:

$$\frac{\varepsilon_i^\Delta}{\sigma_i^\Delta} = \frac{\Delta\varepsilon_i}{\Delta\sigma_i} = \frac{1}{E_x}, \qquad (30)$$

where E_x – the chord modulus of the deformation diagram at the loading step.

Applying the tension-compression test to a rod, one can obtain relations between the first invariants of the tensors of strain increments and stress increments:

$$P_{\Delta\varepsilon} = K_3 P_{\Delta\sigma} = \frac{3}{2} \frac{(1-2\mu)}{(1+\mu)} \frac{1}{E_x}. \qquad (31)$$

Taking into account (30) and (31) dependences (29) take the form:

$$\Delta\varepsilon_{\alpha\beta}^\xi = \frac{3}{2} \frac{1}{E_x} \Delta\sigma_{\alpha\beta} + \frac{1}{3} g_{\alpha\beta} P_{\Delta\sigma} \left(-\frac{3}{2} \frac{1}{E_x} + K_3 \right). \qquad (32)$$

Based on (32), a matrix relation is formed:

$$\{\Delta\varepsilon^\xi\} = [D_3]\{\Delta\sigma_{\alpha\beta}\}. \tag{33}$$
$$\underset{3\times1}{} \quad \underset{3\times3}{} \quad \underset{3\times1}{}$$

Finite element stiffness matrix. When forming the stiffness matrix of the FE described above at the loading step, the principle of equality of the work of internal and external forces is used, which is determined by the expression

$$\Phi = \int_V \Delta\varepsilon^\xi_{\alpha\beta}(\sigma^{\alpha\beta} + \Delta\sigma^{\alpha\beta}) \, dV - \int_F \Delta v^i(P_i + \Delta P_i) \, dF, \tag{34}$$

where $\sigma^{\alpha\beta}$ and $\Delta\sigma^{\alpha\beta}$ – contravariant components of the stress tensor for $(j\text{-}1)$ loading steps and the stress increment tensor at the jth loading step; P_i and ΔP_i are covariant components of the vector of external loads.

Based on the ratios:

$$\Delta\sigma^{\alpha\beta} = g^{\alpha\rho} g^{\beta\tau} \Delta\sigma_{\rho\tau}$$

a matrix expression is compiled:

$$\{\sigma^{\alpha\beta}\} = [g]\{\Delta\sigma_{\alpha\beta}\}. \tag{35}$$
$$\underset{3\times1}{} \quad \underset{3\times3}{} \quad \underset{3\times1}{}$$

To determine the stress increments in an arbitrary shell layer, using (28) and (33), one can obtain the matrix relation:

$$\{\Delta\sigma_{\alpha\beta}\} = [D_m]^{-1}\{\Delta\varepsilon^\xi\}. \tag{36}$$
$$\underset{3\times1}{} \quad \underset{3\times3}{} \quad \underset{3\times1}{}$$

Taking into account (36) and (22), functional (34) can be written as:

$$\Phi =$$

$$\{\Delta V_y^l\}^{\text{T}} \int_V [B]^{\text{T}}[G]^{\text{T}}[g]\{\sigma_{\alpha\beta}\}dV + \{\Delta V_y^l\}^{\text{T}} \int_V [B]^{\text{T}}[G]^{\text{T}}[D_m]^{-1}[g][G][B]\{\Delta V_y^l\}dV -$$
$$\underset{1\times36}{} \quad \underset{36\times6}{} \underset{6\times3}{} \underset{3\times3}{} \underset{3\times1}{} \qquad \underset{1\times36}{} \quad \underset{36\times6}{} \underset{6\times3}{} \underset{3\times3}{} \underset{3\times3}{} \underset{3\times66\times36}{} \underset{36\times1}{}$$

$$\{\Delta V_y^l\}^{\text{T}} \int_F [A]^{\text{T}}\{P\}dF - \{\Delta V_y^l\}^{\text{T}} \int_F [A]^{\text{T}}\{\Delta P\}dF. \tag{37}$$
$$\underset{1\times36}{} \quad \underset{36\times3}{} \underset{3\times1}{} \qquad \underset{1\times36}{} \quad \underset{36\times3}{} \underset{3\times1}{}$$

When using (20) and minimizing the functional (37) with respect to the nodal unknowns $\{\Delta V_y^g\}$, a matrix relation is formed:

$$[M]\{\Delta V_y^g\} = \{F\} + \{f\}, \tag{38}$$
$$\underset{36\times36}{} \underset{36\times1}{} \quad \underset{36\times1}{} \underset{36\times1}{}$$

where $[M] = [H]^T \int_V [B]^{\text{T}}[G]^{\text{T}}[D_m]^{-1}[g][G][B] \, dV \, [H]$ – step stiffness matrix of a
$$\underset{36\times36}{} \quad \underset{36\times36}{} \quad \underset{36\times6}{} \underset{6\times3}{} \underset{3\times3}{} \underset{3\times33\times66\times36}{} \quad \underset{36\times36}{}$$

quadrangular FE; $\{F\} = [H]^T \int_F [A]^{\text{T}}\{\Delta P\}dF$ – step vector of nodal loads; $\{f\} =$
$$\underset{36\times1}{} \quad \underset{36\times36}{} \quad \underset{36\times3}{} \underset{3\times1}{} \qquad\qquad\qquad \underset{36\times1}{}$$

$[H]^T \int_F [A]^{\text{T}}\{P\}dF - [H]^T \int_V [B]^{\text{T}}[G]^{\text{T}}[g]\{\sigma_{\alpha\beta}\}dV$ – the Newton-Raphson residual.
$$\underset{36\times36}{} \quad \underset{36\times3}{} \underset{3\times1}{} \quad \underset{36\times36}{} \quad \underset{36\times6}{} \underset{6\times3}{} \underset{3\times3}{} \underset{3\times1}{}$$

3. Obtained results

In order to verify the proposed algorithms, the problem of calculating the strength of a fragment of an elliptical cylinder shown in Fig. 1 was solved.
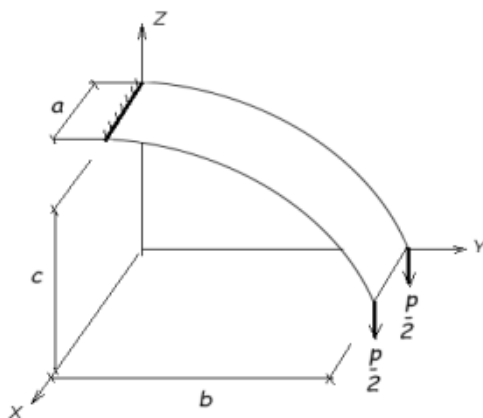

Fig. 1. Calculated structure

On the left edge, the structure is rigidly clamped. At the right edge, the shell is loaded with a tensile force of $p = 160$ N. The initial data were taken as follows: Young's modulus $E = 2 \cdot 10^6$ MPa, transverse strain coefficient $\mu = 0.32$, structure thickness $t = 0.5$ cm. The yield strength was achieved at stress intensity and strain intensity: $\sigma_{iT} = 200$ MPa and $\varepsilon_{iT} = 0.0023$ MPa, respectively. Geometric design parameters: $a = 1$ cm, $b = 10$ cm, $c = 5$ cm.

An analysis of the finite element solutions obtained at the first loading step made it possible to establish the optimal number of discretization elements for further calculations of the structure under consideration. It was taken equal to 24.

Approximation of the deformation diagram for a nonlinear section in the presented example was carried out using the function

$$\sigma_i = A\varepsilon_i^2 + B\varepsilon_i + C . \tag{39}$$

where $A = -23461.55$ MPa, $B = 181201.17$ MPa, $C = 1574.3$ MPa.

The problem was solved in three different variants. In the first variant, the calculation was performed taking into account the hypothesis of the incompressibility of the material as a result of plastic deformations. To determine the dependencies between the first invariants of the strain and stress tensor, the coefficient $K_1 = \frac{1-2\mu}{E}$ was used. The numerical values of the stresses for this option are shown in Table 1. It presents the values of the hoop stresses σ_{22} on the left edge of the structure, depending on the coordinate ξ along the shell thickness and N number of loading steps.

Table 1. Values of hoop stresses in the implementation of the first variant of the defining equations

y coordinate, cm	ξ coordinate, cm	Stress, MPa		
		Number of loading steps, N		
		10	30	70
0.0	-0.25	-300.7	-309.0	-314.4
	-0.166	-259.0	-264.6	-266.2
	-0.083	-176.6	-188.5	-191.9
	0.0	-2.2	-2.8	-2.81
	0.083	172.0	182.9	186.2
	0.166	257.9	263.3	264.9
	0.25	299.6	307.6	310.1

In another variant of the calculation, the hypothesis of the incompressibility of the material was not taken into account and the relationship between the first invariants of the strain and stress tensor was carried out using the coefficient $K_2 = \frac{3}{2}\frac{(1-2\mu)}{(1+\mu)}\frac{1}{E_{sd}}$, obtained from the rod extension test. The numerical values of the hoop stresses for the second calculation variant are presented in Table 2.

The last variant of the calculation used the hypothesis of the proportionality of the components of the strain increment deviators and the components of the stress increment deviators (29). In this case, the dependencies between the first invariants of the strain and stress increment tensors were determined using the coefficient $K_3 = \frac{3}{2}\frac{(1-2\mu)}{(1+\mu)}\frac{1}{E_x}$. Table 3 shows the numerical values of the hoop stresses σ_{22} obtained in this variant of the shell calculation.

Table 2. Values of hoop stresses in the implementation of the second variant of the defining equations

y coordinate, cm	ξ coordinate, cm	Stress, MPa		
		Number of loading steps, N		
		10	30	70
0.0	-0.25	-291.1	-303.3	-306.6
	-0.166	-251.9	-261.1	-263.5
	-0.083	-184.7	-200.9	-205.4
	0.0	-2.6	-2.8	-2.89
	0.083	179.5	195.2	199.6
	0.166	250.7	259.8	262.3
	0.25	289.9	302.1	305.4

Table 3. Values of hoop stresses in the implementation of the third version of the defining equations

y coordinate, cm	ξ coordinate, cm	Stress, MPa		
		Number of loading steps, N		
		10	30	70
0.0	-0.25	-300	-308.8	-311.3
	-0.166	-258.8	-264.5	-266.2
	-0.083	-175.8	-188.6	-192.3
	0.0	-2.2	-2.7	-2.8
	0.083	171.4	183.1	186.4
	0.166	257.6	263.3	264.7
	0.25	299.9	307.8	310

In order to verify the computational process for the point of the left support section, diagrams of hoop stresses were constructed along the thickness of the structure. The number of steps, in this case, was taken equal to $N=70$. These diagrams for each of the calculation options are shown in Figs. 2-4.
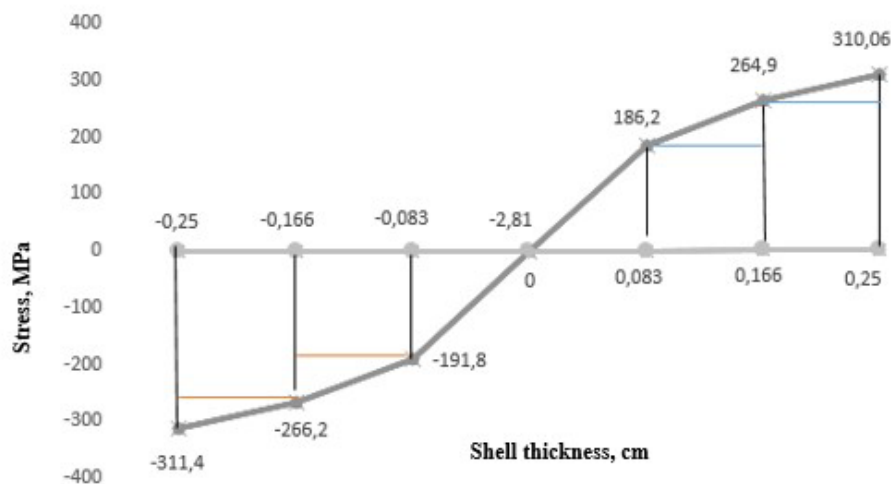
Fig. 2. Graph of stresses σ_{22} in the support section for the first calculation variant
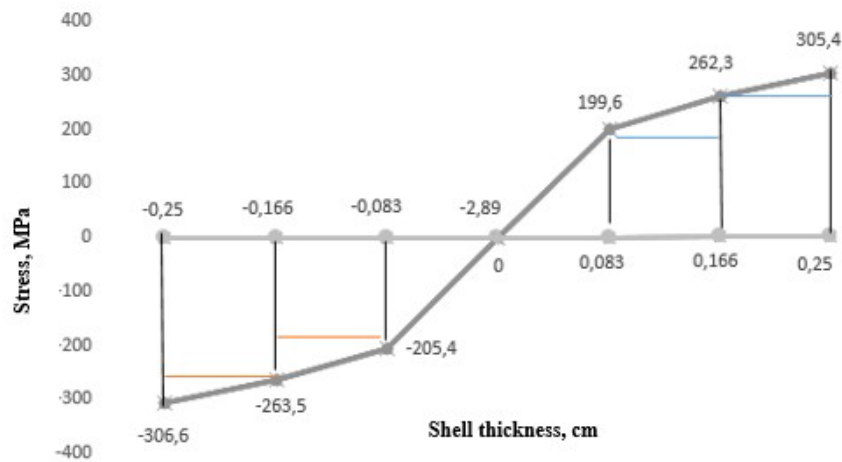
Fig.3. Graph of stresses σ_{22} in the support section for the second calculation variant
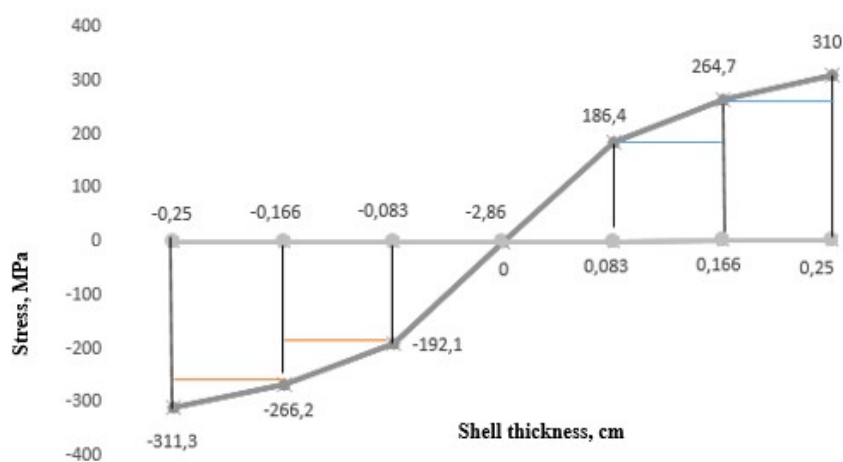
Fig. 4. Graph of stresses σ_{22} in the support section for the third calculation variant

4. Discussion

Verification of the computational process was carried out according to two main criteria. The numerical values of the hoop stress σ_{22} obtained for the considered point of the structure were compared with each other depending on the number of loading steps. With satisfactory convergence of the computational process, the pattern of the stress-strain state should not change significantly with an increase in the number of loading steps.

As can be seen from Tables 1-3, the convergence of the computational process in all the presented calculation options is satisfactory. The values of meridional stresses on the left edge of the shell with the number of steps $N=10$ and $N=30$ differ on average within 3%. With an increase in the number of steps to $N=70$, this difference decreases to 1%. The convergence condition is satisfied.

The second criterion for verifying the computational process is the ability to find the analytical value of the bending moment at the points of the support section and further compare them with the calculated variant indicators.

To determine the bending moment in the support section, the design scheme shown in Fig. 5 is used.
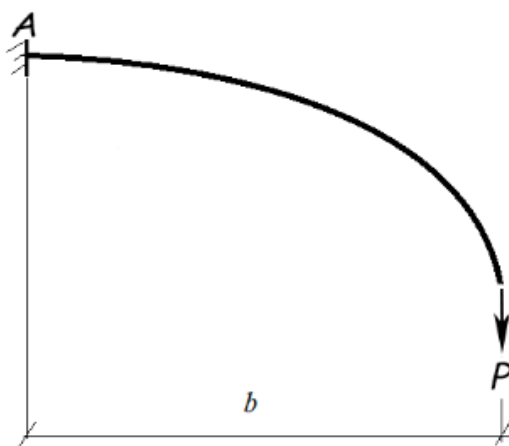
Fig. 5. Design scheme for determining the moment at point A

The numerical value of the bending moment at point A is

$$M_A = P \cdot b = 160 \cdot 10 = 1600 \, H \cdot cm. \tag{40}$$

For each considered variant, the exact values of the bending moments on the left support edge of the shell were found. For this purpose, the corresponding diagram of meridional stresses was divided into simple geometric figures and their areas were calculated. The calculated forces were multiplied by the corresponding shoulders, equal to the distance from the center of gravity of the elementary geometric figure to the middle surface. The sum of all calculated products is equal to the total bending moment.

Taking into account the hypothesis of material incompressibility as a result of plastic deformations (variant 1), the total bending moment at point A was $M_1 = 1582.7$ N·cm, for the second variant $M_2 = 1576.2$ N·cm, and in the third calculation variant, this value was equal to $M_3 = 1583.4$ N·cm. The errors in calculating the moments compared with the result (40) turned out to be equal to $\delta_1 = 1.08\%$, $\delta_2 = 1.48\%$, and $\delta_3 = 1.03\%$ for each of the variants, respectively.

5. Conclusions

The analysis of the presented material allows us to draw the following conclusions. The developed algorithm for taking into account physical nonlinearity makes it possible to obtain reliable finite element solutions in the calculations of arbitrary shell structures, the middle surface of which can be described by equation (1).

In the example of a test problem, numerical values of circumferential stresses satisfactory for computational engineering practice were obtained for various variants of defining equations. The calculation errors do not exceed 2%.

The use of the classical assumption that there is no change in volume as a result of plastic deformations is, according to the authors, not sufficiently correct. The relationship between the average linear strain and the average linear stress at the loading step, as shown by the calculation result, is best calculated using (25). This more fully corresponds to the physical meaning of the deformation process.

Based on the results obtained in the third variant of the calculation, we can conclude that the defining relations without separation into the elastic and plastic parts of the deformations at the loading step, found using the hypothesis of the proportionality of the components of the deviators of the increments of deformations and the components of the deviators of the increments of stresses, are more consistent with the physical meaning of the deformation process. In addition, the implementation of this hypothesis makes it possible to significantly simplify the procedure for forming the plasticity matrix at the loading step, since it eliminates the need to differentiate strains with respect to stresses.

References

[1] Krivoshapko SN. On opportunity of shell structures in modern architecture and building. *Structural Mechanics of Engineering Constructions and Buildings*. 2013;1: 51-56.

[2] Reissner E. Linear and Nonlinear Theory of Shells. Thin-shell structures: theory, experiment and Design. In: *Prentice*. Hall inc.; 1974. p.29-44

[3] Levin VA, Vershinin AV. *Numerical methods*. Moscow: Fizmatlit; 2015. (In Russian)

[4] Levin VA. *Models and methods*. Moscow: Fizmatlit; 2015. (In Russian)

[5] Kayumov RA. Postbuckling behavior of compressed rods in an elastic medium. *Mechanics of Solids*. 2017;52(5): 575-580.

[6] Aldakheei F, Wriggers P, Miehe C. A modified Gurson-type plasticity model at finite strains: formulation, numerical analysis and phase-field coupling. *Computational Mechanics*. 2018;62: 815-833.

[7] Aldakheev F, Miehe C. Coupled thermomechanical response of gradient plasticity. *International Journal of Plasticity*. 2017;91: 1-24.

[8] Aldakheel F. Micromorphic approach for gradient-extended thermo-elastic-plastic solids in the algorithmic strain space. *Continuum Mechanics Thermodynamics*. 2017;29(6): 1207-1217.

[9] Sultanov LU. Analysis of finite elasto-plastic strains. Medium kinematics and constitutive equations. *Lobachevskii Journal of Mathematics*. 2016;37(6); 787-793.

[10] Wriggers P, Hudobivnik B. A low order virtual element formulation for finite elastoplastic deformations. *Computer Methods in Applied Mechanics and Engineering*. 2017;2: 123-134.

[11] Artioli E, Beirao da Veiga L, Lovadina C, Sacco E. Arbitrary order 2D virtual elements for polygonal meshes: Part II, inelastic problem. *Computational Mechanics*. 2017;60: 643-657.

[12] Beirao Da Veiga L, Lovadina C, Mora D. A virtual element method for elastic and inelastic problems on polytope meshes. *Computer Methods in Applied Mechanics and Engineering*. 2017;295: 327-346.

[13] Hudobivnik B, Aldakheel F, Wriggers P. A Low order 3D Virtual element formulation for finite elasto-plastic deformations. *Computational Mechanics*. 2019;63: 253-269.

[14] Pi YL, Bradford MA, Tin-Loi F. Non-linear in-plane buckling of rotationally restrained shallow arches under a central concentrated load. *International Journal of Nonlinear Mechanics*. 2008;43: 1-17.

[15] Tupyshkin ND, Zapara MA. Opredelyayushchiye sootnosheniya tenzornoy teorii plasticheskoy povrezhdayemosti metallov. In: *Problemy prochnosti, plastichnosti i ustoychivosti v mekhanike deformiruyemogo tverdogo tela*. Tver: Izd-voTvGTU; 2011. p.216-219. (In Russian)

[16] Lalin V, Rybakov V, Sergey A. The finite elements for design of frame of thin-walled beams. *Applied Mechanics and materials*. 2014;578-579: 858-863.

[17] Yefanov KV. Raschet neftyanykh apparatov metodom konechnykh elementov. *Litres*: Samizdat.; 2020. (In Russian)

[18] Badriev IB, Paimushin VN. Refined models of contact interaction of a thin plate with postioned on both sides deformable foundations. *Lobachevskii Journal of Mathematics*. 2017;38(5): 779-793.

[19] Krysl P. Mean-strain 8-node hexahedron with optimized energy-sampling stabilization. *Finite elements in Analysis and Design*. 2016;108: 41-53.

[20] Liang K, Ruess M, Abdalla M. Co-rotational finite element formulation used in the Koiter-Newton method for nonlinear buckling analyses. *Finite elements in Analysis and Design*. 2016;116: 38-54.

[21] Magisano D, Leonetti L, Garcea G. Advantages of mixed format in geometrically nonlinear of beams and shells using solid finite elements. *International Journal for Numerikal Methods Engineering*. 2017;109(9): 1237-1262.

[22] Aldakheel F, Hudobivnik B, Wriggers P. Virtual element formulation for phase-field modeling of ductile fracture. *International Journal for Multiscale Computational Engineering*. 2019;17(2): 181-200.

[23] Magisano D, Leonetti L, Garcea G. Koiter asymptotic analysis of multilayered composite structures using mixed solid-shell finite elements. *Composite Structures*. 2016;154: 296-308.

[24] Chi H, Talischi C, Lopez-Pamies O, Paulino GH. Polygonal finite elements for finite elasticity. *International Journal for Numerical Methods in Engineering*. 2015;101: 305-328.

[25] Tyukalov YY. Equilibrium finite elements for plane problems of the elasticity theory. *Magazine of Civil Engineering*. 2019;91(7): 80-97.

[26] Gureyeva NA, Klochkov YV, Nikolayev AP, Klochkov MY. Nepreryvnaya parametrizatsiya sredinnoy poverkhnosti ellipsoidalnoy obolochki i yeye geometricheskiye parametry. *Matematicheskaya fizika i kompyuternoye modelirovaniye*. 2020;23(1): 5-12.

[27] Sedov LI. *Continuum Mechanics*. Moscow: Science; 1976. (In Russian)

[28] Dzhabrailov AS, Klochkov YV, Nikolayev AP, Fomin SD. Opredeleniye napryazheniy v obolochkakh vrashcheniya pri nalichii zon sochleneniya na osnove treugolnogo konechnogo elementa s uchetom uprugoplasticheskogo deformirovaniya. *Izvestiya vysshikh uchebnykh zavedeniy. Aviatsionnaya tekhnika*. 2015;1: 8-13. (In Russian)

[29] A.A. Ilyushin. *Plastichnost. Uprugo-plasticheskiye deformatsii*. S-Peterburg*:* Lenand; 2018. (In Russian)

[30] Malinin MM. *Applied Theory of Plasticity and Creep*. Moscow: Engineering; 1975.

THE AUTHORS

Dzhabrailov A.Sh.
e-mail: arsen82@yandex.ru
ORCID: 0000-0001-6494-1377

Nikolaev A.P.
e-mail: anpetr40@yandex.ru
ORCID: 0000-0002-7098-5998

Klochkov Yu.V.
e-mail: klotchkov@bk.ru
ORCID: 0000-0002-1027-1811

Gureyeva N.A.
e-mail: natalya-gureeva@yandex.ru
ORCID: 0000-0003-3496-2008

Kinetics of the microstructure of targets from FCC alloys under high-strain-rate deformation

S.A. Atroshenko[1,2✉], M.S. Smakovsky[3], G.G. Savenkov[4]

[1]Institute for Problems of Mechanical Engineering RAS, 61, Bolshoi Pr. V.O., St. Petersburg, Russia, 199178

[2]St. Petersburg State University, Universitetskaya embankment, 7/9, St. Petersburg, Russia, 199034

[3]JSC "Armalit", st. Trefoleva, 2, St. Petersburg, Russia

[4]St. Petersburg Institute of Technology (Technical University), 26, Moskovskiy prospect, St. Petersburg, Russia, 190013

✉ satroshe@mail.ru

Abstract. The protection of various objects experiencing shock loads from the impact of irregularly shaped impactors with impact velocities over 1.5-2.0 km/s is of considerable interest and is relevant. Computer modeling of the processes of high-speed interaction of impactors with various objects in order to create optimal designs requires deep knowledge of the physical and mechanical properties and processes occurring in the thickness of at least the material of the barrier (object). However, the existing technical measuring instruments make it possible to register only the kinematic parameters of the deformation and destruction of the barrier and impactor, while the development of internal processes remains inaccessible for visualization. In addition, the physical processes of high-speed deformation and destruction occurring in obstacles are highly dependent on the many contact boundaries that are inherent in irregularly shaped strikers, and in computer modeling and experimental studies, strikers, as a rule, have the correct geometric shape (cylinder, sphere). As a result, there is a significant loss of calculation accuracy. The article is devoted to the analysis of the behavior of various FCC metals – aluminum alloys, stainless steel, and aluminum bronze under impact loading by irregularly shaped projectiles with velocities of 1.5-2.0 km/s. Transformations of the deformed state of materials are revealed and it is shown that they depend little on the initial structure.
Keywords: Aluminum alloy, stainless steel, aluminum bronze, shock loading

Citation: Atroshenko SA, Smakovsky MS, Savenkov GG. Kinetics of the microstructure of targets from FCC alloys under high-strain-rate deformation. *Materials Physics and Mechanics*. 2022;50(2): 331-341. DOI: 10.18149/MPM.5022022_12.

1. Introduction
Protection of various modern technical objects experiencing high-energy loads from the impact of irregularly shaped strikers (for example, ammunition fragments, micrometeorites, etc.) with impact velocities over 1.5-2.0 km/s is of significant scientific and practical interest. In this case, the strain rates in the material reach $\sim 10^5$ s^{-1} and more. Computer simulation of

the processes of high-speed interaction of strikers with various objects in order to create optimal structures requires deep knowledge of the physical and mechanical properties and processes occurring in the thickness, at least of the material of the target (object). However, the existing technical measuring instruments make it possible to register only the kinematic parameters of deformation and destruction of the obstacle and the striker, while the development of internal processes remains inaccessible for visualization. In addition, the physical processes of high-speed deformation and fracture occurring in obstacles are highly dependent on the set of contact boundaries that are inherent in irregularly shaped strikers, and in computer modeling and experimental studies, strikers, as a rule, have the correct geometric shape (cylinder, sphere). As a result, there is a significant loss in the accuracy of calculations.

Therefore, the study of the evolution of the microstructure of the target material under the conditions of a high-speed impact with an irregularly shaped striker comes to the fore, despite the fact that such studies are of a post-factor nature and the state of the microstructure at the moment of dynamic action may differ from that after dynamic loading. But it can be noted that it is the processes of restructuring the internal structure of the material during its dynamic deformation and destruction that determine the physical and mechanical properties of the medium.

Dynamic processes have a multiscale character, as shown in [1], the scale levels of destruction in the spall zone of steel during longitudinal shear and normal separation differ by 1-1.5 orders. The authors of the work [2] show the presence of 4 scale levels in the D-16 aluminum alloy under shock loading. The destruction as a result of dynamic loading of the samples is explained by the dispersion of particle velocities (elementary strain carriers) at different scale-structural levels of deformation and destruction. High-speed fracture most often occurs at an intermediate between the macroscopic and microscopic structural level (mesoscopic), corresponding to the scale of the internal structure of the material [3], and this fact also complicates the interpretation of the results obtained. Dynamic processes occurring at the mesoscale level, as a rule, are nonequilibrium, unstable and chaotic [4-6].

An equally important task is to study changes in the evolution of the microstructure in a lower range of strain rates $\dot{\varepsilon} = 10^2\text{-}10^3 \text{ s}^{-1}$. In particular, this concerns multiphase alloys with an FCC lattice.

2. Samples, materials, and experimental technique

In this work, we studied the microstructure of samples cut from targets made of an aluminum alloy of the AMg6 type (but additionally doped with scandium), BrAlFeNiMn_9-4-4-1 tin-free aluminum bronze, and 18Cr-10Ni-Ti stainless steel (sufficiently detailed information about these materials is given in [7], pierced by irregularly shaped compact impactors (otherwise called impact "cores" [8,9]). The initial velocity of the impact of the striker with the obstacle was ~ 1.8-2.0 km/s. In addition, samples from BrAlFeNiMn_9-4-4-1 were studied after testing by the Kolsky method on a split Hopkinson bar (SHB) [10] with different strain rates. The SHB technique allows one to determine various properties of materials precisely in the specified range of strain rates, which is included in a wider range of strain rates of $10^3\text{-}10^5 \text{ s}^{-1}$ [11]. The maximum speeds of this range are realized using the direct impact method, the Taylor method, and the thin ring expansion method loaded with an electromagnetic pulse, or other short microsecond pulses [12,13,14]. Samples for metallographic studies were cut from targets with a diameter of 90 mm and a thickness of 11 mm. A view of an aluminum alloy target after penetration is shown in Fig. 1a. Samples prepared for metallographic studies are shown in Fig. 1b, 1c.
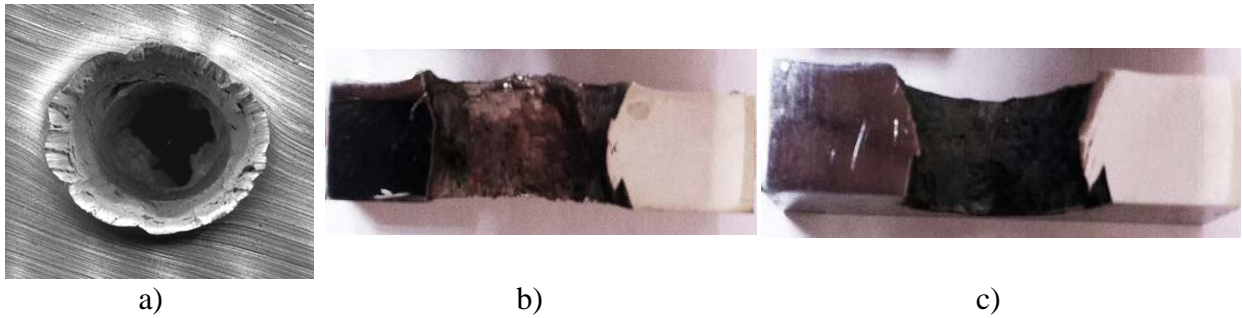
a)   b)   c)

Fig. 1. General view of an aluminum target after penetration (a) and samples for metallographic studies (b, c): b – stainless steel, c – aluminum bronze

A rod (similar to 90 mm in diameter) annealed at 800ºC for three hours, 18 mm in diameter and 450 mm in length was chosen as the initial semi-finished product of BrAlFeNiMn_9-4-4-1 tin-free aluminum bronze for research at the SHB.

The statical mechanical characteristics of the investigated alloys were as follows:

$\sigma_{0,2} = 325$ MPa, $\sigma_B = 430$ MPa, $\delta_5 = 25\%$, $\psi = 30\%$ – for aluminum alloy;

$\sigma_{0,2} = 275$ MPa, $\sigma_B = 620$ MPa, $\delta_5 = 59\%$, $\psi = 70\%$ – for stainless steel;

$\sigma_{0,2} = 385$ MPa, $\sigma_B = 725$ MPa, $\delta_5 = 35\%$, $\psi = 36\%$ – for aluminum tin-free bronze.

Tests on the SHB were carried out at three strain rates $\dot{\varepsilon}$: $\dot{\varepsilon} = 915$ s^{-1}, $\dot{\varepsilon} = 1475$ s^{-1}, $\dot{\varepsilon} = 1750$ s^{-1}. The mechanical properties of the samples obtained at these speeds are presented in Table 1.

Table 1. Dynamic properties of bronze BrAlFeNiMn_9-4-4-1

Strain rate, $\dot{\varepsilon}$, s^{-1}	Yield strength, σ_{Sd}, MPa	Tensile strength σ_{bd}, MPa	Relative elongation δ_d, %	Relative narrowing ψ_d, %
915	480 ± 5	665 ± 15	30 ± 1,0	39 ± 2,5
1475	505 ± 15	710 ± 20	29,5 ± 0,5	39 ± 1,0
1750	610 ± 10	695 ± 55	31 ± 1,0	40 ± 3,0

The structure was studied using an Axio-Observer Z1 M optical microscope in a bright field and in C-DIC contrast. The initial structures of the studied alloys are shown in Fig. 2.

a)   b)   c)
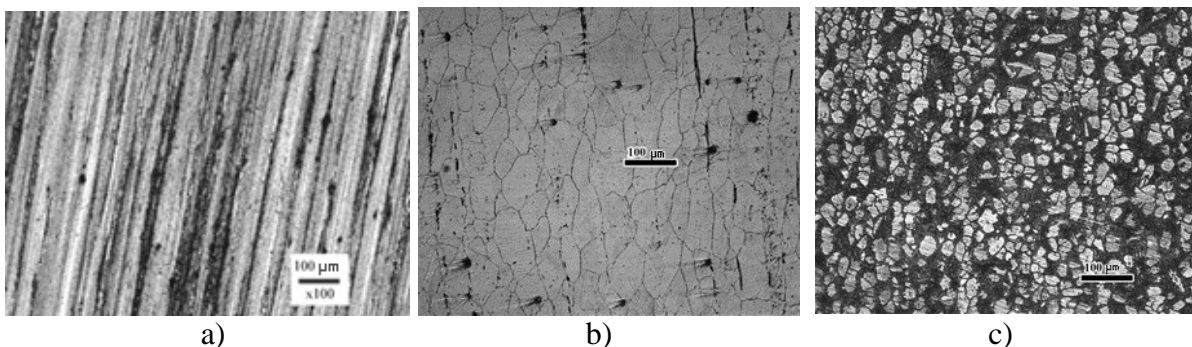
Fig. 2. Initial structures of the investigated alloys: a – aluminum alloy; b – steel; c – bronze

3. Results of microstructural studies of samples after high-velocity impact and their analysis

General remarks and results. In our case, all targets are classified as obstacles of finite thickness. In this case, the mutual influence of the cavity formation zone and the rear free surface becomes a significant factor [15,16]. The compression wave caused by the impact is reflected from the free surface in the form of a tensile wave, which has time to return to the cavity even before the plastic flow of the material stops. If the duration and amplitude of tensile stresses exceed the critical values, then the destruction of the barrier material near the rear surface occurs – it is spalling. If a spall does not form, the unloading changes the stress-strain state in the cavity formation zone (compression along one axis is transformed into a volumetric oppositely deformed state), which contributes to the facilitated penetration of the obstacle by the striker. In our studies, for all three samples on the rear surface, zones of destruction were revealed, which are obviously associated with spalling phenomena (Fig. 1).

In all targets, irrespective of the alloy grade, nodal points between the so-called terrace ledges were found in the macro-relief of the surfaces of the holes formed [17].

Also, in the punched targets, 3 (stainless steel and aluminum bronze) or 4 (aluminum alloy) penetration zones are distinguished (Fig. 1). The first zone, due to the non-stationary stage of penetration [18], corresponds to the depth of ~ 0.3 - 0.5 of the penetration thickness and, the second (and the third for the barrier made of aluminum alloy) ~ 1/3 of the thickness (stationary stage of penetration), the third (the fourth, for the aluminum alloy) (associated with spalling phenomena) ~ 1/6 - 1/3 of the thickness.

Evolution of microstructure in aluminum alloy. The original stripe structure (Fig. 2a) at the very top of the ridge changes to a fragmented one (Figs. 3a - 3b), which indicates large plastic deformations and high temperatures in this layer. As the projectile velocity decreases, the strip structure remains unchanged (Fig. 3c), however, periodic protrusions are formed along the edge of the cavity (Fig. 3d).
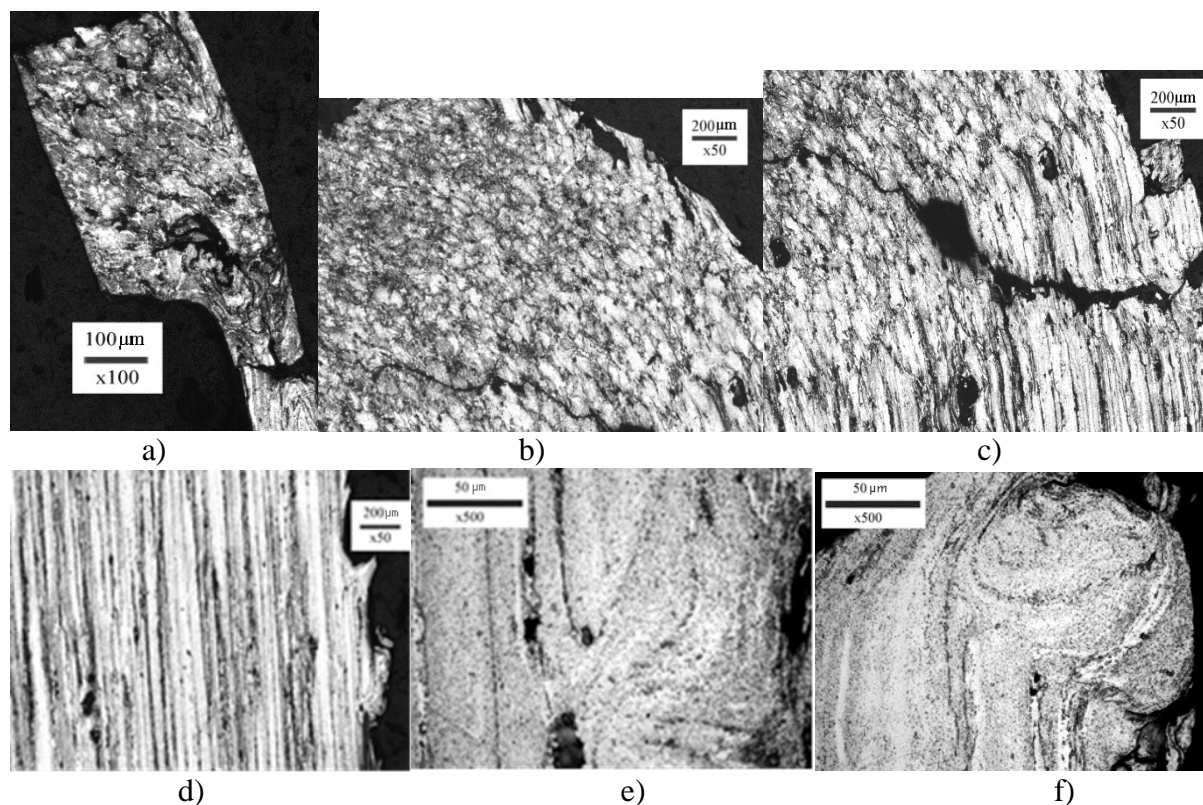
Fig. 3. Consecutive change of the profile of the relief as the target is penetrated

The formation of such protrusions may be due to the fact that as the striker moves, the temperature of the material in front of it increases; in combination with high pressures, this can lead to the appearance of local areas of melting and, accordingly, to a decrease in the friction force. This leads to stress release and a change in the friction mechanism from dry to plastic. The transition to a section with a lower temperature creates some stoppers for the movement of the striker, which again leads to a change in the friction mechanism from plastic to dry. Such a sequence of changes in mechanisms and the appearance of stoppers can lead to the appearance of periodic protrusions.

And, finally, when the speed of the striker becomes much less than the initial one, rotational (vortex) modes of plastic deformation begin to appear intensively (Fig. 3e, d). One of the probable causes of the vorticity of the target material may be that as the projectile velocity decreases, the material in front of it may already be in a friable state due to the appearance of tensile stresses arising from the interaction of the forward and backward unloading waves. Friability of the material increases the number of degrees of freedom, which can lead to the formation of structures that experience pure rotation due to shear stresses.

Microstructure evolution in stainless steel. As noted above, there are three zones of penetration in the stainless steel barrier (Fig. 1b), corresponding to three stages of penetration.

In the first zone, at a distance of 1.5-3.8 mm from the frontal surface and 0.15-0.75 mm from the edge of the cavity, an area of rotational plastic deformation was found, consisting of disks with a practically ideal circular shape. The radius of the discs ranges from 35 to 325 μm (Fig. 4). Inside the large circles are smaller circular elements and friable elements (pores). The microhardness inside the circular formations is higher than the initial hardness of the material outside these regions (HV = 2.62 GPa) by ~ 25% and on average is HV ≈ 3.14 GPa. Near the circular formations, closer to the edge of the cavity, adiabatic shear bands (ASB) were found, which are apparently associated with a high local temperature near the contact surface between the impactor and the target [19] and with the instability of plastic flow resulting from the effect of thermal softening at adiabatic or almost adiabatic plastic deformation. It can be assumed that at the first stage of penetration when the velocity parameters of the striker are still sufficiently high, the target material does not have time to dissipate the mechanical energy of the striker due to the collective motion and multiplication of dislocations. Therefore, to maintain the dissipation rate at the required level, additional rotational modes of plastic deformation are switched on [20].

a)   b)
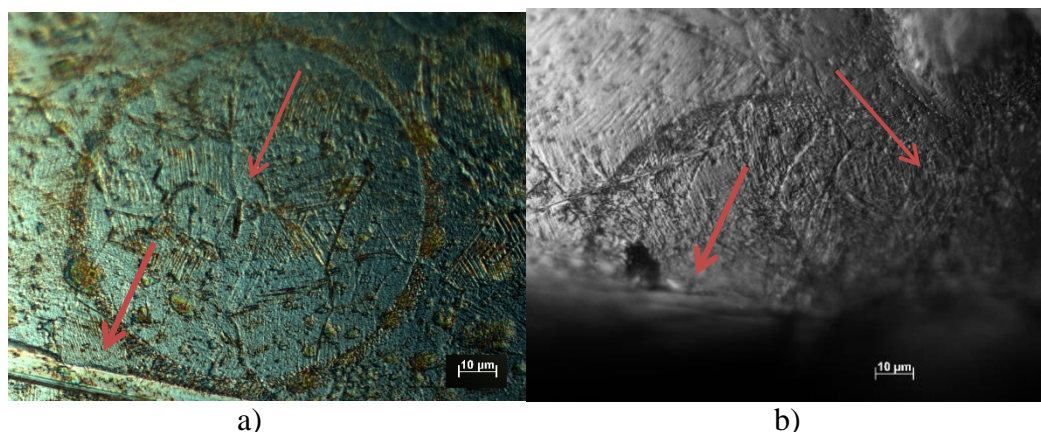
Fig. 4. Region of rotational plasticity ×1000 (a, b) (thin arrows indicate small circular formations, thick arrows indicate adiabatic shear bands)

The second stage of penetration is characterized by the formation of a wavy relief of the cavern edges on the contact surface between the striker and the target material. Signs of rotational (wave-like) plastic deformation inside the grain structure (Fig. 5b) were found in

the same way as for the first zone. In addition, this zone is characterized by recrystallization processes, which manifest themselves in the form of crumbling of ferrite colonies (Fig. 5c) or coarsening of grains (Fig. 5d).
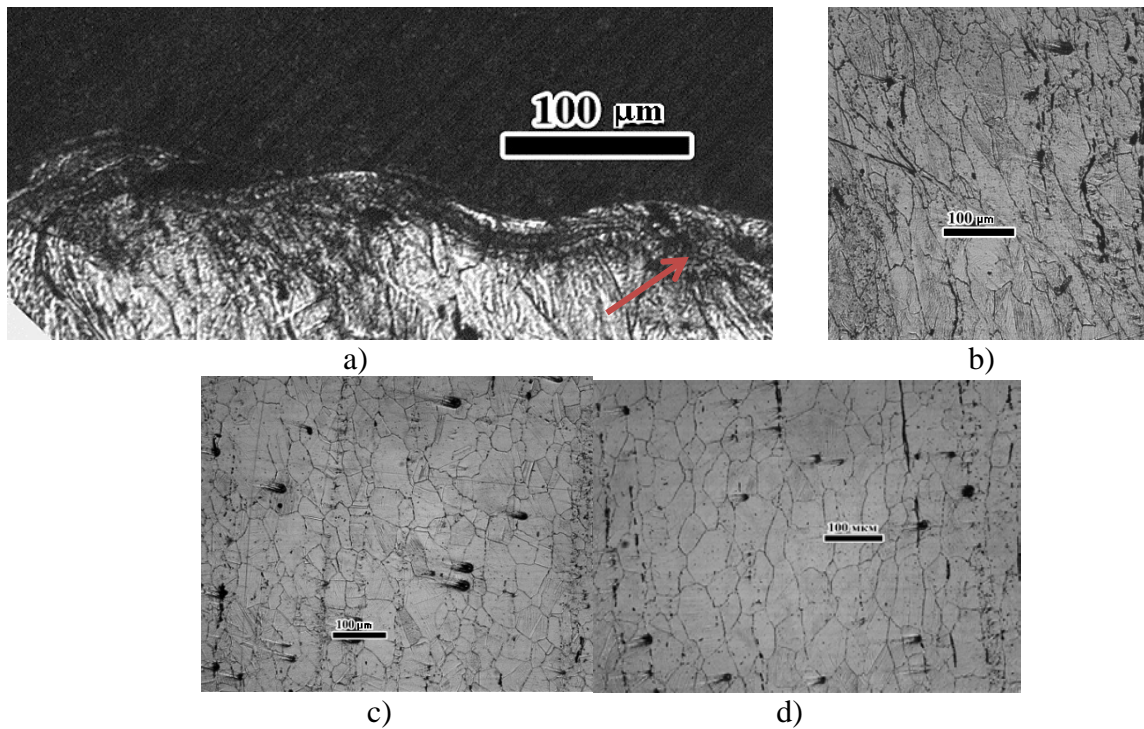

a)

b)

c)

d)

Fig. 5. Steel microstructure in the second target zone: ASB (indicated by an arrow) and wavy traces of plastic deformation – (a, b), crushing of δ-ferrite colonies – (c) and traces of grain coarsening – (d)

Fig. 6. Spall and shear cracks in steel ($\times 100$)

In the third target zone, associated with the interference of loading and unloading waves, two types of cracks were observed: parallel to the rear surface and shear cracks perpendicular to them (Fig. 6). The first type of cracks is caused by tensile stresses during the interference of unloading waves, and the second ones may be due to their appearance by shear stresses in a direct load wave when they reach a critical value.

Evolution of microstructure in aluminum bronze. In the first zone of the aluminum tin-free bronze target, adiabatic shear bands (ASB) were revealed as characteristic features (Fig. 7a).

In the second zone, along with ASB, there are also zones of dynamic recrystallization (Figs. 7b, 7c).

a)   b)   c)
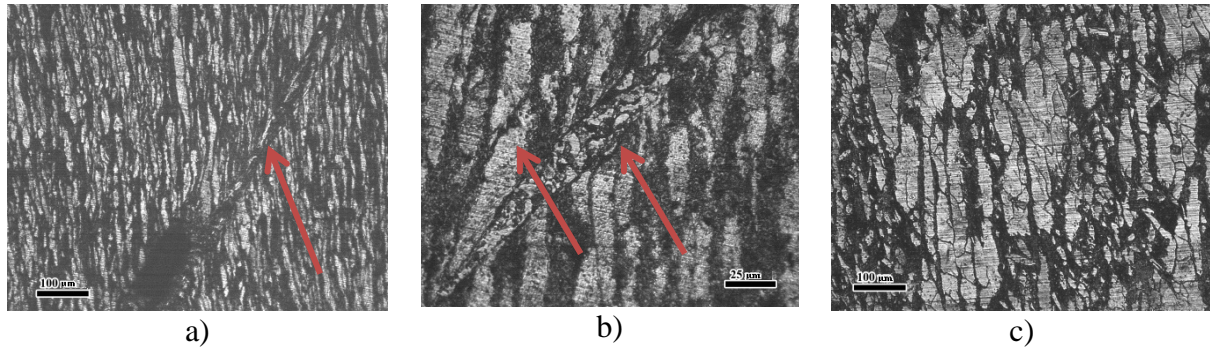
Fig. 7. Adiabatic shear bands – (a, b) (indicated by arrows),
dynamic recrystallization zones – (b), and recrystallized grains – (c)
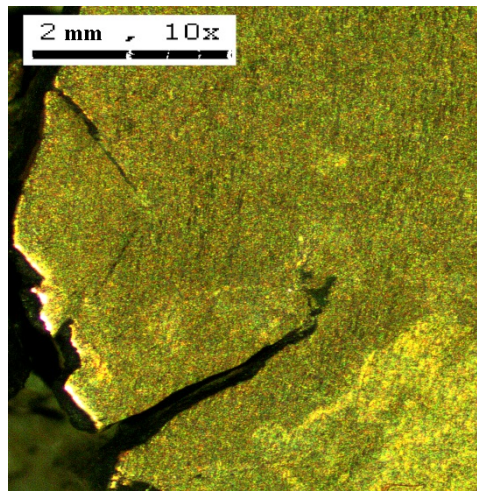
Fig. 8. Cracks in the third zone of the aluminum bronze target

In the third zone, on the sides of the cavity, there are cracks up to 3 mm long, oriented relative to the direction of the striker's action on different sides at an angle of 45° (Fig. 8).

It can be assumed that in this zone, under the conditions of the dynamic impact of the striker, compression along one axis was realized in the target, which was transformed into a volumetric oppositely deformed state, which led to the formation of the indicated oblique cracks.

Thus, based on the totality of the studies of the evolution of the microstructure of obstacle materials after a high-speed impact by a compact impactor of irregular shape, we can draw the following conclusion:

After shock loading with the penetration of targets made of different metals with an FCC lattice, signs of the transformation of the deformed state due to the dissipation of mechanical energy were revealed in the following sequence: slip of dislocations, rotational formations, and localized adiabatic shears, bands of a fragmented state and dynamic recrystallization, local dynamic polygonization and recrystallization. Structural changes are weakly dependent on the initial structure of the metal and are realized with the participation of interference (wave) effects of shock wave scattering.

4. The results of microstructural studies of specimens made of bronze of the brand BrAlFeNiMn_9-4-4-1 after tests on the Split Hopkinson Bar

Figure 9 shows the structure of the sample after loading with a strain rate of $\dot{\varepsilon}$ =915 s^{-1} when moving inward: from the fracture surface to its tail (a $\rightarrow$ d).

    a   b   c   d
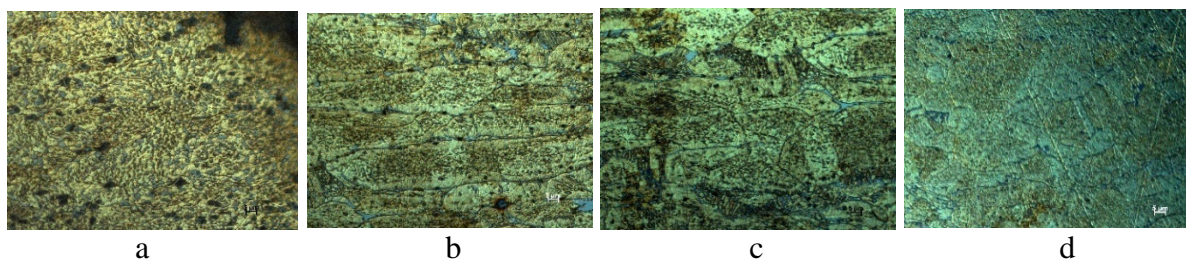
Fig. 9. The structure of bronze brand BrAlFeNiMn_9-4-4-1 after loading SHB-1 when moving from the fracture surface deep into the sample ($\times$1000_C_DIC)

At the fracture surface (Fig. 9a), the structure is practically grain-free - it consists of an α substitutional solution of aluminum in copper and a eutectoid $\alpha + \gamma'$ without clearly defined grain boundaries (quasi-amorphous structure). That is, it can be assumed that in this case, a certain structural phase transition occurred, which is typical for large plastic deformations [21]. When moving deeper, grains elongated along the initial rolling appear (Fig. 9b), consisting of the same two phases, the eutectoid is more often located at the grain junctions. Further, more equiaxed grains appear (Fig. 9c) with a large amount of eutectoid at their boundaries. In addition, many small cracks and pores are observed in the sample, especially near the fracture surface (Fig. 9a). In some places (Fig. 9d), twins are found, which is more typical for metals with FCC and HCP lattices, while in metals with BCC lattice they appear only at high strain rates and high pressures [22].

The characteristic structures of the sample after the rupture with a strain rate of $\dot{\varepsilon}$ = 1475 s^{-1} are shown in Fig. 10. At the discontinuity surface, the structure is similar to the structure shown in Fig. 9a. Figure 10a (slightly farther from the fracture surface) shows the region of dynamic recrystallization, and in Fig. 10b, areas of the amorphized structure are observed (residual formations from amorphization of the structure near the fracture surface). Pores and cracks are observed in the same figures. Figure 10c shows both equiaxed and elongated grains with a large amount of eutectoid.

         a   b   c
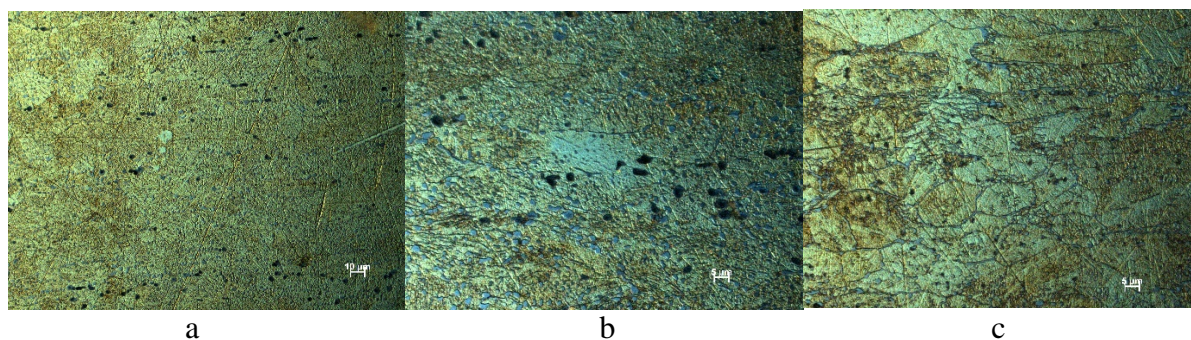
Fig. 10. Sample structure after loading with strain rate $\dot{\varepsilon}$ =1475 s^{-1}: a) $\times$500; b, c) $\times$1000 (C_DIC)

The microstructure of the sample after loading with a strain rate $\dot{\varepsilon}$ = 1750 s^{-1} in the zone slightly removed from the fracture surface (Fig. 11) differs from the microstructures of the previous samples. There are no differences near the fracture surface. Micropores and microcracks are also observed.

| a | b | c | d |
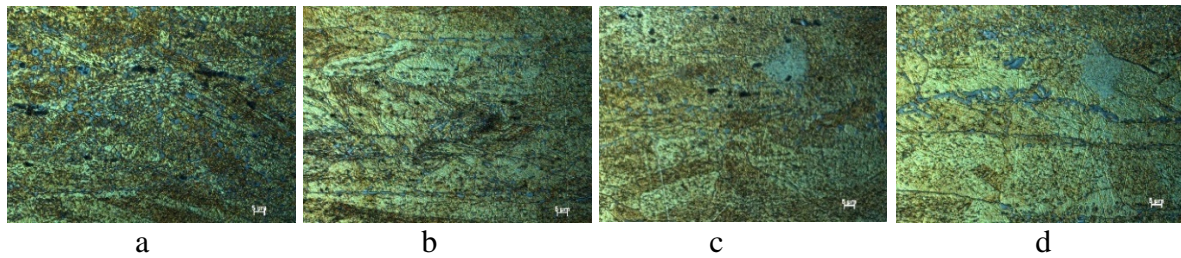
Fig. 11. Sample structure after loading at strain rate $\dot{\varepsilon}$ =1750 s^{-1} ($\times$1000 C_DIC)

But in Figure 11b, vortex-like structures are observed, which indicates that at higher strain rates, additional rotational modes of plastic deformation are switched on to maintain the mechanical energy dissipation rate at the required level, just as in the case of a high-speed impact with a compact impactor (see above). Figures 11c and 11d show areas of amorphization, individual twins, and localization zones.

As a result of the studies of the evolution of the structure of specimens made of bronze of the brand BrAlFeNiMn_9-4-4-1, tested at relatively low strain rates [10], it *can be stated* that it undergoes the entire spectrum of changes that is characteristic of higher values of strain rates and pressures. In addition, it was found that in the region of sample rupture, its microstructure acquires an amorphous (quasi-amorphous) form. This fact indicates that, during deformation and rupture, a structural phase transition occurred in the neck of the sample, associated with the formation of unstable excited regions. The structural-phase transition is also observed at very high strain rates [23]. In an excited state and, accordingly, during a structural-phase transition, which occurs in very short periods of time, the interaction of structures of various levels is observed, the material is in a state far from equilibrium, in which its qualitative rearrangement and an abrupt change in both the properties of the material and its aggregate state [24-26].

5. Conclusions

The study of the kinetics of the microstructure of FCC metals during high-speed penetration revealed the following mechanisms of deformation and destruction:

1. Glide of dislocations
2. Rotational deformation modes
3. Adiabatic shifts
4. Spall destruction
5. Dynamic recrystallization.

When loading at lower rates using a Hopkinson rod, the following features of the microstructure of FCC metals are locally observed, which are typical for high-speed deformation:

1. Microcracks and pores
2. Doubles
3. Dynamic recrystallization
4. Quasi-amorphous structure
5. Vortex structures

Structural changes in FCC metals under high-speed loading weakly depend on the initial structure of the metal.

References
[1] Atroshenko SA. Scale levels of dynamic translational fracture mechanisms. *Materials Physics and Mechanics*. 2016;26(1): 16-18.
[2] Mayer AE, Atroshenko SA, Borodin IN. Experimental and numerical investigations of the scale levels in spall fracture of D16 aluminum. *Materials Physics and Mechanics*. 2016;26(1): 23-25.
[3] Meshcheryakov YI, Khantuleva TA. Non-equilibrium processes in condensed media. Part 1. Experimental studies in the light of nonlocal transport theory. *Physical Mesomechanics*. 2014;17(5): 21-37.
[4] Barakhtin BK, Savenkov GG. Relationship of spall characteristics with the dimension of the fracture fractal structure. *Applied Mechanics and Technical Physics*. 2009;50(6): 61-69.
[5] Kuznetsov AV, Savenkov GG, Bragov AM, Konstantinov AY. Influence of the emerging fractal fracture surface on the dynamic properties of titanium. *Problems of Strength and Plasticity*. 2016;78(2): 218-227.
[6] Savenkov GG, Stolyarov VV, Kuznetsov AV, Meshcheryakov YI. The Nature of Fractal Relief of Fractured Metal Samples after Dynamic Loading. *Journal of Machinery Manufacture and Reliability*. 2020;49(5): 439-445.
[7] Savenkov GG, Kuznetsov AV. Dynamic Properties of Viscous Metals with a Surface Layer Modified by a Pulsed Electron Beam. In: Perspective Materials and Technologies. Vitebsk: EE "VGTU"; 2017. p.73 - 89.
[8] Orlenko LP. (Ed.) *Physics of the explosion*. Moscow: FIZMATLIT; 2002. (In Russian)
[9] Kolpakov VI, Savenkov GG, Rudomyotkin KA, Grigoriev AY. Mathematical modeling of the formation of compact projectiles from low-spherical linings. *Technical Physics*. 2016;86(8): 21-25.
[10] Bragov AM, Lomunov AK. *Using the Kolsky method to study the processes of high-speed deformation of materials of various physical nature: monograph.* Nizhny Novgorod: Publishing house of UNN; 2017. (In Russian)
[11] Morozov VA. *Dynamics of high-speed loading of materials.* St. Petersburg: Publishing House of St. Petersburg University; 2003. (In Russian)
[12] Basalin AV, Konstantinov AY, Krushka L. Development of the direct impact method for determining deformation diagrams of elastoplastic materials under large deformations. *Problems of Strength and Plasticity.* 2020;82(2): 135-146.
[13] Bragov AM, Igumnov LA, Konstantinov AY, Lomunov AK. *High-speed deformation of materials of various physical nature: monograph.* N. Novgorod; 2020.
[14] Zukas JA, Nicholas T. *Impact dynamics.* Krieger Pub Co; 1992.
[15] Merzhievsky LA, Titov VM. High-speed impact. *Physics of combustion and explosion.* 1987;23(5): 92-108.
[16] Fomin VM. (Ed.) *High-speed interaction of bodies.* Novosibirsk: Publishing house of SB RAS; 1999.
[17] Gladyshev SA, Grigoryan VA. *Armor steel.* Moscow: Intermet Engineering; 2010.
[18] Barakhtin BK, Prus AA, Savenkov GG. Microstructural features of deformation of obstacles during high-speed penetration of plane jets. *Applied Mechanics and Technical Physics*. 1989;5: 155-158.
[19] Moss JL. Influence of shock waves on the magnitude, rate and temperature of deformation in adiabatic shear bands. In: *Shock waves and phenomena of high-velocity deformation of metals*. Moscow: Metallurgy; 1984. p.30-40. (In Russian)
[20] Rybin VV. *Large plastic deformation and destruction of metals*. Moscow: Metallurgy; 1986.

[21] Pavlov VA. Amorphization of the structure of metals and alloys with an extremely high degree of plastic deformation. *Fizika Metallov i Metallovedenie*. 1985;59(4): 629-649. (In Russian)

[22] Atroshenko SA. Mechanisms of multiscale dynamic deformation and destruction of various types of metals. *Chemical Physics*. 2002;21(9): 93-99.

[23] Epstein GN, Kaibyshev OA. *High-speed deformation and structure of metals*. Moscow: Metallurgy; 1971.

[24] Murr LE. Formation of defects during deformation by a shock wave. In: Meirs MA, Murra LE. (Eds.) *Shock waves and phenomena of high-speed deformation of metals*. 1984. p.121-151. (In Russian)

[25] Epstein GN. *The structure of metals deformed by an explosion*. Moscow: Metallurgy; 1988. (In Russian)

[26] Savenkov GG, Barakhtin BK, Rudometkin KA. Investigation of structures in a copper cumulative jet using multifractal analysis. *Journal of Technical Physics*. 2015;85(1): 98-103.

THE AUTHORS

Atroshenko S.A.
e-mail: satroshe@mail.ru
ORCID: 0000-0002-5733-5915

Smakovsky M.S.
e-mail: sms84@bk.ru
ORCID: 0000-0002-2904-6200

Savenkov G.G.
e-mail: sav-georgij@yandex.ru
ORCID: 0000-0001-6069-302X

Principal stress-strain states of thin-walled complexly bent pipelines

O.P. Tkachenko[✉]

Computing Center of the Far Eastern Branch of the Russian Academy of Sciences, Kim Yu Chen Str., 65,

Khabarovsk, 680000, Russia

[✉] olegt1964@gmail.com

Abstract. Mathematical model of the pipeline is formulated within the framework of the elastic shell theory, and the basic parameters of this model are determined. For moment and semi-momentless shells, equations of the first approximation with respect to the small curvature parameter are given. The model for calculation by the finite element method in CAE Abaqus is constructed and numerical experiments are performed. Numerical solution to the model problem is found, and stresses and bending moments are calculated on its basis. Stresses and bending moments are compared with their exact values. Numerical analysis is carried out by comparing pipe models within the framework of the shell theory and the rod theory. It is established that the proposed mathematical model makes it possible to find stresses in pipes with high accuracy.
Keywords: numerical experiment, thin-walled shells, mathematical model, adequacy estimates

1. Introduction

With the development of oil and gas fields on the sea shelf, engineers around the world are faced with a problem: pipelines are displaced from their design position [1]. Engineers and scientists are actively developing methods to prevent lateral and vertical displacement of subsea pipelines [2]. Various reasons for such a displacement are studied in [3,4]. Engineering methods for designing underwater pipelines, taking into account their instability, have been included in textbooks (see, for example, [5]), but this fact does not remove the problem of the unexplored phenomena.

In this regard, the question arises of choosing a mathematical model of the pipeline for further analysis of its behavior under various external loads. Rod models are applied for very long pipes [6]. For pipes of medium length, the shell model is adequate (see [7]). The applicability areas of the rod and the shell models are compared in [8]. This is done on the example of the pipeline tunneling problem. It turns out that for underground pipelines there are conditions in which the rod theory approximation is inapplicable due to the fact that the problem is fundamentally three-dimensional [9].

Previously, we have developed mathematical models both in the framework of the shell theory [10] and the rod theory [11]. An asymptotic analysis of the shell dynamics equations is performed, and an algorithm for reducing the initial-boundary value problem to a one-dimensional formulation is developed on the basis of this analysis [12]. The model of a semi-momentless shell is generalized to moment shells of medium thickness in [13]. In the articles [12,13], a numerical method for solving the resulting systems of equations is proposed and its verification is performed.

The purpose of this research is a comparative analysis of mathematical models of the pipeline, finding areas of their application, and verification of the moment shell model by stresses.

The formulation of the general mathematical model for the pipeline is given and the basic parameters of this model are determined. For moment and semi-momentless shells, equations of the first approximation with respect to the small curvature parameter are given. For the model problem of bending a pipeline segment, the acting forces and stresses are calculated. Numerical solution of the model problem is found, stresses and bending moments are calculated on its basis. Model is constructed for finite element method analysis in CAE Abaqus. Stresses and bending moments are compared with their exact values. It is established that the proposed mathematical model makes it possible to find stresses in pipes with high accuracy. Numerical analysis is performed to compare the application areas of the pipe models as the shell and the rod.

2. Formulation of the pipeline mathematical model

A bent segment of the pipeline is considered, which is under the action of fluid pressure and the centrifugal force of the flow inertia. Within the framework of this work, the stress-strain state of the pipe wall is described by the equations of an elastic shell. The curvilinear coordinate system s, θ, and R is described in [12]. It is assumed that the center line Γ is a flat curve of length L. A natural arc of length s is plotted along the axial line, and a polar coordinate system (θ, R) is constructed at each point of the arc.

The model is based on the equations of V.Z. Vlasov [14]:

$$\frac{1}{A}\left(\frac{\partial I_0}{\partial s} + \frac{h^2}{6}H\frac{\partial I_1}{\partial s} + \frac{h^2}{12}\frac{\partial I_2}{\partial s}\right) - (1-\nu)\frac{1}{B}\left(\frac{\partial X_0}{\partial \theta} + \frac{h^2}{6}k_1\frac{\partial X_1}{\partial \theta} + \frac{h^2}{12}\frac{\partial X_2}{\partial \theta}\right) +$$

$$+(1-\nu)\left(Ku - \frac{k_2}{A}\frac{\partial w}{\partial s}\right) = -\frac{1-\nu^2}{Eh}X,$$

$$\frac{1}{B}\left(\frac{\partial I_0}{\partial \theta} + \frac{h^2}{6}H\frac{\partial I_1}{\partial \theta} + \frac{h^2}{12}\frac{\partial I_2}{\partial \theta}\right) + (1-\nu)\frac{1}{A}\left(\frac{\partial X_0}{\partial s} + \frac{h^2}{6}k_2\frac{\partial X_1}{\partial s} + \frac{h^2}{12}\frac{\partial X_2}{\partial s}\right) +$$

$$+(1-\nu)\left(Kv - \frac{k_1}{B}\frac{\partial w}{\partial \theta}\right) = -\frac{1-\nu^2}{Eh}Y, \tag{1}$$

$$-2H \cdot I_0 - \frac{h^2}{6}\left(HI_2 + KI_1\right) + \frac{h^2}{12}\frac{1}{AB}\left\{\frac{\partial}{\partial s}\left[\frac{B}{A}\left(k_2\frac{\partial I_0}{\partial s} + \frac{\partial I_1}{\partial s} - (1-\nu)K\frac{\partial w}{\partial s}\right) - (1-\nu)k_1\frac{\partial X_0}{\partial \theta}\right] +$$

$$+\frac{\partial}{\partial \theta}\left[\frac{A}{B}\left(k_1\frac{\partial I_0}{\partial \theta} + \frac{\partial I_1}{\partial \theta} - (1-\nu)K\frac{\partial w}{\partial \theta}\right) + (1-\nu)k_2\frac{\partial X_0}{\partial s}\right]\right\} +$$

$$+\frac{h^2}{12}\frac{(1-\nu)}{AB}\left[\frac{\partial}{\partial s}(BKk_1u) + \frac{\partial}{\partial \theta}(AKk_2v)\right] + \frac{1-\nu}{AB}\left[2ABKw + \frac{\partial}{\partial s}(Bk_2u) + \frac{\partial}{\partial \theta}(Ak_1v)\right] = -\frac{1-\nu^2}{Eh}Z.$$

In system (1) it is denoted:

$$K = k_1 k_2, \; \mathrm{H} = \frac{1}{2}\left(k_1 + k_2\right), \; L = \frac{1}{2}\left(k_1 - k_2\right);$$

X, *Y*, and *Z* are loads acting on the pipe along the coordinates *s*, θ, and *R*, respectively; *v* is Poisson's ratio, *E* is Young's modulus, *h*, R_0 are wall thickness and radius of the middle surface of the pipe, respectively, *u*, *v*, *w* are displacements of the middle surface along the coordinate axes, k_1, k_2 – principal curvatures of the middle surface. Generalized expressions for functions I_i, X_i in terms of displacements, where $i = 0, 1, 2$, are given in [14].

Denote by $\kappa(s)$ the curvature of the pipe axial line; in the position before deformation, it is equal to $\kappa_0(s)$. Conditions for applicability of the shell theory are:

$$h^* = \frac{h}{R_0} \le \frac{1}{20}, \; \frac{\min\left(L, \frac{1}{\kappa_0}\right)}{R_0} \ge 4 \,, \tag{2}$$

The geometric parameters of equations (1) are expressed by formulas:

$$A = 1 + R_0 \kappa(s) \sin\theta, \; B = R_0,$$

$$k_1 = \kappa(s)\sin\theta \big/\left(1 + \kappa(s)R_0 \sin\theta\right), \; k_2 = 1/R_0 \,.$$

Substituting these expressions into (1), and expressing all the terms in terms of wall displacements, we obtain three equations for three unknown displacements. Introducing dimensionless coordinates and functions:

$$\zeta = s/\ell; \qquad r = R/R_0; \quad \theta = \theta;$$

$$u' = u/R_0; \qquad v' = v/R_0; \quad w' = w/R_0;$$

we bring the resulting system of resolving equations to a dimensionless form. Here ℓ is the characteristic scale. The resulting equations are published in [13]; they are not presented here due to their cumbersomeness.

The pipeline geometry is determined by the curvature parameter:

$$\lambda = R_0 \max\left|\kappa_0\right|.$$

This parameter characterizes the degree of pipe bending. The boundary value problem for a pipe with a kink, when $\lambda \to \infty$, is considered in [15]. For the numerical solution of this problem, which contains a singularity in its coefficients, new methods are being developed in [16-18]. A review of dynamic problems of crack propagation in pipeline walls, which also contain a singularity, is presented in [19].

It is assumed that the inequality performed

$$\lambda \le \frac{1}{20}, \tag{3}$$

which is related to inequalities (2). Inequality (3) allows us to use the smallness of the parameter λ.

3. First approximation equations

The system of equations (1) admits various degrees of approximation. In [12,13], two mathematical models are proposed: one based on the semi-momentum theory of shells in [12] and one based on the moment theory of shells in [13]. It is proved in [13] that there are such conditions for applying the load on the pipe that in both cases the same expansion in powers of a small parameter is applicable:

$$u'(\zeta, \theta) = u_0(\zeta) + \lambda u_1(\zeta)\sin\theta + O\left(\lambda^2\right);$$

$$v'(\zeta, \theta) = \lambda v_2(\zeta)\cos\theta + O\left(\lambda^2\right); \tag{4}$$

$$w'(\zeta, \theta) = w_0(\zeta) + \lambda w_1(\zeta)\sin\theta + O\left(\lambda^2\right).$$

Here the dimensionless variables are introduced, which are defined above. The result of substituting (4) into different models from [12] and [13] differs in the first approximation.

First order resolving equations for a bent shell of medium thickness have the following form:

$$\alpha^2 u_{1\zeta\zeta} + \alpha v w_{1\zeta} - \varepsilon^2 \alpha^3 w_{1\zeta\zeta\zeta} - \frac{1+\nu}{2}\alpha v_{2\zeta} - \frac{1-\nu}{2}u_1 = f_1;$$

$$-w_1 + v_2 - \nu\alpha u_{1\zeta} + \varepsilon^2\left[-\alpha^4 w_{1\zeta\zeta\zeta\zeta} + 2\alpha^2 w_{1\zeta\zeta} + \frac{\nu-3}{2}\alpha^2 v_{2\zeta\zeta} + \alpha^3 u_{1\zeta\zeta\zeta}\right] = f_2;$$

$$\frac{1-\nu}{2}\alpha^2 v_{2\zeta\zeta} - v_2 + \frac{1+\nu}{2}\alpha u_{1\zeta} + w_1 - \varepsilon^2\alpha^2\frac{3-\nu}{2}w_{1\zeta\zeta} = f_3; \qquad (5)$$

$$f_1 = 2\alpha^2 f u_{0\zeta\zeta} + \alpha^2 f_\zeta u_{0\zeta} - \alpha f_\zeta w_0 - \alpha\left[(1-\nu)f + \varepsilon^2\alpha^2 f_{\zeta\zeta}\right]w_{0\zeta} -$$

$$-\left(\frac{1-\nu}{2}f + \varepsilon^2\alpha^2 f_{\zeta\zeta}\right)u_0 - \varepsilon^2\alpha^3\left(4 f_\zeta w_{0\zeta\zeta} + 3 f w_{0\zeta\zeta\zeta}\right) - X_1 \,/\, E^* h^*;$$

$$f_2 = \left(2\nu f - \varepsilon^2\alpha^2 f_{\zeta\zeta}\right)w_0 + \left[(1-\nu)f - \varepsilon^2\alpha^2 f_{\zeta\zeta}\right]\alpha u_{0\zeta} - \varepsilon^2\Big[4\alpha^4 f w_{0\zeta\zeta\zeta\zeta} +$$

$$+6\alpha^4 f_\zeta w_{0\zeta\zeta\zeta} - \left[(1-\nu)f - 4\alpha^2 f_{\zeta\zeta}\right]\alpha^2 w_{0\zeta\zeta} + \left(\nu f_\zeta + \alpha^2 f_{\zeta\zeta\zeta}\right)\alpha^2 w_{0\zeta} -$$

$$-3\alpha^3 f u_{0\zeta\zeta} - 2\alpha^3 f_\zeta u_{0\zeta} - \frac{\alpha}{2}\left[(1+\nu)f_\zeta - 2\alpha^2 f_{\zeta\zeta\zeta}\right]u_0\Big] - Z_1^1 \,/\, E^* h^*;$$

$$f_3 = -\frac{\nu-3}{2}\alpha f u_{0\zeta} - \frac{\nu-1}{2}\alpha f_\zeta u_0 - f w_0 -$$

$$-\varepsilon^2\frac{\alpha^2}{2}\left[(3-\nu)f_\zeta w_{0\zeta} + (7-\nu)f w_{0\zeta\zeta}\right] - Y_2^1 \,/\, E^* h^*.$$

First-order resolving equations for a thin-walled semi-momentless shell have the following form:

$$\alpha^2 u_{1\zeta\zeta} - \frac{1-\nu}{2}u_1 - \frac{1+\nu}{2}\alpha v_{2\zeta} + \nu\alpha w_{1\zeta} + f\left[\frac{1-\nu}{2}u_0 - 2\alpha^2 u_{0\zeta\zeta} + \alpha(1-\nu)w_{0\zeta}\right] -$$

$$-\alpha^3\left(w_{1\zeta}w_{0\zeta\zeta} + w_{0\zeta}w_{1\zeta\zeta}\right) + 3\alpha^3 f\cdot w_{0\zeta}w_{0\zeta\zeta} = \frac{\rho_t R_0^2 \omega^2}{E^*}u_{1\tau\tau}; \qquad (6)$$

$$\frac{1-\nu}{2}\alpha^2 v_{2\zeta\zeta} - v_2 - \frac{1}{E^* h^*}\frac{2u_1^*\mu}{R_0\left(0.5 - \ln\left|\frac{\gamma\rho_e\lambda u_1^*}{4\mu}R_0\right|\right)} + \frac{1+\nu}{2}\alpha u_{1\zeta} +$$

$$+w_1 + f\left(w_0 - \frac{3-\nu}{2}\alpha u_{0\zeta}\right) - \alpha^2 w_{0\zeta}w_{1\zeta} = \frac{\rho_t R_0^2 \omega^2}{E^*}v_{2\tau\tau};$$

$$w_1 + \frac{h^{*2}}{12}\left(\alpha^4 w_{1\zeta\zeta\zeta\zeta} - \alpha^2 w_{1\zeta\zeta}\right) + \nu\alpha u_{1\zeta} - v_2 +$$

$$+f\left[2\nu w_0 + (1-\nu)\alpha u_{0\zeta}\right] - \alpha^2 w_{0\zeta}w_{1\zeta} +$$

$$+\frac{\alpha^2}{2}f\left(w_{0\zeta}\right)^2 = \frac{1}{E^* h^*}\left[\rho_f\vartheta_{s0}^2 f - \frac{2u_1^*\mu}{R_0\left(0.5 - \ln\left|\frac{\gamma\rho_e\lambda u_1^*}{4\mu}R_0\right|\right)}\right] - \frac{\rho_t R_0^2 \omega^2}{E^*}w_{1\tau\tau}.$$

Here denoted:

$$E^* = E\big/\left(1-\nu^2\right),\ \ \varepsilon^2 = h^{*2}\big/12,\ \ \alpha = R_0\big/\ell,\ \ f = \kappa\big/\max|\kappa|.$$

By subscripts ζ, τ denote differentiation with respect to the corresponding variable.

The boundary conditions for the systems of equations are identical and imply hinged pipe edges:

$$u_1 = v_2 = w_1 = 0; \quad \frac{\partial^2 w_1}{\partial \zeta^2} = 0, \text{ for } \zeta = 0;$$

$$u_1 = v_2 = w_1 = 0; \quad \frac{\partial^2 w_1}{\partial \zeta^2} = 0, \text{ for } \zeta = L'. \tag{7}$$

Comparing equations (5) and (6), one can find that the left-hand sides of equations (5) contain additional terms with third-order derivatives. This makes the order of the equations system (5) higher than the order of system (6).

4. Methods and algorithms for the numerical solution of problems

Parameters λ, h^*, E_{irv} are taken as the defining parameters of mathematical models. An analogue of the Irwin parameter [20] is defined in [21]:

$$E_{irv} = \sqrt{\frac{2hE}{\beta\left(R_0 - h/2\right)Lv_{s0}^2}}, \tag{8}$$

where β is the friction coefficient of the flow in the pipe [22].

The constraint on the parameter h^* is established by relations (2). Based on the data of [14], it can be argued that for the applicability of the mathematical model of a semi-momentless shell, a stronger constraint must be satisfied:

$$h^* \le 1/30.$$

If restrictions (2) and restrictions on the parameter E_{irv} are not met, then it is necessary to use the rod model of the pipe, for example, described in [11], or use the medium-thickness shell model described in [14].

For the numerical analysis of problems (6) and (7), a computer program is created in the FORTRAN language, the operation algorithm and the numerical method of which are described in [12]. The numerical solution to problems (5) and (7) can be found using the algorithm described in [13].

Here we will verify and refine the scope of models [12,13] based on their numerical analysis by the finite element method in CAE Abacus [23]. We also use the MATLAB application package to analyze the errors that are introduced in the numerical analysis of the created models in the calculation of bending moments and stresses in the pipe wall. We will also perform numerical experiments to clarify the areas of applicability of mathematical models of the pipeline as the rod and as the shell.

5. Tasks for verifying mathematical model

Task 1. The classic problem of S.P. Timoshenko about a bent pipe under a distributed load [24] is chosen as a test one. A slightly curved beam under a distributed load q_n is considered. Let us define the initial undeformed line of the beam by the function

$$y_0 = b_1 \sin\frac{\pi z}{L}. \tag{9}$$

Let the deflection be described by the function

$$y - y_0 = a_1 \sin\frac{\pi z}{L}.$$

This formula corresponds to the first term of the expansion of the solution in a Fourier series on the interval $[0, L]$, and accurately describes the beam deflection, according to [24]. It is easy to find that for a given geometry:

$$\lambda = \pi^2 \frac{R_0 b_1}{L^2}.$$

Establishing a correspondence between the bending line of the beam and the displacement of the pipe centerline as a shell, we find that for the model problem the exact solution of equations (1) has the form:

$$u' = \lambda \frac{a_1 L}{\pi R_0 b_1} \cos\left(\frac{\pi \zeta}{L'}\right) \sin\theta,$$

$$v' = -\lambda \frac{a_1 L^2}{\pi^2 R_0^2 b_1} \sin\left(\frac{\pi \zeta}{L'}\right) \cos\theta,$$

$$w' = -\lambda \frac{a_1 L^2}{\pi^2 R_0^2 b_1} \sin\left(\frac{\pi \zeta}{L'}\right) \sin\theta.$$

The boundary conditions for this solution should have the form:

$$u' = \lambda \frac{a_1 L}{\pi R_0 b_1} \sin\theta, \ v' = 0, \ w' = 0, \quad \frac{\partial^2 w'}{\partial \zeta^2} = 0 \quad \text{for} \quad \zeta = 0;$$

$$u' = -\lambda \frac{a_1 L}{\pi R_0 b_1} \sin\theta, \ v' = 0, \ w' = 0, \quad \frac{\partial^2 w'}{\partial \zeta^2} = 0 \quad \text{for} \quad \zeta = L'.$$

(10)

The zero approximation functions for both models (5) and (6) vanish. The exact first-order solutions for these models coincide and have the form:

$$u_1(\zeta) = \frac{a_1 L}{\pi R_0 b_1} \cos\left(\frac{\pi \zeta}{L'}\right);$$

$$v_2(\zeta) = -\frac{a_1 L^2}{\pi^2 R_0^2 b_1} \sin\left(\frac{\pi \zeta}{L'}\right);$$

$$w_1(\zeta) = -\frac{a_1 L^2}{\pi^2 R_0^2 b_1} \sin\left(\frac{\pi \zeta}{L'}\right).$$

The right parts for the semi-momentless shell (6) have the form:

$$f_1 = -\frac{a_1}{b_1} \frac{\pi R_0}{L} \cos\frac{\pi \zeta}{L'}; \ f_2 = -\nu \frac{a_1}{b_1} \sin\frac{\pi \zeta}{L'};$$

$$f_3 = -\nu \frac{a_1}{b_1} \sin\frac{\pi \zeta}{L'} + \varepsilon^2 \left(\frac{\pi^2 R_0^2}{L^2} + 1\right) \frac{a_1}{b_1} \sin\frac{\pi \zeta}{L'}.$$

Right-hand sides for the moment shell (5) have the form:

$$f_1 = -\frac{a_1}{b_1} \frac{\pi R_0}{L} \cos\frac{\pi \zeta}{L'} - \varepsilon^2 \frac{a_1}{b_1} \frac{\pi R_0}{L} \cos\frac{\pi \zeta}{L'};$$

$$f_2 = \nu \frac{a_1}{b_1} \sin\frac{\pi \zeta}{L'} + \varepsilon^2 \left(\frac{2\pi^2 R_0^2}{L^2} + \frac{1+\nu}{2}\right) \frac{a_1}{b_1} \sin\frac{\pi \zeta}{L'};$$

$$f_3 = -\nu \frac{a_1}{b_1} \sin\frac{\pi \zeta}{L'} - \varepsilon^2 \frac{3-\nu}{2} \frac{a_1}{b_1} \sin\frac{\pi \zeta}{L'}.$$

The accuracy of the mathematical model (6) is estimated in [12]. We present here the results of numerical experiments to assess the accuracy of finding the bending moments and stresses using the mathematical model (5) with boundary conditions (10).

Numerical data of the model task are: $b_1 = 5.0$ m, $h = 0.01$ m, $L = 120$ m, $R_0 = 0.2$ m, $E = 2.07 \cdot 10^5$ MPa, $\nu = 0.24$, $V_{s0} = 1$ m/s, $\rho_f = 998$ kg/m^3, $\rho_t = 7200$ kg/m^3, $\ell = 1$ m, $S_f = 0.1195$ m^2.

Here denoted: V_{s0} is fluid flow velocity, ρ_f is fluid density, ρ_t is pipe material density, S_f ispipe lumen area.

Task 2. To separate the areas of applicability of the rod model [11] and the thin-walled shell model [12], we choose the dynamic problem of bending an extended pipeline with a profile in the form of a chain. Model parameters are: fluid flow velocity $V_{s0} = 1.5$ m/s, viscosity of the external media $\mu_e = 5000$ Pa·s, fluid viscosity $\mu = 0.1$ Pa·s, wall thickness $h = 0.005$ m, pipe radius $R_0 = 0.23$ m, pipe length $L = 3009$ m. A time interval of 48 hours was calculated.

The chain is a curvewhere the coordinates of the points follow the relation [25]:

$$y = A + B \cdot \cosh\left(\frac{x - x_0}{B} - 1\right).$$

The solution to the problem of finding chain line parameters is known and presented in [25]. In *task 2*, the chain line parameters are as follows: $x_1 = 0$, $y_1 = 0$, $x_2 = 3000$ m, $y_2 = 200$ m, $A = -21901.4$ m, $B = 21901.4$ m, $x_0 = -21859.2$ m. With these parameters, the minimum radius of curvature of the axis is found: $\min | \rho_0 | \approx 17092.4$ m.

Methods for the numerical analysis of *task 2* are described in [11,12].

6. Numerical results and discussion

Task 1. As proved in [24], the solution of the stress problem in a slightly bent rod under a distributed load can be well approximated by the solution of the stress problem in a straight beam with the same cross-section. To obtain numerical estimates of bending moments and stresses, we approximately replace the beam of shape (9) with a circle segment with a chord of 120 m and a 5 m lifting boom, in accordance with the numbers given above. The circle radius is found taking into account the concept of the degree of a point p for the midpoint of the segment *[0, L]* using the Huygens formula (see [25]). We get radius ρ_0=360 m. Calculating the distributed transverse load on the pipe according to the formula (see [11]):

$$q_n = \frac{\rho_f}{\rho_0} S_f V_{s0}^2,$$

we get $q_n \approx 0.3312$ N/m. This load corresponds to the force *P*=39.74 N, distributed along the entire length of the beam.

Solving the problem by the strength of materials methods [26], we find the maximum bending moment in absolute value and the corresponding stress:

$$\max |M_x| \approx 596.1 \text{ Nm}, \ \max |\sigma_z| \approx 486 \text{ kPa}.$$

These values of quantities can be guided by the analysis of the numerical experiment results.

This calculation was verified by the finite element method in the APM WIN Machine software package [27]. Tables 1 and 2 contain excerpts from the tables for calculating bending moments and equivalent stresses, containing the maximum modulo values of these quantities.

Thus, in APM WIN Machine it was found that the maximum bending moment modulo is 596.1 Nm. This value coincided with the value obtained by the methods of strength of materials. The maximum value of the equivalent stress is 0.48461 MPa. The relative deviation from the value obtained by the methods of strength of materials is:

$$\max \varepsilon_z = \frac{\max\left|\sigma_z - \sigma_{eq}\right|}{\max \sigma_{eq}} 100\% = 4.1\%.$$

Table 1. Bending moments

Distance (mm)	Bending moment (Nm)
57600.0	-595.14684
58800.0	-595.86216
60000.0	-596.10060
61200.0	-595.86216
62400.0	-595.14684

Table 2. Equivalent stresses

Distance (mm)	Equivalent stress σ_{eq} (MPa)
57600.0	0.48384
58800.0	0.48442
60000.0	0.48461
61200.0	0.48442
62400.0	0.48384

So, the approximate values of bending moments and equivalent stresses are obtained in two different ways. In this case, the stress values differ from each other within the accuracy of the rod theory (see [26]).

Let us denote J_x as the moment of inertia of the pipe cross-section, W_x as the moment of its section resistance relative to the axis Ox. With the above numerical parameters of the model, J_x=0.0002515 m^4, W_x=0.001223 m^3. The bending moment is related to the beam deflection v_n by the formula (see [26]):

$$M_x = EJ_x \frac{d^2 v_n}{dz^2}, \quad v_n = y - y_0. \tag{11}$$

The stress is related to the bending moment by the relation (see ibid.):

$$\sigma_z = M_x \big/ W_x. \tag{12}$$

Formulas (11) and (12) are applicable when condition (3) is satisfied. Taking into account the smallness of the curvature κ=1/360 m^{-1} and the equality ℓ=1 m, formula (11) does not change when z is replaced by ζ.

The method for finding a numerical solution to the boundary value problem (5), (7) is described in [13] and implemented in the MATLAB software package. It is also established there that the displacement of the axial line of the pipe is associated with unknown functions by the formula:

$$v_{nh} = -\frac{\lambda R_0}{2}\left(v_{2h} + w_{1h}\right). \tag{13}$$

All changes of variables are already taken into account in (13), and the deflection v_{nh} is expressed in meters.

To find a numerical solution, a grid of equally spaced points ζ_I is constructed, and the index i varies from 1 to 4000. The grid step is h=0.03 m. These parameters are chosen to find the best approximation of the exact solution. Problem (5), (10) with the selected data is a rigid boundary value problem; the bvp5c method of the MATLAB package is used to solve it.

Let us determine the errors in finding the bending moments and stresses by the formulas:

$$\varepsilon_M = \frac{|M_x - M_{xh}|}{\max|M_x|}, \ \varepsilon_\sigma = \frac{|\sigma_z - \sigma_{zh}|}{\max|\sigma_z|}.$$

The numerical values of bending moments M_x and normal stresses σ_{zh} on the grid $\{\zeta_i\}$ are found using formulas (11)–(13).

Since the stress σ_z is the main one for a given type of load on the beam (see [26]), the equality $\sigma_{eq} \approx |\sigma_z|$ is actually fulfilled, where σ_{eq} is the von Mises equivalent stress. The absolute values of stresses for exact and numerical solutions are shown in Fig. 1. The figure shows that the exact and approximate stress values are in good agreement.
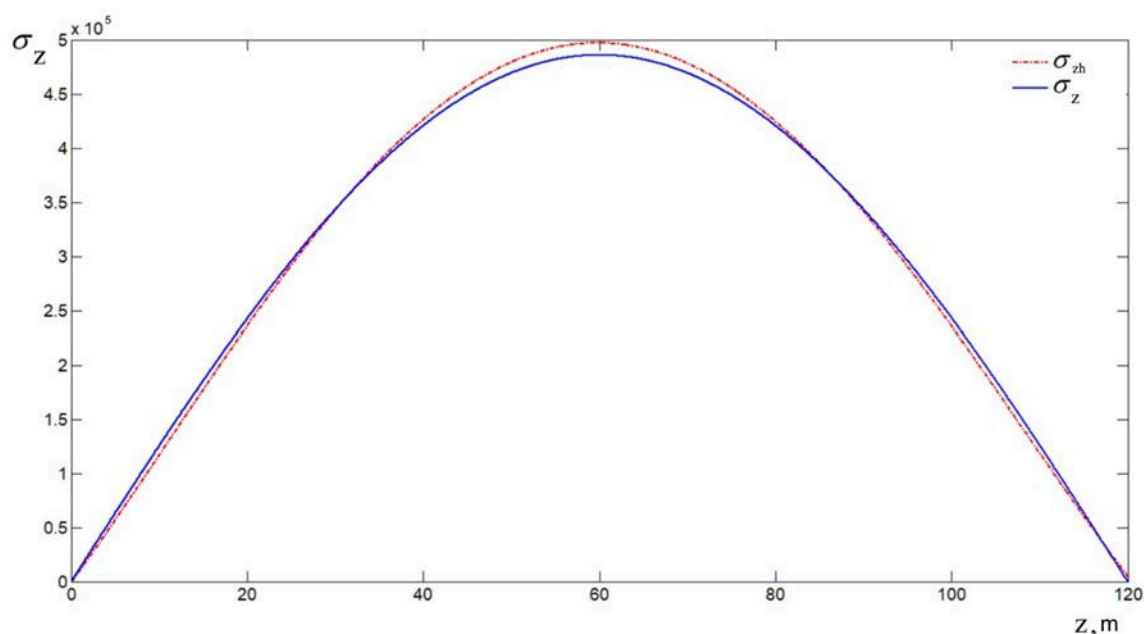
Fig. 1. Modules of maximum stresses in the pipe section, Pa

The quantitative value of the error in the calculation of stresses and moments is given by the analysis of the above-defined values ε_M, ε_σ. These values are shown in Fig. 2.

Maximum error values are: $\max \varepsilon_M = 0.023$, $\max \varepsilon_\sigma = 0.023$.

These results are obtained by approximating the numerical solution v_{2h}, w_{1h} by sixth-order polynomials and using standard MATLAB functions to find derivatives of polynomials.

Let us present the results of the calculation of the same mechanical system by the finite element method in CAE Abaqus. A curved two-bearing beam is built with the geometric parameters of the model problem, loaded with the distributed load q_n=0.3312 N/m calculated above. The construction technique is described in [23].The constructed geometric model contained a one-dimensional FEM grid of 100 elements with a grid step h=1.2 m. The von Mises stresses obtained after the calculations are shown in Fig. 3. It is known [26] that in direct bending of the beam, the equivalent von Mises stress coincides with $|\sigma_z|$, as we obtained in the Abaqus report file.

The maximum value of the stress modulus in the numerical solution in Fig. 1 is $\max|\sigma_z| = 0.49707$ MPa, and the maximum stress in Fig. 3 is $\max\sigma_{eq}$=0.4743 MPa. This numerical value is obtained from the Abaqus report file generated at the end of the calculation.

The graph of the exact solution for stresses as a function of the longitudinal coordinate is shown in Fig. 1. The exact stress values and their numerical approximations in Abaqus are shown in Fig. 4.
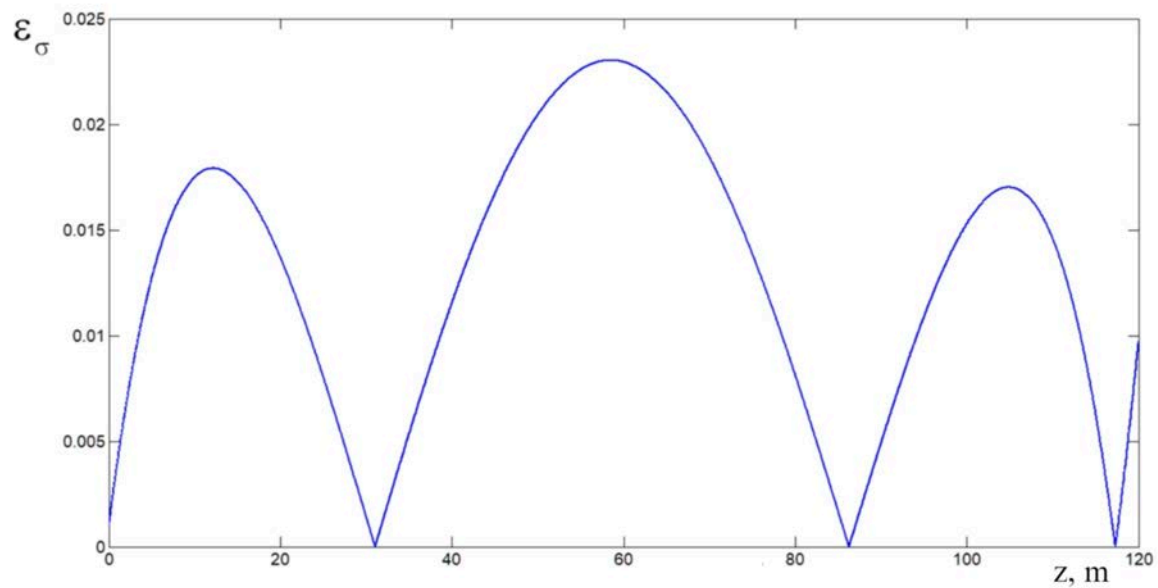
Fig. 2. Error module for calculating stresses in a pipe

Fig. 3. Equivalent stresses calculated in Abaqus
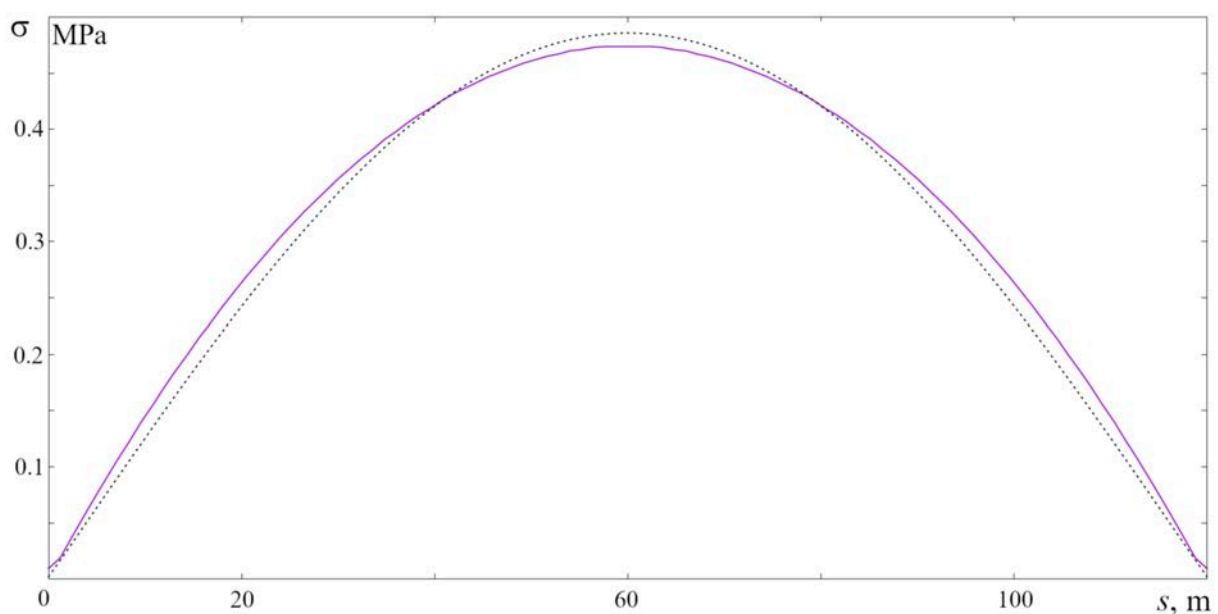
Fig. 4. Exact stress values (dashed line) and numerical solution by FEM (solid line)

In Fig. 4 we can see that the exact and numerical solutions for stresses are in good agreement with each other.

We determine the relative errors for these stresses:

$$\max \varepsilon_{AbNum} = \max \frac{\left| \sigma_{\text{экв}} - |\sigma_{zh}| \right|}{\max |\sigma_{\text{экв}}|}, \quad \max \varepsilon_{\sigma exact} = \max \frac{\left\| \sigma_z \right| - \sigma_{\text{экв}} \right|}{\max |\sigma_z|}.$$

After doing the calculations, we find: $\max \varepsilon_{AbNum} = 0.048$, $\max \varepsilon_{\sigma exact} = 0.0239$.

Thus, the stress found by the model (5) deviates from the solution by the finite element method in CAE Abaqus by no more than 4.8%. On the other hand, the Abaqus system itself gives an error that does not exceed 2.4% for the one-dimensional geometric model we have constructed. It should be noted that the accuracy of the theory of rods and shells does not exceed 5% [26].

Summarizing the solution of *task 1*, we can conclude that the created mathematical model allows us to perform stress calculations in bent pipes with high accuracy. The numerical analysis results are consistent with the known exact and approximate solutions. Restrictions (2) and (3) should be imposed on the parameters of the mathematical model.

Task 2. A comparison is made of the displacement of the axial line of the pipeline according to the proposed mathematical models: the model of a semi-momentless shell in [12] and the model of a bent rod in [11]. Numerical methods of solution are proposed ibid.

Condition (2) is satisfied, which makes it possible to use the shell model (1).A comparison of the dynamics of the center line as the rod and shell is shown in Fig. 5. Figure 5a shows the displacement of the profile when the rod model is chosen, Fig. 5b – when chosen the shell model.
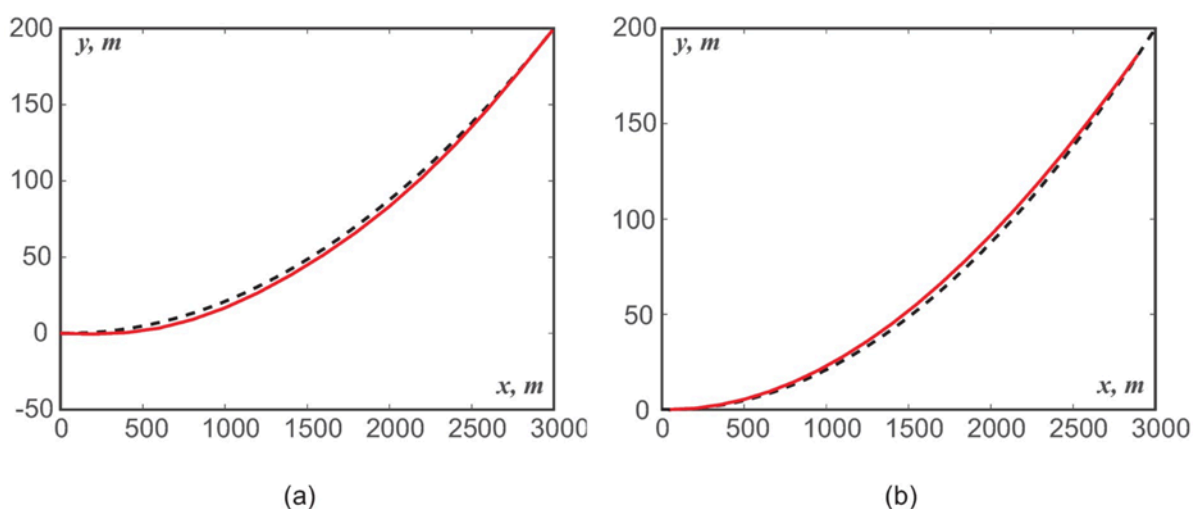
Fig. 5. Pipe displacement: a) rod model; b) shell model

In [28], the phenomenon of "reverse behavior of the pipe" is described, when the centerline moves against the direction of the centrifugal force from the flow. Figure5b shows that the shell model (6) describes this phenomenon. The rod model [11] in this case gives a different behavior of the pipe.

Calculating (8), we find: $E_{irv} \approx 42.4$. The resulting value is significantly less than the value $E_{irv} \geq 286$, at which the rod model is required. This means that the application of the mathematical model [12] as more general is justified.

So, according to *task 2*, we can conclude that our calculations correspond to the results presented in the scientific literature.

7. Conclusion

Comparative analysis of mathematical models of the pipeline is performed, verification of these models based on a comparison of exact and numerical solutions is carried out, and the limits of their applicability are determined.

The formulation of the mathematical model of the pipeline as an elastic shell is given and the basic parameters of this model are determined. The equations of the first approximation with respect to the small curvature parameter are compared for mathematical models of moment and semi-momentless shells. The acting forces and stresses are calculated for the test problem of bending a pipeline segment. Numerical solution to the test problem is found, and the grid functions of stresses and bending moments are calculated on its basis. The geometry and finite element model of a bent pipe under transverse load are constructed in CAE Abaqus. Stresses and bending moments in all approximate models are compared with exact values of these quantities, and numerical values of errors are found. It has been established that the proposed mathematical model makes it possible to find stresses in pipes with high accuracy. It has been established that the proposed mathematical models have areas of applicability confirmed by known scientific data.

References

1. Liu R, Xiong H, Wu X, Yan Sh. Numerical studies on global buckling of subsea pipelines. *Ocean Engineering*. 2014;78: 62-72.
2. Liu R, Wang W, Yan Sh, Wu X. Engineering measures for preventing upheaval buckling of buried submarine pipelines. *Applied Mathematics and Mechanics (Engl. Ed.).* 2012;33(6): 781-796.
3. Feodosiev VI. *Advanced Stress and Stability Analysis: Worked Examples*. Berlin: Springer; 2005.
4. Towhata I. *Geotechnical Earthquake Engineering*. Berlin: Springer; 2008.
5. Bai Y. *Pipelines and Risers*. Amsterdam: Elsevier; 2003.
6. Svetlitsky VA. *Dynamics of Rods*. Berlin: Springer; 2005.
7. Bucalem ML, Bathe KJ. Finite element analysis of shell structures. *Archives of Computational Methods in Engineering*. 1997;4(1): 3-61.
8. Klar A, Marshall AM. Shell versus beam representation of pipes in the evaluation of tunneling effects on pipelines. *Tunnelling and Underground Space Technology*. 2008;23(4): 431-437.
9. Yifei Y, Bing S, Jianjun W, Xiangzhen Y. A study on stress of buried oil and gas pipeline crossing a fault based on thin shell FEM model. *Tunneling and Underground Space Technology*. 2018;81: 472-479.
10. Rukavishnikov VA, Tkachenko OP. Numerical and asymptotic solution of the equations of propagation of hydroelastic vibrations in a curved pipe. *Journal of Applied Mechanics and Technical Physics*. 2000;41: 1102-1110.
11. Rukavishnikov VA, Tkachenko OP. Nonlinear equations of motion of an extensible underground pipeline: derivation and numerical modeling. *Journal of Applied Mechanics and Technical Physics*. 2003;44(4): 571-583.
12. Rukavishnikov VA, Tkachenko OP. Dynamics of a fluid-filled curvilinear pipeline. *Applied Mathematics and Mechanics*. 2018;39(6): 905-922.
13. Rukavishnikov VA, Tkachenko OP. Approximate resolving equations of mathematical model of a curved thin-walled cylinder. *Applied Mathematics and Computation*. 2022;422: 12696.
14. Vlasov VS. *Basic Differential Equations in General Theory of Elastic Shells. Technical Memorandum 1241*. Washington: NACA; 1951.

15. Rukavishnikov VA, Tkachenko OP. Mathematical model of the pipeline with angular joint of elements. *Mathematical Methods in the Applied Sciences*. 2020;43(13): 7550-7568.

16. Rukavishnikov VA. Weighted FEM for two-dimensional elasticity problem with corner singularity. *Lecture Notes in Computational Science and Engineering*. 2016;112: 411-419.

17. Rukavishnikov VA, Rukavishnikova EI. On the dirichlet problem with corner singularity. *Mathematics*. 2020;8(11): 1870.

18. Rukavishnikov VA, Mosolapov AO, Rukavishnikova EI. Weighted finite element method for elasticity problem with a crack. *Computers & Structures*. 2021;243: 106400.

19. Bratov VA. Numerical simulations of dynamic fracture. Crack propagation and fracture of initially intact media. *Materials Physics and Mechanics.* 2021;47(3): 455-474.

20. Hover FS, Triantafyllou MS. Linear dynamics of curved tensioned elastic beams. *Journal of Sound and Vibration*. 1999;228(4): 923-930.

21. Tkachenko OP. Comparison of the computational experiment´s results on the two mathematical models of pipeline. *Mathematical modeling, computer and field experiment in natural sciences*. 2018;1. Available from: http://mathmod.esrae.ru/17-59 [Accessed: 23th August 2022]. (In Russian)

22. Loitsyansky LG. *Mechanics of Fluid and Gas*. Moscow: Drofa; 2003. (In Russian)

23. Lavrinenkov AD, Yakimov ID, Levadny EV, Boyko AB, Ostapov AV, Ziginov NV. *SIMULA Abaqus. Solving Applied Problems*. Moscow: TESIS; 2015. (In Russian)

24. Timoshenko SP. *Strength and Vibrations of Structural Elements*. Moscow: Science; 1975. (In Russian)

25. Bronshtein IN, Semendyayev KA. *A Guide Book to Mathematics: Fundamental Formulas, Tables, Graphs, Method*s. Zürich: Springer; 1973.

26. Alexandrov AV, Potapov VD, Derzhavin BP. *Resistance of Materials*. Moscow: Higher School; 2000. (In Russian)

27. Shelofast VV, Chugunova TB. *Fundamentals of machine design. Examples of problem solving.* Moscow: APM; 2007. (In Russian)

28. Athisakul Ch, Monprapussorn T, Pulngern T, Chucheepsakul S. The effect of axial extensibility on three-dimensional behavior of tensioned pipes/risers transporting fluid. In: *Proceedings of the Eighth (2008) ISOPE Pacific/Asia Offshore Mechanics Symposium*. 2008. p.97-104.

THE AUTHORS

Tkachenko O.P.
e-mail: olegt1964@gmail.com
ORCID: 0000-0003-1806-0274

Effect of plasticizers on the mechanical and technological properties of styrene-isoprene block copolymer composites under cyclic loading

V.V. Avdonin[1]✉, Yu.V. Yurkin[1], E.S. Shirokova[2], D.A. Varankina[1], R.S. Rogozhkin[1]

[1]Vyatka State University, 36, Moskovskaya Street, Kirov Region, Russia

[2]VPO "Vyatka State University", 610000, Russia, Kirov region, Kirov Str. Moscow, 36, Russia

✉ avdoninvalerii@bk.ru

Abstract. In various applications, there is a demand for materials with damping properties. One of the promising materials in this respect is polymer composite material based on thermoplastic elastomers. When studying the experience of using thermoplastic elastomers as damping materials, it was found that one of the most promising TPEs for this purpose is block copolymer of the styrene-isoprene-styrene type. In this article, composites based on SIS VECTOR 4111NS and SIS VECTOR 4113NS thermoplastic elastomers with different plasticizer content were tested. The results showed that the composite based on SIS VECTOR 4113NS for the manufacture of damping pads is more promising. It also revealed the optimal amount of plasticizer required for the manufacture of high-quality material with the best mechanical characteristics.

Keywords: polymer composite materials, thermoplastics, vibration absorption, damping materials, styrene-isoprene block copolymer, building structures

Citation: Avdonin VV, Yurkin YuV, Shirokova ES, Varankina DA, Rogozhkin RS. Effect of plasticizers on the mechanical and technological properties of styrene-isoprene block copolymer composites under cyclic loading. *Materials Physics and Mechanics*. 2022;50(2): 355-363. DOI: 10.18149/MPM.5022022_14.

1. Introduction

There has been a growing demand for materials with damping properties, i.e., capable of dissipating the mechanical energy of the system. Damping plays a major role in such areas as electronics, sound insulation, automotive and transportation industry, construction, shipbuilding, household appliances, industrial equipment, firearms, health care, and medical devices, personal protective equipment, and/or sports gear [1-3]. Polymer composite materials show much promise in this regard [4,5].

An example of successful vibration dampers is elastomeric bearing pad, used in the construction of bridges and buildings for over 70 years. Such pads prevent structural damage and reduce repair and maintenance costs [6].

Currently, elastomeric pads are fabricated from natural or synthetic rubbers [7]. However, this type of material is becoming less popular with the recent advent of

thermoplastic elastomers (TPE), which are a group of materials capable of large reversible deformations during operation, like rubbers, and suitable for recycling, like plastics [8,9]. Using TPE instead of rubbers allows for increasing productivity by 2-4 times, increasing the production outputs by 2-2.5 times; reducing labor and energy costs by 30% (as it is possible to forego blanking, vulcanization, and waste removal); reducing the material consumption of the product by 25-30% (by reducing the specific weight of the material); reducing gas emissions by 10-20 times; ensuring complete waste recycling, and, ultimately, fabricating high-quality products [10,11].

TPE include two large groups of materials: block copolymers (e.g., styrene block copolymers, ester copolymers, thermoplastic polyurethanes, block polyamides) and composites based on a mixture of rubber and thermoplastic (e.g., olefin thermoplastics) [12,13].

Considering the experience of adopting thermoplastic elastomers as damping materials, studies have established that block copolymers of the styrene-isoprene-styrene type are one of the most promising TPE for this purpose [14].

This study aimed to achieve the following goals:
1. Determine the most promising TPE with the best damping properties;
2. Determine the options for fabricating a finished product from this material.

2. Method

Materials. We considered styrene-isoprene-styrene type block copolymers Vector 4111NS and Vector 4113NS (TSRC, Republic of China) and copolymer SKEPT-50 (Nizhnekamskneftekhim, Russia). Vector 4111NS is a linear triblock, and Vector 4113NS is a mixture of linear triblock and diblock, which gives the composition greater softness. Industrial oil I-40 (Gazpromneft, Russia) was used as a softening agent in the compound; the filler combined chalk MICARB (Geocom, Russia), an inert filler with a low price [15], and Newsil 1165 silica (People's Republic of China).

To select the optimal composition for the compound, providing the best combination of technological (recyclability) and operational (damping) properties, the type of thermoplastic elastomer used and the content of industrial oil I-40 were varied, bringing its content to 70 weight parts per 100 weight parts of the polymer [16].

Preparation of compounds. The components were mixed in a Brabender-type micromixer at 180ºC for 20 minutes.

The compositions of model mixtures and their notations are presented in Table 1.

The test specimens were prepared in an injection molding machine at 190ºC.

The notations for the model mixtures correspond to the brand of thermoplastic elastomer (Vector 4111 or Vector 4113) and oil contents (M) in the compound for weight parts per 100 parts of polymer. The mixing modes are presented in Table 2.

The operational properties of the specimens were subsequently assessed; the specimens were molded via an SZS-series thermoplastic testing machine at 190ºC and an injection pressure of 5 atmospheres.

Assessment of operational (rheological) properties. The rheological characteristics, determining the options for subsequent processing by injection molding, were measured for the obtained compounds. The melt flow index (MFI) was evaluated by ASTM D 1238 at a temperature of 190°C and a load of 5 kg with the PTR-Lab-02 device (St. Petersburg, Russia).

Assessment of operational properties. Mechanical tensile tests were carried out using an Autograph AG-X 5 kN tensile testing machine by Shimadzu (Kyoto, Japan) at room temperature and a travel speed of 500 mm/min for dumbbell-shaped specimens (Fig. 1) in accordance with GOST 270-75 [17].

Table 1. Compositions of the studied compounds

Ingredient	Content, weight parts per 100 weight parts of polymer									
	SIS VECTOR 4111NS					SIS VECTOR 4113NS				
	V4111 M30	V4111 M40	V4111 M50	V4111 M60	V4111 M70	V4113 M30	V4113 M40	V4113 M50	V4113 M60	V4113 M70
SKEPT-50	20	20	20	20	20	20	20	20	20	20
SIS Vector 4111NS (18% Styrene)	80	80	80	80	80	-	-	-	-	-
SIS Vector 4113NS (15% Styrene)	-	-	-	-	-	80	80	80	80	80
MICARB chalk	40	40	40	40	40	40	40	40	40	40
Newsil 1165 silica	30	30	30	30	30	30	30	30	30	30
I-40 industrial oil	30	40	50	60	70	30	40	50	60	70
Stearic acid	2.5	2.5	2.5	2.5	2.5	2.5	2.5	2.5	2.5	2.5
Total	202.5	212.5	222.5	232.5	242.5	202.5	212.5	222.5	232.5	242.5

Table 2. Compound preparation conditions

Ingredient	Time, min	Speed, rpm	Temperature, °C
Stage 1			
SKEPT-50 and thermoplastic elastomer	3–5	60	180
30% oil/filler	3–5		
30% oil/filler	3–5		
30% oil/filler	3–5		
Stage 2			
Stage 1 mixture	5–7	60	180

Intermittent cyclic tensile tests at 100% elongation were carried out with the Autograph AG–X 5 kN machine by Shimadzu (Kyoto, Japan) at a travel speed of 500 mm/min for dumbbell-shaped specimens (Fig. 1). Figure 2 shows a schematic diagram of the loading-unloading cycle and the resulting hysteresis loop, with arrows indicating the unloading and reloading sequences. The dissipated energy, or hysteresis energy loss, WD, corresponds to the area enclosed in this hysteresis loop, while the area under the lower curve (corresponding to unloading) of the hysteresis loop represents the stored elastic energy, WE. Specific dissipated and elastic energies were determined by dividing WD and WE by the initial volume of the specimen. The specific damping capacity is the ratio of the energy dissipated in five cycles to the elastic or potential energy accumulated in this cycle [19], and was found from:

$$\Psi = W_D/W_E. \tag{1}$$

Fig. 1. Dumbbell-shaped specimens for testing
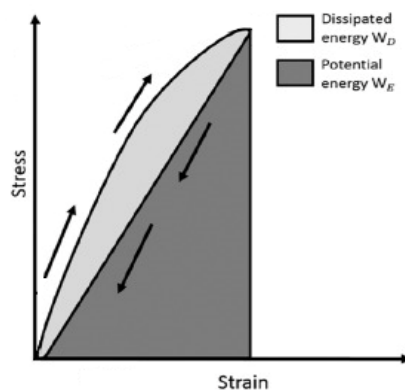
Fig. 2. Schematic diagram of an unloading-loading cycle showing the amount of dissipated energy and elastic energy. The graph is constructed based on the data from Ref. [18]

This characteristic reflects the damping capacity of the material, i.e., indicates how effectively the material dissipates directed kinetic energy. The greater the ratio of the scattered energy in the material to the potential energy stored in it, the more effectively the material absorbs vibrations.

The ultimate tensile strength was determined by the formula:

$$R_S = Q_{max}/A, \tag{2}$$

where Q_{max} is the maximum load, and A is the cross-sectional area.

Ultimate tensile strength serves as a measure for estimating the seismic or other loads that the material can withstand before tensile failure.

The equivalent stiffness was calculated by the formula:

$$E_{100} = \sigma_{100}/\varepsilon_{100} , \tag{3}$$

where σ_{100} is the stress at 100% elongation, $\varepsilon_{100} = 1 - 100\%$ elongation.

The equivalent stiffness serves as a measure for comparing the stiffness of the material at the same elongation. The higher E100, the stiffer the material. This means that the material can absorb a greater load at the same elongation.

Shore A hardness was measured with a durometer in accordance with GOST 263-75 [20].

This characteristic allows estimating the magnitude of the vertical load that the material can withstand before failure. Shore A hardness is important because the material developed is to be used as a damping pad.

3. Results and discussion

Technological properties. The compound's suitability for injection molding can be estimated from the magnitude of MFI.

Molding failed in specimens V4111M20, V4111M25, V4113M20, and V4113M25 shown in Fig. 3. The low oil content in the specimens (20 and 25 weight parts) did not allow producing of high-quality specimens by injection molding. High-quality specimens were produced from mixtures with the oil contents of 30, 40, 50, 60, and 70 weight parts (Fig. 4). The results obtained are consistent with the data on MFI (Fig. 5).

Thus, we found that the compounds suitable for molding using a thermoplastic machine under a pressure of 5 atmospheres are those with MFI over 30 g/10 min, which is the minimum value required. Specimens acceptable for testing can be obtained at this MFI.

Fig. 3. Specimens 1 and 2 with the oil contents of 20 and 25 weight parts, respectively, for SIS VECTOR 4111NS
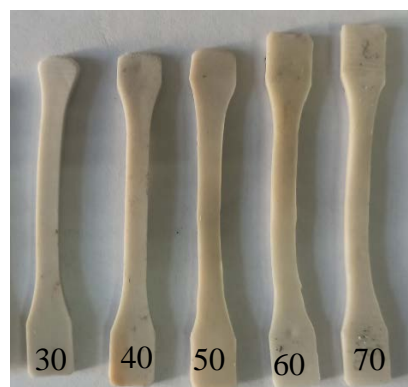
Fig. 4. Specimens with the oil contents of 30, 40, 50, 60, and 70 weight parts for SIS VECTOR 4111NS
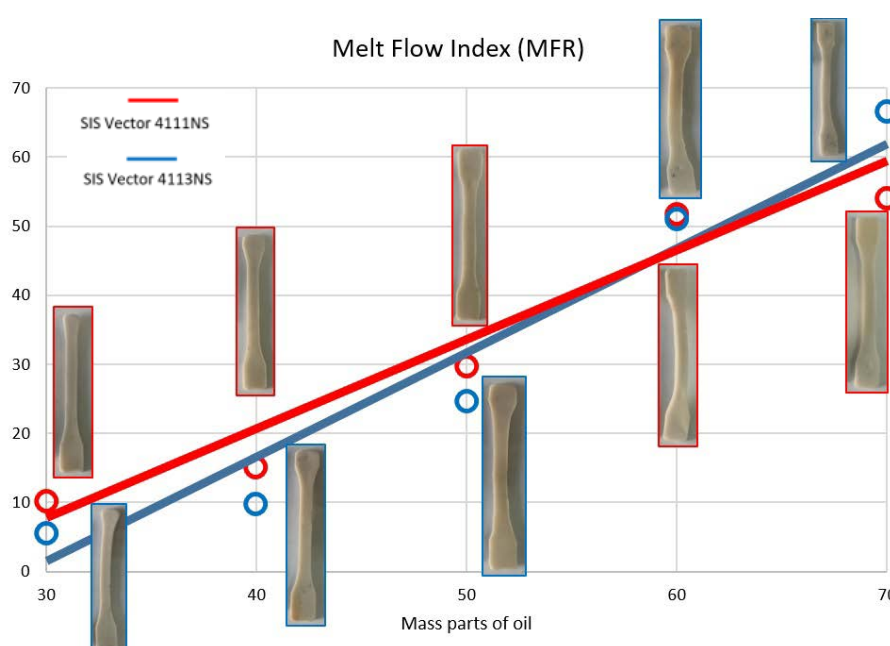
Fig. 5. MFI of compounds as a function of oil contents (for 30, 40, 50, 60, and 70 weight parts)

Monotonic tensile testing. Comparing materials based on SIS VECTOR 4111NS and SIS VECTOR 4113 NS, we can observe that equivalent stiffness, strength and hardness are higher in the material based on SIS 4111NS (Figs. 6-8). The elongation is higher in the material based on SIS 4113NS (Fig. 9).

In addition, the mechanical characteristics of materials vary depending on the oil content in the mixture, with a similar dependence observed for both materials [17]. It can be seen from the graphs that increasing the oil content produces a decrease in the following mechanical characteristics: equivalent stiffness, strength, and Shore A hardness. The elongation at break first increases with increasing oil content but then decreases as well. It can be concluded that the material has optimal mechanical properties at an oil content of 50 weight parts per 100 weight parts of polymer.
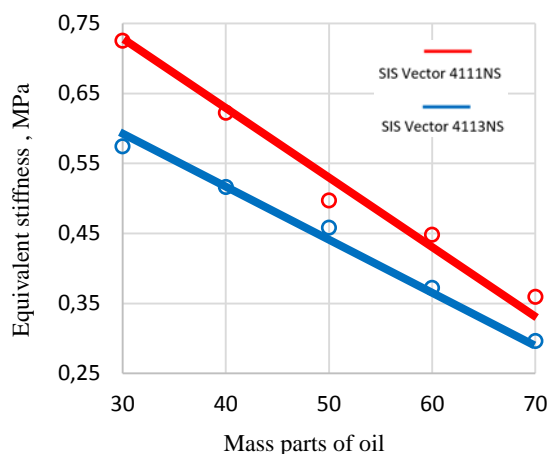
Fig. 6. Effect of oil content on equivalent stiffness of the compound
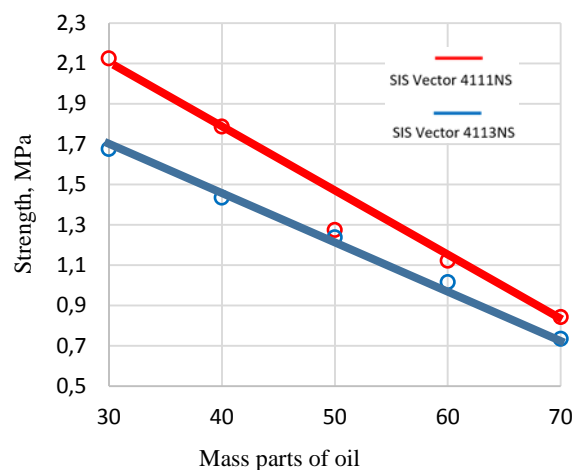
Fig. 7. Effect of oil content on strength characteristics of the compound
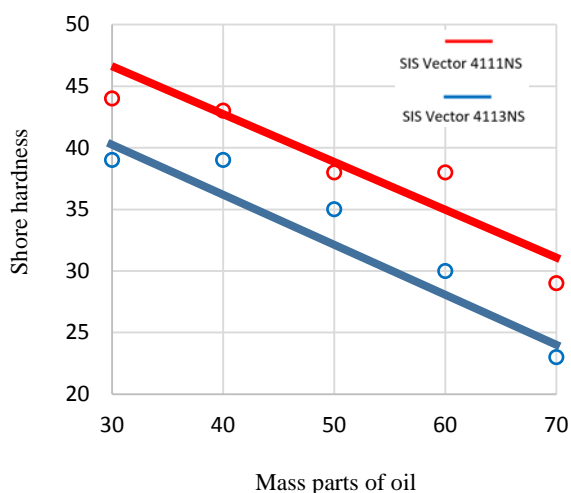
Fig. 8. Effect of oil content on the Shore hardness of the compound
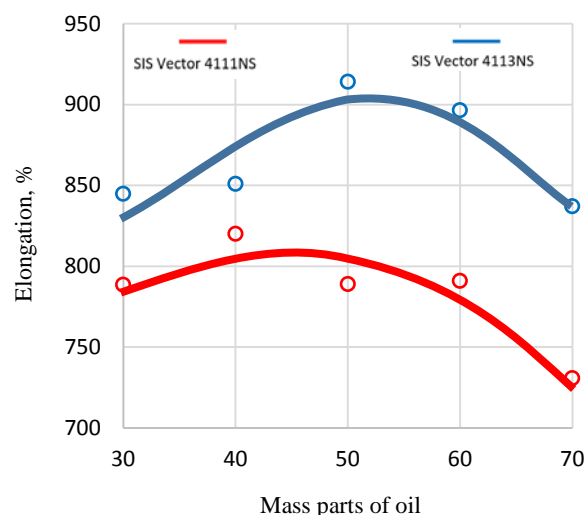
Fig. 9. Effect of oil content on maximum elongation of the compound

Repeated cyclic tensile tests. The cyclic tensile responses of the compounds are shown in Fig. 10. A large hysteresis loop occurs between the first loading-unloading cycle, while much smaller loops can be observed for subsequent loading cycles. Moreover, a constant deformation of 20% appears after the first loading-unloading cycle, which practically does not increase with subsequent cycles. This suggests that all fractures within the composite structure mainly occur in the first cycle. The nature of hysteresis has not changed in different brands of thermoplastic elastomers.

Comparing materials based on SIS Vector 4111NS and SIS VECTOR 4113NS with different weight parts of oil, we can conclude that the specific damping capacity is better for the material based on SIS VECTOR 4113NS, and oil content has little effect on the damping capacity (Fig. 11).

(a)

(b)
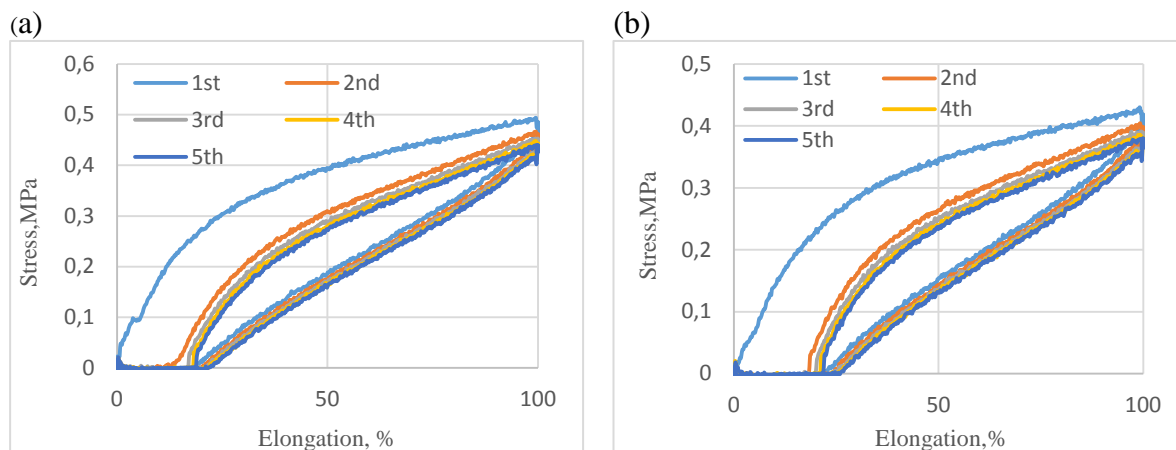
Fig. 10. Standard cyclic tensile reactions of composites based on SIS VECTOR 4111NS (a) and based on SIS VECTOR 4113NS (b), respectively
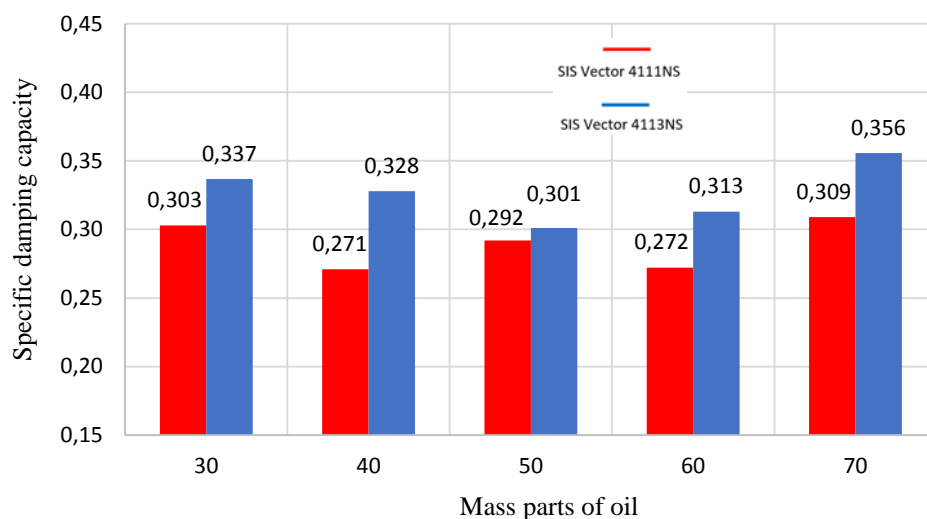
Fig. 11. Specific damping capacity for SIS VECTOR 4111NS and SIS VECTOR 4113NS

4. Conclusion

To summarize, we have obtained the following results:

1. SIS 4113NS shows the greatest promise for manufacturing damping pads because it has the best damping properties; the optimal amount of oil for the compound based on it is 50 weight parts of oil per 100 weight parts of polymer. Materials with such ratios of oil and block copolymer exhibit sufficiently high mechanical properties, while specimens can still be produced by injection molding. Increasing the oil content leads to a decrease in the mechanical characteristics of the material.

2. The MFI for obtaining a product by injection molding using an SZS-series thermoplastic testing machine at a temperature of 190°C and an injection pressure of 5 atmospheres had to be at least 30 g in 10 min. This melt flow rate is the minimum required.

References
1. Wang HQ, Jiang ZG, Huang L, Yuan HB, Li XY. Development of damping materials. *Chinese Polymer Bulletin*. 2006;3: 24.
2. Fan R, Meng G, Yang J, He C. Experimental study of the effect of viscoelastic damping materials on noise and vibration reduction within railway vehicles. *Journal of Sound and Vibration*. 2009;319(1-2): 58-76.
3. Sytyy YV, Sagomonova VA, Kislyakova VI, Bolshakov VA. Novel vibroadsorbic materials *Aviation Materials and Technologies*. 2012;2: 51-54. (In Russian)
4. Joseph PG. *Automotive Plastics and Composites*. William Andrew; 2021.
5. Kumar S, Krishnan S, Mohanty S. *Elastomer Blends and Composites*. Elsevier; 2022.
6. Galeeva KV, Polusurova AY, Korobkov SV. Stroitel'stvo sejsmostojkih zdanij i sooruzhenij. *Intellektual'nye tekhnologii i tekhnika v proizvodstve i promyshlennosti*. 2017;1: 31-36. (In Russian)
7. Sagomonova VA, Dolgopolov SS, Sorokin AYe, Tselikin VV. Otsenka vozmozhnosti primeneniya vibropogloshchayushchego materiala na osnove poliuretana v kachestve uplotniteley. *Trudy Viam*. 2021;10: 28-35. (In Russian)
8. Kaliyathan AV, Rane AV, Kanny K, Maria HJ, Thomas S. *Reference Module in Materials Science and Materials Engineering*. Elsevier; 2022.
9. Dolinskaya RM, Prokopchuk NR. Izmeneniye svoystv elastomernykh kompozitsiy pri razlichnykh vidakh stareniya. *Trudy BGTU*. 2018;2: 30-34.
10. Abitha VK, Rane VA, Kanny K, Hanna JM, Thomas S. *Encyclopedia of Materials: Plastics and Polymers: Plastics and Polymers*. Elsevier; 2022.
11. Waseem SK, Eylem A, Md Nizam U, Asmatulu R. *Recycling and Reusing of Engineering Materials*. Elsevier; 2022.
12. Prut EV, Cherkashina NI, Yastrebinskaya AV. Razrabotka polimernykh kompozitsionnykh materialov na osnove termoplastichnykh elastomerov. *Vestnik BGTU im. V.G. Shukhova*. 2016;12: 195-199. (In Russian)
13. Hui H, Guannan T, Qingqing G, Haiqing H, Jian Z, Junyu Li. Wall slip of styrene-isoprene-styrene (SIS) triblock copolymer induced by micro elastic phase. *Polymer*. 2020;209: 122990.
14. Hancock M, Rothon RN. *Particulate-Filled Polymer Composites*. Rapra Technology Limited; 2003.
15. Yurkin YV, Mansurova IA, Belozerov VS, Zlobina EA. Morphological and dynamic mechanical analysis of vibration damping composite material based on different elastomers. *Materiale Plastice*. 2018;55: 469-473.
16. Zeyuan S, Jincheng W, Siyuang Y, Shiqiang S. Novel polysiloxane microspheres: Preparation and application in chlorinated butyl rubber (CIIR) damping composites. *Advanced Powder Technology*. 2019;30: 632-643.
17. Russian Federation State Standard. GOST 270-75. *Rubber. Method of the determination elastic and tensile stress-strain properties*. Moscow: Standartinform; 2003. (In Russian)
18. Liu S, Li A, He S, Xuan P. Cyclic compression behavior and energy dissipation of aluminum foam–polyurethane interpenetrating phase composites. *Composites Part A: Applied Science and Manufacturing*. 2015;78: 35-41.
19. Zhang J, Perez RJ, Lavernia EJ. Documentation of damping capacity of metallic, ceramic and metal-matrix composite materials. *Journal of Materials Science*. 1993;28: 2395-2404.
20. Russian Federation State Standard. GOST 263-75. *Rubber. Method for determination of Shore A hardness*. Moscow: Standartinform; 1988. (In Russian)

THE AUTHORS

Avdonin V.V.
e-mail: avdoninvalerii@bk.ru
ORCID: 0000-0002-1069-2413

Yurkin Yu.V.
e-mail: yurkinuv@gmail.com
ORCID: 0000-0003-4310-3379

Shirokova E.S.
e-mail: usr06779@vyatsu.ru
ORCID: 0000-0001-5735-3489

Varankina D.A.
e-mail: gasha.1998.varankina@mail.ru
ORCID: 0000-0002-1651-5098

Rogozhkin R.S.
e-mail: r.rogozhkin1@mail.ru
ORCID: 0000-0003-3966-232X

PAPER TITLE: CENTERED,

TIMES NEW ROMAN 14 BOLD, CAPITAL LETTERS

A.B. Firstauthor[1], C.D. Secondauthor[2*] - Times New Roman 12, bold, centered

[1]Affiliation, address, country - Times New Roman 10, centered

*e-mail: e-mail of the corresponding author - Times New Roman 10, centered

Abstract. Times New Roman 12 font, single line spacing. Abstract should not exceed 12 lines.
Keywords: please, specify paper keywords right after the abstract.

Paper organization. Use Times New Roman 12 font with single line spacing. Use *Italic* font in order to stress something; if possible, please, use **bold** for headlines only.

Page numbering. Please, do not use page numbering.

Tables, Figures, Equations. Please, see the sample file at http://www.mpm.spbstu.ru for more details.

References
References should be subsequently numbered by Arabic numerals in square brackets, e.g. [1,3,5-9], following the sample style below:
[1] Koch CC, Ovid'ko IA, Seal S, Veprek S. *Structural Nanocrystalline Materials: Fundamentals and Applications*. Cambridge: Cambridge University Press; 2007.
[2] Hull D, Bacon DJ. *Introduction to Dislocations*. 5nd ed. Amsterdam: Butterworth-Heinemann; 2011 Available from: https://www.sciencedirect.com/science/book// 9780080966724?via%3Dihub [Accessed 19th June 2018].
[3] Romanov AE, Vladimirov VI. Disclinations in crystalline solids. In: Nabarro FRN (ed.) *Dislocations in Solids*. Amsterdam: North Holland; 1992;9. p.191-402.
[4] Mukherjee AK. An examination of the constitutive equation for elevated temperature plasticity. *Materials Science and Engineering: A*. 2002;322(1-2): 1-22.

[5] Soer WA, De Hosson JTM, Minor AM, Morris JW, Stach EA. Effects of solute Mg on grain boundary and dislocation dynamics during nanoindentation of Al–Mg thin films. *Acta Materialia*. 2004;52(20): 5783-5790.

[6] Matzen ME, Bischoff M. A weighted point-based formulation for isogeometric contact. *Computer Methods in Applied Mechanics and Engineering*. 2016;308: 73-95. Available from: doi.org/10.1016/j.cma.2016.04.010.

[7] Joseph S, Lindley TC, Dye D. Dislocation interactions and crack nucleation in a fatigued near-alpha titanium alloy. To be published in *International Journal of Plasticity. Arxiv.* [Preprint] 2018. Available from: https://arxiv.org/abs/1806.06367 [Accessed 19th June 2018].

[8] Pollak W, Blecha M, Specht G. *Process for the production of molded bodies from silicon-infiltrated, reaction-bonded silicon carbide*. US4572848A (Patent) 1983.

[9] Brogan C. *Experts build pulsed air rig to test 3D printed parts for low carbon engines*. Available from: http://www.imperial.ac.uk/news/186572/experts-build-pulsed-test-3d-printed/ [Accessed 19th June 2018].

Правила подготовки статей:

Рукопись (**английский язык, MS Word и копия PDF**) должна быть направлена в редакцию журнала по электронной почте: **mpmjournal@spbstu.ru**.

После подтверждения принятия статьи в печать, авторы должны отправить подписанные:

1. Соглашение о передаче авторских прав (http://www.mpm.spbstu.ru, раздел «Авторам»);

2. Экспертные заключения о том, что материалы статьи не содержат сведений, составляющих государственную тайну, и информацию, подлежащую экспортному контролю; по адресу:

Россия, 195251, Санкт-Петербург, Политехническая, д. 29, Санкт-Петербургский политехнический университет Петра Великого, Институт передовых производственных технологий, Редакция периодических изданий.

Скан-копии подписанных документов просим направить по электронной почте: mpmjournal@spbstu.ru

Тип файла:

Редакция принимает **файлы MS Word с копией в формате PDF**. Статья должна быть подготовлена в соответствии с настоящей инструкцией, мы просим авторов также следовать более подробным инструкциям на сайте журнала http://www.mpm.spbstu.ru в разделе «Авторам».

Длина статьи:

Статья не должна превышать 30 страниц формата А4, включая Таблицы и Рисунки, размещенные непосредственно в соответствующих местах.

Общие правила оформления статьи:

<div align="center">

НАЗВАНИЕ СТАТЬИ: ВЫРОВНЯТЬ ПО ЦЕНТРУ, ШРИФТ, TIMES NEW ROMAN 14 BOLD, ЗАГЛАВНЫЕ БУКВЫ

</div>

Автор(ы): **А.Б. Первыйавтор[1], В.Г. Автор[2*]** - шрифт Times New Roman 12, bold, по центру

[1]Наименование организации, адрес, страна - шрифт Times New Roman 10, по центру

* e-mail автора, представившего статью - шрифт Times New Roman 10, по центру

Аннотация. Аннотация статьи составляет не более 12 строк. Используйте шрифт Times New Roman 12, одинарный межстрочный интервал.

Ключевые слова: укажите ключевые слова после аннотации.

Как организовать текст статьи. Используйте шрифт Times New Roman 12, одинарный межстрочный интервал. При необходимости выделить какую-либо информацию используйте *курсив*. Используйте **полужирный** шрифт только для заголовков и подзаголовков.

Номера страниц. Пожалуйста, не используйте нумерацию страниц

Таблицы, Рисунки, Уравнения. Подробные правила оформления данных элементов статьи приведены в инструкции на сайте журнала http://www.mpm.spbstu.ru

Литература

Ссылки приводятся в тексте в квадратных скобках [1,3,5-9]. Стиль оформления ссылок:

[1] Koch CC, Ovid'ko IA, Seal S, Veprek S. *Structural Nanocrystalline Materials: Fundamentals and Applications*. Cambridge: Cambridge University Press; 2007.

[2] Hull D, Bacon DJ. *Introduction to Dislocations*. 5nd ed. Amsterdam: Butterworth-Heinemann; 2011 Available from: https://www.sciencedirect.com/science/book// 9780080966724?via%3Dihub [Accessed 19th June 2018].

[3] Romanov AE, Vladimirov VI. Disclinations in crystalline solids. In: Nabarro FRN (ed.) *Dislocations in Solids*. Amsterdam: North Holland; 1992;9. p.191-402.

[4] Mukherjee AK. An examination of the constitutive equation for elevated temperature plasticity. *Materials Science and Engineering: A*. 2002;322(1-2): 1-22.

[5] Soer WA, De Hosson JTM, Minor AM, Morris JW, Stach EA. Effects of solute Mg on grain boundary and dislocation dynamics during nanoindentation of Al–Mg thin films. *Acta Materialia*. 2004;52(20): 5783-5790.

[6] Matzen ME, Bischoff M. A weighted point-based formulation for isogeometric contact. *Computer Methods in Applied Mechanics and Engineering*. 2016;308: 73-95. Available from: doi.org/10.1016/j.cma.2016.04.010.

[7] Joseph S, Lindley TC, Dye D. Dislocation interactions and crack nucleation in a fatigued near-alpha titanium alloy. To be published in *International Journal of Plasticity. Arxiv*. [Preprint] 2018. Available from: https://arxiv.org/abs/1806.06367 [Accessed 19th June 2018].

[8] Pollak W, Blecha M, Specht G. *Process for the production of molded bodies from silicon-infiltrated, reaction-bonded silicon carbide*. US4572848A (Patent) 1983.

[9] Brogan C. *Experts build pulsed air rig to test 3D printed parts for low carbon engines*. Available from: http://www.imperial.ac.uk/news/186572/experts-build-pulsed-test-3d-printed/ [Accessed 19th June 2018].

MPM
SCIENTIFIC
JOURNAL